DESIGN, SYNTHESIS, AND CHARACTERIZATION OF LANTHANIDE-BASED NEAR-INFRARED DENDRIMER COMPLEXES AND METAL-ORGANIC FRAMEWORKS FOR NOVEL MODALITIES IN OPTICAL BIOLOGICAL IMAGING

by

Kristy A. Gogick

B.S., The University of Scranton, 2007

Submitted to the Graduate Faculty of the

Kenneth P. Dietrich School of Arts and Sciences in partial fulfillment

of the requirements for the degree of

Doctor of Philosophy

University of Pittsburgh

2015

UNIVERSITY OF PITTSBURGH

KENNETH P. DIETRICH SCHOOL OF ARTS AND SCIENCES

This dissertation was presented

by

Kristy A. Gogick

It was defended on

April 9, 2015

and approved by

David H. Waldeck, Professor, Department of Chemistry

Marcel Bruchez, Associate Professor, Department of Chemistry, Carnegie Mellon Unviersity

Dissertation Co-Advisor: Nathaniel L. Rosi, Associate Professor, Department of Chemistry

Dissertation Co-Advisor: Stéphane Petoud, Adjunct Professor, Department of Chemistry

DESIGN, SYNTHESIS, AND CHARACTERIZATION OF LANTHANIDE-BASED NEAR-INFRARED DENDRIMER COMPLEXES AND METAL-ORGANIC FRAMEWORKS FOR NOVEL MODALITIES IN OPTICAL BIOLOGICAL IMAGING

Kristy A. Gogick, PhD

University of Pittsburgh, 2015

Biological imaging in the near-infrared (NIR) region is advantageous because: (i) there is low biological autofluorescence, (ii) less interaction with and perturbation of biological materials, and (iii) NIR light scatters less than visible light. Several lanthanide cations emit in the NIR and in complexes they display: (i) narrow emission bands, (ii) constant emission wavelengths not affected by the environment, and (iii) enhanced photostability relative to organic fluorophores. Initially we studied the generation-3 poly(amido amine) dendrimer as a platform for organizing and sensitizing europium cations. We demonstrated the capability of this functionalized material to preferentially accumulate in tumors and be utilized for both *in vivo* and *ex vivo* imaging. In order to more rigidly organize the lanthanides cations we transitioned to using them as the metal in metal-organic frameworks (MOFs). We developed a barcoded MOF, Er_xYb_{1-x}-PVDC-1, exhibiting enhanced erbium emission relative to Er-PVDC-1, making it a promising material for telecommunications devices. A slight modification to the synthesis yielded a MOF with a different crystal structure, Yb-PVDC-3. The analogous nanoscale version of this MOF, nano-Yb-PVDC-3 was attained through a reverse microemulsion synthesis. Altering the ratio of the lanthanides in the synthesis resulted in nanoscale barcoded MOFs, nano-Nd_xYb_{1-x}-PVDC-3, with tunable photophysical properties. The nano-Yb-PVDC-3 was extensively studied for use as a biological imaging agent. It was taken up by cells (HeLa and NIH 3T3) and successfully used for live imaging in both the visible and NIR regions. Focusing on biologically-friendly ligands,

a series of size-controllable Yb(BTC)(H_2O) MOFs were synthesized using sodium acetate as a modulator. The photophysical properties of these MOFs were not size-dependent, allowing for the selection of material based solely on size considerations. In order to shift the excitation wavelength to the NIR region a dye which absorbs at lower energy was incorporated with a Yb(BTC)(H_2O) nanoMOF to produce a dye-incorporated material. Despite the incorporation of only a very small amount of the dye, its excitation generated sensitized Yb^{3+} emission. The dye-incorporated material was coated with a silica shell to enhance the NIR emission intensity in water. This material has great potential to be used as a biological imaging agent.

TABLE OF CONTENTS

LIST OF TABLES

LIST OF FIGURES

LIST OF EQUATIONS

ACKNOWLEDGMENTS

The completion of this dissertation has been a long journey in which many people have played a role. I will do my best to thank everyone, but please know that if I inadvertently missed you, you are no less appreciated.

I am grateful to Prof. Stéphane Petoud for serving as my advisor and illuminating the world of lanthanide luminescence for me. Operating on two different continents for a majority of my time in graduate school was certainly a challenge, but traveling to France for two months to work with my counterparts across the ocean was undoubtedly the highlight of my research experience. I have learned so much because of you. Prof. Nathaniel Rosi welcomed me into his group and provided insightful commentary on so much more than just MOFs; thank you for making me a better scientist. I also want to thank the other members of my thesis committee, Prof. David Waldeck and Prof. Marcel Bruchez, for their time and helpful suggestions.

I am honored to have received the Mary E. Warga Pre-doctoral Fellowship. This award not only allowed me to focus on research instead of teaching early in my studies, but it helped fund my research trip to France. I am humbled to be named among the recipients of this award.

I want to express my gratitude to all of the members of the Petoud group who provided me with so much wisdom and support, even after moving on to bigger and better things: Paul Badger, Demetra Chengelis Czegan, Adrienne Yingling Oxley, Samuel Oxley, Chad Shade, Hyounsoo Uh, and Jian Zhang. I am thankful to the members of the Petoud group in Orléans,

France, who worked with me, patiently translated everything into English, and endured many Skype meetings: Guillaume Collet, Svetlana Eliseeva, Josef Hamacek, Claudine Kieda, Agnès Pallier, Sunčica Vujica, but most especially Alexandra Foucault-Collet and Sandrine Villette for both their excellent work and their hospitality while I was in Orléans. I am ever appreciative of the Rosi group for their inclusiveness and sharing not only their MOF expertise but also their instruments and ovens: Jihyun An, Leekyoung Hwang, Tao Li, Chong Liu, Tianyi Luo, Andre Merg, Patrick Muldoon, Soumitra Mokashi Punekar, Ryan Ruenroeng, Jessica Sammons, Chengyi Song, Alex Spore, Chen Zhang, Yicheng Zhou, and in a special way Kiley White who was not only my first collaborator but also a great friend. I am grateful to Christopher Andolina for many enlightening conversations.

Thank you to Prof. Alexander Star and Gordon Chiu in our Department of Chemistry, the Department of Mechanical Engineering and Materials Science (MEMS) in the Swanson School of Engineering, and the Nanoscale Fabrication and Characterization Facility (NFCF) in the Petersen Institute of NanoScience and Engineering (PINSE) for training and access to instrumentation. I will forever be grateful to Prof. Michelle Ward for use of her instruments, but more importantly unparalleled mentorship and a wonderful teaching experience in which I learned at least as much as the students.

Often working behind the scenes, but still very much appreciated are the entire staff of the Main Office, the Stockroom, the Machine Shop, the Electronics Shop, the Glass Shop, and the Materials Characterization Facility.

Much gratitude goes to my friends for being there to laugh and to cry, to commiserate and to celebrate, to challenge and to support. Specials thanks and many hugs to Jennifer Zurek, my partner in crime for as long as I can remember; I don't know what I'd do without you. Much

love to my fiancé, Jason Marshall, for supporting me in everything and always telling me everything would work out. I know I haven't always been the easiest person to deal with, but there's no one else I'd want to make this journey with. Finally, my eternal gratitude to my family. To my grandmothers, Bacie and Nana, who made sure I didn't starve while I was on the other side of the state. Pittsburgh does have food, but it just doesn't compare to those homemade delicacies you made with so much love. To my cousin, Patti, who was continuously ready for a roadtrip and was always, always there for me. To my parents, Karen and Al, who have supported and loved me my entire life. There are no words to adequately express my gratitude and love.

I only wish Ma was here to see this dissertation brought to a completion.

1.0 INTRODUCTION

1.1 NEAR-INFRARED PHOTONS

The near-infrared (NIR) region of the electromagnetic spectrum is on the lower energy side of the visible region; that is to say at wavelengths greater than ~700 nm which cannot be detected by the human eye. The lower energy boundary of the region is less well defined. The Commission Internationale de l'Eclairage (CIE)[1] defines it as the 700-1400 nm wavelength range; the International Organization for Standardization (ISO)[1] specifies the range 780-3000 nm; the Infrared Processing and Analysis Center (IPAC)[2] at the California Institute of Technology utilizes the larger region of 700-5000 nm. For the purpose of this document, the NIR range will refer to the region 650-1600 nm unless otherwise stated.

1.1.1 NIR barcodes and encryption

Barcodes are optical representations of data, generally relating to the material to which they are affixed, which can be read rapidly by a machine. The most well-known style of barcode is a series of parallel vertical black lines on a white background in which the width and spacing of each line is varied in order create unique patterns. This is known as a linear or one-dimensional (1-D) barcode. The barcodes that now appear universally on consumer merchandise are termed universal product codes (UPC).[3] The first instance of such a barcode being used in a grocery store checkout was on a pack of Wrigley's chewing gum in 1974.[3,4] Over time barcodes have evolved to include shapes other than lines and have expanded to be two-dimensional (2-D).

The universality of these types of barcodes in terms of both generating and reading are advantageous in that they allow many users to interface using a common system with well-developed technology.[3] That same universality and ubiquity make them undesirable, however, for encryption tags. There are a multitude of materials that benefit from authentication such as identification cards, currency, pharmaceuticals, and military shipments. In these instances it is a security risk for the barcode to be easily reproducible or even noticeable. For this very reason NIR barcodes are being explored.

NIR emission cannot be detected by the naked human eye, making it impossible to know the readout of a NIR barcode without specialized equipment. Handheld spectrometers are becoming more common and should not be a roadblock to utilizing such technology.[5,6] Being unable to know the readout makes it almost impossible to duplicate the barcode and use it on an unauthentic material. This can help in a variety of areas including reducing forged currency being placed into circulation as well as ensuring that pharmaceuticals are untainted.

1.1.2 NIR biological imaging

Ideally, all biological imaging would take place in the NIR region of the electromagnetic spectrum. There is a "NIR Window" in which biological species have very little native fluorescence (autofluorescence) compared to the ultraviolet (UV) and visible (vis) regions.[7,8] This advantage allows for more sensitive detection as well as easier discrimination of the signal from the background. In the NIR region biological materials have a lower molar absorptivity (Figure 1.1) which allows for deeper penetration and leads to less invasive imaging and diagnostics.[7,8] In addition to NIR light allowing for deeper penetration in tissues, it also provides improved resolution optical imaging because NIR light scatters less than visible light.[9,10]

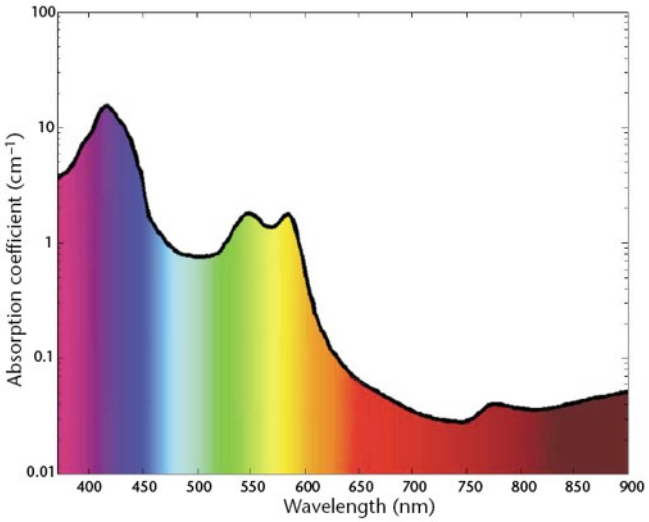

Figure 1.1. Graphical representation of the reduced absorption of biological materials in the 650-900 nm region. Adapted by permission from Macmillan Publishers Ltd: *Nature Medicine* (*Nat. Med*. **2003,** *9,* 123-128.), copyright 2003.

1.2 LANTHANIDES

The elements with atomic numbers fifty-seven to seventy-one, lanthanum to lutecium are the lanthanides (Ln). These elements comprise a portion of the larger group of elements known as the rare-earths. With the exception of promethium they are all found in nature, most often as ores in the form of lanthanide orthophosphates.[11,12] Promethium is not found in nature but as a result of the spontaneous fission of ^{238}U and is known to have isotopes ranging from ^{140}Pm to ^{156}Pm.[12] The lanthanides are often present as a mixture in nature and are difficult to separate given their similar reactivities.[12]

Figure 1.2. Lanthanide series.

Lanthanide cations (Ln^{3+}) can have coordination numbers that range from three to twelve, but eight and nine are the most common for complexes in solution.[12] Lanthanide complexes can be formed with ligands containing nitrogen, sulfur, and phosphorus, but the most stable complexes are formed with ligands that possess oxygen donating groups; Ln^{3+} acts as a hard Lewis acid and forms the most stable bonds with hard Lewis bases.[12] The lanthanides are the most stable in the tripositive oxidation state (Ln^{3+}), but some lanthanides can also be observed in the 2+ oxidation state: Sm^{2+}, Eu^{2+}, and Yb^{2+}, as well as the 4+ oxidation state: Ce^{4+}, Pr^{4+}, and Tb^{4+}.[12] As the atomic number of the lanthanides increases, the cationic radius (Ln^{3+}) decreases from 1.17 Å for lanthanum to 1.00 Å for lutecium in what has been dubbed the "Lanthanide Contraction".[12]

1.2.1 Lanthanide luminescence

The lanthanide cations have the electronic configuration [Xe]$4f^n$ where n = 0-14 increasing by one electron for each element from lanthanum to lutecium.[11-13] These 4*f* electrons are well shielded from external fields by the $5s^2$ and $5p^6$ shells, resulting in sharp emission bands that are largely unaffected by the environment of the lanthanide.[11-13] The lanthanides emit in both the visible and NIR regions of the electromagnetic spectrum (Figure 1.3). Eu^{3+} and Tb^{3+} emit in the

visible; Nd^{3+}, Ho^{3+}, Er^{3+}, Tm^{3+}, and Yb^{3+} emit in the NIR; Sm^{3+}, Dy^{3+} have transitions in both visible and NIR domains.[11,13-15]

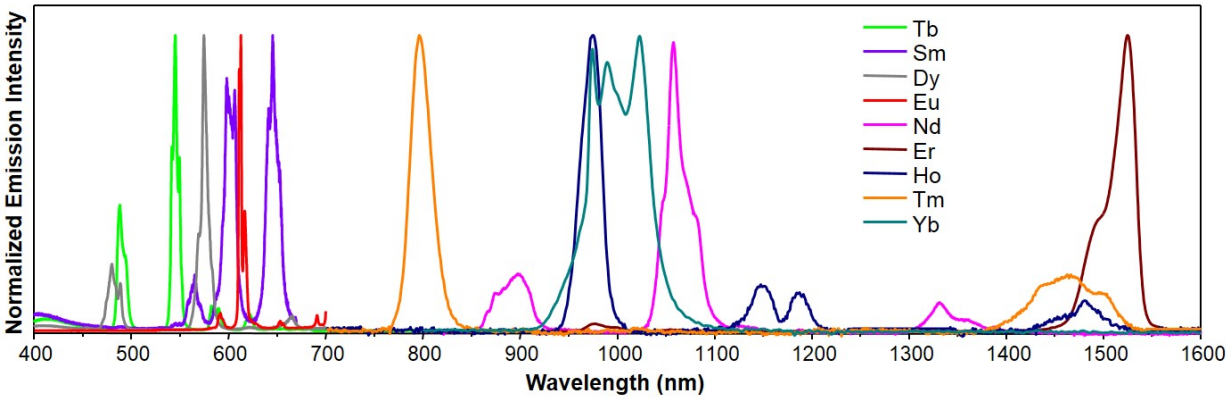

Figure 1.3. Normalized emission spectra for selected lanthanide cations.[14,15]

The sharp, distinct bands exhibited by Ln^{3+} allow for spectral discrimination among different lanthanides, whereas organic emission is typically broad (often on the order of 100 nm) and consequently more difficult to discriminate.[11-13] Lanthanides also have large spectral gaps between their excitation and emission bands which prevent re-absorption processes for more accurate quantitative detection.[11] Lanthanide complexes are not as prone to photobleaching as organic fluorophores which allows lanthanide complexes to endure repeated light exposure with a negligible loss of signal making them well suited for imaging applications.[16] In addition, lanthanide complexes have longer lifetimes (micro- to milliseconds) than organic fluorophores (nanoseconds) which facilitates temporal discrimination from shorter lived autofluorescence (Figure 1.4) and makes them especially advantageous for biological imaging.[17]

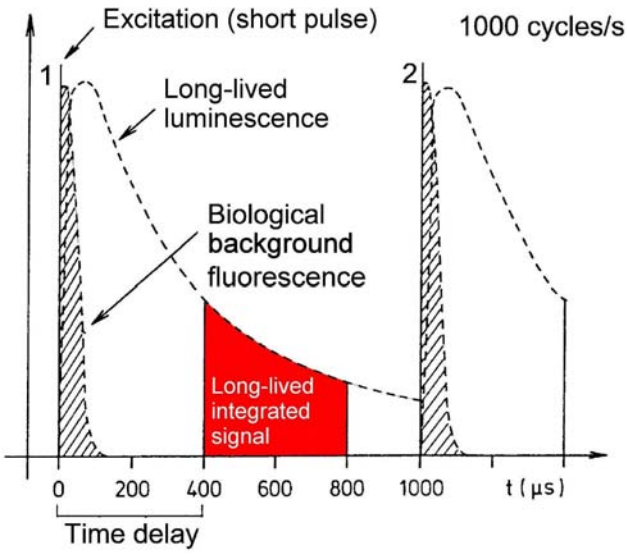

Figure 1.4. Graphical representation of the time delay that can be fixed after the excitation flash during spectroscopic measurements to discriminate Ln^{3+} signal from background autofluorescence as a result of the longer luminescence lifetimes of Ln^{3+}.[18]

1.2.2 Antennae effect

The $f \rightarrow f$ transitions which occur in Ln^{3+} are formally LaPorte forbidden. This first selection rule states that transitions are only allowed if there is a change of parity.[11,13,19] Therefore, $f \rightarrow f$ transitions are statistically unlikely because of the difficulty of populating their excited states due to their small molar absorptivity; however, they are still possible as some parameters will decrease the level of forbiddenness.[11,13,19] In order to overcome this limitation, energy can be transferred to the excited states of lanthanide via the "antenna effect."[20] In this process, a chromophore in close proximity to the Ln^{3+} absorbs as much light as possible and subsequently transfers the resulting energy to the accepting excited state of the lanthanides. The chromophore

absorbs a photon of light and promotes an electron to an excited vibrational level of the excited electronic state. There is non-radiative decay to the lowest vibrational level of the excited singlet state followed by either emission (fluorescence) or an intersystem crossing to the lower-energy triplet state. Once in the triplet state there is a route for non-radiative decay to the lowest vibrational level followed by either emission (phosphorescence) or transfer to the accepting excited state of the lanthanide. The lanthanide excited state can be depopulated through non-radiative decay or emit via an $f \rightarrow f$ electronic transition (luminescence). The most common sources of non-radiative decay of the excited state Ln^{3+} are -OH, -NH, and -CH oscillators.[11] Therefore, an ideal antenna must not only efficiently transfer energy to the Ln^{3+} but must also protect it from solvent molecules.

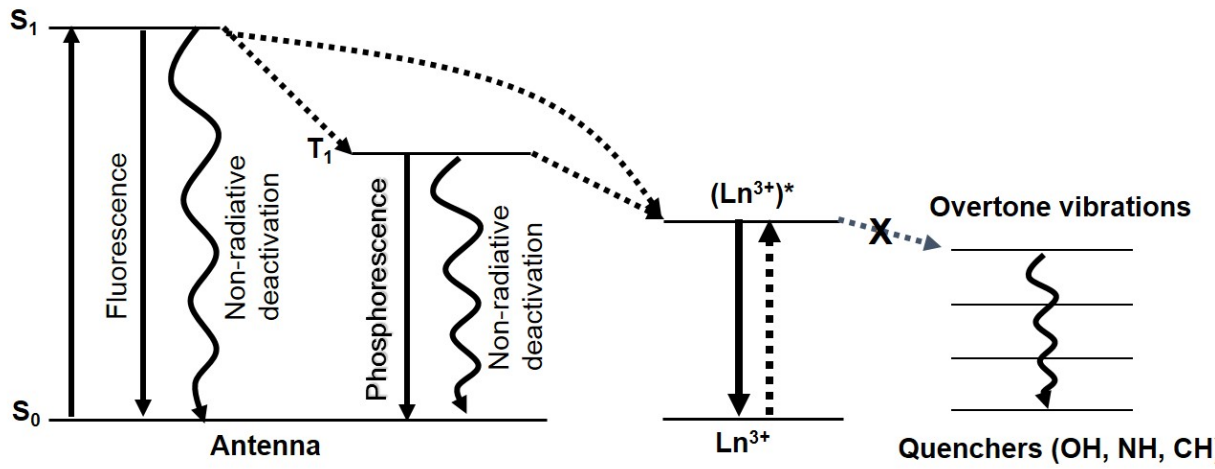

Figure 1.5. Perrin-Jablonski diagram demonstrating both the mechanism of sensitization of Ln^{3+} via the antenna effect and the potential for relaxation via radiative and non-radiative deactivation.

There are three mechanisms of the transfer of energy from the chromophore to the lanthanide – Förster, Dexter, and non-concerted electron transfer. Förster theory[21] states that

energy transfer takes place through dipole-dipole interactions between a donor and an acceptor, and the probability of energy transfer is inversely proportional to R^6, where R is the distance between the two species. This mechanism is different from the process of light re-absorption and can only take place over limited distances (50-100 Å). The donor absorbs energy and is excited to a vibrational level of the excited electronic state. Through the process of obtaining thermal equilibrium with its surroundings it relaxes to the lowest vibrational level of the excited state where it remains for at least 10^{-8} seconds before relaxing to the ground state. The acceptor must have an absorption transition whose energy matches the emission transition of the donor. When this requirement is met, and there is energetic coupling between the donor and the acceptor, the transfer of excitation energy from donor to acceptor takes place. Dexter theory[22] states that energy transfer occurs via an exchange interaction through orbital overlap between the donor and the acceptor. This requires the donor and the acceptor to be in much closer proximity than necessary for the Förster mechanism. As most lanthanide cations cannot be reduced due to their redox potential, the electron exchange between the donor and the acceptor must be concerted to avoid any change in the oxidation state of the Ln^{3+}. In addition, Dexter's theory is expanded from Förster's theory to include forbidden transitions.

For some specific lanthanide cations (Eu, Sm, and Yb) a redox or electron transfer mechanism has been used to describe the energy transfer.[23,24] In these complexes the excited state ligand reduces the Ln^{3+}, so the oxidation potential of the donor and the reduction potential of the Ln^{3+} determine the feasibility of the process.[23,24]

1.2.3 Luminescence quenching

Not all lanthanides emit with the same intensity. The strength of emission depends on how easily the excited state(s) can be populated and how easily they can be de-populated via non-radiative decay.[11,13] Population of the excited state(s) depends a great deal on the efficiency of sensitization by the chromophore. The ease of non-radiative decay is directly related to the size of the energy gap between the accepting level and ground state of the lanthanide.[11,13] The smaller the gap, the more opportunities for non-radiative decay due to overtones of-CH, -NH, or -OH oscillations. Eu^{3+} and Tb^{3+} both have relatively large energy gaps, which is part of the reason why extensive work has been done with these lanthanides.[11,13,25]

Special attention has been paid to -OH oscillations because of the interaction that occurs in aqueous solutions. It has been shown that the rate of non-radiative deactivation of Ln^{3+} is directly proportional to the number of -OH oscillators in the inner coordination sphere of the lanthanide.[26-30] Extensive experimental work has been done to develop an empirical relationship that helps quantify the number of water molecules interacting in the inner coordination sphere (q).[31-35] The general equation is[11,13]:

$$q = A(k_{H_2O} - k_{D_2O} - B) - C$$

Equation 1.1.

where k_{H2O} and k_{D2O} are the deactivation rate constants (which are inversely proportional to the observed lifetimes) in H_2O and D_2O, respectively; and A, B, and C are lanthanide-specific values determined experimentally. A represents the sensitivity to inner sphere quenching, and experimentally determined values have been greatly debated in the literature. C is a constant which represents the quenching of outer sphere water molecules.[36] The value of B is equal to the value of k_{XH} in the equation:

$$k_{XH} = \alpha + \beta_{nOH} + \gamma_{nNH} + \delta_{nO=CNH}$$

Equation 1.2.

where α, β, γ, and δ are the respective contributions of the oscillators to deactivation of the excited state of a particular Ln^{3+}, and n_{OH}, n_{NH}, and $n_{O=CNH}$ are the number of -OH, -NH, and carboxylic oxygens of the amide -NH oscillators that are in the inner coordination sphere of Ln^{3+}, respectively.[32,34]

1.3 DENDRIMERS

One way to increase the emitted signals of lanthanide complexes and the corresponding detection sensitivity is to create polymetallic complexes which possess a large number of sensitizers per unit volume. This strategy can be achieved by coordinating a large number of emitting lanthanide cations within the interior of a dendrimer where their need for a high coordination number can be satisfied while placing them in proximity to several chromophores attached to the ends of the branches of the dendrimer.

1.3.1 Dendrimer structure and synthesis

Dendrimers are a class of highly branched star-like molecules.[37-39] There are three main regions of a dendrimer: the core, the interior branches (sometimes called the dendritic structure), and the terminal functional groups.[37,38] At the heart of the dendrimer is the core, from which branches extend. The core plus one series of branches extending from the termini is referred to as generation zero (G0) dendrimer. Adding another series of branches to each of the termini results

in a generation-1 (G1) dendrimer. As the number of generations increase, so too do the number of terminal groups.

Taking the poly(amido amine) (PAMAM) dendrimer[39] as an example: the core, ethylenediamine, can be seen in Figure 1.6.

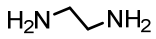

Figure 1.6. Ethylenediamine core of the PAMAM dendrimer.

Adding branches to the two nitrogen atoms results in a G0 PAMAM dendrimer, which can be seen in Figure 1.7. There are now four terminal amine groups.

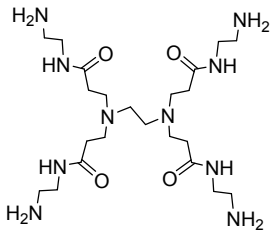

Figure 1.7. Structure of G0 PAMAM dendrimer.

Adding branches to the terminal amines results in a G1 PAMAM dendrimer, which can be seen in Figure 1.8. There are now eight terminal amine groups.

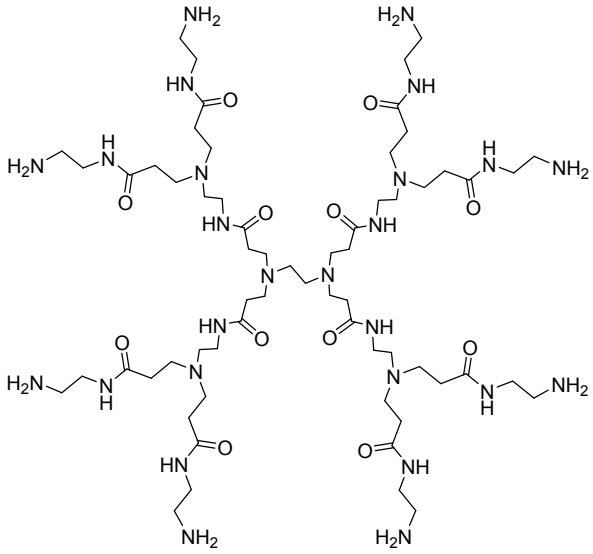

Figure 1.8. Structure of G1 PAMAM dendrimer.

Adding branches to the terminal amines results in a generation-2 (G2) PAMAM dendrimer, which can be seen in Figure 1.9. There are now 16 terminal amine groups.

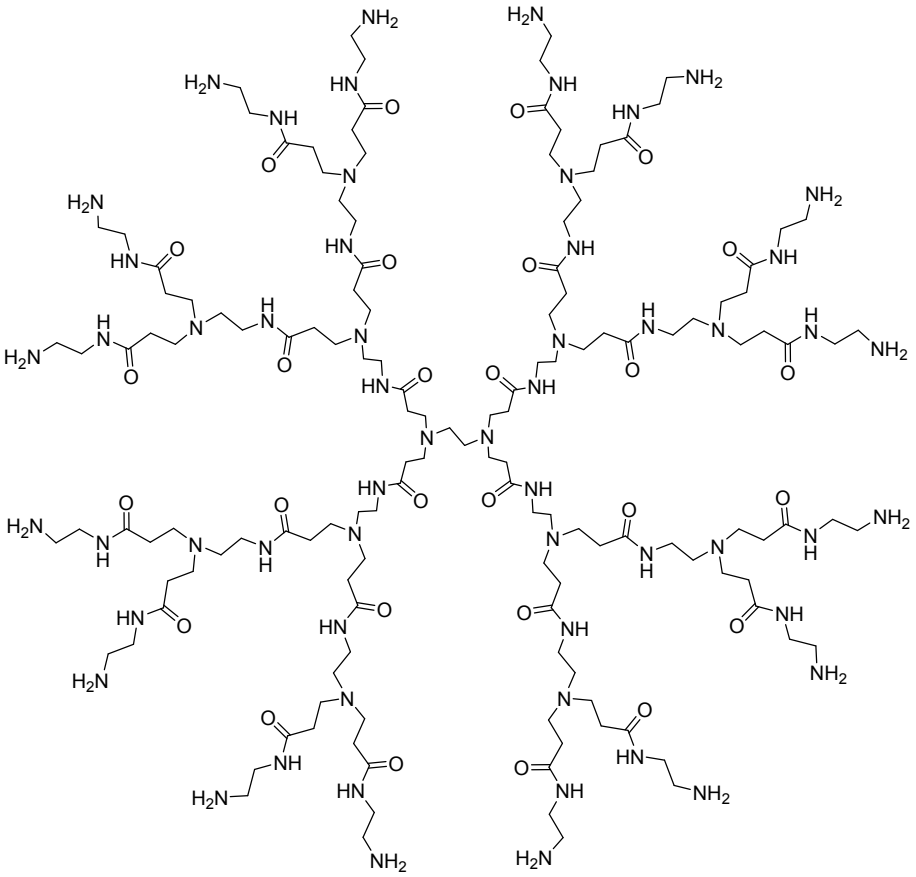

Figure 1.9. Structure of G2 PAMAM dendrimer.

Adding branches to the terminal amines results in a generation-3 (G3) PAMAM dendrimer, which can be seen in Figure 1.10. There are now 32 terminal amine groups.

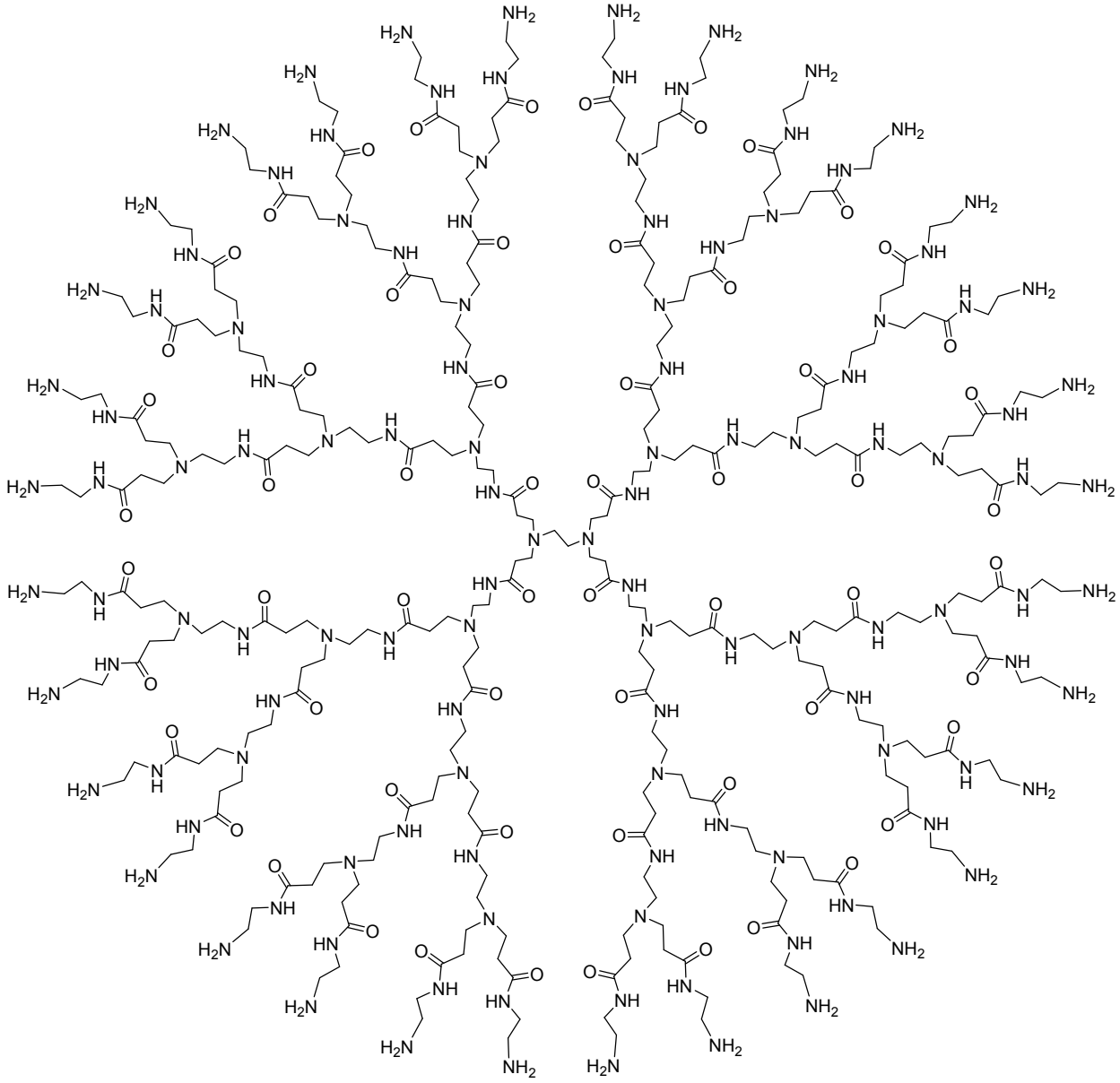

Figure 1.10. Structure of G3 PAMAM dendrimer.

This process of increasing the number of branches for this particular dendrimer can be continued through generation-11 (G11).[40]

While perhaps most well-known because of their commercial availability[41], PAMAM dendrimers are only one of many reported dendrimers. Based on different chemical

functionalities, some examples include: poly(propylene imine) (PPI), poly(propylene amine) (POPAM), and poly(ethylene imine) (PEI).[37,42]

There are two basic, but fundamentally different, ways of synthesizing dendrimers. The divergent method is similar to the example above in which the dendrimer branches are extended outward from the core.[38,39,42] This method was initially used to synthesize a series of PAMAM dendrimers.[39] Conversely, the convergent method starts at the termini and builds toward the core of the dendrimer.[38,42,43] In this case, several dendritic wedges are synthesized and then coordinated to a multi-functional core to deliver a complete dendrimer structure.[43] Both methods are represented in Figure 1.11.

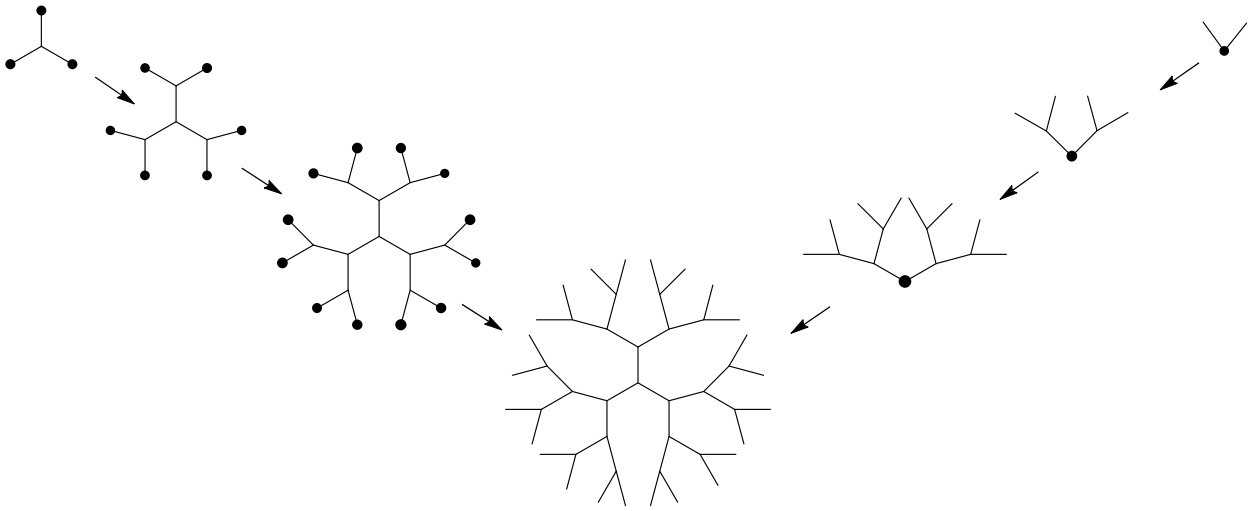

Figure 1.11. Schematic representation of the divergent (*left*) and convergent (*right*) methods for synthesizing a dendrimer where the black dots represent the reaction sites.[42]

1.3.2 Dendrimer applications

Due to the relative ease with which the dendrimer scaffold can be modified to suit a variety of purposes and functions, dendrimers have been synthesized and modified for an assortment of applications. They have been used as sensors for metal cations[44], inorganic anions[45], and small organic molecules[46]. Amphiphillic dendrimers have been compared to micelles[38,47] in that they have distinct interior and exterior regions and as such have been used to solubilize both hydrophobic[48-51] and hydrophilic[52-54] molecules and have been explored as vehicles for drug delivery[49,55-66] and photodynamic therapy[65,67-69]. Dendrimers are also being probed for potential use in health care applications such a gene therapy[65,66,70-72] and as magnetic resonance imaging (MRI) contrast agents[65,73-76].

1.3.3 Lanthanide-containing dendrimers

When used as MRI contrast agents, dendrimers often contain gadolinium ions (Gd^{3+}) which are coordinated within the branches. This strategy has been used with other lanthanides[77-82], often with a goal of enhanced lanthanide luminescence. This placement is advantageous in that it has the potential for the coordination of multiple lanthanides within a single dendritic architecture and helps to protect the lanthanide ions from unfavorable interactions with quenching molecules such as water. In a few cases a single lanthanide cation has been utilized as the core of a dendrimer.[83-86] In these structures it is possible to determine the exact location of the lanthanide cation.

1.4 METAL-ORGANIC FRAMEWORKS

Another way in which the advantageous NIR emission of the lanthanides may be utilized while simultaneously fulfilling the requirements of sensitization via the antennae effect and protection from quenching vibrations is to use lanthanides as the metal ions in metal-organic frameworks (MOFs). As previously described for dendrimer complexes, MOFs can possess a high density of lanthanide cations and sensitizers per unit volume. In contrast to dendrimer complexes, however, it is possible to unambiguously identify the location of each lanthanide within the rigid structure.

1.4.1 Metal-organic frameworks

MOFs are a class of crystalline solid-state materials consisting of metal ions or clusters that are periodically linked together by polytopic organic linkers. Changing the metal ion, the organic linker, or any of the synthetic conditions such as solvent, concentration, time, temperature, pressure, or pH can change the composition, structure, and properties of the final material. Since MOFs are crystalline structures it is possible to unambiguously identify the position of every single atom, making it easier to fully characterize the material and elucidate structure-function relationships. Due to their modular construction, chemical tailorability, and their intrinsic porosity, MOFs have been targeted for applications in gas storage[87,88], separations[87,88], catalysis[87-89], sensors[90,91], drug delivery[88,90,92-94], and biological imaging[88,90,92,94,95].

1.4.2 Secondary building units

The rigid metal-carboxylate units that are formed may be referred to as secondary building units (SBUs). SBUs have a definite geometry which can be used to predict possible MOF structures. SBUs can be discrete clusters[96,97] with distinct geometries including triangles, tetrahedrons, octahedrons, and cubes. As an example, the octahedral $Zn_4O(CO_2)_6$ unit in MOF-5 (Figure 1.12) can be viewed as a "joint."[98,99] These joints are connected together by the benzene ring of terephthalate, which can be viewed as a "strut."[99]

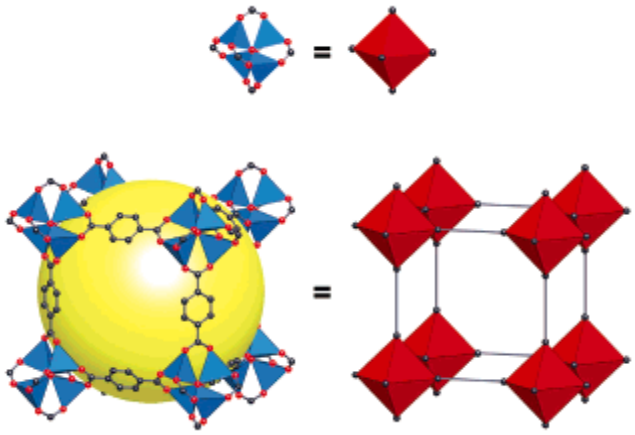

Figure 1.12. The $Zn_4O(CO_2)_6$ (Zn tetrahedra, blue; O, red sphere; C, gray sphere) SBU and an equivalent representation of the SBU as a red octahedron (*top*). MOF-5 with the same SBUs linked together by benzenes in the terephthalate ligand to form a cubic network (*bottom*). Reprinted with permission from *J. Am. Chem. Soc.* **2005,** *127,* 1504-1518. Copyright 2005 American Chemical Society.

SBUs can also take the form of infinite rods or chains as in MOF-75 (Figure l.13) in which eight-coordinate Tb^{3+} ions are coordinated by four carboxyl groups, one bidentate nitrate ligand, and two terminal solvent molecules.[99]

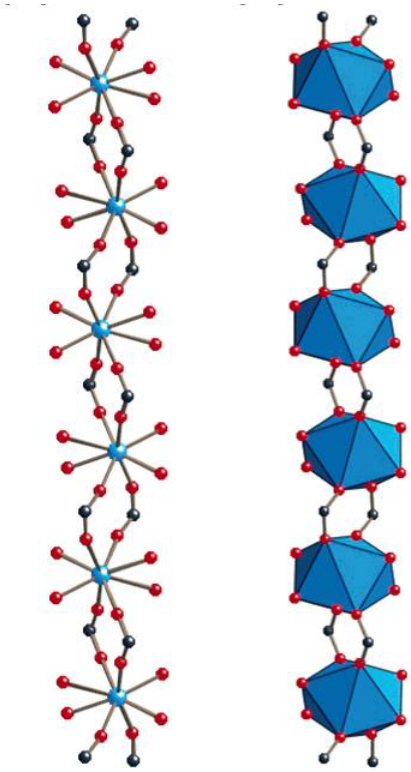

Figure 1.13. Ball and stick representation of MOF-75 SBU (Tb, blue; O, red; C, black) (*left*). SBU with Tb shown as blue polyhedra (*right*). Reprinted with permission from *J. Am. Chem. Soc.* **2005,** *127,* 1504-1518. Copyright 2005 American Chemical Society.

1.4.3 Organic ligands

Organic ligands are often chosen based on the structure and function they are anticipated to impart to a MOF. By maintaining the same SBU and altering the linker the pore size can be systematically increased as was demonstrated with MOF-5 (IRMOF-1).[100] The organic ligand in MOF-5 is 1,4-benzenedicarboxylic acid (BDC).[98] In a series of syntheses progressively longer

ligands were used to generate a collection of MOFs having the same topology, but increasing pore dimensions (Figure 1.14).[100]

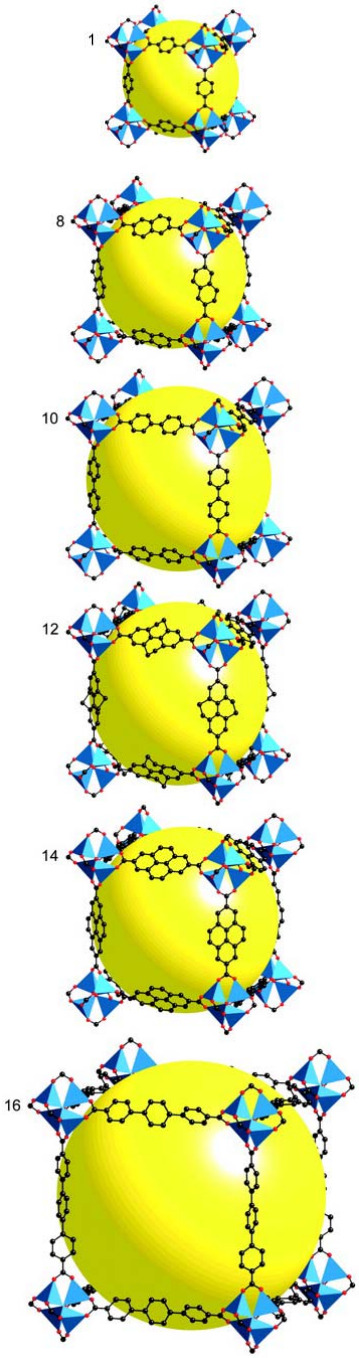

Figure 1.14. IRMOF-n (n = 1, 8, 10, 12, 14, 16; top to bottom) demonstrating the increase in pore size (represented by the yellow sphere) as the organic linker increases in length (Zn, blue polyhedra; O, red spheres; C, black spheres). From *Science* **2002,** *295,* 469-472. Reprinted with permission from AAAS.

The same system was used to demonstrate that it is also possible to change the functionality of the organic ligand while maintaining the same topology.[100] The BDC was modified with bromo, amino, *n*-propoxy, *n*-pentoxy, cyclobutyl, and fused benzene functional groups before being used to synthesize IRMOF-2 through IRMOF-7, respectively, which can be seen in Figure 1.15.[100]

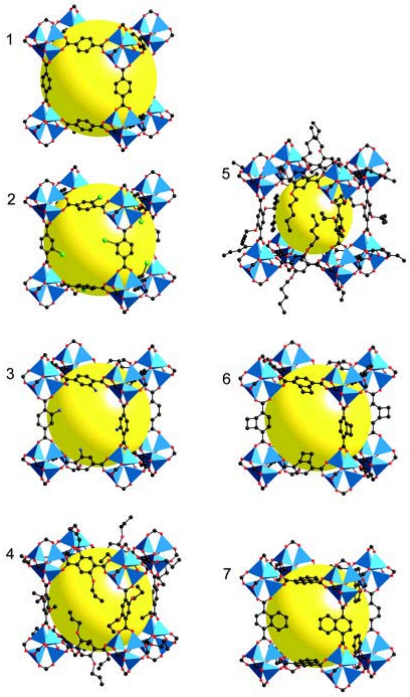

Figure 1.15. IRMOF-1 through IRMOF-7 demonstrating different ligand functionality while maintaining the same topology (Zn, blue polyhedra; O, red spheres; C, black spheres; Br, green spheres; amino-groups, blue spheres in IRMOF-3). From *Science* **2002,** *295,* 469-472. Reprinted with permission from AAAS.

1.4.4 Lanthanide metal-organic frameworks

While MOFs are most commonly constructed using transition metal ions, lanthanide ions have also been widely used.[90,91,95] The ligands are able to fulfill the high coordination number necessary for lanthanide cations (Ln^{3+}) as well as protecting them from quenchers. Additionally the ligands function as antennae and can sensitize multiple lanthanides. As an example, Serre et al.[101] synthesized a yttrium MOF, MIL-78, and separately doped in europium (Eu^{3+}), terbium (Tb^{3+}), or dysprosium (Dy^{3+}). Excitation at 252 nm resulted in emission of each of those lanthanides (Figure 1.16).

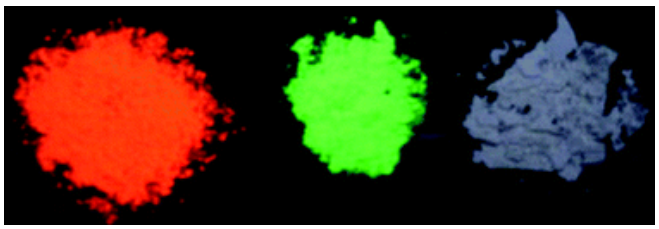

Figure 1.16. Optical emission upon excitation at 252 nm of MIL-78 doped with Eu^{3+} (*left*), Tb^{3+} (*center*), and Dy^{3+} (*right)*. Reproduced from *J. Mater. Chem.* **2004,** *14,* 1540-1543 with permission of The Royal Society of Chemistry.

Since all Ln^{3+} possess similar reactivities it is not uncommon to have a series of isostructural MOFs in which the ligand stays constant but a variety of lanthanides are independently incorporated.[90,95] One such example is a series of 1,3,5-benzenetricarboxylic acid (BTC) MOFs with the formula $Ln(BTC)(DMF)_2 \cdot H_2O$ (Ln = Tb, Dy, Ho, Er, Tm, Yb; DMF = dimethylformamide).[102] The only thing that was altered in each synthesis was the $Ln(NO_3)_3 \cdot xH_2O$ (Ln = Tb, Dy, Ho, Er, Tm, Yb) salt. Using the ligand 1,4-benzenedicarboxylic

acid (BDC) another series of isostructural MOFs, $[Ln_2(bdc)(H_2O)_4]_n$ (Ln = Y, La, Ce, Pr, Nd, Sm, Eu, Gd, Tb, Dy, Ho, Er, Tm), were synthesized.[103]

MOFs are polymetallic with many Ln^{3+} per unit volume which enables the system to overcome the notoriously small quantum yields of NIR-emitting luminescent lanthanide materials. Often only the luminescence properties of the Eu^{3+} and Tb^{3+} MOFs are explored due to their prominent visible signals (Figure 1.17).[90,95] Gadolinium MOFs, while not luminescent, have been explored for their potential as a magnetic resonance imaging (MRI) contrast agents (Figure 1.17).[104-106]

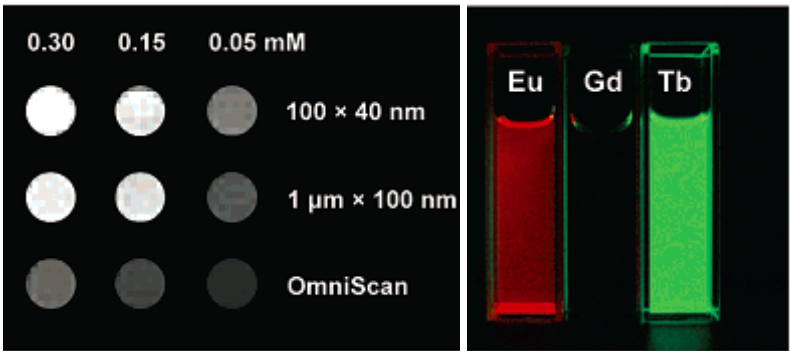

Figure 1.17. Magnetic resonance images of the $Gd(BDC)_{1.5}(H_2O)_2$ nanoscale MOF (*left*). Luminescence images (*right*) of $Gd(BDC)_{1.5}(H_2O)_2$ nanoscale MOF (*center*, no emission) and the same nanoMOF doped with 5 mol % Eu (*left*, red emission) and 5 mol % Tb (*right*, green emission). Reprinted from *J. Am. Chem. Soc.* **2006,** *128,* 9024-9025. Copyright 2006 American Chemical Society.

1.4.5 Nanoscale metal-organic frameworks

In order to be most effective for biological applications, such as imaging, MOFs need to be nanoscale in size. Lin's group achieved the creation of nanoscale MOFs (nanoMOFs) through a reverse microemulsion synthesis whereby varying the molar ratio of water to surfactant (*W*) altered the size of the resulting particle (Figure 1.18).[104,105,107,108] Other methods that have been developed include the use of modulators[109-111], microwaves[112-114], and sonicators[114,115], as well as a technique called nanoprecipitation in which a poor solvent is added to the reaction mixture, causing the nanomaterials to precipitate.[116,117]

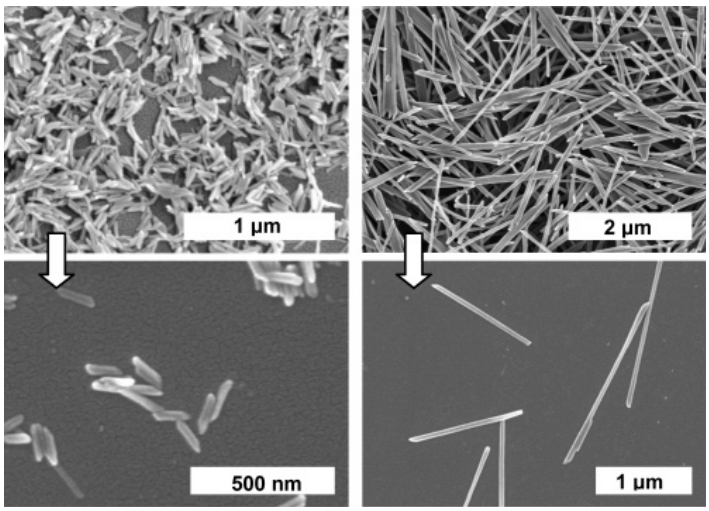

Figure 1.18. Scanning electron microscopy images of the $Gd(BDC)_{1.5}(H_2O)_2$ nanoMOF synthesized with different *W* ratios: *W* = 5 (*left*) and *W* = 10 (*right*). Reprinted from *J. Am. Chem. Soc.* **2006,** *128,* 9024-9025. Copyright 2006 American Chemical Society.

In order to increase applicability and water stability, nanoMOFs have been coated in silica.[107,113,116] This extra layer serves multiple purposes in that it keeps potentially toxic metal

ions such as Gd^{3+} from leaching out of the system as free metal ions as well as making the material biocompatible.[107] Altering the concentration of the silica reagent and the reaction time alters the thickness of the shell.[107,113,116]

1.5 THIS DISSERTATION

In this dissertation we present a series of lanthanide-containing polymetallic species which emit in the far red portion of the visible spectrum through the NIR.

Initially we utilized a dendrimer structure to organize and sensitize Eu^{3+} ions. In Chapter 2 we demonstrate that this material can preferentially accumulate within tumors and is easily visualized both *ex vivo* and *in vivo* using a variety of methods and techniques. Unfortunately, this structure lacks rigidity making it difficult to determine the exact placement of the lanthanides.

In order to more rigorously organize the lanthanides within an architecture, we transitioned to using lanthanides as the metal in MOFs. In our previous work, a barcoded MOF (Er_xYb_{1-x}-PVDC-1) in which the molar ratio of lanthanides in the synthesis correlated with both the composition and emission intensity of the lanthanide in the MOF was created. In Chapter 3 we study the Yb-Er energy transfer in this material that makes it suited for use in telecommunication devices.

In Chapter 4 the same ligand is utilized, but through a slightly different synthesis, a new MOF resulted, Yb-PVDC-3. We then sought to miniaturize the MOFs in order to more effectively utilize the NIR emission for biological imaging in living cells. A reverse microemulsion synthesis was employed to generate nano-Yb-PVDC-3 and a series of

isostructural barcoded nanoMOFs: nano-Nd_xYb_{1-x}-PVDC-3 which exhibited the expected Yb^{3+} and/or Nd^{3+} NIR emission. The nano-Yb-PVDC-3 was not cytotoxic, was stable in water and cell lysate, did not photobleach, and was taken up by HeLa and NIH 3T3 cells. These factors allowed for the use of the nanoMOF for what is believed to be the first demonstration of utilizing a nanoMOF for lanthanide NIR imaging in living cells using single photon excitation.

While the previous results were exciting, the limitations of nano-Yb-PVDC-3 were its limited monodispersity and the difficulty in reducing its size below 120 nm. In Chapter 5, an alternate approach was to a switch to the biologically friendly 1,3,5-benezentricarboxylic acid (BTC) ligand. Needle-like Yb(BTC)(H_2O) crystals were synthesized following literature procedures. Using a modulator approach to demonstrate size-control, various sizes of nano-Yb(BTC)(H_2O) were achieved, ranging from micro-scale rods all the way down to nanoscale spheres. Regardless of their size, these materials all exhibited similar luminescence properties: excitation wavelength, Yb^{3+} NIR emission, quantum yields, and luminescence lifetimes. This material was most efficiently excited using high energy wavelengths, and that could limit their use for biological systems. We therefore chose to use an alternate chromophore for the sensitization of the NIR-emitting Yb^{3+}. The 4-hydroxyl-1-(4-methyl-2-sulfoanilino)-anthraquinone, was incubated with the nanoMOF in order to shift the excitation wavelength to the NIR region, thereby creating the first nanoMOF material which exhibits both excitation and emission in the NIR. A silica shell was added to further enhance the luminescence intensity in aqueous environments.

1.6 REFERENCES

(1) Robles-Kelly, A.; Huynh, C. In *Imaging Spectroscopy for Scene Analysis*; Springer London: 2013, p 9-15.

(2) *Near, Mid & Far Infrared* http://www.ipac.caltech.edu/outreach/Edu/Regions/irregions.html (accessed June 3, 2014)

(3) *UPC: The Transofrmation of Retail* http://www-03.ibm.com/ibm/history/ibm100/us/en/icons/upc/ (accessed September 8, 2014).

(4) Hirst, E. J. In *Chicago Tribune* 2014.

(5) *FluoroSELECT™ single channel fluorometer* htttp://www.sigmaaldrich.com/catalog/product/fluka/z805491?lang=en&region=US (accessed September 8, 2014).

(6) Thayer, A. M. In *Chemical & Engineering News*; American Chemical Society: 2012; Vol. 90, p 11-15.

(7) Mahmood, U.; Weissleder, R. *Mol. Cancer Ther.* **2003**, *2*, 489-496.

(8) Weissleder, R.; Ntziachristos, V. *Nat. Med.* **2003**, *9*, 123-128.

(9) Taik Lim, Y.; Kim, S.; Nakayama, A.; Stott, N. E.; Bawendi, M. G.; Frangioni, J. V. *Mol. Imag.* **2003**, *2*, 50-64.

(10) Frangioni, J. V. *Curr. Opin. Chem. Biol.* **2003**, *7*, 626-634.

(11) Eliseeva, S. V.; Bünzli, J.-C. G. *Chem. Soc. Rev.* **2010**, *39*, 189-227.

(12) Cotton, F. A.; Wilkinson, G.; Murillo, C.; Bochmann, M. *Advanced Inorganic Chemistry*; 6th ed.; John Wiley and Sons, Inc.: New York, 1999.

(13) Bünzli, J.-C. G.; Piguet, C. *Chem. Soc. Rev.* **2005**, *34*, 1048-1077.

(14) Petoud, S.; Cohen, S. M.; Bünzli, J.-C. G.; Raymond, K. N. *J. Am. Chem. Soc.* **2003**, *125*, 13324-13325.

(15) Zhang, J.; Badger, P. D.; Geib, S. J.; Petoud, S. *Angew. Chem., Int. Ed.* **2005**, *44*, 2508-2512.

(16) Ye, Z.; Tan, M.; Wang, G.; Yuan, J. *Anal. Chem.* **2003**, *76*, 513-518.

(17) Beeby, A.; Botchway, S. W.; Clarkson, I. M.; Faulkner, S.; Parker, A. W.; Parker, D.; Williams, J. A. G. *J. Photochem. Photobiol., B* **2000**, *57*, 83-89.

(18) Bünzli, J.-C. G. In *Lanthanide Probes in Life, Chemical and Earth Sciences*; Bünzli, J.-C. G., Choppin, G. R., Eds.; Elsevier Science Publishers B.V.: Amsterdam, 1989, p 219-293.

(19) Huheey, J. E.; Keiter, E. A.; Keiter, R. L. *Inorganic Chemistry: Principles of Structure and Reactivity*; 4th ed.; HarperCollins College Publishers: New York, 1993.

(20) Weissman, S. I. *J. Chem. Phys.* **1942**, *10*, 214-217.

(21) Förster, T. *Discuss. Faraday Soc.* **1959**, *27*, 7-17.

(22) Dexter, D. L. *J. Chem. Phys.* **1953**, *21*, 836-850.

(23) Faulkner, S.; Beeby, A.; Carrié, M.-C.; Dadabhoy, A.; Kenwright, A. M.; Sammes, P. G. *Inorg. Chem. Commun.* **2001**, *4*, 187-190.

(24) Horrocks, W. D.; Bolender, J. P.; Smith, W. D.; Supkowski, R. M. *J. Am. Chem. Soc.* **1997**, *119*, 5972-5973.

(25) Moore, E. G.; Samuel, A. P. S.; Raymond, K. N. *Acc. Chem. Res.* **2009**, *42*, 542-552.

(26) Kropp, J. L.; Windsor, M. W. *J. Chem. Phys.* **1965**, *42*, 1599-1608.

(27) Heller, A. *J. Am. Chem. Soc.* **1966**, *88*, 2058-2059.
(28) Haas, Y.; Stein, G. *J. Phys. Chem.* **1971**, *75*, 3668-3677.
(29) Haas, Y.; Stein, G. *J. Phys. Chem.* **1971**, *75*, 3677-3681.
(30) Horrocks, W. D.; Sudnick, D. R. *J. Am. Chem. Soc.* **1979**, *101*, 334-340.
(31) Horrocks, W. D.; Sudnick, D. R. *Acc. Chem. Res.* **1981**, *14*, 384-392.
(32) Supkowski, R. M.; Horrocks, W. D. *Inorg. Chim. Acta* **2002**, *340*, 44-48.
(33) Dickins, R. S.; Parker, D.; de Sousa, A. S.; Williams, J. A. G. *Chem. Commun.* **1996**, 697-698.
(34) Supkowski, R. M.; Horrocks, W. D. *Inorg. Chem.* **1999**, *38*, 5616-5619.
(35) Beeby, A.; Clarkson, I. M.; Dickins, R. S.; Faulkner, S.; Parker, D.; Royle, L.; de Sousa, A. S.; Williams, J. A. G.; Woods, M. *J. Chem. Soc., Perkin Trans. 2* **1999**, 493-504.
(36) Beeby, A.; Dickins, R. S.; Faulkner, S.; Parker, D.; Williams, J. A. G. *Chem. Commun.* **1997**, 1401-1402.
(37) Vögtle, F.; Richardt, G.; Werner, N. *Dendrimer Chemistry*; WILEY-VCH Verlag GmbH & Co. KGaA: Weinheim, 2009.
(38) *Dendrimers and Other Dendritic Polymers*; John Wiley & Sons, Ltd.: West Sussex, 2001.
(39) Tomalia, D. A.; Baker, H.; Dewald, J.; Hall, M.; Kallos, G.; Martin, S.; Roeck, J.; Ryder, J.; Smith, P. *Polym. J.* **1985**, *17*, 117-132.
(40) Maiti, P. K.; Cagin, T.; Wang, G.; Goddard, W. A. *Macromolecules* **2004**, *37*, 6236-6254.
(41) *PAMAM Dendrimers* http://www.sigmaaldrich.com/materials-science/material-science-products.html?TablePage=9539880 (accessed January 26, 2015).
(42) Boas, U.; Christensen, J. B.; Heegaard, P. M. H. *J. Mater. Chem.* **2006**, *16*, 3785-3798.
(43) Hawker, C. J.; Fréchet, J. M. J. *J. Am. Chem. Soc.* **1990**, *112*, 7638-7647.
(44) Balzani, V.; Ceroni, P.; Gestermann, S.; Kauffmann, C.; Gorka, M.; Vogtle, F. *Chem. Commun.* **2000**, 853-854.
(45) Valério, C.; Fillaut, J.-L.; Ruiz, J.; Guittard, J.; Blais, J.-C.; Astruc, D. *J. Am. Chem. Soc.* **1997**, *119*, 2588-2589.
(46) James, T. D.; Shinmori, H.; Takeuchi, M.; Shinkai, S. *Chem. Commun.* **1996**, 705-706.
(47) Dykes, G. M. *J. Chem. Technol. Biotechnol.* **2001**, *76*, 903-918.
(48) Hawker, C. J.; Wooley, K. L.; Fréchet, J. M. J. *J. Chem. Soc., Perkin Trans. 1* **1993**, 1287-1297.
(49) Twyman, L. J.; Beezer, A. E.; Esfand, R.; Hardy, M. J.; Mitchell, J. C. *Tetrahedron Lett.* **1999**, *40*, 1743-1746.
(50) Milhem, O. M.; Myles, C.; McKeown, N. B.; Attwood, D.; D'Emanuele, A. *Int. J. Pharm.* **2000**, *197*, 239-241.
(51) Patel, J.; Garala, K.; Basu, B.; Raval, M.; Dharamsi, A. *Int. J. Pharma. Investig.* **2011**, *1*, 135-138.
(52) Baars, M. W. P. L.; Meijer, E. W.; Froehling, P. E. *Chem. Commun.* **1997**, 1959-1960.
(53) Schenning, A. P. H. J.; Peeters, E.; Meijer, E. W. *J. Am. Chem. Soc.* **2000**, *122*, 4489-4495.
(54) Pan, Y.; Ford, W. T. *Macromolecules* **2000**, *33*, 3731-3738.
(55) Kolhe, P.; Misra, E.; Kannan, R. M.; Kannan, S.; Lieh-Lai, M. *Int. J. Pharm.* **2003**, *259*, 143-160.

(56) Chauhan, A. S.; Sridevi, S.; Chalasani, K. B.; Jain, A. K.; Jain, S. K.; Jain, N. K.; Diwan, P. V. *J. Control. Release* **2003**, *90*, 335-343.
(57) Tomalia, D. A.; Reyna, L. A.; Svenson, S. *Biochem. Soc. Trans.* **2007**, *35*, 61-67.
(58) Lai, P.-S.; Lou, P.-J.; Peng, C.-L.; Pai, C.-L.; Yen, W.-N.; Huang, M.-Y.; Young, T.-H.; Shieh, M.-J. *J. Control. Release* **2007**, *122*, 39-46.
(59) Zhuo, R. X.; Du, B.; Lu, Z. R. *J. Control. Release* **1999**, *57*, 249-257.
(60) Malik, N.; Evagorou, E. G.; Duncan, R. *Anticancer Drugs* **1999**, *10*, 767-776.
(61) Ihre, H. R.; Padilla De Jesús, O. L.; Szoka, F. C.; Fréchet, J. M. J. *Bioconjugate Chem.* **2002**, *13*, 443-452.
(62) Wang, D.; Kopečková, P.; Minko, T.; Nanayakkara, V.; Kopeček, J. *Biomacromolecules* **2000**, *1*, 313-319.
(63) Hussain, M.; Shchepinov, M.; Sohail, M.; Benter, I. F.; Hollins, A. J.; Southern, E. M.; Akhtar, S. *J. Control. Release* **2004**, *99*, 139-155.
(64) Medina, S. H.; El-Sayed, M. E. H. *Chem. Rev.* **2009**, *109*, 3141-3157.
(65) Tekade, R. K.; Kumar, P. V.; Jain, N. K. *Chem. Rev.* **2008**, *109*, 49-87.
(66) Boas, U.; Heegaard, P. M. H. *Chem. Soc. Rev.* **2004**, *33*, 43-63.
(67) Zhang, G.-D.; Harada, A.; Nishiyama, N.; Jiang, D.-L.; Koyama, H.; Aida, T.; Kataoka, K. *J. Control. Release* **2003**, *93*, 141-150.
(68) van Nostrum, C. F. *Adv. Drug Delivery Rev.* **2004**, *56*, 9-16.
(69) Battah, S.; Balaratnam, S.; Casas, A.; O'Neill, S.; Edwards, C.; Batlle, A.; Dobbin, P.; MacRobert, A. J. *Mol. Cancer Ther.* **2007**, *6*, 876-885.
(70) Bielinska, A. U.; Chen, C.; Johnson, J.; Baker, J. R. *Bioconjugate Chem.* **1999**, *10*, 843-850.
(71) Shah, D. S.; Sakthivel, T.; Toth, I.; Florence, A. T.; Wilderspin, A. F. *Int. J. Pharm.* **2000**, *208*, 41-48.
(72) Dufès, C.; Uchegbu, I. F.; Schätzlein, A. G. *Adv. Drug Delivery Rev.* **2005**, *57*, 2177-2202.
(73) Kobayashi, H.; Brechbiel, M. W. *Mol Imaging* **2003**, *2*, 1-10.
(74) Kobayashi, H.; Reijnders, K.; English, S.; Yordanov, A. T.; Milenic, D. E.; Sowers, A. L.; Citrin, D.; Krishna, M. C.; Waldmann, T. A.; Mitchell, J. B.; Brechbiel, M. W. *Clin. Cancer Res.* **2004**, *10*, 7712-7720.
(75) Talanov, V. S.; Regino, C. A. S.; Kobayashi, H.; Bernardo, M.; Choyke, P. L.; Brechbiel, M. W. *Nano Lett.* **2006**, *6*, 1459-1463.
(76) Kobayashi, H.; Kawamoto, S.; Jo, S.-K.; Bryant, H. L.; Brechbiel, M. W.; Star, R. A. *Bioconjugate Chem.* **2003**, *14*, 388-394.
(77) Vögtle, F.; Gorka, M.; Vicinelli, V.; Ceroni, P.; Maestri, M.; Balzani, V. *Chem. Phys. Chem.* **2001**, *2*, 769-773.
(78) Vicinelli, V.; Ceroni, P.; Maestri, M.; Balzani, V.; Gorka, M.; Vögtle, F. *J. Am. Chem. Soc.* **2002**, *124*, 6461-6468.
(79) Saudan, C.; Ceroni, P.; Vicinelli, V.; Maestri, M.; Balzani, V.; Gorka, M.; Lee, S.-K.; van Heyst, J.; Vogtle, F. *Dalton Trans.* **2004**, 1597-1600.
(80) Tsukube, H.; Suzuki, Y.; Paul, D.; Kataoka, Y.; Shinoda, S. *Chem. Commun.* **2007**, 2533-2535.
(81) Antoni, P.; Malkoch, M.; Vamvounis, G.; Nystrom, D.; Nystrom, A.; Lindgren, M.; Hult, A. *J. Mater. Chem.* **2008**, *18*, 2545-2554.

(82) Giansante, C.; Ceroni, P.; Balzani, V.; Vögtle, F. *Angew. Chem., Int. Ed.* **2008**, *47*, 5422-5425.
(83) Kawa, M.; Fréchet, J. M. J. *Chem. Mater.* **1998**, *10*, 286-296.
(84) Kim, H.; Roh, S.; Hong, K.-S.; Ka, J.-W.; Baek, N.; Oh, J.; Nah, M.; Cha, Y.; Ko, J. *Macromol. Res.* **2003**, *11*, 133-145.
(85) Terazzi, E.; Bocquet, B.; Campidelli, S.; Donnio, B.; Guillon, D.; Deschenaux, R.; Piguet, C. *Chem. Commun.* **2006**, 2922-2924.
(86) Baek, N. S.; Kim, Y. H.; Kim, H. K. *J. Nonlinear Opt. Phys. Mater.* **2006**, *15*, 369-379.
(87) Furukawa, H.; Cordova, K. E.; O'Keeffe, M.; Yaghi, O. M. *Science* **2013**, *341*, 974-986.
(88) Férey, G. *Chem. Soc. Rev.* **2008**, *37*, 191-214.
(89) Ma, L.; Lin, W. In *Functional Metal-Organic Frameworks: Gas Storage, Separation and Catalysis*; Schröder, M., Ed.; Springer Berlin / Heidelberg: 2010; Vol. 293, p 175-205.
(90) Cui, Y.; Yue, Y.; Qian, G.; Chen, B. *Chem. Rev.* **2011**, *112*, 1126-1162.
(91) Hu, Z.; Deibert, B. J.; Li, J. *Chem. Soc. Rev.* **2014**, *43*, 5815-5840.
(92) Della Rocca, J.; Liu, D.; Lin, W. *Acc. Chem. Res.* **2011**, *44*, 957-968.
(93) Huxford, R. C.; Della Rocca, J.; Lin, W. *Curr. Opin. Chem. Biol.* **2010**, *14*, 262-268.
(94) Horcajada, P.; Chalati, T.; Serre, C.; Gillet, B.; Sebrie, C.; Baati, T.; Eubank, J. F.; Heurtaux, D.; Clayette, P.; Kreuz, C.; Chang, J.-S.; Hwang, Y. K.; Marsaud, V.; Bories, P.-N.; Cynober, L.; Gil, S.; Férey, G.; Couvreur, P.; Gref, R. *Nat. Mater.* **2010**, *9*, 172-178.
(95) Allendorf, M. D.; Bauer, C. A.; Bhakta, R. K.; Houk, R. J. T. *Chem. Soc. Rev.* **2009**, *38*, 1330-1352.
(96) Yaghi, O. M.; O'Keeffe, M.; Ockwig, N. W.; Chae, H. K.; Eddaoudi, M.; Kim, J. *Nature* **2003**, *423*, 705-714.
(97) Tranchemontagne, D. J.; Mendoza-Cortes, J. L.; O'Keeffe, M.; Yaghi, O. M. *Chem. Soc. Rev.* **2009**, *38*, 1257-1283.
(98) Li, H.; Eddaoudi, M.; O'Keeffe, M.; Yaghi, O. M. *Nature* **1999**, *402*, 276-279.
(99) Rosi, N. L.; Kim, J.; Eddaoudi, M.; Chen, B.; O'Keeffe, M.; Yaghi, O. M. *J. Am. Chem. Soc.* **2005**, *127*, 1504-1518.
(100) Eddaoudi, M.; Kim, J.; Rosi, N.; Vodak, D.; Wachter, J.; O'Keeffe, M.; Yaghi, O. M. *Science* **2002**, *295*, 469-472.
(101) Serre, C.; Millange, F.; Thouvenot, C.; Gardant, N.; Pelle, F.; Férey, G. *J. Mater. Chem.* **2004**, *14*, 1540-1543.
(102) Li, Z.; Zhu, G.; Guo, X.; Zhao, X.; Jin, Z.; Qiu, S. *Inorg. Chem.* **2007**, *46*, 5174-5178.
(103) Daiguebonne, C.; Kerbellec, N.; Guillou, O.; Bünzli, J.-C.; Gumy, F.; Catala, L.; Mallah, T.; Audebrand, N.; Gérault, Y.; Bernot, K.; Calvez, G. *Inorg. Chem.* **2008**, *47*, 3700-3708.
(104) Rieter, W. J.; Taylor, K. M. L.; An, H.; Lin, W.; Lin, W. *J. Am. Chem. Soc.* **2006**, *128*, 9024-9025.
(105) Taylor, K. M. L.; Jin, A.; Lin, W. *Angew. Chem., Int. Ed.* **2008**, *47*, 7722-7725.
(106) Hatakeyama, W.; Sanchez, T. J.; Rowe, M. D.; Serkova, N. J.; Liberatore, M. W.; Boyes, S. G. *ACS Appl. Mater. Interfaces* **2011**, *3*, 1502-1510.
(107) Rieter, W. J.; Taylor, K. M. L.; Lin, W. *J. Am. Chem. Soc.* **2007**, *129*, 9852-9853.
(108) Taylor, K. M. L.; Rieter, W. J.; Lin, W. *J. Am. Chem. Soc.* **2008**, *130*, 14358-14359.
(109) Tsuruoka, T.; Furukawa, S.; Takashima, Y.; Yoshida, K.; Isoda, S.; Kitagawa, S. *Angew. Chem., Int. Ed.* **2009**, *48*, 4739-4743.

(110) Diring, S.; Furukawa, S.; Takashima, Y.; Tsuruoka, T.; Kitagawa, S. *Chem. Mater.* **2010**, *22*, 4531-4538.
(111) Guo, H.; Zhu, Y.; Wang, S.; Su, S.; Zhou, L.; Zhang, H. *Chem. Mater.* **2012**, *24*, 444-450.
(112) Klinowski, J.; Almeida Paz, F. A.; Silva, P.; Rocha, J. *Dalton Trans.* **2011**, *40*, 321-330.
(113) Taylor-Pashow, K. M. L.; Rocca, J. D.; Xie, Z.; Tran, S.; Lin, W. *J. Am. Chem. Soc.* **2009**, *131*, 14261-14263.
(114) Stock, N.; Biswas, S. *Chem. Rev.* **2011**, *112*, 933-969.
(115) Khan, N. A.; Haque, M. M.; Jhung, S. H. *Eur. J. Inorg. Chem.* **2010**, *2010*, 4975-4981.
(116) Rieter, W. J.; Pott, K. M.; Taylor, K. M. L.; Lin, W. *J. Am. Chem. Soc.* **2008**, *130*, 11584-11585.
(117) Spokoyny, A. M.; Kim, D.; Sumrein, A.; Mirkin, C. A. *Chem. Soc. Rev.* **2009**, *38*, 1218-1227.

2.0 PREFERENTIAL ACCUMULATION WITHIN TUMORS AND IN VIVO IMAGING BY FUNCTIONALIZED LUMINESCENT DENDRIMER LANTHANIDE COMPLEXES

The work presented in this chapter has been published as "Preferential accumulation within tumors and *in vivo* imaging by functionalized luminescent dendrimer lanthanide complexes" in *Biomaterials,* **2011,** *32,* 9343-9352.

This work was done in collaboration with Chad M. Shade, Hyounsoo Uh, Matthias Bischof, Zachary P. Thompson (Stéphane Petoud Research Group, University of Pittsburgh), Marco A. Alcala, David L. Bartlett, Charles K. Brown (Department of Surgery, University of Pittsburgh School of Medicine), Yong J. Lee (Department of Surgery and Department of Pharmacology, University of Pittsburgh School of Medicine), Adam R. Meier, Timothy G. Strein (Department of Chemistry, Bucknell University), Ruth A. Modzelewski (Department of Medicine, University of Pittsburgh School of Medicine), and Shu Ying Kwan (Department of Biological Sciences, Carnegie Mellon University).

2.1 INTRODUCTION

Approximately one-third to one-half of the 150,000 Americans diagnosed with colorectal cancer (CRC) each year[1] will develop hepatic metastasis, and only about 20% of these patients are operable. The five-year survival rate for patients with liver metastasis without treatment is only 5%.[2] Current therapies for treating metastatic lesions include local tumor ablation (i.e., radiofrequency ablation, cryotherapy or direct injection of alcohol or acetic acid directly into the metastatic lesions)[3], transarterial chemoembolization (TACE)[4], embolization with radioactive microspheres, surgical resection and/or systemic therapy consisting of chemotherapeutic and biological agents[5]. While all of these strategies can be used to treat hepatic malignancies, some are surgically invasive and others are associated with significant systemic toxicity due to lack of tumor-specific accumulation. However, the attainment of a tumor-specific agent that maximizes treatment efficacy while minimizing systemic toxicity remains a difficult feat in cancer therapeutics.

One of our aims is to target with high specificity and image liver tumors in colorectal liver metastases with *in vivo* and *ex vivo* WAG/RijHsd rat models. A main requirement to achieve the goal of targeting and evidencing liver metastasis is the creation of a luminescent reporter that will allow for the preferential accumulation in this type of tumor and which will emit a stable luminescence signal that can be discriminated from autofluorescence present in biological systems. In this study we have developed a nanoscale dendrimer that preferentially

accumulates within tumors in a rat hepatic metastasis model and demonstrated its capacity to optically image liver tumors *in vivo*.

Dendrimers are discrete, organized polymers whose versatility in the fields of drug-delivery, site-specific targeting and labeling have been the subject of many articles and reviews.[6-12] Apart from the core of the dendrimer, the interior branches and surface functional groups offer two regions which can be manipulated in a versatile way to meet the needs of the designers, such as being functionalized to incorporate luminescent molecules.[13] As often observed with small organic fluorophores, photobleaching can be a strong limitation by leading to fluorescent signal decay thereby preventing their use for long term or repetitive measurements in biological applications. Trivalent lanthanide cations such as europium (Eu^{3+}) have been hypothesized to provide a unique solution to prevent/limit the effects of photobleaching.[14] In this work, we have created a dendrimer-lanthanide complex by attaching luminescent moieties to the surface of the dendrimer through the end branches and incorporating Eu^{3+} cations in the internal sites, and demonstrated the unique luminescence stability of this complex and its application in our WAG/RijHsd rat models.

2.2 EXPERIMENTAL

2.2.1 Reagents

All reagents were used as received, unless otherwise stated. Generation-3 poly (amido amine) dendrimer (G3 PAMAM) was purchased from Dendritech, Inc. *N,N*-dimethylformamide (DMF), dimethylsulfoxide (DMSO) and *N,N*-diisopropylethylamine (DIPEA) were purchased from

Sigma-Aldrich. 1-[bis(dimethylamino)methylene]-1*H*-1,2,3-triazolo[4,5-*b*]pyridinium 3-oxid hexafluorophosphate (HATU) was purchased from Aldrich. Regenerated cellulose membrane (nominal molecular weight cut-off 12,000-14,000) was purchased from Fisher Scientific. Deuterated dimethylsulfoxide (DMSO-d_6; 99.9% D) was purchased from Cambridge Isotope Laboratories. Europium (III) nitrate ($Eu(NO_3)_3$; 99.99%) was purchased from Alfa Aesar. Ketamine and Buprenorphine were purchased from Bedford Labs. Acepromazine was purchased from Boehringer Ingleheim Vetmedica, Inc. Dulbecco's Modified Eagle Medium (DMEM) was purchased from Gibco. Trypsin was purchased from Sigma.

2.2.2 Synthesis of the generation-3 PAMAM 4-amino-1,8-naphthalimide dendrimer containing europium ions (Eu-G3P4A18N)

Glycine-conjugated 4-amino-1,8-naphthalimide was synthesized by a reported method.[15] Glycine-conjugated 4-amino-1,8-naphthalimide was attached on the amine-terminated G3 PAMAM dendrimer by a standard amide coupling condition: 54.1 mg (2.00×10^{-4} mol) of glycine-naphthalimide conjugate was added to a solution of 29.4 mg (4.26×10^{-6} mol) of G3 PAMAM dendrimer in 5 mL of DMF. 92.1 mg (2.42×10^{-4} mol) of HATU and 70 mL (52 mg; 4.0×10^{-4} mol) of DIPEA were added. The reaction mixture was stirred at room temperature for 2 days under nitrogen atmosphere while monitoring the disappearance of G3 PAMAM dendrimer by thin layer chromatography (TLC). The compound was purified by dialysis using a regenerated cellulose membrane in DMSO for 3 days. The solution recovered from the dialysis membrane was dried in a vacuum oven (40 °C, 50 mbar) to yield G3P4A18N as a brown solid (52.5 mg, 82%). ^{1}H NMR (300 MHz, DMSO-d_6, δ): 8.54 (br s, 32H), 8.32 (br s, 32H), 8.15 (br s, 32H), 8.10 (br s, 32H), 7.90 (br s, 32H), 7.76 (m, 28H), 7.56 (br s, 32H), 7.40 (br s, 64H), 6.78

(br s, 32H), 4.56 (br s, 64H), 3.08 (m, 184H), 2.61 (m, 120H), 2.39 (m, 60H), 2.16 (m, 120H) (Figure 2.1). Elemental analysis (EA) calcd for $C_{750}H_{864}N_{186}O_{156}\cdot 32DMSO\cdot 64H_2O$: C, 52.47; H, 6.40; N, 13.98. Found: C, 51.74; H, 6.29; N, 13.76. The Eu^{3+} complex of G3P4A18N (Eu-G3P4A18N) was synthesized with the following method adapted from one of our procedures[16]: 22.67 mg (1.513×10^{-6} mol) of G3P4A18N was dissolved in 10 mL of DMSO. 647.5 mL of 18.7 mM $Eu(NO_3)_3$ solution in DMSO (1.21×10^{-5} mol) was added to the dendrimer solution. The mixture was diluted to 25.00 mL and incubated at room temperature for 7 days. The resulting solution (60.5 mM) was used as obtained.

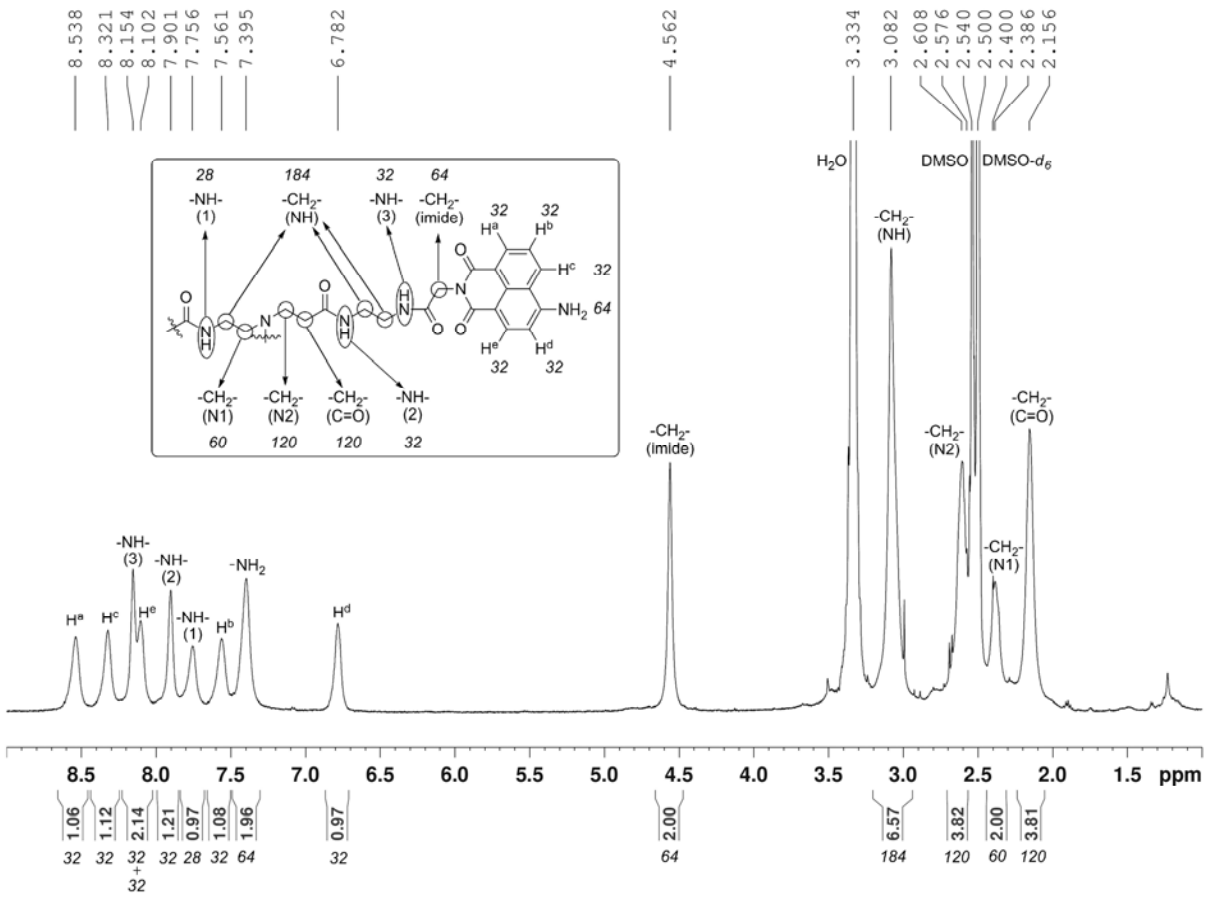

Figure 2.1. ^{1}H-NMR spectrum and peak assignment for G3P4A18N in DMSO-d_6.

2.2.3 Mobility determination by capillary zone electrophoresis

The Eu-G3P4A18N dendrimer samples were characterized with electrophoretic analysis by capillary zone electrophoresis (CZE) with diode array ultraviolet (UV) absorbance detection with an Agilent CE system (Agilent Technologies). A 75.0 mm interior diameter unmodified fused silica capillary (Polymicro Technologies) 34.0 cm in total length and 8.5 cm to the detector (short end) was employed. The background electrolyte was 40 mM phosphoric acid in 30% DMSO and 70% 18 MΩ-cm water at pH of 2.3. Each day prior to use, the capillary was preconditioned with 1 M sodium hydroxide (NaOH) for 5 minutes, 18 MΩ-cm water for 15 minutes, and running buffer for 15 minutes. The capillary was flushed with running buffer for 2 minutes in between analysis. A separation potential of 17.0 kV was employed and a co-flow pressure of 10 mbar was also applied during the electrophoresis. Dendrimer samples were tested at a concentration of 3 mg/mL in DMSO. Hydrodynamic injection (50 mbar, 1.5 s) was employed, and the capillary was maintained at 25 °C. Detection was performed at 450 nm and 280 nm, and ultraviolet-visible (UV-vis) spectra were collected for each peak. A small co-flow pressure of 10 mbar during electrophoresis was needed to reliably detect the neutral zone corresponding to the DMSO from the injection plug, and the migration time for this solvent zone was used to calculate the electroosmotic mobility of the system.

2.2.4 Spectroscopic characterization of Eu-G3P4A18N

Absorption spectra were recorded on samples in a PerkinElmer Lambda 9 BX Spectrometer, coupled with a personal computer using software supplied by PerkinElmer.

Steady-state emission and excitation spectra were analyzed using a modified Horiba Jobin Yvon Spex Fluorolog-322 Spectrofluorometer coupled to a personal computer with software supplied by Horiba Jobin Yvon Inc. Emission and excitation spectra were corrected for the instrumental function. Samples were placed in 1 mm quartz fluorescence cells purchased from NSG Precision Cells, Inc.

The Eu^{3+} luminescence lifetime measurements were performed using a neodymium yttrium aluminum garnet (Nd:YAG) Continuum Powerlite 8010 laser (354 nm, third harmonic) as the excitation source. Emission was collected at a right angle to the excitation beam, and signals arising from the $^5D_0 \rightarrow {}^7F_2$ Eu^{3+} transition (615 nm) were selected by a Spectral Products CM 110 1/8 m monochromator. The signal was monitored using a Hamamatsu R928 photomultiplier coupled to a 500 MHz bandpass digital oscilloscope (Tektronix TDS 754D). For each flash, the experimental decay was recorded with a resolution of 50,000 points. To minimize experimental contribution, signals from >1000 flashes were collected and averaged. Luminescence decay curves were analyzed with Origin 7.0 software. The experimental decay curves were fitted to single, double, and triple exponential models using the Chi-squared criteria to discriminate the best exponential fit. Four independent decay curves were collected for the sample.

For the photobleaching experiments, approximately 0.9 mL of each solution (0.2 mM in 30% DMSO/H_2O) was transferred into a 0.9 mL semimicro absorbance cuvette supplied by Varian (catalog number 66-100127-00). The cuvette was stoppered and parafilmed at the

beginning of each trial to prevent solvent evaporation. Photobleaching was quantified with a PerkinElmer UV/Vis, collecting at 240 nm/min scan rates. Samples were exposed to white light from the Xenon lamp of the Horiba Jobin Yvon Spex Fluorolog-322 Spectrofluorometer in-between scans. A water circulator was used to maintain constant room temperature (23 °C) within the fluorimeter during long periods of exposure.

For the quantum yield experiments, spectra were collected and analyzed using the Horiba Jobin Yvon Spex Fluorolog-322 fitted with an integrating sphere[17] using quartz tubes as sample holders. A 20 mM solution of Eu-G3P4A18N in 30% DMSO/H_2O was used for this analysis, and all spectra were corrected for the response of the lamp before integration of the signals. Integrated values were used to determine the quantum yield by calculating the ratio of the number of photons emitted by the sample divided by the number photons absorbed by the sample.

2.2.5 Animals

Four- to six-week-old male WAG/RijHsd rats were purchased from Harlan, Netherlands. Rats were fed ad libitum and maintained in environments with controlled temperature of 22-24 °C and 12 hour light and dark cycles. All procedures involving the rats were in accordance with the Guide for the Care and Use of Laboratory Animals (National Research Council, 1996) and on a protocol approved by the Institutional Animal Care and Use Committee of the University of Pittsburgh.

2.2.6 Generation of colorectal metastasis by single tumor implantation

While others have initiated colorectal metastasis by injecting cancer cells via the portal vein, superior mesenteric vein[18] or spleen[19], these approaches lead to small diffuse lesions which are difficult to study[20]. We generated the isolated hepatic colorectal metastasis model by way of implanting CC531 tumor pieces into rat livers. Fourteen twenty-to-thirty-week-old WAG/RijHsd rats were anesthetized with a single intraperitoneal injection of 70 mg/kg of Ketamine and 2.5 mg/kg of Acepromazine. An intramuscular injection of 0.1 mg/kg of Buprenorphine was also administered for analgesia prior to incision. Following midline incision, CC531 tumor nodules (1 × 2 mm weighing 25 mg) were implanted in the subcapsular area of the left lateral lobe (LLL) of the rat. These implanted tumor nodules were isolated from CC531 tumors grown hepatic implants in WAG/RijHsd rats. The tumors were placed about 5 mm deep to the subcapsular area of the LLL of the liver where it was easily found 20-30 days later when the rat underwent a second laparotomy for gastroduodenal artery (GDA) cannulation and hepatic infusion of the Eu-G3P4A18N solution.

2.2.7 Cell culture and generation of colorectal metastasis by splenic injection

CC531 cell line is a moderately differentiated colon adenocarcinoma syngeneic to WAG/RijHsd rats.[21] Tumor cells were tested and found to be virus- and mycoplasma-free. CC531 cells were cultured in Dulbecco's Modified Eagle Medium (DMEM) supplemented with 10% fetal bovine serum. Cells were maintained by serial passage. Tumor cells were then harvested with a solution of 0.25% trypsin, washed three times in 0.9% NaCl solution buffered with 1.4 mM phosphate (PBS), and adjusted to a suspension containing 2×10^6 viable (trypan blue exclusion

test) tumor cells per 200 mL of PBS, which were then injected into the spleen to generate metastatic tumor nodules in the liver. Metastatic lesions to the liver were observed 20-25 days later after a midline incision was performed.

2.2.8 Luminescence imaging of hepatic tumors

In vivo administration of the Eu-G3P4A18N (300 mL of a 60 mM solution in 10% DMSO/H_2O) was captured as it was being infused and selectively associating with the liver tumor. The imaging system used to detect the luminescence of the dendrimer is custom-made, combining either a Andor DU 434-BR-DD cooled charge coupled device (CCD) camera (Andor Technology; South Windsor, CT, USA) or Rolera XR fast digital CCD camera (QImaging; Surrey, Canada) fitted with a 50 mm AF Nikkor lens containing a minimum aperture of F16 and maximum aperture of F1.4. The emission filters used were 610/30 nm and a 740/140 nm cutoff in wavelength (Chroma Technologies). The rat livers on living animals were excited using four 5 Watt LEDs emitting at 450 nm (Lumileds Lighting). Qcapture software (QImaging) was used for the data acquisition.

Luminescence imaging of 10 mm tumor sections following hepatic arterial infusion of functionalized dendrimers was accomplished with an Olympus FV1000MPE multi-photon laser-scanning unit fitted to an IX81 microscope (Olympus Corp.). Illumination for two-photon excitation at 820 nm was provided by a mode-locked Chameleon Ultra Ti:Sapphire laser (Coherent, Inc.). An Olympus 25× objective with N.A. of 1.05 was used to acquire images. Luminescence emission was collected with an external photomultiplier tube using a 570-625 nm bandpass filter. Scan resolution was set to 1024 × 1024 pixels at 4096 grey scales.

2.2.9 Histopathology of liver tumor sections

Tissue sections (10 microns) from dendrimer-infused livers were also processed for routine hematoxylin and eosin (H&E) and immunohistochemistry staining. Tissues were fixed with 2% paraformaldehyde for 2 hours at 4 °C, and then left overnight in 30% sucrose at 4 °C. The samples were frozen in a liquid nitrogen-cooled bath of 2-methyl-butane and cryosectioned. Sections were labeled with monoclonal CD31 (ABR MA1-26196) and Alexa Fluor 647 phalloidin (Invitrogen A22287). Goat anti mouse Cy3 secondary antibody for CD31 and DAPI followed. Images were then recorded on an Olympus FV1000 confocal microscope.

2.3 RESULTS AND DISCUSSION

2.3.1 Functionalized dendrimer with Eu^{3+}

We have designed and synthesized a nanoscale dendrimer complex that achieves site-specificity requirements and tested its use in live animal imaging. The dendrimer provides a versatile organic framework to which multiple fluorophores have been covalently attached. Connecting organic fluorophores to the surface of the dendrimer can drastically improve the stability of the association when compared to occupying the interior cavities and being secured through secondary interactions. As a luminescent moiety, we have chosen 4-amino-1,8-naphthalimide since this molecule is hypothesized to emit a significant amount of photons in the red/near-infrared region of the electromagnetic spectrum. Such emission wavelengths allow for sensitive detection due to the absence of native fluorescence of biological systems in this spectral region

(improvement of the signal-to-noise ratio). Higher generation dendrimers have a larger number of terminal branches, which correlates to the number of fluorophores which can be substituted on the surface of each dendrimer, thereby increasing the overall absorptivity and number of emitted photons per unit volume and further improving signal intensity.

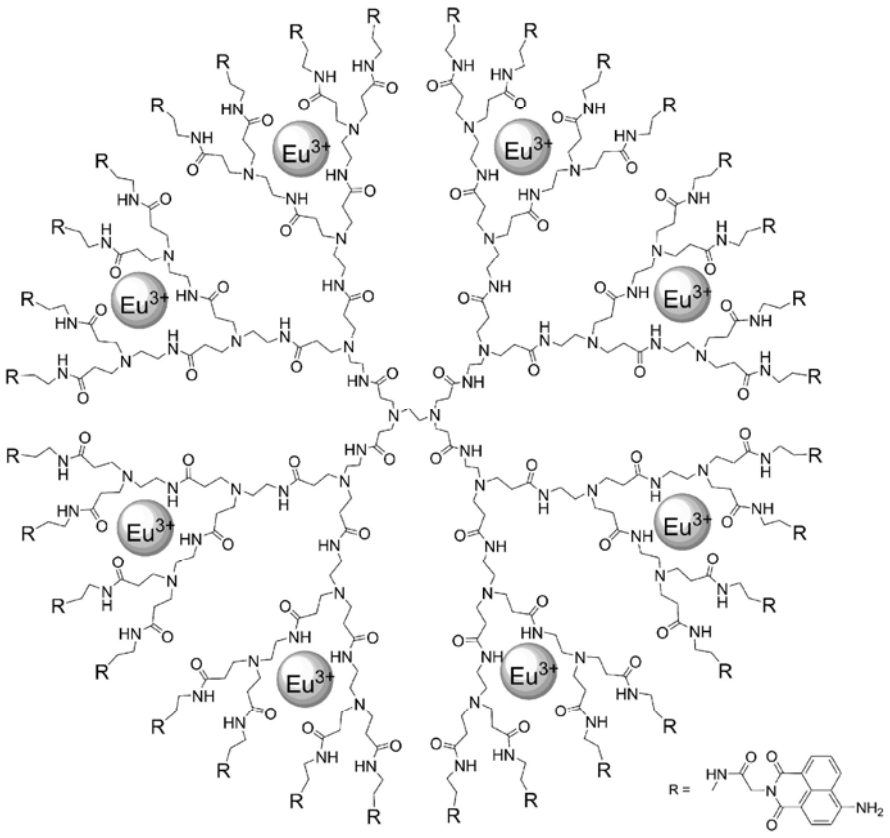

Figure 2.2. The chemical structure of the Eu-G3P4A18N dendrimer. Substitution of the end branches is designated by R, glycine-conjugated 4-amino-1,8-naphthalimide (shown at the bottom right corner). The gray spheres indicate the hypothesized coordination of eight lanthanide cations (Eu^{3+}) within the dendrimer nanocomplex (modified dendrimer size approximately 3 nm).

By providing alternate routes of energy transfer with respect to photoreaction, luminescent lanthanide cations such as Eu^{3+} are hypothesized to partially depopulate the excited state(s) of fluorophores when the donor-acceptor energy levels are sufficiently well matched, thereby preventing significant photobleaching from occurring. Poly(amido amine) dendrimers (PAMAM) contain numerous binding sites along the alternating amide bond architecture of their arms, a requirement for coordinating metal cations.[22] A lanthanide complex was based on a generation-3 PAMAM dendrimer (G3 PAMAM or G3P), capable of coordinating multiple Eu^{3+} cations within the interior. The 32 amino end branches of the generation-3 dendrimer were functionalized with 4-amino-1,8-naphthalimide fluorophores (4A18N) using glycine linkers to yield the functionalized dendrimer: generation-3-PAMAM-(glycine-4-amino-1,8-naphthalimide)$_{32}$ (G3P4A18N). The complete functionalization of each dendrimer branch was confirmed by ^{1}H NMR and elemental analysis (*see Section 2.2.2*). Eight Eu^{3+} cations were coordinated within the branches to yield the Eu^{3+} complex Eu-G3P4A18N by following a procedure that we have previously developed for a dendrimer carrying different fluorophores[16]. Capillary zone electrophoresis (CZE) analysis of the Eu-G3P4A18N dendrimer with detection at 450 nm gave rise to one major peak with a cationic electrophoretic mobility of 1.39×10^{-4} cm^2/Vs (Figure 2.3). A minor component present in some samples represented no more than 7% by peak area and had a mobility of about 6.8×10^{-5} cm^2/Vs. The UV-vis spectrum obtained from the major peak is consistent with the expected spectrum for the dendrimer. These data are consistent with a well-defined species not indicating any significant dispersity. The chemical structure of Eu-G3P4A18N is depicted in Figure 2.2. The substitution of end branches is designated by "R", defined in the lower right corner with glycine-conjugated 4A18N. The gray spheres indicate the hypothesized coordination of the lanthanide, Eu^{3+}, within the dendrimer nanocomplex.

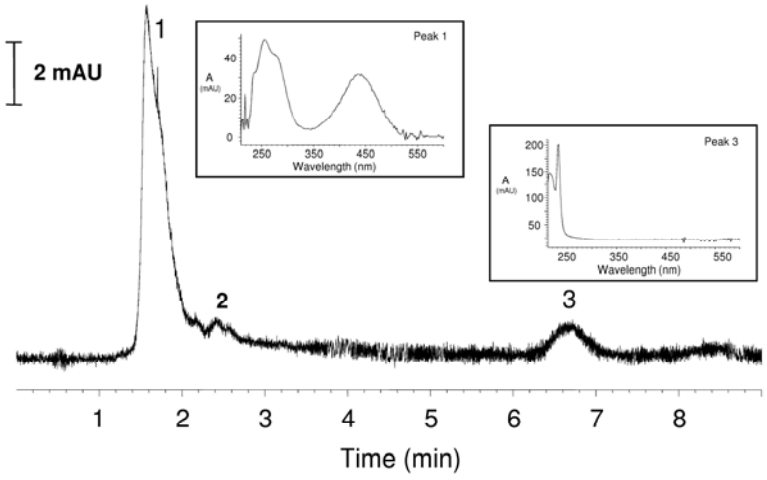

Figure 2.3. Electropherogram of Eu-G3P4A18N obtained at 450 nm upon CZE analysis of 3 mg/mL (in DMSO) sample of Eu-G3P4A18N. Peak 1 corresponds to the dendrimer; Peak 2 reveals the presence of an impurity; Peak 3 is DMSO solvent zone (to mark flow). The insets are UV-vis spectra collected from peaks 1 and 3.

The absorption spectrum indicates an apparent maximum at approximately 440 nm (Figure 2.4, dotted line); however, it is worth noting that the compound does absorb significantly at longer wavelengths. The molar extinction coefficient is 5000 $cm^{-1}mol^{-1}L$ at 630 nm, which is almost two times larger than that of Photofrin at the same wavelength[23]. Absorption at longer wavelengths is attractive for biological imaging since photons at these wavelengths generate very little autofluorescence and are not harmful for biological systems, preventing any perturbation of the system to be monitored. The luminescence emission spectrum indicates the presence of a prominent broad band with a significant component in the red/NIR part of the electromagnetic spectrum (Figure 2.4, solid line).

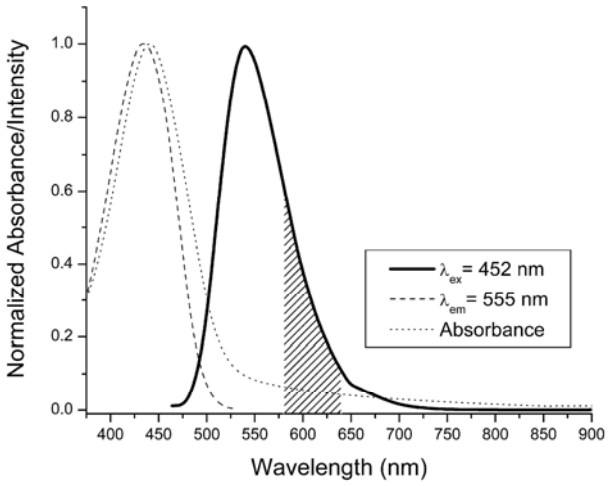

Figure 2.4. Spectra of the Eu-G3P4A18N dendrimer complex used for luminescence imaging experiments. The luminescence emission spectrum (λ_{ex} = 452 nm, solid line) displays a prominent band with an intensity maximum at 550 nm and a tail extending into the red/NIR part of the spectrum. The shaded area of the emission spectrum indicates the luminescence signal detected during the confocal microscopy experiments. A steady-state excitation spectrum (λ_{em} = 555 nm, dashed line) collected upon monitoring the maximum intensity of the luminescence band, overlaps significantly with the absorption spectrum (dotted line).

The collection of luminescence lifetime measurements arising from Eu^{3+}-centered emission was made possible with the help of the spectroscopic resolution of a laser exciting at 354 nm. A monoexponential decay of 1.09(±0.03) ms was fitted best from the experimental decay curve. This value is in good agreement with comparable systems[16] and provides good evidence that each of the eight Eu^{3+} cations located within the dendrimer are both well protected and are surrounded by a similar coordination environment inside the dendritic architecture. The similar coordination environment around each of the lanthanide cations is a strong indication that only one well-defined species is present in solution. Polydispersity would result in several

luminescence lifetimes as these cations are highly sensitive to their environment. The quantum yield of the compound upon excitation at 450 nm is 2.9(±0.1)%. This value is relatively low, but the overall sensitivity provided by the imaging agent will be related to the number of emitted photons per unit of volume and, in this case, the small quantum yield will be compensated by the high density of luminescent 4-amino-1,8-naphthalimide groups.

When specific conditions are met, the electronic structures of lanthanide cations are hypothesized[14] to stabilize the excited states of organic fluorophores against photobleaching. To analyze this hypothesis, the absorbance of the 1,8-naphthalimide derivative was monitored as a function of time upon exposure to white excitation light (Figure 2.5). In the absence of Eu^{3+}, the absorbance of G3P4A18N decreased exponentially. This behavior indicates that the fluorophores are vulnerable to photobleaching. In the presence of Eu^{3+}, the absorbance of Eu-G3P4A18N experienced a modest decrease within the first hour of exposure to white light; however, the absorbance maintained constant values for the remainder of the experiment. Indeed, the exciting side-by-side comparison depicted in Figure 2.5 lends evidence to the idea that the eight Eu^{3+} provide increased stabilization to the electronic structure of the thirty-two 4-amino-1,8-naphthalimide fluorophores (singlet and triplet states). This feature is advantageous for applications, allowing for an extended shelf life, longer exposure time to excitation light, and repeatability of experiments. Such stabilization for a molecular complex in solution has been, to the best of our knowledge, only reported in one previously published article.[14]

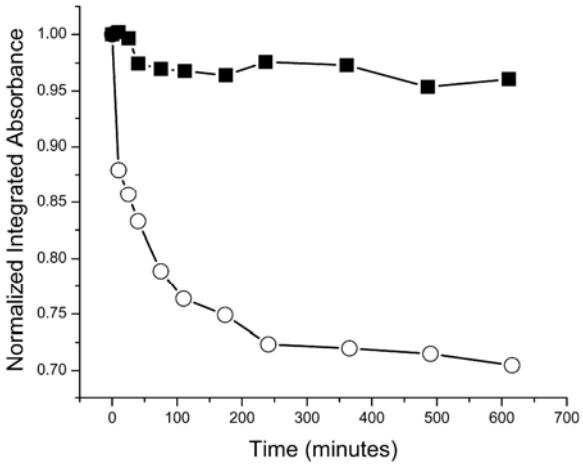

Figure 2.5. Photobleaching analysis of the Eu-G3P4A18N dendrimer complex used in luminescence imaging experiments. The absorbance of G3P4A18N was monitored as a function of time upon exposure to white light. In the absence of Eu^{3+} (open circle), the absorption decreased exponentially for the duration of the experiment, leading to an overall decrease approaching 30%. The trend observed in the presence of Eu^{3+} (filled square) was a modest decrease in absorbance during the first minutes, followed by an impressive level of stability for the same duration.

We plan to analyze more deeply this exciting phenomenon in order to obtain control of it. We will test the different luminescent lanthanide cations to identify the one that is the most efficient. These future experiments will be useful for elucidating the underlying mechanism of chromophore stabilization.

2.3.2 Hepatic arterial infusion of Eu-G3P4A18N

Regional hepatic delivery of Eu-G3P4A18N was made possible by infusion via the gastroduodenal artery (GDA) of 160-330 gm WAG/RijHsd rats. This technique involves the

isolation of the vasculature of the liver by clamping closed the common hepatic artery, portal vein and infra-hepatic inferior vena cava (Figure 2.6). A polyethylene 10 (PE-10) catheter was inserted retrograde into the GDA for a length of approximately 4 mm and secured with two 6-0 silk sutures (Figure 2.7). Infusion of 7 mL of 100 units/mL of heparinized normal saline was made into the GDA of a live WAG/RijHsd rat to temporarily evacuate the hepatic blood volume prior to delivery of the functionalized dendrimer complex. To demonstrate its preferential accumulation in tumors, Eu-G3P4A18N (0.8 mg/g total body weight) was infused through the GDA followed by 5 mL of normal saline to ensure full distribution of the dendrimer into the liver. The liver was excised following infusion to evaluate the luminescence signal emitted by the Eu-G3P4A18N in the tumor and the background liver parenchyma.

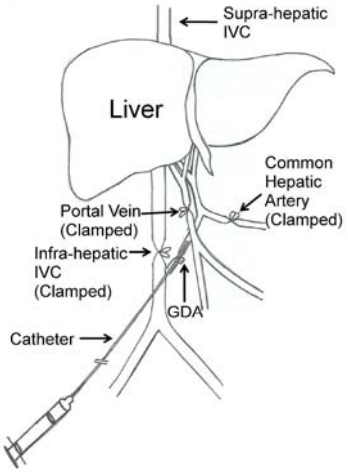

Figure 2.6. Diagram of the GDA cannulation illustrating the isolation of the liver with clamping of the major vessels: portal vein, infra-hepatic inferior vena cava, and the common hepatic artery. The cannulation is indicated by a syringe and catheter leading into the site of the GDA.

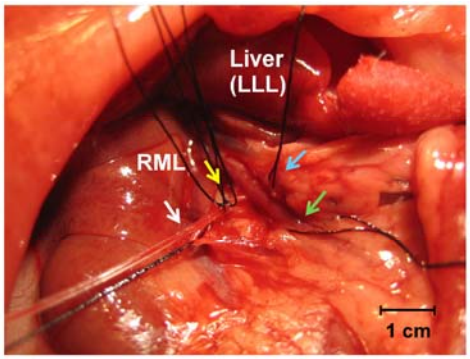

Figure 2.7. Cannulation of the GDA. A 1 mm polyethylene catheter was inserted into the GDA (white arrow) and then secured with two 6-0 silk ties (yellow arrow). The hepatic artery was isolated with a silk tie (blue arrow). The portal vein was also isolated using a silk tie (green arrow). The liver is shown above with the dome of the left lateral lobe (LLL) reflected at the top of the photo and the right medial lobe (RML) immediately to the left of the LLL. Liver is being shown in the anterior to posterior view.

2.3.3 *Ex vivo* imaging of Eu-G3P4A18N infusion

Imaging of *ex vivo* rat livers demonstrated that high-intensity luminescence was observable in the tumors only seconds following an *ex vivo* Eu-G3P4A18N infusion (Figure 2.8) when observing emission signals at 610 nm or at 740 nm. Although some minor uptake by the non-tumorous portion of the liver was observed, these background signals were negligible in the red/NIR range of imaging. In animals with extra-hepatic intra-abdominal tumor deposits, no luminescence was observed in these tissues (data not shown). To confirm that Eu-G3P4A18N enhancement is occurring specifically in the tumor tissues, histological evaluation of the luminescent foci demonstrated that they were adenocarcinomas (Figure 2.9).

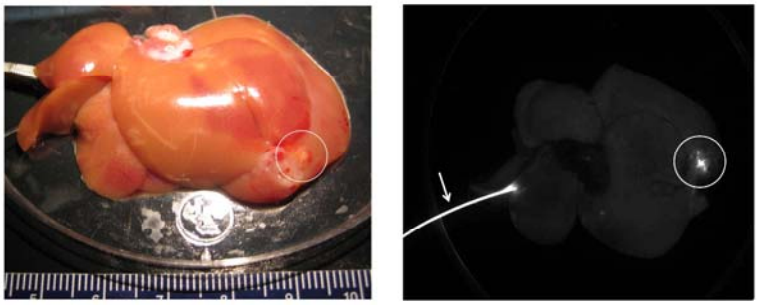

Figure 2.8. A cannulated *ex vivo* liver infused with Eu^{3+}, G3P or Eu-G3P4A18N with luminescence imaging and analysis. *Left:* White light image of an *ex vivo* liver with an established tumor implant. The white circle indicates the location of the tumor within the liver. *Right:* Luminescence image (λ_{ex} = 450 nm, λ_{em} = 610/30 nm) of liver after Eu-G3P4A18N infusion. The circle shows the luminescence emitted by the tumor area only seconds after infusion of the Eu-G3P4A18N complex.

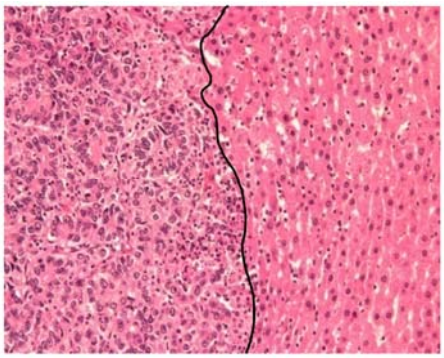

Figure 2.9. 20× Hematoxylin and eosin (H&E) stained section of the tumor from the same liver showing the transition zone between adenocarcinoma on the left and normal liver parenchyma on the right of the solid black line.

To verify that Eu-G3P4A18N has the exclusive capacity to label tumors in the liver, rat livers were infused *in vivo* with Eu^{3+} cations only, dendrimers without Eu^{3+} or naphthalimide (G3P), or Eu-G3P4A18N. Figure 2.10 demonstrates the gross and luminescence images of the livers infused with the three different molecules or cations. The Eu^{3+}-only infusion and the dendrimer-only infusion both show minimal or no luminescence arising from the tumor when compared to the tissue autofluorescence. However, intrahepatic Eu-G3P4A18N infusion demonstrated specific higher intensity luminescence in the tumor. These data are represented quantitatively in Figure 2.10.

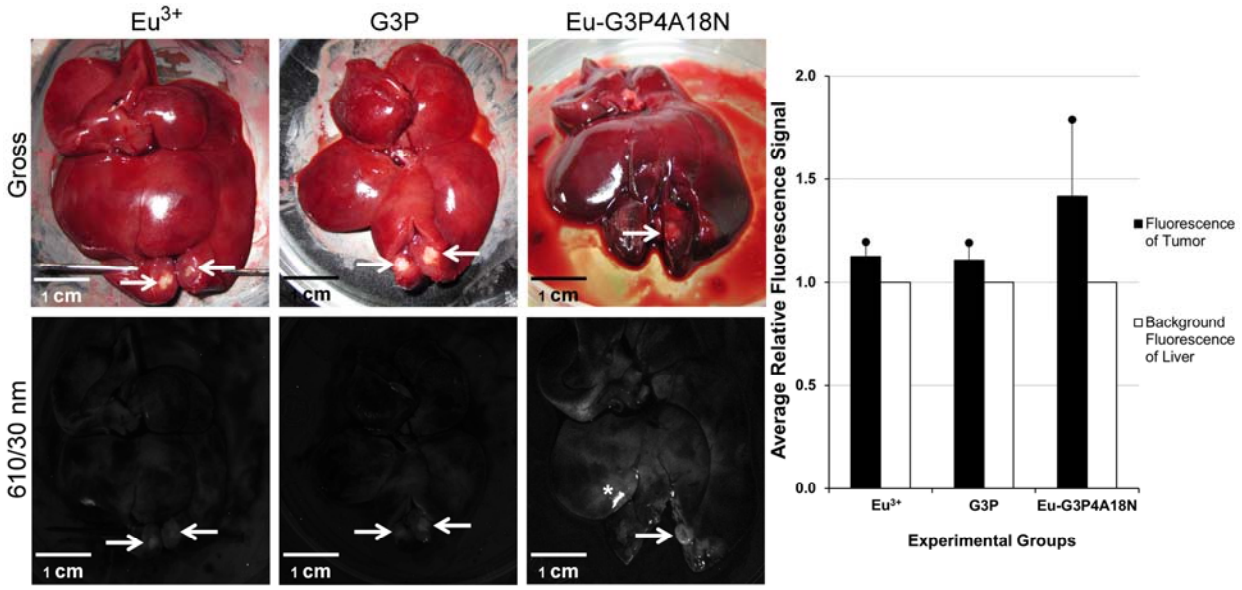

Figure 2.10. Gross photographs (*top row*) and luminescence images (*bottom row*) of the livers containing tumors (arrows) that were implanted 20–30 days prior to infusion and excised at 0 hour time point. Images are from liver infused with Eu^{3+} only (*first column*), G3P (non-functionalized dendrimer without Eu^{3+}; *second column*), or Eu-G3P4A18N (*third column*). Average tumor luminescence was corrected for background autofluorescence in the resulting graph. Asterisks represent specular reflection of the liver. Scale bars represent 1 cm.

2.3.4 Multiple tumor imaging with Eu-G3P4A18N

Multiple metastatic tumor nodules were generated in a rat liver via a splenic injection of CC531 colorectal cancer cells. After infusion of Eu-G3P4A18N, the rat liver was excised and imaged by luminescence. Figure 2.11 (*top row*) shows the gross and corresponding luminescence photographs of an *ex vivo* liver. This liver was used as a control and was not infused with the dendrimer complex to demonstrate that the metastatic tumor nodules themselves have minimal native fluorescence within the spectral region of detection (595-625 nm). Figure 2.11 (*bottom row*) presents the gross and corresponding luminescence photographs of another *ex vivo* rat liver with metastatic lesions. The metastatic nodules display a more intense luminescence signal than the background after infusion of Eu-G3P4A18N.

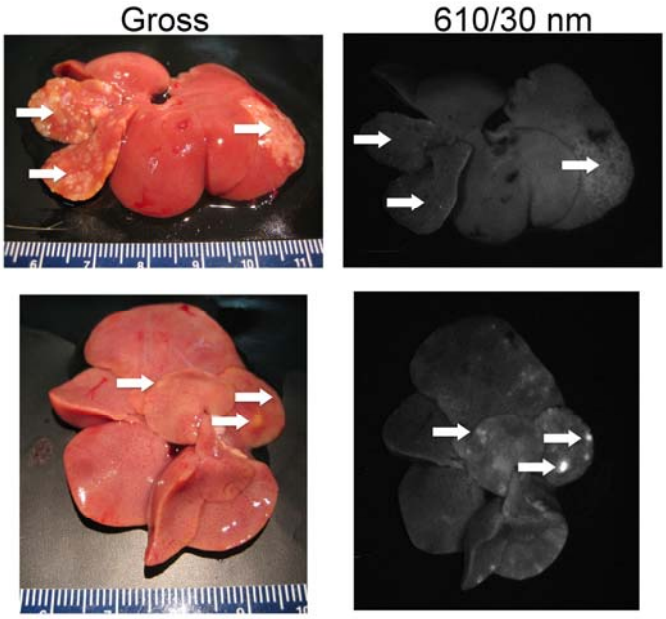

Figure 2.11. Colorectal metastasis to the liver without (*top row*) and with (*bottom row*) infusion of Eu-G3P4A18N. In the top row arrows show tumor nodules in the liver of a rat generated after a splenic injection of CC531 tumor cells. No dendrimer was infused into this liver. The second image shows the absence of luminescence in the nodules. In the bottom row arrows show metastatic lesions in another liver of a rat from a splenic injection of CC531 tumor cells. The liver was infused with Eu-G3P4A18N (300 μL of a 60 μM solution in 10% DMSO/H_2O). Luminescence images (λ_{ex} = 450 nm, λ_{em} = 610/30 nm) were taken with a Rolera XR NIR-sensitive CCD camera.

2.3.5 Retention time of the Eu-G3P4A18N in tumors

To determine the retention time of the dendrimer in the tumor post-infusion, rats were injected intrahepatically with Eu-G3P4A18N and sacrificed at the following time points: 0 hours, 4 hours, 24 hours, and 72 hours (Figure 2.12). Sustained luminescence signals from the tumors

were observed at every time point post-infusion. Background autofluorescence of the liver was accounted for and the resulting bar graph (Figure 2.12) demonstrates quantitatively that signals from the tumors were present up to 72 hours post injection.

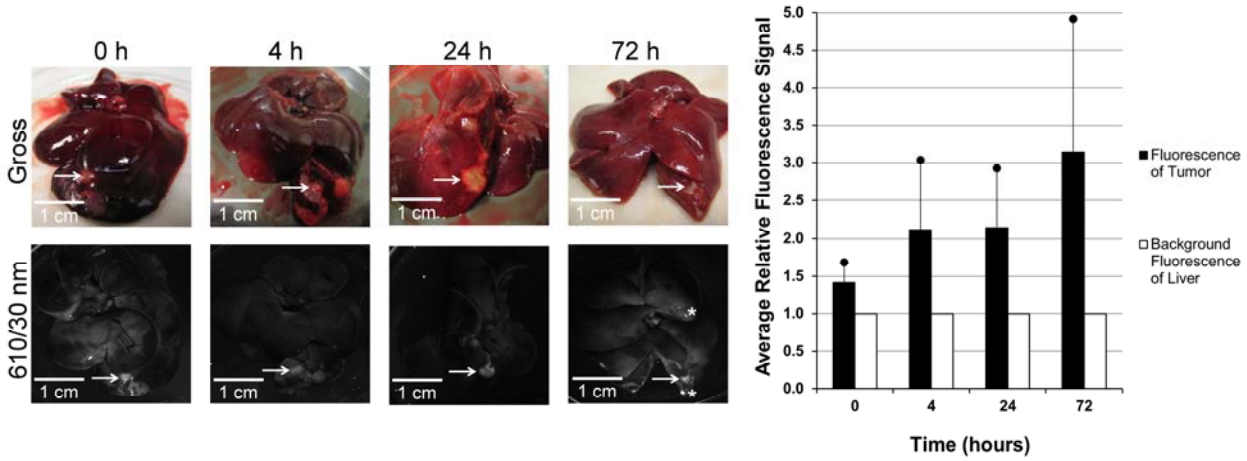

Figure 2.12. Gross and luminescent photographs of tumors located in the livers of rats with analysis of the tumor luminescence. Gross (*top row*) and luminescent (*bottom row*) images of the livers containing tumors (arrows) that were implanted 20–30 days prior to infusion and excised at 0 hour, 4 hour, 24 hour, and 72 hour time points after hepatic infusion with Eu-G3P4A18N. Average signals obtained from the tumors were compared to that of tissue autofluorescence and displayed in the resulting graph. Asterisks represent specular reflection. Scale bars represent 1 cm.

2.3.6 *In vivo* imaging of the Eu-G3P4A18N infusion

To evaluate the preferential accumulation in tumors of our functionalized dendrimer *in vivo*, *in vivo* intrahepatic infusion of Eu-G3P4A18N in anesthetized rats (Figure 2.13) was performed.

Localized luminescence was observed in the tumor tissues within seconds following the beginning of the infusion. This result is consistent with our previous observations in the *ex vivo* setting. The infused liver was excised and sectioned for red/NIR microscopy. We found that the signal-to-noise ratio was improved when luminescence was detected at 740/140 nm (image not shown) as compared to 610/30 nm.

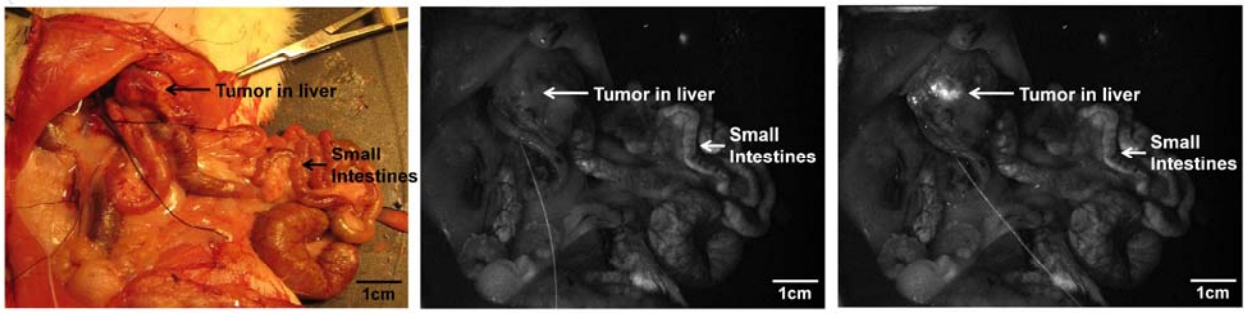

Figure 2.13. *In vivo* colorectal hepatic tumor localization after the infusion of Eu-G3P4A18N and histological imaging using confocal and multi-photon scanning microscopy. *Left:* White light photograph of an *in vivo* rat liver containing a tumor. *Center and Right:* Luminescent images (λ_{ex} = 450 nm, λ_{em} = 610/30 nm) of the abdominal cavity of the rat before (*center*) and after (*right*) Eu-G3P4A18N infusion.

The use of a two-photon excitation scanning confocal microscope allowed us to confirm that the luminescence signal of the dendrimer was present within the vasculature of the liver (Figure 2.14, *left*). Higher magnifications of the tissue sections revealed that the luminescence is located outside of the vessels in the perivascular space (Figure 2.14, *right*). Figure 2.15 also show a section of tumor from a rat liver that was infused with Eu-G3P4A18N displaying the same association of the dendrimer with the vasculature under confocal microscopy. Tumor vasculature is disorganized and displays widened inter-endothelial junctions and fenestrae that

range from 400 to 800 nm in size.[24] Thus, tumor vasculature is often described as "leaky", allowing for larger molecules to extravasate the vascular endothelium into the extravascular space and in the process bypass normal liver parenchyma. The relatively small size of our dendrimer[25] facilitates its exit through the fenestrae and allows it to be trapped in the extravascular spaces of the tumor. The confocal microscopy observations are consistent with the hypothesis that the Eu-G3P4A18N complex has increased extravasation from the leaky tumor vasculature and, therefore, is more likely to be trapped in the perivascular spaces of the tumor.

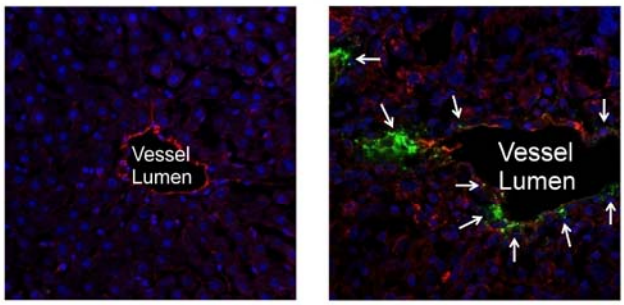

Figure 2.14. *Left:* 20× confocal microscopic image of a section of liver without the tumor after Eu-G3P4A18N infusion, no luminescence of the dendrimer is observed (λ_{ex} = 488 nm, λ_{em} = 567 nm). Vessels are labeled with CD-31 (red), nuclei of hepatocytes with DAPI (blue) and dendrimer (green). *Right:* Eu-G3P4A18N can be seen in green (arrows) with the 40× magnification of a confocal microscopic image of tumor in the liver after infusion. The same colored labels are used.

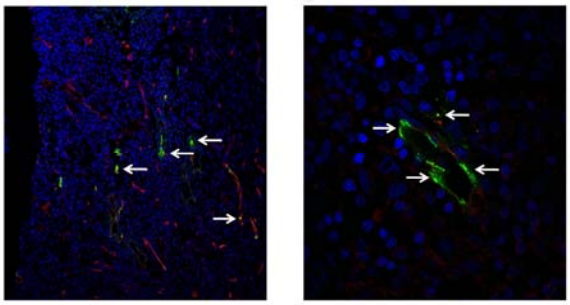

Figure 2.15. *Left:* 25× magnification of a tumor section in a rat liver after infusion of Eu-G3P4A18N (two-photon λ_{ex} = 820 nm, λ_{em} = 570–625 nm). The nuclei of cancer cells are seen in blue, the aberrant vessels are depicted in red, and the dendrimer is designated in green (arrows) to show the association of Eu-G3P4A18N with the tumor vasculature seen in red. *Right:* 60× magnification of another section of tumor within the same liver also demonstrating the same concept.

2.4 CONCLUSION

We have designed and synthesized a luminescent marker based on a generation-3 dendrimer covalently substituted with thirty-two luminescent 4-amino-1,8-naphthalimide groups via glycine linkers, and complexed with eight equivalents of trivalent europium cations (Eu-G3P4A18N). The large number of luminescent groups results in more sensitive detection due to the large number of fluorophores per unit volume. Lanthanide cations coordinated within the dendrimer branches allow for stabilization of the fluorophores against photobleaching and result in a robust luminescent marker. These unique properties make real-time luminescence imaging of hepatic tumors in the WAG/RijHsd rat model possible. We have observed that the luminescence located in the tumor was visible within seconds following hepatic arterial infusion of the dendrimer.

This rapid visualization compares favorably with other fluorescent agents such as pH sensitive fluorescent markers[26], the incorporation of which may take hours in order to achieve observable fluorescence, or green fluorescent proteins (GFPs) and luciferase-based strategies where there is also limited control over the timing of the genetic expression. In addition, luciferase-based strategies require tumor cells to express this gene prior to inducing tumors, a method that is not compatible with clinical studies. Moreover, small molecule fluorophores such as fluorescein and cyanine dyes tend to photobleach rapidly, thus limiting their usefulness in the diagnostic setting.

Our modified dendrimer complex[25] is significantly smaller than the 100 nm and 300 nm sized nanoparticles used in other tumor detection studies[27], minimizing disturbance of the biological system to be observed. Size-specificity is advantageous for improved distribution, thereby maximizing potential tumor tissue penetration and preferential accumulation.[28] In our proposed metastatic tumor model, we have demonstrated our ability to unambiguously detect the presence of a tumor within seconds post-infusion and up to 72 hours *in vivo* within the liver tumor tissue. The enhanced viability of the luminescent dendrimer complex localized within tumor tissue avails the strategy to multiple potential clinical applications in both imaging and therapeutic settings. As demonstrated in this study, by utilizing the nanoscale size and photophysical stability of the Eu^{3+} dendrimer complex, we were able to preferentially accumulate within and image tumor tissue in our rat hepatic metastasis model with near-infrared imaging.

Peptide molecules, such as the RGD peptide[29,30], and tumor-specific antibodies have been demonstrated to have tumor targeting specificity[31-33]. The attachment of such peptide and antibody entities to the dendrimer complex described in this report is anticipated to further improve preferential accumulation within tumors. The synthetic versatility of our functionalized

dendrimer platform allows us to adapt this preferentially-accumulating system to address a wide array of biological questions. For example, coordination of a radionuclide such as yttrium-90 by our dendrimer should allow for targeted delivery of radiotherapeutic agents to the interior of tumors. The many opportunities which exist for modifying the dendrimer platform will lead to a broad field of applications in detecting and monitoring biological events.

2.5 REFERENCES

(1) Jemal, A.; Siegel, R.; Ward, E.; Hao, Y.; Xu, J.; Murray, T.; Thun, M. J. *CA Cancer J. Clin.* **2008**, *58*, 71-96.
(2) Park, J. O.; Brown, C. K. In *Holland-Frei Manual of Cancer Medicine*; Brown, C. K., Rini, B. I., Connell, P. P., Posner, M. C., Eds.; B.C. Decker, Inc.: 2005, p 184-204.
(3) Abdalla, E. K.; Vauthey, J.-N.; Ellis, L. M.; Ellis, V.; Pollock, R.; Broglio, K. R.; Hess, K.; Curley, S. A. *Ann. Surg.* **2004**, *239*, 818-827.
(4) Fiorentini, G.; Aliberti, C.; Benea, G.; Montagnani, F.; Mambrini, A.; Ballardini, P. L.; Cantore, M. *Hepato-gastroenterology* **2008**, *55*, 2077-2082.
(5) Bartlett, D. L.; Libutti, S. K.; Figg, W. D.; Fraker, D. L.; Alexander, H. R. *Surgery* **2001**, *129*, 176-187.
(6) Agarwal, A.; Asthana, A.; Gupta, U.; Jain, N. K. *J. Pharm. Pharmacol.* **2008**, *60*, 671-688.
(7) Medina, S. H.; El-Sayed, M. E. H. *Chem. Rev.* **2009**, *109*, 3141-3157.
(8) Tekade, R. K.; Kumar, P. V.; Jain, N. K. *Chem. Rev.* **2008**, *109*, 49-87.
(9) Majoros, I. J.; Myc, A.; Thomas, T.; Mehta, C. B.; Baker, J. R. *Biomacromolecules* **2006**, *7*, 572-579.
(10) Wolinsky, J. B.; Grinstaff, M. W. *Adv. Drug Deliv. Rev.* **2008**, *60*, 1037-1055.
(11) Kaminskas, L. M.; Kelly, B. D.; McLeod, V. M.; Boyd, B. J.; Krippner, G. Y.; Williams, E. D.; Porter, C. J. H. *Mol. Pharmaceutics* **2009**, *6*, 1190-1204.
(12) Stiriba, S.-E.; Frey, H.; Haag, R. *Angew. Chem., Int. Ed.* **2002**, *41*, 1329-1334.
(13) Dykes, G. M. *J. Chem. Technol. Biotechnol.* **2001**, *76*, 903-918.
(14) Nockemann, P.; Beurer, E.; Driesen, K.; Van Deun, R.; Van Hecke, K.; Van Meervelt, L.; Binnemans, K. *Chem. Commun.* **2005**, 4354-4356.
(15) Yuan, D.; Brown, R. G.; Hepworth, J. D.; Alexiou, M. S.; Tyman, J. H. P. *J. Heterocyclic Chem.* **2008**, *45*, 397-404.
(16) Cross, J. P.; Lauz, M.; Badger, P. D.; Petoud, S. *J. Am. Chem. Soc.* **2004**, *126*, 16278-16279.
(17) Aebischer, A.; Gumy, F.; Bünzli, J.-C. G. *Phys. Chem. Chem. Phys.* **2009**, *11*, 1346-1353.

(18) Wittmer, A.; Khazaie, K.; Berger, M. *Clin. Exp. Metastasis* **1999**, *17*, 369-376.
(19) Bouvet, M.; Tsuji, K.; Yang, M.; Jiang, P.; Moossa, A. R.; Hoffman, R. M. *Cancer Res.* **2006**, *66*, 11293-11297.
(20) Kollmar, O.; Schilling, M. K.; Menger, M. D. *Clin. Exp. Metastasis* **2004**, *21*, 453-460.
(21) Hagenaars, M.; Ensink, N. G.; Basse, P. H.; Hokland, M.; Nannmark, U.; Eggermont, A. M.; van de Velde, C. J.; Fleuren, G. J.; Kuppen, P. J. *Clin. Exp. Metastasis* **2000**, *18*, 189-196.
(22) Imaoka, T.; Horiguchi, H.; Yamamoto, K. *J. Am. Chem. Soc.* **2002**, *125*, 340-341.
(23) Dougherty, T. J. *Photochem. Photobiol.* **1987**, *45*, 879-889.
(24) Svenson, S.; Tomalia, D. A. *Adv. Drug Deliv. Rev.* **2005**, *57*, 2106-2129.
(25) Maiti, P. K.; Cagin, T.; Wang, G.; Goddard, W. A. *Macromolecules* **2004**, *37*, 6236-6254.
(26) Urano, Y.; Asanuma, D.; Hama, Y.; Koyama, Y.; Barrett, T.; Kamiya, M.; Nagano, T.; Watanabe, T.; Hasegawa, A.; Choyke, P. L.; Kobayashi, H. *Nat. Med.* **2009**, *15*, 104-109.
(27) Liu, P.; Zhang, A.; Zhou, M.; Xu, Y.; Xu, L. X. In *Eng. Med. Biol. Soc., 2004. IEMBS '04. 26th Annual International Conference of the IEEE* 2004; Vol. 1, p 2662-2665.
(28) di Tomaso, E.; Capen, D.; Haskell, A.; Hart, J.; Logie, J. J.; Jain, R. K.; McDonald, D. M.; Jones, R.; Munn, L. L. *Cancer Res.* **2005**, *65*, 5740-5749.
(29) Weller, G. E.; Wong, M. K.; Modzelewski, R. A.; Lu, E.; Klibanov, A. L.; Wagner, W. R.; Villanueva, F. S. *Cancer Res.* **2005**, *65*, 533-539.
(30) Dunehoo, A. L.; Anderson, M.; Majumdar, S.; Kobayashi, N.; Berkland, C.; Siahaan, T. J. *J. Pharm. Sci.* **2006**, *95*, 1856-1872.
(31) Brown, C. K.; Modzelewski, R. A.; Johnson, C. S.; Wong, M. K. *Ann. Surg. Oncol.* **2000**, *7*, 743-749.
(32) Ruoslahti, E. *Drug Discov. Today* **2002**, *7*, 1138-1143.
(33) Ruoslahti, E.; Bhatia, S. N.; Sailor, M. J. *J. Cell Biol.* **2010**, *188*, 759-768.

3.0 YB TO ER ENERGY TRANSFER WITHIN A METAL-ORGANIC FRAMEWORK FOR TELECOMMUNICATION DEVICES WITH ENHANCED ERBIUM EMISSION

This work was performed in collaboration with Kiley A. White (Nathaniel L. Rosi Research Group, University of Pittsburgh), Demetra A. Czegan (Stéphane Petoud Research Group, University of Pittsburgh), and Svetlana V. Eliseeva (Centre de Biophysique Moléculaire, Centre National de la Recherche Scientifique, Orléans, France).

3.1 INTRODUCTION

The luminescent lanthanide erbium has been widely studied for practical use in photonic materials and optical telecommunication devices.[1,2] Due to the shielding of the 4*f* electrons by the 5*s* and 5*p* electrons the atom-like, sharp emission bands of the lanthanide cations occur at fixed wavelengths which have constant values regardless of environmental conditions such as pH and temperature.[3] The characteristic emission of erbium (III) cations, Er^{3+}, at 1.5 μm is located in the minimum-loss transmission window of silica fibers in optical telecommunication devices, making it ideally suited for use in such applications.[1,2,4,5] Due to the forbidden nature of the 4*f* → 4*f* transition, the direct excitation of erbium ions in an efficient manner is difficult. It is well-established that the "antennae effect" can be used to overcome this limitation and increase lanthanide luminescence.[6] In this approach lanthanide cations are placed in close proximity to antennae, chromophoric molecules with high absorptivity that transfer energy to sensitize the lanthanide cations. The coordination environment around lanthanide cations, and thus the organization of antennae, significantly impacts the luminescent properties of the complex. In order to obtain a sufficient luminescence intensity, lanthanide cations need to be well protected from -OH, -NH, and -CH vibrations, the overtones of which quench luminescence intensity and decrease luminescence lifetimes.[7]

In order to effectively utilize erbium in telecommunication devices the challenge of low molar absorptivity needs to be overcome. One strategy is based on ytterbium to erbium energy transfer since Yb^{3+} has an absorption cross-section that is ~10x greater than that of Er^{3+}.[8] Yb^{3+}

and Er^{3+} have been co-doped into a variety of materials such as a yttrium aluminum garnet (YAG) matrix[9], glass[10,11], thin films[4,5,12,13], and crystals[14]. In order to realize Er^{3+} emission these materials were excited at ~940 nm or ~980 nm by pumping the excited state of Yb^{3+}. The energy was transferred to the excited state of Er^{3+} from Yb^{3+}, and enhanced Er^{3+} emission was observed. Additionally, there have been Yb-Er complexes in which the Yb^{3+} ions were not directly pumped, but instead the ligands were excited and subsequently sensitized the Yb^{3+}, allowing for Yb^{3+} to Er^{3+} energy transfer.[15-17] We have taken a novel approach of using Yb^{3+} and Er^{3+} in various ratios as the metal in fixed and constant distances in metal-organic frameworks.

Metal-organic frameworks (MOFs), composed of metal ions or clusters linked together by organic ligands, are an attractive class of materials for organizing and protecting lanthanide cations. MOFs have been used for many applications such as gas storage, drug delivery, catalysis, sensing, and biomedical imaging.[18-23] MOFs have been previously shown to enhance the photophysical properties of the lanthanide cations due to some of their advantageous features. First, they have rigid structures in which the metal ions and ligands are well-organized and spatially constrained. These structures can incorporate a large number of metal cations per unit of volume and the metal ion coordination spheres are often completely saturated by the ligands. In the context of lanthanide luminescence, these features are important because increasing the density of lanthanide cations within a material will result in the increase of emission intensity per unit of volume.[24] The high number of chromophoric groups will help maximize the absorption of excitation light, also leading to more photons emitted by the MOF. Second, MOFs exhibit a variety of topologies and in some cases their structures can be designed. Therefore, one can control the positions of the metal ions and ligands within a MOF, which permits precise tuning of MOF properties. For example, Chen et al. demonstrated enhanced Er^{3+} emission within a

MOF by replacing terephthalate with perfluoranated terephthalate.[25] Third, one can target multiple metal ion MOFs[26-28], allowing for the incorporation of multiple luminescent lanthanides and multiple signals into a single material. Using this strategy, we incorporated both Yb^{3+} and Er^{3+} into a MOF and demonstrated an increase in the quantum yield of Er^{3+} upon increasing the amount of Yb^{3+}. To the best of our knowledge this is the first report of using a mixed-metal MOF to enhance the intensity of Er^{3+} emission.

3.2 EXPERIMENTAL

3.2.1 Reagents

Reagents were obtained from commercial sources and used as received without further purification. The H_2-PVDC was synthesized according to a previously published method.[29]
The 1,4-dimethoxybenzene (99%), paraformaldehyde (PFA; 95%), sodium methoxide (0.05 M in methanol), anhydrous methanol (99.8%), ytterbium (III) nitrate pentahydrate ($Yb(NO_3)_3 \cdot 5H_2O$; 99.999%), and erbium (III) nitrate pentahydrate ($Er(NO_3)_3 \cdot 5H_2O$; 99.9999%) were purchased from Sigma–Aldrich. Hydrobromic acid (HBr; 33 wt% in acetic acid) was purchased from Fluka. Anhydrous chloroform ($CHCl_3$; 99.8%) and anhydrous toluene (99.8%) were purchased from Acros. Triphenylphosphine was purchased from MCB Reagents. Methanol (Certified ACS), tetrahydrofuran (Certified ACS), and potassium hydroxide (KOH; Certified ACS pellets) were purchased from Fisher. Methyl 4-formylbenzoate (>98%) was purchased from TCI. *N,N*-dimethylformamide (DMF; ACS grade) was purchased from Emmanuel Merck Darmstadt. Nitric acid (HNO_3; ACS Reagent, 36.5–38.0%) and glacial acetic acid (Baker Analyzed

Reagent), and hydrochloric acid (HCl, 36.5-38.0%, Baker Analyzed ACS Reagent) were purchased from J. T. Baker. Ethanol (EtOH; 200 proof) was purchased from Decon Laboratories, Inc.

3.2.2 Synthesis of Er_xYb_{1-x}-PVDC-1 MOFs

The procedures for the synthesis of the Yb-PVDC-1[29] and Er_xYb_{1-x}-PVDC-1[28] have been previously reported in the literature.

3.2.2.1 Synthesis of Yb-PVDC-1

In a glass vial (4 mL), a solution of 4,4'-(1*E*,1'*E*)-2,2'-(2,5-dimethoxy-1,4-phenylene)bis(ethene-2,1-diyl)dibenzoic acid (H_2-PVDC) (8.60 mg, 0.020 mmol) in DMF (0.4 mL) was added to a solution of $Yb(NO_3)_3 \cdot 5H_2O$ (6.75 mg, 0.015 mmol) and 1M HNO_3(aq) (20.0 μL) in DMF (0.3 mL) to produce a neon green solution. The vial was capped and placed in an 85 ºC isotemp oven for 48 hours to produce yellow crystalline needles of the product. The crystals were collected, washed with DMF (4 × 3 mL), and air dried.

3.2.2.2 Synthesis of $Er_{0.32}Yb_{0.68}$-PVDC-1

In a glass vial (4 mL), a solution of 4,4'-(1*E*,1'*E*)-2,2'-(2,5-dimethoxy-1,4-phenylene)bis(ethene-2,1-diyl)dibenzoic acid (H_2-PVDC) (8.60 mg, 0.020 mmol) in DMF (0.4 mL) was added to a solution of $Yb(NO_3)_3 \cdot 5H_2O$ (1.02 mg, 0.0025 mmol) in DMF (0.050 mL), $Er(NO_3)_3 \cdot 5H_2O$ (0.55 mg, 0.00125 mmol) in DMF (0.025 mL), and 1M HNO_3(aq) (10.0 μL) to produce a neon green solution. The vial was capped and placed in a 100 ºC isotemp oven for 72 hours to produce

yellow crystalline needles. The crystals were collected, washed with DMF (4 × 3 mL), and air dried.

3.2.2.3 Synthesis of $Er_{0.58}Yb_{0.42}$-PVDC-1

In a glass vial (4 mL), a solution of 4,4'-(1*E*,1'*E*)-2,2'-(2,5-dimethoxy-1,4-phenylene)bis(ethene-2,1-diyl)dibenzoic acid (H_2-PVDC) (8.60 mg, 0.020 mmol) in DMF (0.4 mL) was added to a solution of $Yb(NO_3)_3 \cdot 5H_2O$ (1.02 mg, 0.0025 mmol) in DMF (0.050 mL), $Er(NO_3)_3 \cdot 5H_2O$ (1.66 mg, 0.00375 mmol) in DMF (0.075 mL), and 1M HNO_3(aq) (10.0 μL) to produce a neon green solution. The vial was capped and placed in a 100 ºC isotemp oven for 72 hours to produce yellow crystalline needles. The crystals were collected, washed with DMF (4 × 3 mL), and air dried.

3.2.2.4 Synthesis of $Er_{0.70}Yb_{0.30}$-PVDC-1

In a glass vial (4 mL), a solution of 4,4'-(1*E*,1'*E*)-2,2'-(2,5-dimethoxy-1,4-phenylene)bis(ethene-2,1-diyl)dibenzoic acid (H_2-PVDC) (8.60 mg, 0.020 mmol) in DMF (0.4 mL) was added to a solution of $Yb(NO_3)_3 \cdot 5H_2O$ (1.02 mg, 0.0025 mmol) in DMF (0.050 mL), $Er(NO_3)_3 \cdot 5H_2O$ (2.77 mg, 0.00625 mmol) in DMF (0.125 mL), and 1M HNO_3(aq) (10.0 μL) to produce a neon green solution. The vial was capped and placed in a 100 ºC isotemp oven for 72 hours to produce yellow crystalline needles. The crystals were collected, washed with DMF (4 × 3 mL), and air dried.

3.2.2.5 Synthesis of $Er_{0.81}Yb_{0.19}$-PVDC-1

In a glass vial (4 mL), a solution of 4,4'-(1*E*,1'*E*)-2,2'-(2,5-dimethoxy-1,4-phenylene)bis(ethene-2,1-diyl)dibenzoic acid (H_2-PVDC) (8.60 mg, 0.020 mmol) in DMF (0.4 mL) was added to a

solution of $Yb(NO_3)_3 \cdot 5H_2O$ (0.56 mg, 0.00125 mmol) in DMF (0.025 mL), $Er(NO_3)_3 \cdot 5H_2O$ (2.77 mg, 0.00625 mmol) in DMF (0.125 mL), and 1M HNO_3(aq) (10.0 μL) to produce a neon green solution. The vial was capped and placed in a 100 ºC isotemp oven for 72 hours to produce yellow crystalline needles. The crystals were collected, washed with DMF (4 × 3 mL), and air dried.

3.2.2.6 Synthesis of Er-PVDC-1

In a glass vial (4 mL), a solution of 4,4'-(1*E*,1'*E*)-2,2'-(2,5-dimethoxy-1,4-phenylene)bis(ethene-2,1-diyl)dibenzoic acid (H_2-PVDC) (8.60 mg, 0.020 mmol) in DMF (0.4 mL) and a solution of $Er(NO_3)_3 \cdot 5H_2O$ (4.43 mg, 0.01 mmol) in DMF (0.2 mL) were combined with ethanol (95%, 100.0 μL) to produce a neon green solution. The vial was capped and placed in a 100 ºC isotemp oven for 12 hours to produce yellow crystalline needles of the product. The crystals were collected, washed with DMF (4 × 3 mL), and air dried (2.3 mg, 42.4%).

Elemental analysis (EA) calcd (%) for $Er_2(C_{26}H_{20}O_6)_3(H_2O)_2 \cdot (DMF)_6(H_2O)_{8.5}$: C, 51.04; H, 5.49; N, 3.72. Found: C, 50.97; H, 4.57; N, 3.91. EA calcd (%) for the chloroform exchanged product, $Yb_2(C_{26}H_{20}O_6)_3(H_2O)_2 \cdot (CHCl_3)_{2.75}(DMF)_{0.3}$: C, 48.61; H, 3.44; N, 0.21. Found: C, 48.79; H, 3.10; N, 0.21. FT-IR (KBr 4000-700 cm^{-1}): 3309 (broad, br), 1658 (DMF C=O; medium, m), 1601 (m), 1541 (strong, s), 1415 (COO^-; very strong, vs), 1209 (s), 1180 (weak, w), 1107 (w), 1043 (s), 967 (m), 867 (w), 781 (trans C=C-H, s).

3.2.3 Instrumentation

3.2.3.1 Elemental analysis

The elemental microanalysis (CHN) was performed by the Microanalysis Laboratory at the University of Illinois Urbana-Champaign. Samples were dried under nitrogen flow to remove excess solvent prior to submission for analysis. Energy-dispersive X-ray analysis (EDX) was measured on a Philips XL 30 SEM equipped with an EDAX CDU leap detector.

3.2.3.2 Fourier transform infrared spectroscopy

Fourier transform infrared (FT-IR) spectra were measured on a Nicolet Avatar 360 FT-IR spectrometer using KBr pellet samples.

3.2.3.3 Powder X-ray diffraction

Powder X-ray diffraction (PXRD) patterns were collected using a Phillips PW 1830 diffractometer at 40 kV, 40 mA, for Cu Kα (λ = 1.54056 Å) with a scan speed of 0.20 seconds per step and a step size of 0.020°.

3.2.3.4 Luminescence spectroscopy

Excitation and emission spectra were measured using a HORIBA Jobin Yvon Fluorolog 3-22 spectrofluorometer equipped with a R928 Hamamatsu detector for visible detection and with either a DSS-IGA020L detector (Electro-Optical Systems, Inc.) for the NIR. The sample holder was an integrating sphere using quartz tubes developed by Frédéric Gumy and Jean-Claude G. Bünzli (Laboratory of Lanthanide Supramolecular Chemistry, École Polytechnique Féderale de Lausanne, Lausanne, Switzerland) as an accessory to the Fluorolog 3-22 spectrofluorometer

(patent pending) and commercialized and manufactured by GMP.[30] Spectra were corrected for variations in lamp intensity over the spectra range, as well as for excitation monochromator, emission monochromator, and detector responses. The data were analyzed using OriginPro 7.1 software.

The spectra were corrected using the following process. The MOF and background (solvent) spectra were each offset to zero at 1600 nm and corrected for variations in the lamp intensity. The background spectrum was subtracted from the MOF spectrum using a scaling factor, *k*. The value of *k* was calculated using the equation:

$$Bk = S$$

Equation 3.1.

where *B* represents the background and *S* represents the sample, using the intensities of the respective spectra at 1300 nm (chosen because there is no Ln^{3+} signal in that region). The value of *k* was optimized in order to achieve the flattest baseline. The resulting spectrum was then corrected for the detector.

3.2.3.5 Quantum yield measurements

Quantum yield measurements were also collected on the Fluorolog-322 with the integrating sphere. Collecting NIR quantum yields requires the use of both a visible detector and a NIR detector; ytterbium tropolonate and erbium tropolonate ($[Ln(trop)_4]^-$ in DMSO, $\Phi_{Yb} = 1.9(\pm 0.1)\times 10^{-3}$; $\Phi_{Er} = 1.7(\pm 0.1)\times 10^{-4}$) were used as a references[31] for the respective lanthanides. The process for collecting a relative quantum yield using the integrating sphere is the following step by step process:

1) Emission spectra of the lamp were collected for the sample (R_{S+SB}), the solvent in which the sample is placed (R_{SB}), the reference (*see above*, R_{R+RB}), and the solvent in which the

reference is dissolved (R_{RB}). Neutral density filters were placed at the excitation port of the integrating sphere to control the high intensity of the lamp. The spectra were corrected, as described above, and the bands were integrated. The resulting integration values were used to determine the amount of light that was absorbed by the sample and the reference, given by:

$$R_S = R_{SB} - R_{S+SB}$$

Equation 3.2.

and

$$R_R = R_{RB} - R_{R+RB}$$

Equation 3.3.

2) Emission spectra of the sample (I_{S+SB}), of the sample solvent (I_{SB}), of the reference (I_{R+RB}), and of the reference solvent (I_{RB}) were collected in the NIR range. A 780 nm long-pass filter was placed at the NIR emission port of the integrating sphere to eliminate contributions from second order bands. Emission spectra were corrected for the lamp variation, the solvent spectra were subtracted from the appropriate sample and reference spectra:

$$I_S = I_{S+SB} - I_{SB}$$

Equation 3.4.

and

$$I_R = I_{R+RB} - I_{RB}$$

Equation 3.5.

and the resulting spectra were corrected for detector response. The spectra were not corrected for the filters because in the case of a relative quantum yield measurement the use of a scalar (*see below how such scalar is calculated*) corrects for the filters during the calculations.

3) The known quantum yield of the reference was used to create a scalar ($X_{NIR-VIS}$) which accounts for the use of two different detectors in the visible and in the NIR with a domain of overlapping response:

$$X_{NIR-VIS} = \frac{\Phi_R R_R}{I_R}$$

Equation 3.6.

4) The quantum yield of the sample was calculated using the following equation:

$$\Phi_S = \frac{X_{NIR-VIS} I_S}{R_S}$$

Equation 3.7.

3.2.3.6 Luminescence lifetimes

Luminescence lifetimes were measured using a neodymium yttrium aluminum garnet (Nd:YAG) Continuum Powerlite 8010 laser (355 nm, third harmonic) as the excitation source. Emission was collected at a right angle to the excitation beam, and wavelengths were selected by a Spectral Products CM110 1/8m monochromator. The signal was monitored by a Hamamatsu R316-02 photomultiplier tube and collected on a 500-MHz bandpass digital oscilloscope (Tektronix TDS 754D). Signals from >1,000 flashes were collected and averaged. Three decay curves were collected for each sample, and the data were analyzed using OriginPro 9.1 software with exponential fitting modes.

3.3 RESULTS AND DISCUSSION

Yb-PVDC-1 and barcoded Er_xYb_{1-x}-PVDC-1 materials have been previously synthesized in our lab.[28,29] We demonstrated near-infrared (NIR) emission via the antennae effect including simultaneous emission of the ytterbium and erbium cations when using the barcoded materials.[28] We showed that by altering the amount of lanthanide cation within the MOF, we could directly alter the resulting lanthanide emission intensity. For the barcoded materials, the resulting ratio of Yb^{3+} to Er^{3+} emission intensities varied linearly with the lanthanide atomic content. Interestingly, the Er^{3+} emission signal appeared brighter than that of the Yb^{3+} regardless of the lanthanide content. This result prompted us to probe further as to what was occurring spectroscopically.

3.3.1 Er-PVDC-1

For a complete study of photophysical properties within the Ln-PVDC-1 system, Er-PVDC-1 was then synthesized. Powder X-ray diffraction studies show that Er-PVDC-1 is isostructural with Yb-PVDC-1 and Er_xYb_{1-x}-PVDC-1.

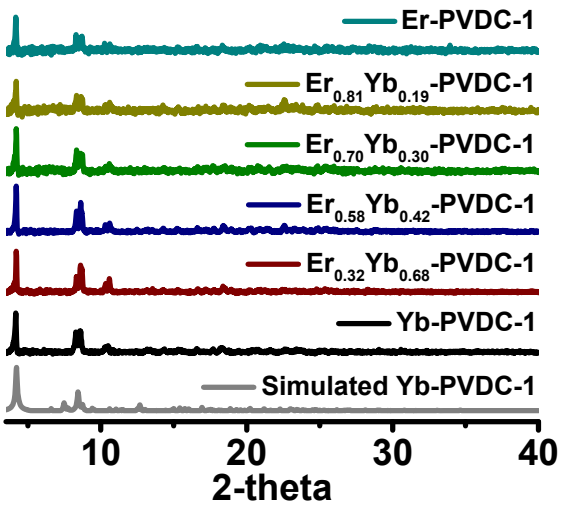

Figure 3.1. Powder X-ray diffraction (PXRD) patterns showing Er-PVDC-1 is isostructural with Yb-PVDC-1 and Er_xYb_{1-x}-PVDC-1.

The excitation profile for Er-PVDC-1 shows apparent maxima centered at 280 nm, 370 nm, and 470 nm, which corresponds to the same maxima observed for Yb-PVDC-1 and Er_xYb_{1-x}-PVDC-1.[28,29] Exciting through any of these three wavelengths results in the generation of Er^{3+} emission centered at 1530 nm (Figure 3.2).

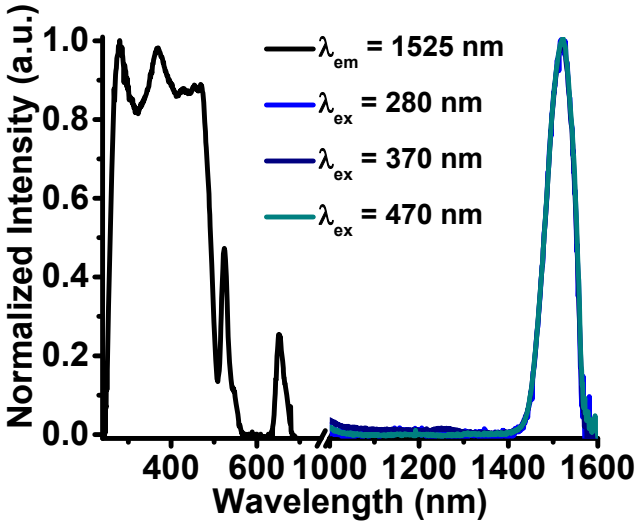

Figure 3.2. Normalized excitation and emission spectra of Er-PVDC-1 under DMF.

To elucidate how the photophysical properties compare between the doped and the single lanthanide MOFs, quantum yields and luminescence lifetimes were systematically collected.

3.3.2 Quantum yields

To quantify the overall efficiency of the antenna effect in the MOF material, quantum yields were measured (Table 3.1) and plotted as a function of percent of each lanthanide in the MOF (Figure 3.3).

Table 3.1. Relative Yb^{3+} and Er^{3+} quantum yields (Φ_{Yb}, Φ_{Er}) for Yb-PVDC-1, Er_xYb_{1-x}-PVDC-1, and Er-PVDC-1 MOFs*.

	Φ_{Yb}†	Φ_{Er}†
Yb-PVDC-1	$3.3(\pm0.5)\times10^{-3}$	-
$Er_{0.32}Yb_{0.68}$-PVDC-1	$6.5(\pm0.8)\times10^{-4}$	$1.8(\pm0.4)\times10^{-4}$
$Er_{0.58}Yb_{0.42}$-PVDC-1	$1.8(\pm0.4)\times10^{-4}$	$1.7(\pm0.4)\times10^{-4}$
$Er_{0.70}Yb_{0.30}$-PVDC-1	$8(\pm2)\times10^{-5}$	$9.98(\pm0.01)\times10^{-5}$
$Er_{0.81}Yb_{0.19}$-PVDC-1	$3.4(\pm0.4)\times10^{-5}$	$6(\pm1)\times10^{-5}$
Er-PVDC-1	-	$8.5(\pm0.44)\times10^{-5}$

*MOFs as crystalline solids under chloroform; †λ_{ex} = 490 nm

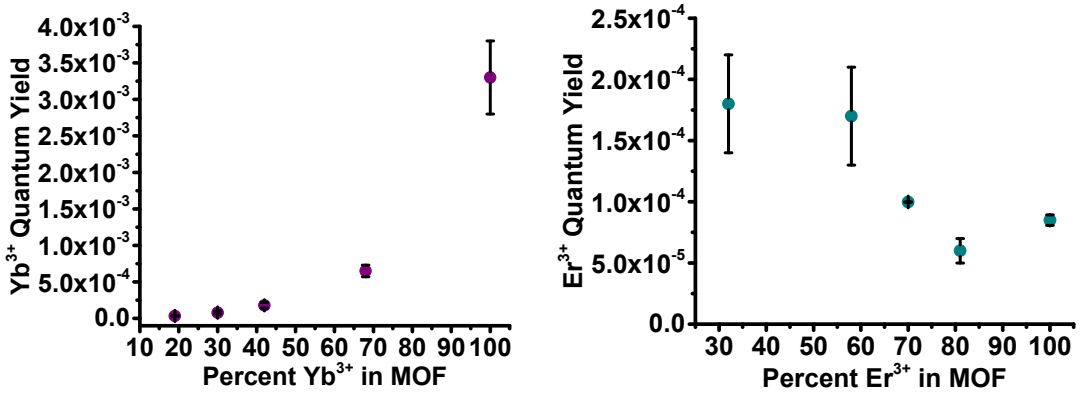

Figure 3.3. *Left:* Plot depicting Yb^{3+} quantum yields (λ_{ex} = 490 nm) versus the percent Yb^{3+} in the MOF for Yb-PVDC-1 and Er_xYb_{1-x}-PVDC-1. *Right:* Plot depicting Er^{3+} quantum yields (λ_{ex} = 490 nm) versus the percent Er^{3+} in the MOF for Er-PVDC-1 and Er_xYb_{1-x}-PVDC-1.

The quantum yield value measured for Yb-PVDC-1 (3.3×10^{-3}) is amongst the highest reported for materials under solvent[31]. However, the quantum yield for Er-PVDC-1 is much lower with a value of 8.5×10^{-5}. The NIR emission of Er^{3+} is easily quenched from the second vibrational overtones of C-H and O-H bonds (Figure 3.4) resulting in non-radiative deactivation due to the small energy difference between the ground and the excited states.

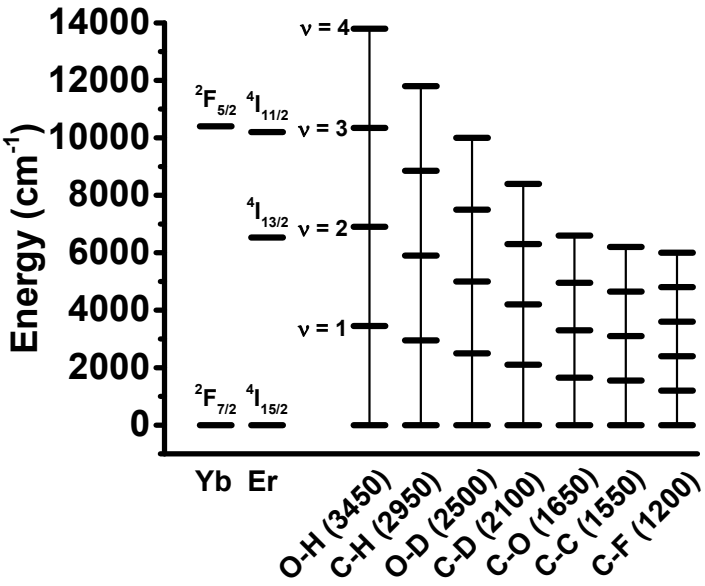

Figure 3.4. Energy levels for Yb, Er, and various vibrational overtones typically responsible for quenching.

The quantum yields for the mixed lanthanide system suggest the presence of Yb^{3+} to Er^{3+} energy transfer. Instead of the quantum yields for each lanthanide increasing/decreasing linearly with the corresponding amount of lanthanide content in the crystal, the quantum yield for Yb^{3+} decreases quickly. As the amount of Er^{3+} decreases and the Yb^{3+} increases, the quantum yield for Er^{3+} actually increases. We rationalize this increase in quantum yield as a result of energy transfer from the $^2F_{5/2}$ level of Yb^{3+} to the accepting $^4I_{11/2}$ level of Er^{3+}.

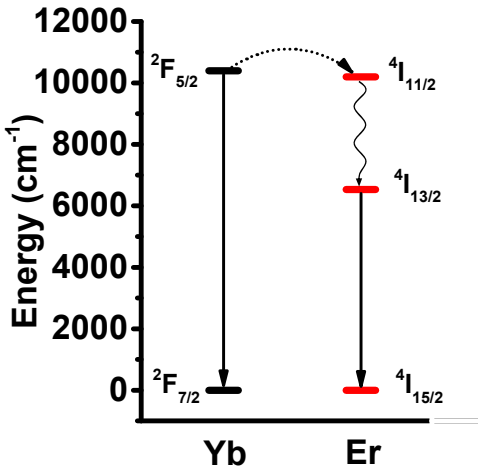

Figure 3.5. Jablonski diagram showing the potential energy pathways from the $^2F_{5/2}$ excited state of Yb^{3+}. Solid lines represent luminescence, the dotted line represents energy transfer, and the wavy line represents non-radiative decay.

It is hypothesized that such energy transfer (Figure 3.5) would take place according to the following process based upon existing literature.[15-17] Incident light excites the ligand from the ground state to the excited singlet state ($S_0 \rightarrow S_1$) followed by intersystem crossing to the triplet state (T_1). From the triplet state, energy is transferred to the accepting $^2F_{5/2}$ level of Yb^{3+}. This is consistent with the Yb^{3+} being sensitized via the antennae effect which was previously demonstrated.[29] Some energy is released as NIR emission via $^2F_{5/2} \rightarrow {}^2F_{7/2}$ transition to Yb^{3+} ground state (~980 nm). Some energy is transferred from the $^2F_{5/2}$ level of Yb^{3+} to $^4I_{11/2}$ level of Er^{3+} followed by fast non-radiative relaxation to $^4I_{13/2}$ level of Er^{3+}, ultimately resulting in the generation of NIR emission (1550 nm) upon relaxation from the $^4I_{13/2}$ state to the $^4I_{15/2}$ ground state.

3.3.3 Luminescence lifetimes

In order to confirm our hypothesis we collected luminescence lifetimes and performed an in-depth analysis. If indeed there is energy transfer from Yb^{3+} to Er^{3+}, the lifetime of Yb^{3+} in the mixed metal MOFs should be shorter than the value observed in Yb-PVDC-1.

When Yb-PVDC-1 was first synthesized its lifetime decay curve (λ_{ex} = 354 nm) was best fit to a four component multi-exponential decay with values of 29(±2), 10(±1), 1.5(±0.5), and 0.34(±0.06) μs.[29] This was rationalized as arising from the four distinct environments of the Yb^{3+} cations present in the MOF, hexa- and octa-coordinated sites on the interior and along the external edges of the crystal.

At the time it was difficult to distinguish the Yb^{3+} signal from noise in the Er_xYb_{1-x}-PVDC-1 system, and we did not have a detector with the required capabilities to collect Er^{3+} lifetimes and fully analyze the system.

Once we gained access to a detector with a sufficient detection range to monitor Er^{3+} luminescence lifetimes, additional samples were synthesized in order to complete the full characterization of the system and study the energy transfer. The measured lifetimes are summarized in Table 3.2. The lifetimes of Yb^{3+} in the mixed-metal system were indeed shorter than that of the Yb-PVDC-1.

In this set of experiments, the Yb-PVDC-1 lifetime was best fit to a mono-exponential function and was more than 40 times shorter (0.7 μs versus 29 μs).

Table 3.2. Yb^{3+} (λ_{em} = 980 nm) and Er^{3+} (λ_{em} = 1550 nm) lifetimes (τ) for Yb-PVDC-1, Er_xYb_{1-x}-PVDC-1, and Er-PVDC-1 MOFs*.

	Yb^{3+}		Er^{3+}	
	τ_1† (µs)	τ_2† (µs)	τ_1† (µs)	τ_2† (µs)
Yb-PVDC-1	0.729(±0.009)	-	-	-
$Er_{0.32}Yb_{0.68}$-PVDC-1	0.44(±0.01)	0.13(±0.01)	0.75(±0.01)	0.131(±0.004)
$Er_{0.58}Yb_{0.42}$-PVDC-1	0.27(±0.02)	0.081(±0.002)	0.46(±0.01)	0.118(±0.002)
$Er_{0.70}Yb_{0.30}$-PVDC-1	0.18(±0.02)	0.054(±0.002)	0.35(±0.04)	0.102(±0.005)
$Er_{0.81}Yb_{0.19}$-PVDC-1	0.21(±0.01)	0.063(±0.01)	0.50(±0.02)	0.123(±0.001)
Er-PVDC-1	-	-	0.35(±0.01)	0.110(±0.004)

*MOFs as a crystalline solid under chloroform; †λ_{ex} = 354 nm

The luminescence lifetime values reported in the Table 3.2 follow a clear trend. The Yb^{3+} lifetimes in Er_xYb_{1-x}-PVDC-1 are shorter than that of Yb-PVDC-1. The Er^{3+} lifetimes in Er_xYb_{1-x}-PVDC-1 are all longer than or equal to those of Er-PVDC-1. This is more easily visualized with plots of lifetime versus percentage of Ln^{3+} in the MOF (Figure 3.6).

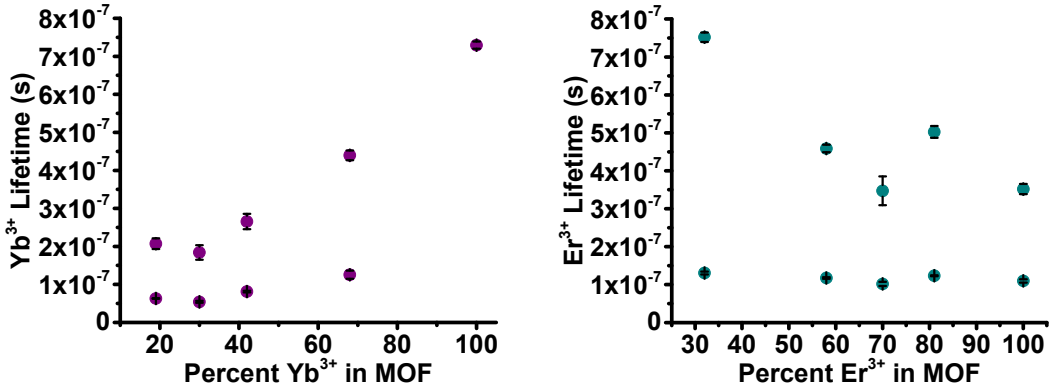

Figure 3.6. *Left:* Plot of Yb^{3+} luminescence lifetimes (λ_{em} = 980 nm) versus the percent Yb^{3+} in the MOF for Yb-PVDC-1 and barcoded Er_xYb_{1-x}-PVDC-1. *Right:* Plot of Er^{3+} lifetimes (λ_{em} = 1550 nm) versus the percent Er^{3+} in the MOF for Er-PVDC-1 and Er_xYb_{1-x}-PVDC-1.

The trend of the lifetimes depicted in Figure 3.6 is consistent with the trend of the quantum yields in Figure 3.3. This suggests that energy transfer from Yb^{3+} to Er^{3+} is taking place, as Er^{3+} emission in indeed enhanced in the presence of Yb^{3+}. To have a deeper understanding we will need to unambiguously determine the lifetimes of these materials, optimally in a variety of solvents as well as in the solid state.

3.4 CONCLUSION

In a follow-up to previously reported Yb-PVDC-1 and barcoded Er_xYb_{1-x}-PVDC-1, we synthesized Er-PVDC-1 and studied the luminescence properties of an array of materials. The Er-PVDC-1 MOF, which was isostructural to the other materials, exhibited an excitation spectrum that is consistent with the other MOFs as well as characteristic NIR Er^{3+} emission. Interestingly, the quantum yields did not correlate linearly with the percentage of each Ln^{3+} present in the MOF. Notably, the Er_xYb_{1-x}-PVDC-1 MOFs had larger Er^{3+} quantum yield values than Er-PVDC-1. Luminescence lifetimes were collected in order to confirm that this effect can be attributed to Yb^{3+} to Er^{3+} energy transfer. The Yb^{3+} lifetime for Yb-PVDC-1 was larger than the Yb^{3+} lifetimes for any of the barcoded Er_xYb_{1-x}-PVDC-1 MOFs. The Er^{3+} lifetimes of Er_xYb_{1-x}-PVDC-1 were longer than or equal to those of Er-PVDC-1. This is a strong indication that energy transfer from Yb^{3+} to Er^{3+} is indeed taking place. However, the discrepancies in the Yb^{3+} lifetimes collected for Yb-PVDC-1 on different batches using different instrumentation must be identified. Nonetheless, these mixed metal Er_xYb_{1-x}-PVDC-1 MOFs demonstrate

enhanced erbium emission in comparison to Er-PVDC-1 and hold promise for use in telecommunication devices.

3.5 REFERENCES

(1) Comby, S.; Bünzli, J.-C. In *Handbook on the Physics and Chemistry and Rare Earths*; Gschneidner, K. A., Bünzli, J.-C., Pecharsky, V. K., Eds.; Elsevier: Amsterdam, 2007; Vol. 37.
(2) Eliseeva, S. V.; Bünzli, J.-C. G. *New J. Chem.* **2011**, *35*, 1165-1176.
(3) Eliseeva, S. V.; Bünzli, J.-C. G. *Chem. Soc. Rev.* **2010**, *39*, 189-227.
(4) Song, L.; Liu, X.; Zhen, Z.; Chen, C.; Zhang, D. *J. Mater. Chem.* **2007**, *17*, 4586-4590.
(5) Cardile, P.; Miritello, M.; Priolo, F. *Appl. Phys. Lett.* **2012**, *100*, 251913.
(6) Weissman, S. I. *J. Chem. Phys.* **1942**, *10*, 214-217.
(7) Beeby, A.; Clarkson, I. M.; Dickins, R. S.; Faulkner, S.; Parker, D.; Royle, L.; de Sousa, A. S.; Williams, J. A. G.; Woods, M. *J. Chem. Soc., Perkin Trans. 2* **1999**, 493-504.
(8) Barbier, D.; Hyde, R. L. In *Integrated Optical Circuits and Components: Design and Applications*; Murphy, E. J., Ed.; CRC Press: New York, New York, 1999.
(9) Vega-Duran, J. T.; Barbosa-Garcia, O.; Diaz-Torres, L. A.; Meneses-Nava, M. A.; Sumida, D. S. *Appl. Phys. Lett.* **2000**, *76*, 2032-2034.
(10) da Vila, L. D.; Gomes, L.; Tarelho, L. V. G.; Ribeiro, S. J. L.; Messadeq, Y. *J. Appl. Phys.* **2003**, *93*, 3873-3880.
(11) Hehlen, M. P.; Cockroft, N. J.; Gosnell, T. R.; Bruce, A. J. *Phys. Rev. B* **1997**, *56*, 9302-9318.
(12) Suarez-Garcia, A.; Serna, R.; de Castro, M. J.; Afonso, C. N.; Vickridge, I. *Appl. Phys. Lett.* **2004**, *84*, 2151-2153.
(13) Wong, W. H.; Pun, E. Y. B.; Chan, K. S. *Appl. Phys. Lett.* **2004**, *84*, 176-178.
(14) You, W.; Huang, Y.; Chen, Y.; Lin, Y.; Luo, Z. *Opt. Commun.* **2008**, *281*, 4936-4939.
(15) Zhong, Q.; Wang, H.; Qian, G.; Wang, Z.; Zhang, J.; Qiu, J.; Wang, M. *Inorg. Chem.* **2006**, *45*, 4537-4543.
(16) Song, L.; Wang, Q.; Tang, D.; Liu, X.; Zhen, Z. *New J. Chem.* **2007**, *31*, 506-511.
(17) Artizzu, F.; Quochi, F.; Marchiò, L.; Sessini, E.; Saba, M.; Serpe, A.; Mura, A.; Mercuri, M. L.; Bongiovanni, G.; Deplano, P. *J. Phys. Chem. Lett.* **2013**, *4*, 3062-3066.
(18) Férey, G. *Chem. Soc. Rev.* **2008**, *37*, 191-214.
(19) Tanabe, K. K.; Cohen, S. M. *Chem. Soc. Rev.* **2011**, *40*, 498-519.
(20) Cui, Y.; Yue, Y.; Qian, G.; Chen, B. *Chem. Rev.* **2011**, *112*, 1126-1162.
(21) Horcajada, P.; Gref, R.; Baati, T.; Allan, P. K.; Maurin, G.; Couvreur, P.; Férey, G.; Morris, R. E.; Serre, C. *Chem. Rev.* **2011**, *112*, 1232-1268.
(22) Hu, Z.; Deibert, B. J.; Li, J. *Chem. Soc. Rev.* **2014**, *43*, 5815-5840.

(23) Foucault-Collet, A.; Gogick, K. A.; White, K. A.; Villette, S.; Pallier, A.; Collet, G.; Kieda, C.; Li, T.; Geib, S. J.; Rosi, N. L.; Petoud, S. *Proc. Natl. Acad. Sci.* **2013**, *110*, 17199-17204.
(24) Cross, J. P.; Lauz, M.; Badger, P. D.; Petoud, S. *J. Am. Chem. Soc.* **2004**, *126*, 16278-16279.
(25) Chen, B.; Yang, Y.; Zapata, F.; Qian, G.; Luo, Y.; Zhang, J.; Lobkovsky, E. B. *Inorg. Chem.* **2006**, *45*, 8882-8886.
(26) Chen, B.; Fronczek, F. R.; Maverick, A. W. *Inorg. Chem.* **2004**, *43*, 8209-8211.
(27) Rieter, W. J.; Taylor, K. M. L.; An, H.; Lin, W.; Lin, W. *J. Am. Chem. Soc.* **2006**, *128*, 9024-9025.
(28) White, K. A.; Chengelis, D. A.; Gogick, K. A.; Stehman, J.; Rosi, N. L.; Petoud, S. *J. Am. Chem. Soc.* **2009**, *131*, 18069-18071.
(29) White, K. A.; Chengelis, D. A.; Zeller, M.; Geib, S. J.; Szakos, J.; Petoud, S.; Rosi, N. L. *Chem. Commun.* **2009**, 4506-4508.
(30) Aebischer, A.; Gumy, F.; Bünzli, J.-C. G. *Phys. Chem. Chem. Phys.* **2009**, *11*, 1346-1353.
(31) Zhang, J.; Badger, P. D.; Geib, S. J.; Petoud, S. *Angew. Chem., Int. Ed.* **2005**, *44*, 2508-2512.

4.0 LANTHANIDE NEAR-INFRARED IMAGING IN LIVING CELLS WITH YB^{3+} NANO METAL-ORGANIC FRAMEWORKS

Part of the work presented in this chapter has been published as: "Lanthanide near infrared imaging in living cells with Yb^{3+} nano metal organic frameworks" in the *Proceedings of the National Academy of Sciences* **2013,** *110(43),* 17199-17204.

This work was performed in collaboration with Alexandra Foucault-Collet, Sandrine Villette, Agnès Pallier, Guillaume Collet, and Claudine Kieda (Centre de Biophysique Moléculaire, Centre National de la Recherche Scientifique, Orléans, France), Kiley A. White and Tao Li (Nathaniel L. Rosi Research Group, University of Pittsburgh), and Steven J. Geib (Crystallographer, University of Pittsburgh).

4.1 INTRODUCTION

Luminescent reporters emitting in the near-infrared (NIR) region of the electromagnetic spectrum are highly advantageous for biological imaging applications for several reasons. Biological material has low autofluorescence in the NIR window, which allows facile discrimination between the desired signal of the reporter and the background, leading to enhanced signal-to-noise ratio and improved detection sensitivity.[1] Additionally, NIR light scatters less than visible light and therefore results in increased optical imaging resolution.[2,3] Finally, NIR photons interact less with biological material compared to visible photons, thus decreasing the risk of disturbing or damaging the biological systems being observed.

NIR reporters such as cyanine dyes[4,5] and quantum dots[6] have previously been shown to be useful for biological imaging applications. However, these materials possess broad emission bands that limit their ability to be easily discriminated from the background fluorescence due to their overlap. Additionally, cyanine dyes exhibit limited photostability, and quantum dots can display blinking emission making it difficult to conduct repeated or long-term experiments for such purposes as tracking a moiety or monitoring a rapid occurring process.

Several lanthanide cations emit in the NIR and have some advantages with respect to organic fluorophores and semi-conductor nanocrystals. Lanthanide cations have narrower emission bandwidths than organic fluorophores and semiconductor nanocrystals. Their emission wavelengths are not affected by the environment, allowing them to be used in a broad range of conditions, including varied pH and biological environment. Most luminescent lanthanide

reporters are more resistant to photobleaching than organic fluorophores, which enables them to be used repeatedly and/or over long periods of time.[7-9]

Free lanthanide cations have low extinction coefficients due to the partially forbidden nature of the $f \rightarrow f$ transition. Therefore, lanthanides must be sensitized using a photonic converter such as an organic chromophore through the "antennae effect."[10] "Antennae" must be placed in sufficiently close proximity to the lanthanide to provide sensitization, resulting in the compound emitting a sufficient number of photons for detection. Lanthanides must also be protected from -OH, -NH, and -CH vibrational overtones which can quench lanthanide luminescence.[11]

Despite the fact that several lanthanide complexes emitting in the NIR have been described in the literature, as they have exciting properties for biological imaging *in vivo*[11-16], we are aware of only one example used for imaging in living cells[17]. In that example, two-photon excitation was used, requiring specialized laser equipment.

We have tested a new strategy by designing novel NIR-emitting lanthanide metal-organic frameworks (MOFs) that overcome these limitations by incorporating a large number of NIR-emitting Ln^{3+} cations and PVDC sensitizers in a small volume. Using lanthanides as the metal in a MOF allows for the creation of well-defined crystalline species that can emit a large number of photons per unit volume to promote sensitive detection. This method provides an avenue for both the sensitization and the protection of the lanthanide cations, while simultaneously fulfilling their requirement for large coordination numbers.

We previously reported Yb^{3+}-PVDC NIR-emitting lanthanide MOFs which exhibit tunable photophysical properties as bulk materials.[18,19] To take advantage of utilizing the PVDC ligand/sensitizer, we modified the synthesis and created a new crystalline framework in the bulk

phase, Yb-PVDC-3. Through a reverse microemulsion synthesis[20-22], we were able to create a nanoscale version of the same MOF (nano-Yb-PVDC-3), an analogous nanoMOF using Nd^{3+} in place of Yb^{3+} (nano-Nd-PVDC-3), and a series of barcoded nanoMOFs (nano-Nd_xYb_{1-x}-PVDC-3). In first proof-of-principle experiments, we demonstrate the ability of nano-Yb-PVDC-3 to operate as a NIR imaging agent in living HeLa and NIH 3T3 cells.

To date, there have been reports of nanoscale MOFs and coordination polymers for use as biosensors[21], contrast agents for magnetic resonance imaging (MRI)[20,22-25] and computed tomography (CT)[26], and drug delivery[24,25,27]; in this chapter, we demonstrate that NIR-emitting nanoMOFs can be designed as imaging agents for biological systems.

4.2 EXPERIMENTAL

4.2.1 Reagents

Reagents were obtained from commercial sources and used as received without further purification. The H_2-PVDC was synthesized according to a previously published method[18]. The 1,4-dimethoxybenzene (99%), paraformaldehyde (PFA; 95%), sodium methoxide (0.05 M in methanol), anhydrous methanol (99.8%), anhydrous benzene (99.8%), methylamine (40 wt% in water), hexadecyltrimethylammonium bromide (CTAB; >98% powder), heptane (Reagent Plus, 99%), ytterbium (III) nitrate pentahydrate ($Yb(NO_3)_3 \cdot 5H_2O$; 99.999%), ytterbium (III) chloride hexahydrate ($YbCl_3 \cdot 6H_2O$; 99.998%), erbium (III) chloride hexahydrate ($ErCl_3 \cdot 6H_2O$), neodymium (III) chloride hexahydrate ($NdCl_3 \cdot 6H_2O$), and dimethylsulfoxide (DMSO; ACS Reagent, >99.9%) were purchased from Sigma–Aldrich. Hydrobromic acid (HBr; 33 wt% in

acetic acid) was purchased from Fluka. Anhydrous chloroform ($CHCl_3$; 99.8%) and anhydrous toluene (99.8%) were purchased from Acros. Triphenylphosphine was purchased from MCB Reagents. Methanol (Certified ACS), tetrahydrofuran (Certified ACS), and potassium hydroxide (Certified ACS pellets) were purchased from Fisher. Methyl 4-formylbenzoate (>98%) was purchased from TCI. *N,N*-dimethylformamide (DMF; ACS grade) was purchased from Emmanuel Merck Darmstadt. Nitric acid (HNO_3; ACS Reagent, 36.5–38.0%) and glacial acetic acid (Baker Analyzed Reagent) were purchased from J. T. Baker. Hexanol (purified) was purchased from Spectrum. Ethanol (200 proof) was purchased from Decon Laboratories, Inc.

4.2.2 Synthesis of MOFs

4.2.2.1 Synthesis of Yb-PVDC-3 MOF

In a 20-mL glass vial, a solution of 4,4′-(1*E*,1′*E*)-2,2′-(2,5-dimethoxy-1,4-phenylene)bis(ethene-2,1-diyl)dibenzoic acid (H_2-PVDC; 86.0 mg, 0.20 mmol) in DMF (4.0 mL) was added to a solution of $Yb(NO_3)_3 \cdot 5H_2O$ (22.5 mg, 0.05 mmol) in DMF (1.0 mL) and 1 M HNO_3(aq) (1 mL) to produce a neon green solution. The vial was capped and placed in a 105 °C isotemp oven for 12 hours to produce yellow crystalline needles of the product. The crystals were collected, washed with DMF (4 × 5 mL), and air-dried (29.7 mg, 61.8%).

Elemental analysis (EA) calcd (%) for $Yb_1(C_{26}H_{20}O_6)_{1.5}(DMF) \cdot 0.65DMF \cdot H_2O$: C, 55.31; H, 4.60; N, 2.42. Found: C, 54.87; H, 4.22; N, 2.51. EA calcd (%) for the water exchange product, $Yb_1(C_{26}H_{20}O_6)_{1.5}(H_2O)_2 \cdot 0.25DMF \cdot 2.25H_2O$: C, 52.43; H, 4.46; N, 0.38. Found: C, 52.12; H, 3.68; N, 0.30. FTIR (KBr, 4,000-700 cm^{-1}): 3,424 (broad, br), 3,054 (weak, w), 2,998 (w), 2,936 (w), 2,830 (w), 1,665 (DMF C=O; medium, m), 1,601 (m), 1,544 (m), 1,413 (COO^-;

very strong, vs), 1,338 (w), 1,260 (w), 1,211 (strong, s), 1,181 (m), 1,108 (w), 1,044 (s), 965 (m), 861 (w), 779 (trans C=C−H, s), and 709 (w).

4.2.3 Synthesis of nano-Ln-PVDC-3 MOFs

These procedures are based on previously reported reverse microemulsion nanoMOF synthesis[20-22].

4.2.3.1 Synthesis of nano-Yb-PVDC-3

The methylammonium salt of the H_2-PVDC ligand (PVDC-$(NH_2CH_3)_2$) was prepared by dissolving H_2-PVDC in methylamine (40 wt% in water), removing the solvent under reduced pressure, and adding a known amount of water to achieve the desired concentration. A 0.05 M solution of CTAB was prepared by dissolving CTAB in a 9:1 (vol/vol) ratio of heptane/hexanol and stirring for 30 minutes. A $w = 10$ (where w is the H_2O/CTAB molar ratio) reaction mixture was prepared as follows. A solution of $YbCl_3 \cdot 6H_2O$ (225 μL, 0.05 M in H_2O) was added to a flask containing the CTAB mixture (25 mL, 0.05 M in heptane/hexanol). A solution of PVDC-$(NH_2CH_3)_2$ (225 μL, 0.05 M in H_2O) was added to another flask also containing the CTAB mixture (25 mL, 0.05 M). The flasks were stirred separately for at least 10 minutes until both solutions became clear. The Yb^{3+} solution was then added to the PVDC solution and stirred for 24 hours at room temperature. A yellow solid was isolated via centrifugation at 3,313×g for 30 minutes, followed by washing with ethanol (3 × 35 mL). The product was purified by dialysis using a regenerated cellulose membrane (nominal molecular weight cut off of 3,500; Fisher Scientific) in DMSO for 3 days. The solid recovered from the dialysis membrane was dried in a vacuum oven (40 °C, 40 mbar).

4.2.3.2 Synthesis of nano-Er-PVDC-3

The methylammonium salt of the H_2-PVDC ligand (PVDC-$(NH_2CH_3)_2$) was prepared by dissolving H_2-PVDC in methylamine (40 wt% in water), removing the solvent under reduced pressure, and adding a known amount of water to achieve the desired concentration. A 0.05 M solution of CTAB was prepared by dissolving CTAB in a 9:1 (vol/vol) ratio of heptane/hexanol and stirring for 30 minutes. A $w = 10$ (where w is the H_2O/CTAB molar ratio) reaction mixture was prepared as follows. A solution of $ErCl_3 \cdot 6H_2O$ (225 μL, 0.05 M in H_2O) was added to a flask containing the CTAB mixture (25 mL, 0.05 M in heptane/hexanol). A solution of PVDC-$(NH_2CH_3)_2$ (225 μL, 0.05 M in H_2O) was added to another flask also containing the CTAB mixture (25 mL, 0.05 M). The flasks were stirred separately for at least 10 minutes until both solutions become clear. The Er^{3+} solution was then added to the PVDC solution and stirred for 24 hours at room temperature. A yellow solid was isolated via centrifugation at 3,313×g for 30 minutes, followed by washing with ethanol (3 × 35 mL).

4.2.3.3 Synthesis of nano-Nd-PVDC-3

The methylammonium salt of the H_2-PVDC ligand (PVDC-$(NH_2CH_3)_2$) was prepared by dissolving H_2-PVDC in methylamine (40 wt% in water), removing the solvent under reduced pressure, and adding a known amount of water to achieve the desired concentration. A 0.05 M solution of CTAB was prepared by dissolving CTAB in a 9:1 (vol/vol) ratio of heptane/hexanol and stirring for 30 minutes. A $w = 10$ (where w is the H_2O/CTAB molar ratio) reaction mixture was prepared as follows. A solution of $NdCl_3 \cdot 6H_2O$ (225 μL, 0.05 M in H_2O) was added to a flask containing the CTAB mixture (25 mL, 0.05 M in heptane/hexanol). A solution of PVDC-$(NH_2CH_3)_2$ (225 μL, 0.05 M in H_2O) was added to another flask also containing the CTAB mixture (25 mL, 0.05 M). The flasks were stirred separately for at least 10 minutes until both

solutions became clear. The Nd^{3+} solution was then added to the PVDC solution and stirred for 24 hours at room temperature. A yellow solid was isolated via centrifugation at 3,313×g for 30 minutes, followed by washing with ethanol (3 × 35 mL).

4.2.4 Synthesis of barcoded nano-Nd_xYb_{1-x}-PVDC-3 MOFs

4.2.4.1 Synthesis of nano-$Nd_{0.25}Yb_{0.75}$-PVDC-3

The methylammonium salt of the H_2-PVDC ligand (PVDC-$(NH_2CH_3)_2$) was prepared by dissolving H_2-PVDC in methylamine (40 wt% in water), removing the solvent under reduced pressure, and adding a known amount of water to achieve the desired concentration. A 0.05 M solution of CTAB was prepared by dissolving CTAB in a 9:1 (vol/vol) ratio of heptane/hexanol and stirring for 30 minutes. A $w = 10$ (where w is the H_2O/CTAB molar ratio) reaction mixture was prepared as follows. A solution of $YbCl_3 \cdot 6H_2O$ (168 µL, 0.05 M in H_2O) and a solution of $NdCl_3 \cdot 6H_2O$ (56 µL, 0.05 M in H_2O) were added to a flask containing the CTAB mixture (25 mL, 0.05 M in heptane/hexanol). A solution of PVDC-$(NH_2CH_3)_2$ (225 µL, 0.05 M in H_2O) was added to another flask also containing the CTAB mixture (25 mL, 0.05 M). The flasks were stirred separately for at least 10 minutes until both solutions became clear. The Nd^{3+}/Yb^{3+} solution was then added to the PVDC solution and stirred for 24 hours at room temperature. Yellow solid was isolated via centrifugation at 3,313×g for 30 minutes, followed by washing with ethanol (3 × 35 mL).

4.2.4.2 Synthesis of nano-$Nd_{0.50}Yb_{0.50}$-PVDC-3

The methylammonium salt of the H_2-PVDC ligand (PVDC-$(NH_2CH_3)_2$) was prepared by dissolving H_2-PVDC in methylamine (40 wt% in water), removing the solvent under reduced

pressure, and adding a known amount of water to achieve the desired concentration. A 0.05 M solution of CTAB was prepared by dissolving CTAB in a 9:1 (vol/vol) ratio of heptane/hexanol and stirring for 30 minutes. A $w = 10$ (where w is the H_2O/CTAB molar ratio) reaction mixture was prepared as follows. A solution of $YbCl_3 \cdot 6H_2O$ (112 µL, 0.05 M in H_2O) and a solution of $NdCl_3 \cdot 6H_2O$ (112 µL, 0.05 M in H_2O) were added to a flask containing the CTAB mixture (25 mL, 0.05 M in heptane/hexanol). A solution of PVDC-$(NH_2CH_3)_2$ (225 µL, 0.05 M in H_2O) was added to another flask also containing the CTAB mixture (25 mL, 0.05 M). The flasks were stirred separately for at least 10 minutes until both solutions became clear. The Nd^{3+}/Yb^{3+} solution was then added to the PVDC solution and stirred for 24 hours at room temperature. A yellow solid was isolated via centrifugation at 3,313×g for 30 minutes, followed by washing with ethanol (3 × 35 mL).

4.2.4.3 Synthesis of nano-$Nd_{0.75}Yb_{0.25}$-PVDC-3

The methylammonium salt of the H_2-PVDC ligand (PVDC-$(NH_2CH_3)_2$) was prepared by dissolving H_2-PVDC in methylamine (40 wt% in water), removing the solvent under reduced pressure, and adding a known amount of water to achieve the desired concentration. A 0.05 M solution of CTAB was prepared by dissolving CTAB in a 9:1 (vol/vol) ratio of heptane/hexanol and stirring for 30 minutes. A $w = 10$ (where w is the H_2O/CTAB molar ratio) reaction mixture was prepared as follows. A solution of $YbCl_3 \cdot 6H_2O$ (56 µL, 0.05 M in H_2O) and a solution of $NdCl_3 \cdot 6H_2O$ (168 µL, 0.05 M in H_2O) were added to a flask containing the CTAB mixture (25 mL, 0.05 M in heptane/hexanol). A solution of PVDC-$(NH_2CH_3)_2$ (225 µL, 0.05 M in H_2O) was added to another flask also containing the CTAB mixture (25 mL, 0.05 M). The flasks were stirred separately for at least 10 minutes until both solutions became clear. The Nd^{3+}/Yb^{3+} solution was then added to the PVDC solution and stirred for 24 hours at room temperature. A

yellow solid was isolated via centrifugation at 3,313×g for 30 minutes, followed by washing with ethanol (3 × 35 mL).

4.2.5 Instrumentation

4.2.5.1 Fourier transform infrared spectroscopy

Fourier transform infrared (FTIR) spectra were measured on a Nicolet Avatar 360 FTIR spectrometer using KBr pellet samples. Data were analyzed using the Omnic Software Package (Thermo Scientific).

4.2.5.2 Powder X-ray diffraction

Powder X-ray diffraction (PXRD) patterns were collected using a Bruker AXS D8 Discover powder diffractometer at 40 kV, 40 mA, for Cu Kα (λ = 1.5406 Å) with a scan speed of either 0.20 s per step or 0.50 s per step and a step size of 0.02018°. PXRD patterns for the nano-Yb-PVDC-3 were collected using a Philips PW1830 diffractometer at 40 kV, 40 mA, for Cu Kα (λ = 1.54056 Å) with a scan speed of 0.50 s per step and a step size of 0.020°.

4.2.5.3 Scanning electron microscopy

Samples were coated with palladium for 60 seconds before analysis with a Philips XL 30 scanning electron microscope (SEM) equipped with an EDAX CDU leap detector for energy dispersive X-ray (EDX) analysis. ImageJ 1.47f software (National Institutes of Health) was used to measure the particle dimensions, and OriginPro 8.6 software (OriginLab Corporation) was used to process the data.

4.2.5.4 Absorption spectroscopy

Absorption spectra were recorded on a Perkin-Elmer Lambda 9 Spectrometer coupled with a personal computer using software supplied by Perkin-Elmer.

4.2.5.5 Luminescence spectroscopy

Excitation and emission spectra were measured using a HORIBA Jobin Yvon Fluorolog 3-22 spectrofluorometer equipped with a R928 Hamamatsu detector for visible detection and a DSS-IGA020L detector (Electro-Optical Systems, Inc.) for the NIR domain. All materials were measured as crystalline solids in water. Nano-Yb-PVDC-3 samples were measured as colloidal suspensions at 30 μg/mL in 0.1 M HEPES (pH 7.3). An integrating sphere utilizing quartz tube sample holders developed by Frédéric Gumy and Jean-Claude G. Bünzli (Laboratory of Lanthanide Supramolecular Chemistry, École Polytechnique Féderale de Lausanne, Lausanne, Switzerland) as an accessory to the Fluorolog 3-22 spectrofluorometer (patent pending) and commercialized and manufactured by GMP[28] was used.

The spectra were corrected using the following process. The MOF and background (solvent) spectra were each offset to zero at 1600 nm and corrected for variations in the lamp intensity. The background spectrum was subtracted from the MOF spectrum using a scaling factor, *k*. The value of *k* was calculated using the equation:

$$Bk = S$$

Equation 4.1.

where *B* represents the background and *S* represents the sample, using the intensities of the respective spectra at 1550 nm (chosen because there is no Ln^{3+} signal in that region). The value of *k* was optimized in order to achieve the flattest baseline. The resulting spectrum was then corrected for the detector.

4.2.5.6 Quantum yield measurements

Quantum yield measurements were also collected on the Fluorolog-322 with the integrating sphere. Collecting NIR quantum yields requires the use of both a visible detector and a NIR detector; ytterbium tropolonate and neodymium tropolonate were used as references[13] ($[Ln(trop)_4]^-$ in DMSO, $\Phi_{Yb} = 1.9\times10^{-2}$; $\Phi_{Nd} = 2.1\times10^{-3}$) for the respective lanthanides. The process for collecting a relative quantum yield using the integrating sphere is the following step by step process:

1) Emission spectra of the lamp were collected for the sample (R_{S+SB}), the solvent in which the sample is placed (R_{SB}), the reference (*see above*, R_{R+RB}), and the solvent in which the reference is dissolved (R_{RB}). Neutral density filters were placed at the excitation port of the integrating sphere to control the high intensity of the lamp. The spectra were corrected, as described above, and the bands were integrated. The resulting integration values were used to determine the amount of light that was absorbed by the sample and the reference, given by:

$$R_S = R_{SB} - R_{S+SB}$$

Equation 4.2.

and

$$R_R = R_{RB} - R_{R+RB}$$

Equation 4.3.

2) Emission spectra of the sample (I_{S+SB}), of the sample solvent (I_{SB}), of the reference (I_{R+RB}), and of the reference solvent (I_{RB}) were collected in the NIR range. A 780 nm long-pass filter was placed at the NIR emission port of the integrating sphere to eliminate contributions from second order bands. Emission spectra were corrected for the lamp

variation, the solvent spectra were subtracted from the appropriate sample and reference spectra:

$$I_S = I_{S+SB} - I_{SB}$$

Equation 4.4.

and

$$I_R = I_{R+RB} - I_{RB}$$

Equation 4.5.

and the resulting spectra were corrected for detector response. The spectra were not corrected for the filters because in the case of a relative quantum yield measurement the use of a scalar (*see below how such scalar is calculated*) corrects for the filters during the calculations.

All three Nd^{3+} bands were integrated; the band centered at 880 nm was integrated over the range 820-910 nm, and the band centered at 1330 nm was integrated over the range 1265-1385 nm. The Yb^{3+} band centered at 980 nm overlapped with the Nd^{3+} band centered at 1060 nm, so the spectrum was deconvoluted using the DataMax software supplied by Jobin Yvon-Horiba. The deconvolution analysis was applied in the region 1018-1100 nm for Nd^{3+} and 910-1018 nm for Yb^{3+}. The resulting deconvoluted spectra were integrated over their entire range of wavelengths.

3) The known quantum yield of the reference was used to create a scalar ($X_{NIR-VIS}$) which accounts for the use of two different detectors in the visible and in the NIR with a domain of overlapping response:

$$X_{NIR-VIS} = \frac{\Phi_R R_R}{I_R}$$

Equation 4.6.

4) The quantum yield of the sample was calculated using the following equation:

$$\Phi_S = \frac{X_{NIR-VIS} I_S}{R_S}$$

Equation 4.7.

4.2.5.7 Photobleaching studies

Using the Fluorolog 3-22 setup described above, emission spectra (λ_{ex} = 355 nm) were collected every 30 minutes for a photobleaching study. The samples were exposed to white light from the 450W Xenon lamp of the Fluorolog 3-22 between collection of emission spectra.

4.2.5.8 Luminescence lifetimes

Luminescence lifetimes were measured using a neodymium yttrium aluminum garnet (Nd:YAG) Continuum Powerlite 8010 laser (355 nm, third harmonic) as the excitation source. Emission was collected at a right angle to the excitation beam, and wavelengths were selected by a Spectral Products CM110 1/8m monochromator. The signal was monitored by a Hamamatsu R316-02 photomultiplier tube and collected on a 500-MHz bandpass digital oscilloscope (Tektronix TDS 754D). Signals from >1,000 flashes were collected and averaged. Three decay curves were collected for each sample, and the data were analyzed using OriginPro 8.6 software with exponential fitting modes.

4.2.5.9 Alamar Blue assay

For the cytotoxicity test, 1×10^4 cells per well were seeded in a 96-well microplate. After 24 hours of cell attachment, the cells were treated with increasing concentrations of nano-Yb-PVDC-3 diluted for 24 hours at 37 °C. The cytotoxicity was evaluated with the Alamar Blue assay (Invitrogen). Alamar Blue was added to the medium (10% vol/vol), and its fluorescence (λ_{ex} = 530 nm, λ_{em} = 590 nm) was measured after 4 hours at 37 °C with a microplate reader

(Victor 3V; PerkinElmer). This assay compared the fluorescence of untreated cells with the fluorescence of cells after incubation with nano-Yb-PVDC-3.

4.2.5.10 Stability in biological media

The emission of nano-Yb-PVDC-3 was followed during 6 hours in cell lysate. For this, 1×10^6 cells (HeLa and NIH 3T3) were collected. After centrifugation, the pellets were re-suspended in water and cell membranes were lysed using a 25-gauge syringe for a mechanical lyse. The lysates were centrifuged again to exclude cell membrane fragments. Nano-Yb-PVDC-3 was diluted in the supernatant, and the emission spectra were measured using the Fluorolog 3-22.

4.2.5.11 Inductively coupled plasma

To quantify the concentration of Yb^{3+} in cells, 1×10^6 cells were seeded in a six-well microplate. After 24 hours of attachment, the cells were incubated with 20, 30, or 40 mg/L of nano-Yb-PVDC-3 for 24 hours at 37 °C. Cells were treated with trypsin and centrifuged for 5 minutes at 423×g. The pellets were re-suspended in nitric acid overnight before adding PBS buffer to achieve a final concentration of 5% nitric acid. The measurements were taken on an inductively coupled plasma (ICP; Ultimate; Jobin Yvon) coupled with a photomultiplier tube and a high dynamic detection system.

4.2.5.12 Confocal microscopy

Confocal fluorescence imaging was realized with an Axio Observer Z1 fluorescence inverted microscope (Zeiss) equipped with an ORCA-R2 high-resolution CCD camera linked to a computer driving the Axiovision (Zeiss) acquisition software. Confocality was obtained by means of a Zeiss-ApoTome module of optical sectioning using structured illumination by grids

oscillations. The Zeiss HXP-120 light source (metal halide) was used as an excitation system and was combined with an ultraviolet (UV) cube filter unit (λ_{ex} = 365/12 nm, λ_{em} = 445/50 nm) to observe phenylene emission. Optical sections were recorded at magnifications of 20× and 40× with Zeiss Plan- APOCHROMAT 20×/0.8 and 40×/1.4 objectives, respectively.

4.2.5.13 Near-infrared microscopy

Near-infrared (NIR) epifluorescence microscopy was realized on the same microscope as for confocal images, except that the microscope was equipped with an EMCCD Evolve 512 Photometrics camera. The Zeiss HXP 120 was combined with a cube filter to observe phenylene emission (λ_{ex} = 365/12 nm, λ_{em} = 445/50 nm) with 280 ms of exposure and to observe Yb^{3+} emission (λ_{ex} = 377/50 nm, λ_{em} = long pass 770 nm) with 1 second of exposure.

4.2.5.14 Spectral fluorescence microscopy

Cells were plated onto 25-mm round quartz coverslips and incubated for 24 hours with 30 µg/mL nano-Yb-PVDC-3 before fixation with 4% PFA. Fluorescence spectra were recorded on the POLYPHEME, the deep ultraviolet inverted microspectrofluorometer installed at the DISCO (Dichroïsme, Imagerie, Spectrométrie de masse pour la Chimie et la biOlogie) beamline at Synchrotron SOLEIL[29]. Excitation at 280 or 340 nm was provided by the continuous emittance from the DISCO synchrotron beamline bending magnet and focused on the sample using a 100× microscope objective (Zeiss). One full fluorescence emission spectrum was recorded on each point of the image (6 × 10 pixels) with an acquisition time of 10 seconds each. A fluorescence intensity map was reconstructed in the spectral region of interest.

4.2.6 Cellular studies

4.2.6.1 Cell culture

HeLa (human epithelial ovarian carcinoma) and NIH 3T3 (mouse embryonic fibroblast) cell lines obtained from the American Type Culture Collection were grown at 37 °C in a 5% CO_2-humidified atmosphere. Every 3–4 days, 5×10^5 cells were seeded into a 25-cm^2 plastic flask. Cells were cultivated in Minimal Essential Medium (MEM) and in Dulbecco's Modified Eagle's Medium (DMEM), respectively, supplemented with 10% FBS and, for HeLa cells, 1% L-glutamine, 1% penicillin/streptomycin, and 1% of a 100-fold nonessential amino acid solution.

4.3 RESULTS AND DISCUSSION

4.3.1 Bulk and nanoscale Ln-PVDC-3 MOFs

Yb-PVDC-3 crystallizes in the low-symmetry space group *P*-1 and exhibits infinite Yb-carboxylate secondary building units (SBUs) along the *a*-crystallographic direction. All crystallographic data can be found in Appendix A. The SBU consists of octa-coordinated Yb^{3+} with six carboxylates from three ligands and two oxygen atoms from two DMF molecules. The SBU and crystal structure can be seen in Figure 4.1. Analogous nanoMOFs: nano-Yb-PVDC-3, nano-Er-PVDC-3, and nano-Nd-PVDC-3, were determined to be isostructural to the bulk Yb-PVDC-3, as evidenced by comparison of their respective powder X-ray diffraction (PXRD) patterns (Figure 4.2). Compared with the previously reported Yb-PVDC-1 and Yb-PVDC-2[18], Yb-PVDC-3 has lower symmetry and its structure is significantly more condensed, with 1-D

channels along the *a*-crystallographic direction measuring ~43 × 9 Å (Yb^{3+}-Yb^{3+} center-to-center distances). The 1-D channels are very narrow: close contacts (e.g., 0.281, 0.637, and 0.706 Å) exist between the PVDC linkers lining opposite channel walls.

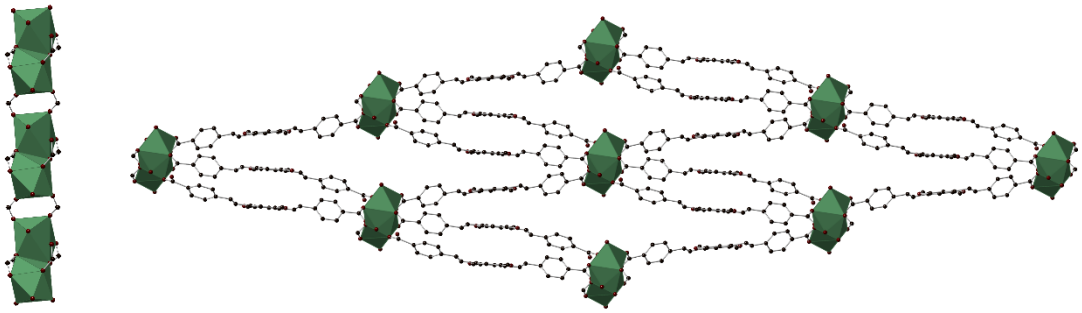

Figure 4.1. Infinite secondary building unit (SBU) of Yb-PVDC-3 (*left*) (C, dark gray; O, red; Yb^{3+}, green) and crystal structure of Yb-PVDC-3 viewed along the *a*-crystallographic axis (*right*).

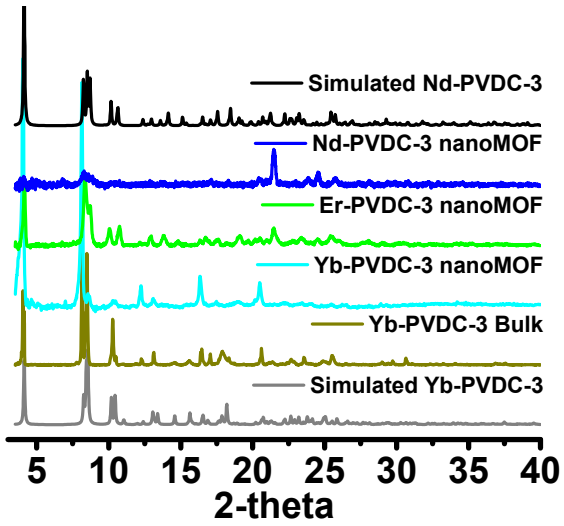

Figure 4.2. Powder X-ray diffraction (PXRD) patterns for simulated and bulk Yb-PVDC-3, nano-Yb-PVDC-3, nano-Er-PVDC-3, nano-Nd-PVDC-3, and simulated Nd-PVDC-3.

Scanning electron microscopy (SEM) was used to study the size of nano-Yb-PVDC-3. The nano-Yb-PVDC-3 MOFs exhibit a block-like morphology (Figure 4.3), having average dimensions of 0.5(±0.3) μm (length) by 316(±156) nm (width) by 176(±52) nm (thickness) (Figures 4.4-4.6).

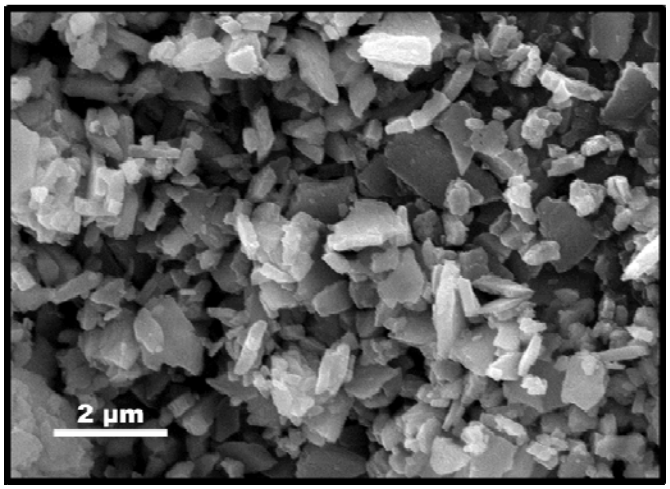

Figure 4.3. Representative scanning electron microscopy (SEM) image of nano-Yb-PVDC-3.

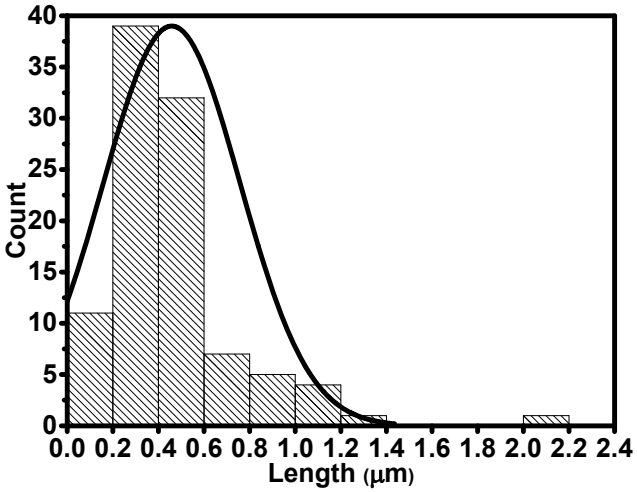

Figure 4.4. Histogram for the measured length of nano-Yb-PVDC-3.

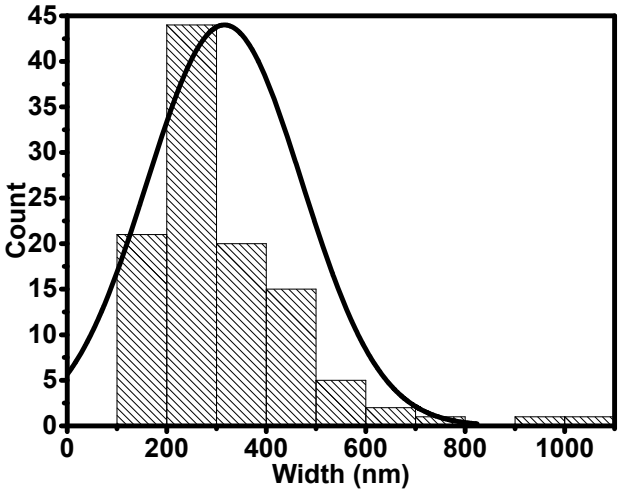

Figure 4.5. Histogram for the measured width of nano-Yb-PVDC-3.

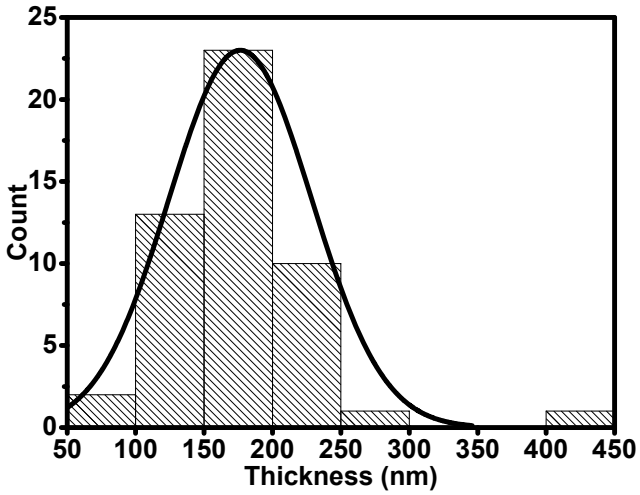

Figure 4.6. Histogram for the measured thickness of nano-Yb-PVDC-3.

4.3.2 Spectroscopic characterization of nano-Ln-PVDC-3 in water

The luminescence properties of nano-Yb-PVDC-3, nano-Er-PVDC-3, and nano-Nd-PVDC-3 were studied in water. The nano-Er-PVDC-3 exhibited no emission signal. In the case of both nano-Yb-PVDC-3 and nano-Nd-PVDC-3, their excitation spectra (monitoring their Ln^{3+} centered emission at 980 nm and 1060 nm, respectively) were broad with three apparent maxima at 280 nm, 365 nm, and 450 nm. Excitation through any of those bands resulted in Yb^{3+} emission centered at 980 nm for the nano-Yb-PVDC-3 (Figure 4.7) and Nd^{3+} emission with bands centered at 875 nm, 1060 nm, and 1330 nm for the nano-Nd-PVDC-3 (Figure 4.8).

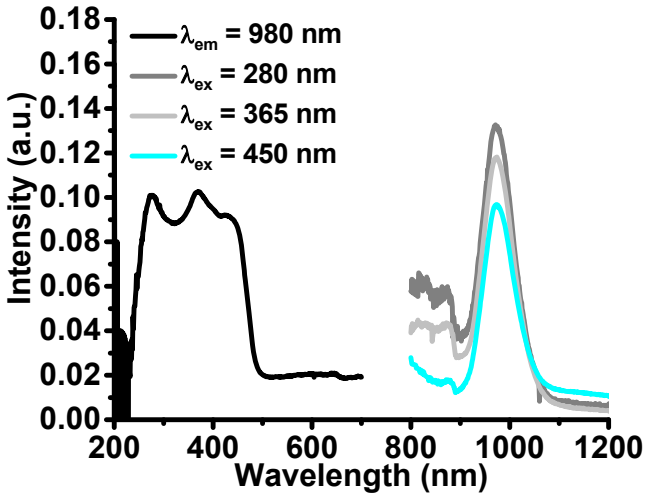

Figure 4.7. Excitation (λ_{em} = 980 nm) and emission (λ_{ex} = 280 nm, 365 nm, and 450 nm) spectra for the nano-Yb-PVDC-3 in water.

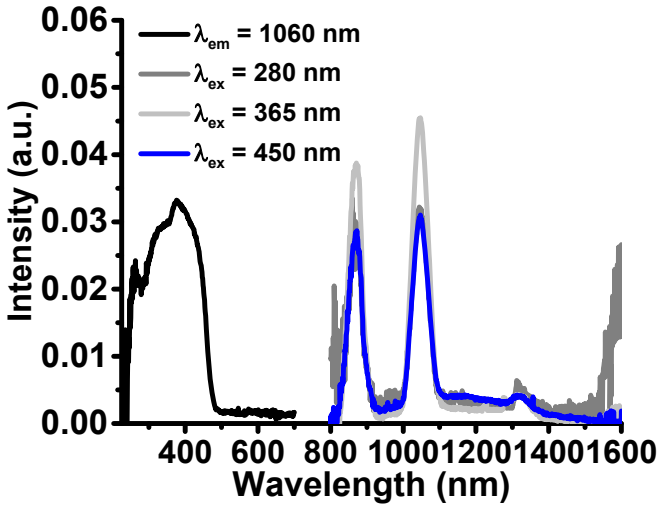

Figure 4.8. Excitation (λ_{em} = 1060 nm) and emission (λ_{ex} = 280 nm, 365 nm, and 450 nm) spectra for nano-Nd-PVDC-3 in water.

4.3.3 Barcoded nano-Nd_xYb_{1-x}-PVDC-3 MOFs

Since both nano-Yb-PVDC-3 and nano-Nd-PVDC-3 generated NIR emission when excited in the visible region, a series of barcoded nanoMOFs with various amounts of Yb^{3+} and Nd^{3+} were synthesized and studied: nano-$Nd_{0.75}Yb_{0.25}$-PVDC-3, nano-$Nd_{0.50}Yb_{0.50}$-PVDC-3, and nano-$Nd_{0.25}Yb_{0.75}$-PVDC-3. Comparison of the PXRD patterns to that of simulated Nd-PVDC-3 (Figure 4.9) demonstrated that they were isostructural to each other and Nd-PVDC-3, and therefore to nano-Yb-PVDC-3 and nano-Nd-PVDC-3 as well. This experiment allows for the assessment of the structure of the nano-Ln-PVDC-3 MOFs as their crystals are too small to determine their structures by single crystal X-ray diffraction.

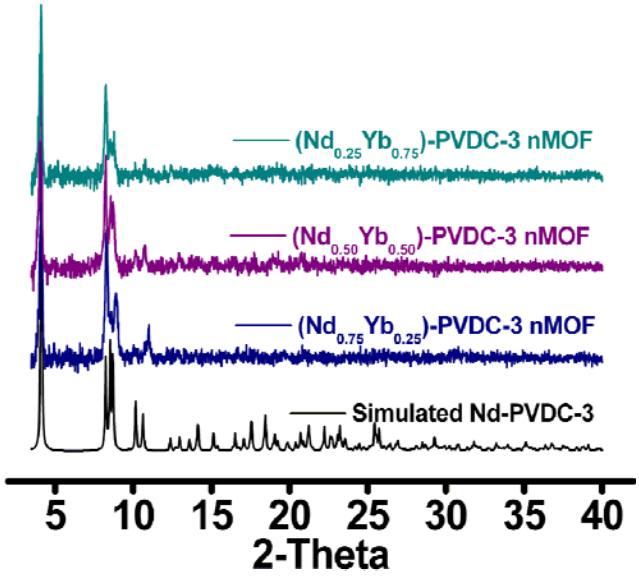

Figure 4.9. Powder X-ray diffraction (PXRD) patterns for simulated Nd-PVDC-3 and the barcoded series of nano-Nd_xYb_{1-x}-PVDC-3 MOFs.

The theoretical amounts of Nd^{3+} and Yb^{3+} incorporated into the nanoMOFs (stoichiometric amounts) were used for naming the materials, but energy dispersive X-ray (EDX) analysis was used to determine the actual amount incorporated during synthesis and to verify that both lanthanide ions were present within the materials (Table 4.1). A good correlation between the theoretical and experimental values was observed, suggesting that neither of the two Ln^{3+} is preferentially incorporated into the nanoMOF.

Table 4.1. Theoretical and experimental values of Yb^{3+} and Nd^{3+} present within the series of nano-Nd_xYb_{1-x}-PVDC-3 MOFs.

	Percent Yb^{3+}		Percent Nd^{3+}	
	Theoretical	**EDX**	**Theoretical**	**EDX**
nano-$Nd_{0.25}Yb_{0.75}$-PVDC-3	75	70	25	30
nano-$Nd_{0.50}Yb_{0.50}$-PVDC-3	50	50	50	50
nano-$Nd_{0.75}Yb_{0.25}$-PVDC-3	25	26	75	74

4.3.4 Spectroscopic characterization of nano-Nd_xYb_{1-x}-PVDC-3

The luminescence properties of the entire series of barcoded nanoMOFs were explored in water. The nano-$Nd_{0.25}Yb_{0.75}$-PVDC-3, nano-$Nd_{0.50}Yb_{0.50}$-PVDC-3, and nano-$Nd_{0.75}Yb_{0.25}$-PVDC-3 all had excitation spectra with apparent maxima of their bands located at 280 nm, 365 nm, and 450 nm upon monitoring emission at 980 nm (Yb^{3+}) or 1060 nm (Nd^{3+}). Excitation through any of those bands resulted in the simultaneous Yb^{3+} (980 nm) and Nd^{3+} emission (875 nm, 1060 nm, and 1330 nm). The intensities of the emission bands are proportional to the amount of each lanthanide present. In Figure 4.10, the spectra are normalized to the Yb^{3+} emission signal at 980 nm. As the relative amount of Nd^{3+} present increased, so did the emission intensity. A similar situation was observed for the Yb^{3+} emission in the spectra normalized to Nd^{3+} emission at 1060 nm (Figure 4.11).

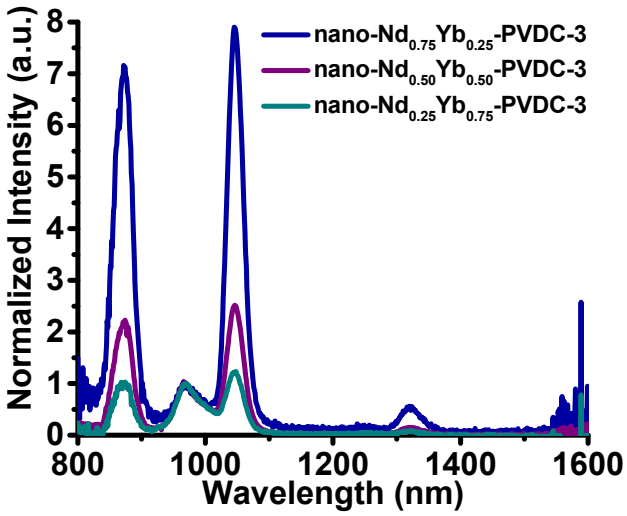

Figure 4.10. Emission (λ_{ex} = 450 nm) spectra for nano-Nd_xYb_{1-x}-PVDC-3 in water normalized to the maximum of the Yb^{3+} emission signal at 980 nm.

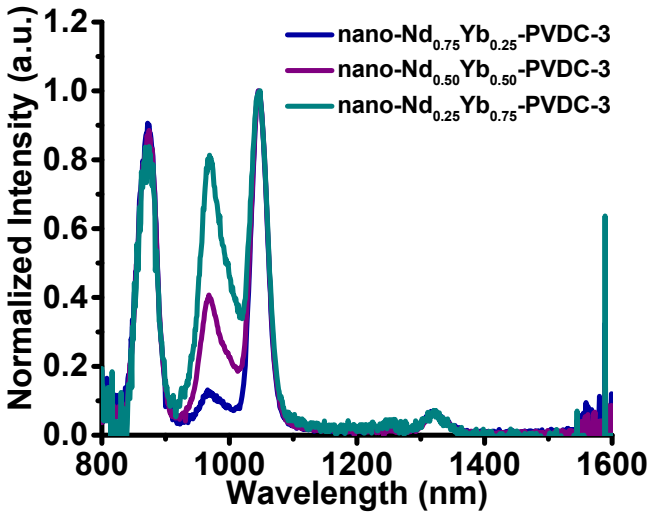

Figure 4.11. Emission (λ_{ex} = 450 nm) spectra for nano-Nd_xYb_{1-x}-PVDC-3 in water normalized to the maximum of the Nd^{3+} emission at 1060 nm.

The Yb^{3+} and Nd^{3+} bands were integrated and the fraction of each Ln^{3+} signal was plotted against the fraction of Ln^{3+} present in the MOF for both Yb^{3+} and Nd^{3+} (Figure 4.12). In both cases the observed relationship appeared to be linear.

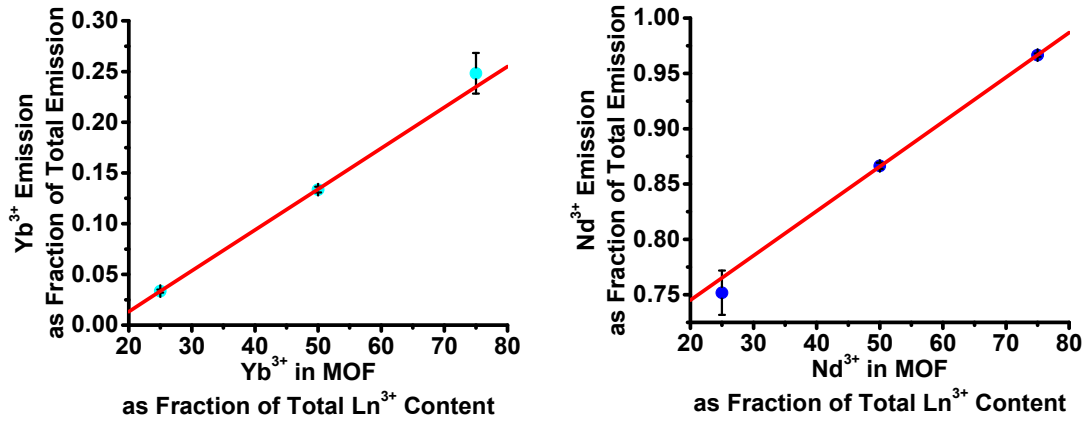

Figure 4.12. Plots of the fraction of integrated emission for each Ln^{3+} versus fraction of Ln^{3+} present for Yb^{3+} (*left*) and Nd^{3+} (*right*).

Relative quantum yields were collected for both Yb^{3+} and Nd^{3+} in each barcoded nanoMOF in order to quantify luminescence efficiencies. A slight overlap is observed between the Yb^{3+} band at 980 nm and the Nd^{3+} band at 1060 nm (Figures 4.10 and 4.11). In order to separate these bands for integration they were first deconvoluted, which is a contributing factor to the large errors observed in the quantum yield values (Table 4.2). Despite these errors, we can observe an overall trend of the increasing of the quantum yield value with the increasing amount of corresponding lanthanide while the quantum yield value of the other lanthanide decreases as the amount of that lanthanide decreases.

Table 4.2. Relative quantum yields (Φ) for Yb (Φ_{Yb}) and Nd (Φ_{Nd}) emission for nano-Yb-PVDC-3, nano-Nd_xYb_{1-x}-PVDC-3, and nano-Nd-PVDC-3 MOFs*.

	Φ_{Yb}†	Φ_{Nd}†
nano-Yb-PVDC-3	$1.0(\pm0.3)\times10^{-4}$	-
nano-$Nd_{0.25}Yb_{0.75}$-PVDC-3	$1.0(\pm0.4)\times10^{-4}$	$7(\pm3)\times10^{-4}$
nano-$Nd_{0.50}Yb_{0.50}$-PVDC-3	$6(\pm2)\times10^{-5}$	$8(\pm1)\times10^{-4}$
nano-$Nd_{0.75}Yb_{0.25}$-PVDC-3	$4(\pm1)\times10^{-5}$	$1.0(\pm0.1)\times10^{-3}$
nano-Nd-PVDC-3	-	$4(\pm1)\times10^{-3}$

*nanoMOFs as a crystalline solid under H_2O; †λ_{ex} = 450 nm

Nano-Yb-PVDC-3 was subsequently studied in greater detail for use in cellular imaging.

4.3.5 Spectroscopic characterization of nano-Yb-PVDC-3 in HEPES buffer

Luminescence properties of the nano-Yb-PVDC-3 were studied in 0.1 M HEPES buffer (pH 7.3) (Figure 4.13) to be close to physiological conditions. As observed in water, nano-Yb-PVDC-3 exhibited Yb^{3+} luminescence centered at 980 nm upon excitation of the PVDC sensitizer. The overlap of the absorption spectrum of H_2-PVDC with the excitation spectrum of the MOF (upon monitoring the Ln^{3+} emission) indicates that the sensitization is occurring via an antenna effect through the electronic structure of the PVDC. Because Yb^{3+} does not have accepting levels in the visible, the observed Yb^{3+} luminescence must result from the sensitization provided by PVDC located in sufficiently close proximity to the lanthanide cations.

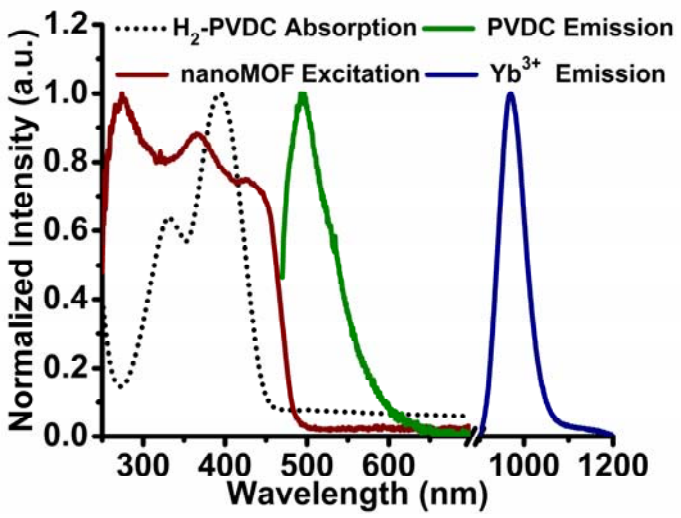

Figure 4.13. Overlay of H_2-PVDC absorption, nano-Yb-PVDC-3 excitation (λ_{em} = 980 nm), visible PVDC emission (λ_{ex} = 355 nm), and NIR Yb^{3+} emission (λ_{ex} = 355 nm) spectra recorded in 0.1 M HEPES at room temperature.

Ideally, reagents for bioanalytical applications and for imaging should emit a constant number of photons over time, and their signals should not be affected by species and parameters other than the targeted analyte. A common limitation for organic fluorophores is their tendency to photobleach when exposed to light. Photobleaching test experiments were therefore performed by exposing a suspension of nano-Yb-PVDC-3 in 0.1 M HEPES (pH 7.3) to light over a period of 13 hours. Results showed that the Yb^{3+} signal does not significantly change (Figure. 4.14), a strong indication that the material is stable in these conditions and usable over this extended period.

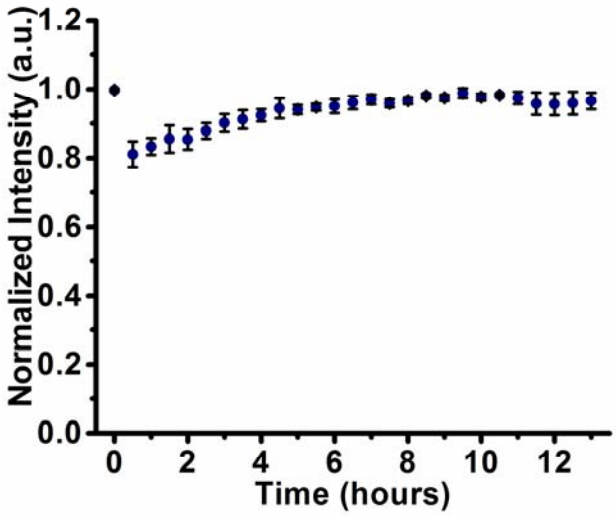

Figure 4.14. Photobleaching study by monitoring the Yb^{3+} emission at 970 nm in 0.1 M HEPES over a period of 13 hours. Error bars represent the standard deviation based on three independent experiments.

Quantum yields were recorded to quantify the efficiency of the energy transfer between the antenna and Yb^{3+} and the protection of the lanthanide cations against sources of non-radiative deactivation. Upon excitation at 450 nm, the quantum yield value for the nano-Yb-PVDC-3 is $5.2(\pm 0.8)\times 10^{-5}$ in 0.1 M HEPES (pH 7.3) (Table 4.3). Such a value is relatively small in comparison to the best luminescent lanthanide compounds[11-16], but our approach of using a MOF system to maximize the number of chromophores and lanthanide cations per unit volume is expected to reduce the negative impact of this limitation (*see below*).

Table 4.3. Relative quantum yields (Φ) and luminescence lifetimes (τ) of Yb^{3+}-centered emission at 980 nm.

	Solvent*	Φ_{Yb}†	τ_1‡ (μs)	τ_2‡ (μs)
nano-Yb-PVDC-3	H_2O	$1.0(\pm0.3)\times10^{-4}$	7.01(±0.07)	1.51(±0.01)
	0.1 M HEPES	$5.2(\pm0.8)\times10^{-5}$	4.6(±0.1)	1.04(±0.02)

*nanoMOFs as a crystalline solid under solvent; † λ_{ex} = 450 nm; ‡ λ_{ex} = 354 nm

Luminescence lifetime experimental data (Table 4.3) were best fit with a bi-exponential decay curve, indicating that the Yb^{3+} cations are present within two distinct environments. All the Yb^{3+} ions have a coordination number of eight (octa-coordinate), and the different environments are attributed to the Yb^{3+} present in the interior of the nanoMOF and the Yb^{3+} on the edges/faces of the crystallites (exterior). Exterior Yb^{3+} are more susceptible to non-radiative deactivation and are likely responsible for the shorter lifetime values.

4.3.6 Material stability studies

The stability of Yb-PVDC-3 and nano-Yb-PVDC-3 was rigorously evaluated in various conditions, including water, 0.1 M HEPES buffer (pH 7.3), and cellular media. First, samples of Yb-PVDC-3 were soaked in water or 0.1 M HEPES. At different time points, SEM images were collected to visualize bulk structure and PXRD patterns were obtained to confirm retention of crystallinity. In general, SEM images indicate that the crystals remain intact after soaking in water (Figure 4.15) or HEPES (Figure 4.16) for up to 4 weeks; however, crystallite fragmentation occurs during this time, and the average crystallite size consequently decreases. Notably, the faces of the crystallites remain smooth, and no significant pitting was observed on

the crystal surfaces. PXRD patterns of crystallites collected after soaking in either water or HEPES buffer for different time intervals indicate retention of crystallinity (Figure 4.17).

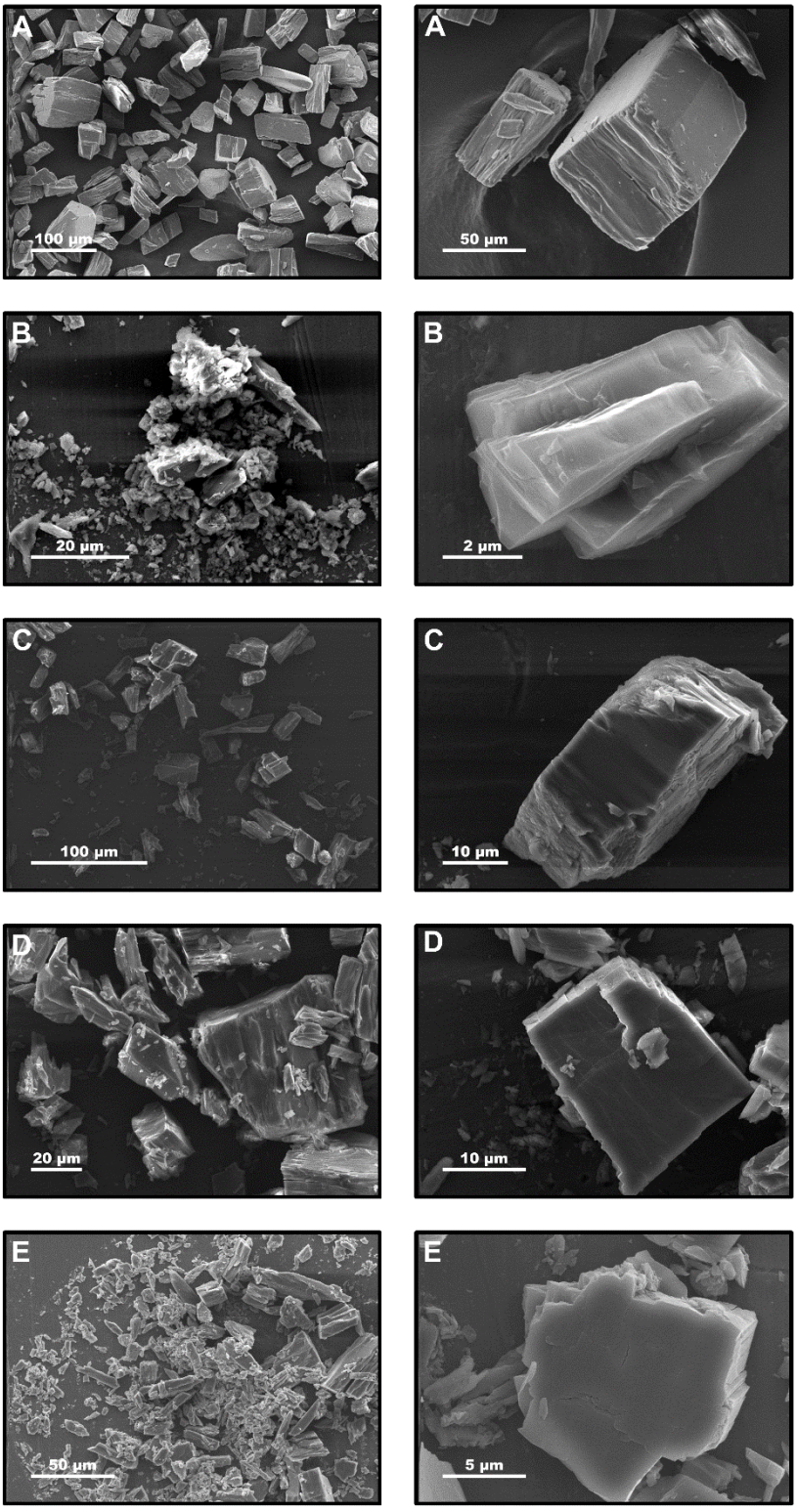

Figure 4.15. Scanning electron microscopy images of Yb-PVDC-3 (A) soaked in water for 1 week (B), 2 weeks (C), 3 weeks (D), and 4 weeks (E).

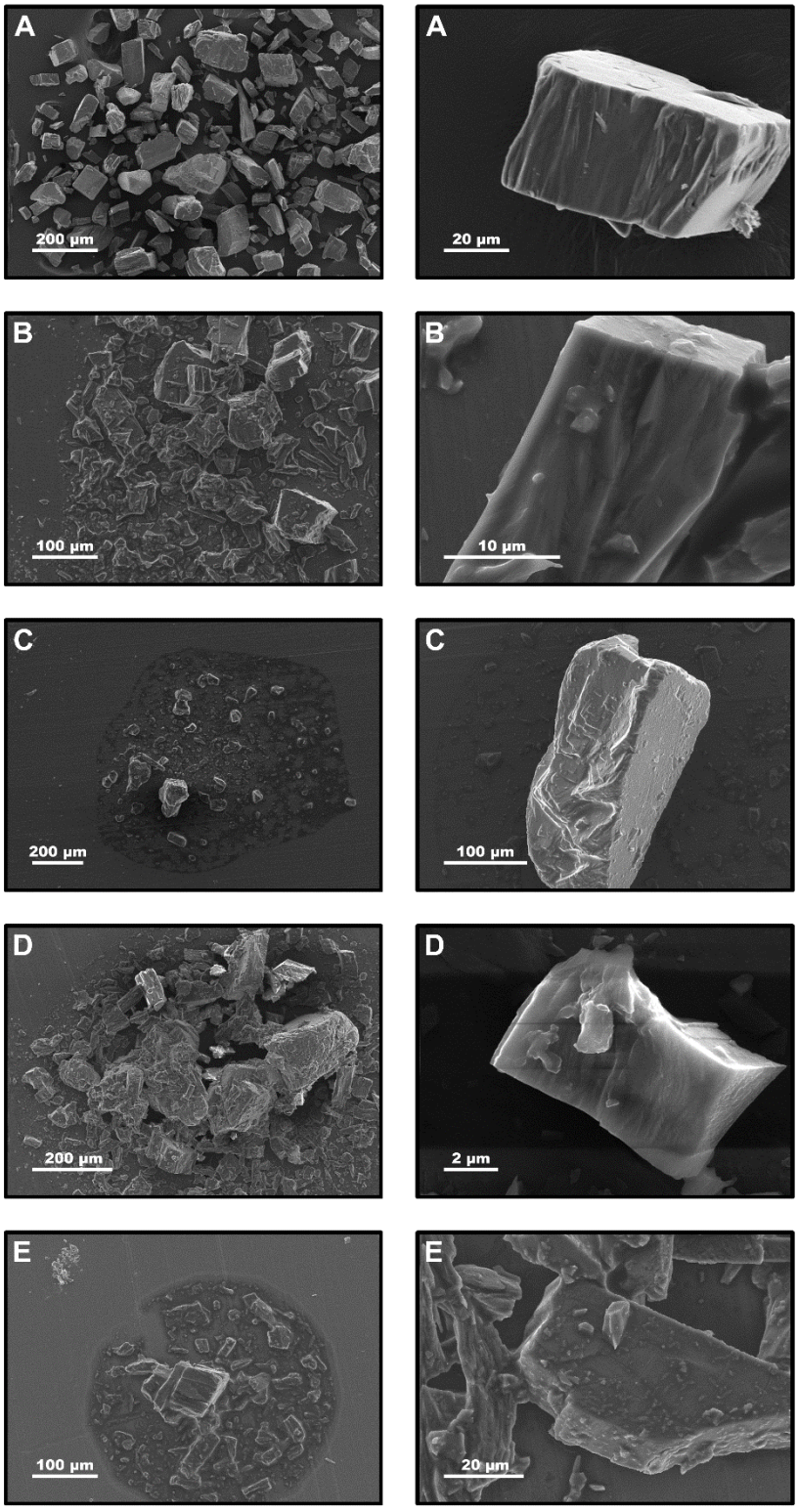

Figure 4.16. Scanning electron microscopy images of Yb-PVDC-3 (A) soaked in 0.1 M HEPES for 1 week (B), 2 weeks (C), 3 weeks (D), and 4 weeks (E).

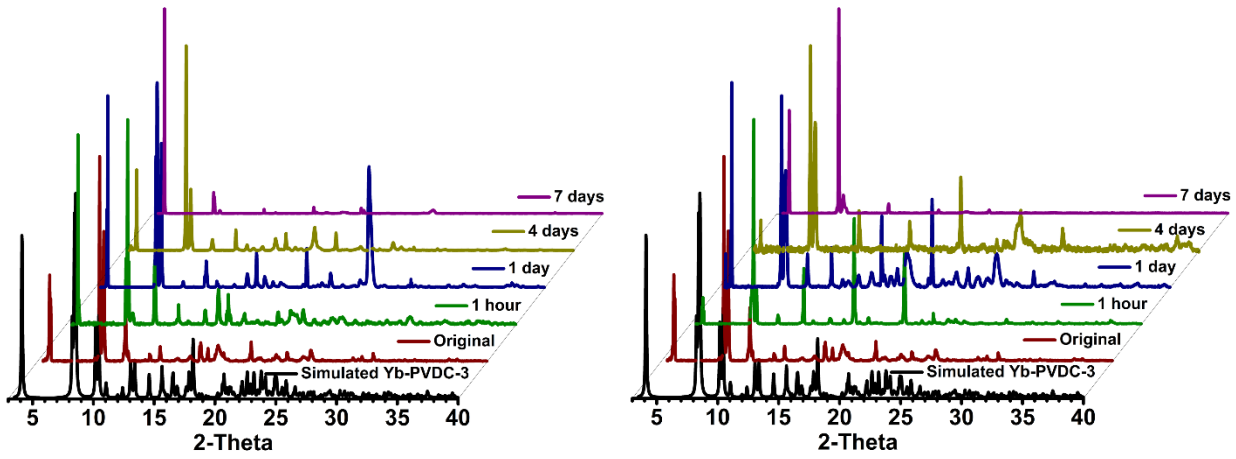

Figure 4.17. Powder X-ray diffraction patterns recorded over a period of seven days for Yb-PVDC-3 soaked in water (*left*) or 0.1 M HEPES (*right*).

In order to preserve the luminescence properties of the NIR-emitting reagents and to prevent the release of free lanthanide cations in cellular media creating risks of toxicity, the nano-Yb-PVDC-3 must remain intact. Therefore, the crystallite stability was quantitatively evaluated in cellular media by monitoring the Yb^{3+} emission signal upon excitation of the antenna. The signal of the lanthanide cation can only be generated if the antenna effect is present and only if the sensitizer is located sufficiently close to the lanthanide. Therefore, if the MOF dissociates via hydrolysis of the Yb-carboxylate bonds, for example, one would expect a significant decrease in the luminescence. The signal arising from Yb^{3+} was measured at regular time intervals after dilution of the nano-Yb-PVDC-3 in cell lysate (HeLa or NIH 3T3 cells) and in water as a control. Intensities of the emission bands compared with initial intensity (recorded

upon monitoring the Yb^{3+} band at 970 nm) are reported in Figure 4.18. The emission intensity remained constant over time, which suggests that the nano-Yb-PVDC-3 structure is not significantly modified by cellular components. Indeed, the constant total intensity of the Yb^{3+} emission signal is a quantitative indication that the measured nanoMOFs retain most of their integrity in this environment. Therefore, we expect that nano-Yb-PVDC-3 will remain intact inside of the cell.

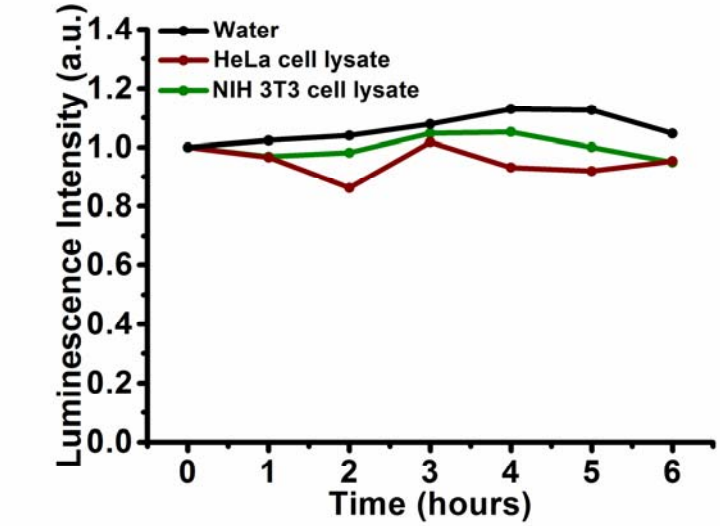

Figure 4.18. Spectroscopic evaluation of nano-Yb-PVDC-3 in water and cell lysate. Emission intensity values correspond to the maximum of Yb^{3+} emission (970 nm).

4.3.7 Cytotoxicity of nano-Yb-PVDC-3

A principal aim of this study was to test nano-Yb-PVDC-3 in cells as NIR imaging agents. Human cancer (HeLa) and mouse (NIH 3T3) cells were chosen as representative cell lines. The

nano-Yb-PVDC-3 cytotoxicity was first evaluated for both cell lines using the Alamar Blue assay. The cell proliferation test (Figure 4.19) indicated a similar effect on the two cell lines after 24 hours of incubation. The compound was found to have relatively low toxicity for concentrations up to 50 μg/mL. A working concentration was chosen on the criterion of 90% of cellular viability (30 μg/mL).

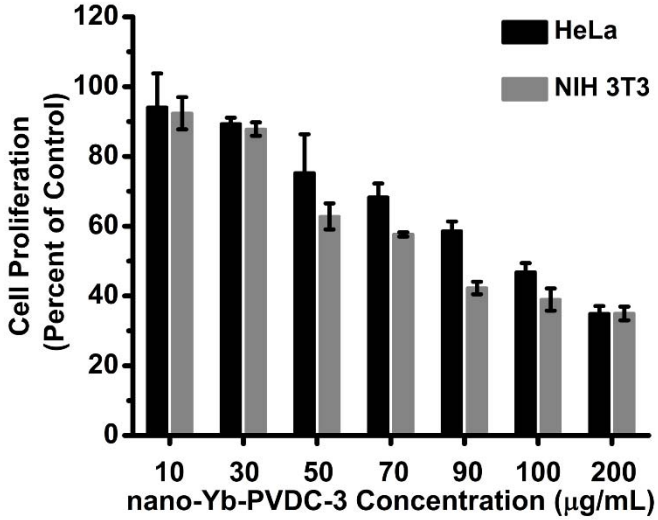

Figure 4.19. Cellular viability by Alamar Blue assay on HeLa and NIH 3T3 cells after 24 hours of incubation with increasing concentrations of nano-Yb-PVDC-3.

4.3.8 Cellular uptake

Internalization of nano-Yb-PVDC-3 by the cells was confirmed with confocal microscopy and inductively coupled plasma (ICP) spectrometry experiments. Microscopy images in Figure 4.20 show that nano-Yb-PVDC-3 is internalized by cells. Optical slices of 1 μm (less than cell

thickness) were obtained for NIH 3T3 cells after incubation with nano-Yb-PVDC-3 at 30 µg/mL. Despite the fact that untreated cells generate autofluorescence at these wavelengths (λ_{ex} = 365 nm, λ_{em} = 445/50 nm), the chromophore signal could be unambiguously detected inside cells. This fluorescence signal is located preferentially in the cytoplasm (and not in the nucleus).

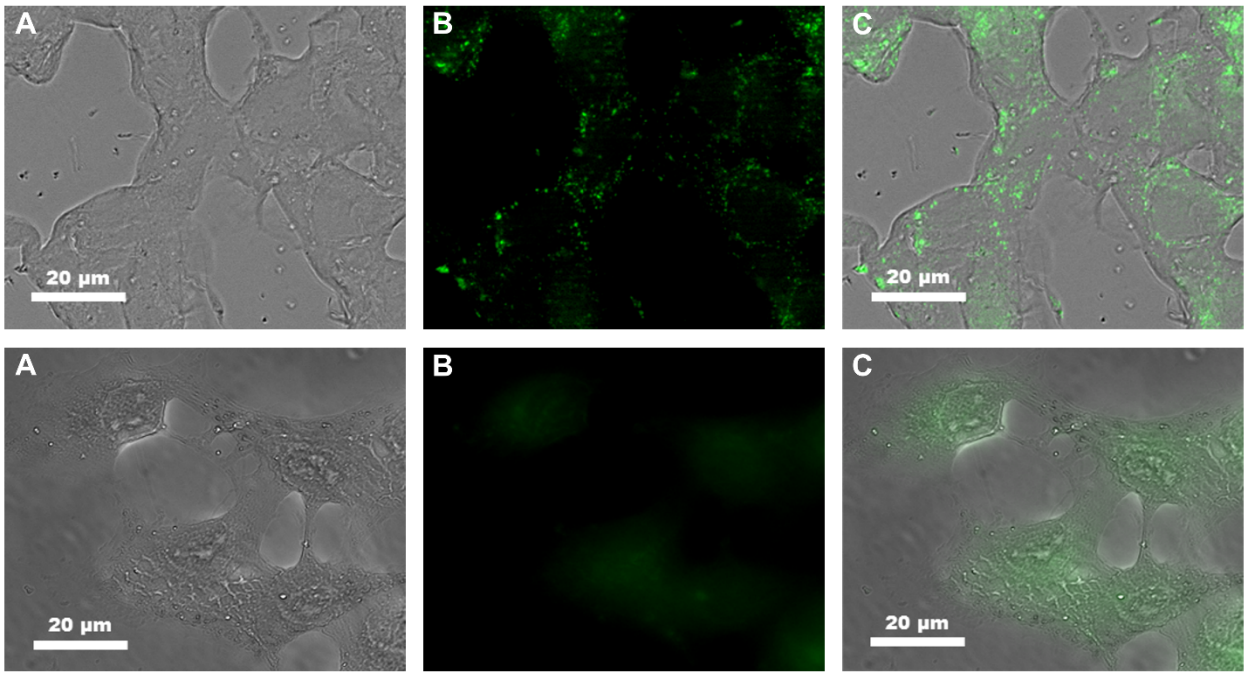

Figure 4.20. Cellular uptake of nano-Yb-PVDC-3 as demonstrated by confocal microscopy of NIH 3T3 cells after incubation with nano-Yb-PVDC-3 (*upper*) and of untreated cells (*lower*). Brightfield (A), H_2-PVDC emission (λ_{ex} = 365/12 nm, λ_{em} 445/50 nm) (B), and merged (C) images are shown.

To confirm results of confocal microscopy, the quantity of nano-Yb-PVDC-3 associated with 1×10^6 cells was measured by ICP (Table 4.4). More specifically, the amount of Yb^{3+} in cells was measured after 24 hours of incubation of HeLa and NIH 3T3 cells with nano-Yb-PVDC-3. ICP results confirm the presence of nano-Yb-PVDC-3 in the cells. For both cell lines,

the Yb^{3+} amount in cells increases with the amount of nano-Yb-PVDC-3 present in cell incubation medium. No saturation of cellular uptake has been observed at these concentrations. The uptake is more pronounced in NIH 3T3 cells than in HeLa cells. The mechanism of cell uptake has not been analyzed at this time and is currently under investigation.

Table 4.4. Determination of cellular uptake by ICP.

Sample	Concentration of nano-Yb-PVDC-3 in Cell Media (µg/mL)	Theoretical Concentration of Yb^{3+} in Cell Media (µg/mL)	Concentration of Yb^{3+} in 1×10^6 cells (µg/mL)
HeLa Cells	0	0	0.000(±0.002)
	20	4.06	0.113(±0.003)
	30	6.09	0.213(±0.003)
	40	8.12	0.270(±0.003)
NIH 3T3 Cells	0	0	0.000(±0.002)
	20	4.06	0.466(±0.010)
	30	6.09	0.996(±0.020)
	40	8.12	1.130(±0.003)

4.3.9 Spectral microscopy

Several cellular compounds are excited by UV light and emit in the visible, such as tryptophan (λ_{ex} = 275 nm, λ_{em} = 335 nm), collagen (λ_{ex} = 335 nm, λ_{em} = 405 nm), and NAD(P)H (λ_{ex} = 340 nm, λ_{em} = 460 nm)[30]. To confirm that the detected signal observed with confocal microscopy is arising from PVDC emission, spectral fluorescence microscopy analysis was conducted on cells

after 24 hours of incubation with nano-Yb-PVDC-3. At each individual point of the image (step size = 3 μm), an emission spectrum was recorded. The intensity value averaged between 400 and 600 nm was used to create an intensity map of the cell (Figure 4.21). This spectral fluorescence microscopy experiment permits the discrimination of nano-Yb-PVDC-3 emission from cellular autofluorescence. The signal obtained from untreated cells can be attributed to cellular autofluorescence with a maximum of the emission band located at 420 nm (Figure 4.22). Spectra obtained from treated cells result from the overlay of autofluorescence emission and PVDC emission signals (λ_{em} = 455 nm). This result is a third confirmation that the nanoMOF was able to enter incubated cells.

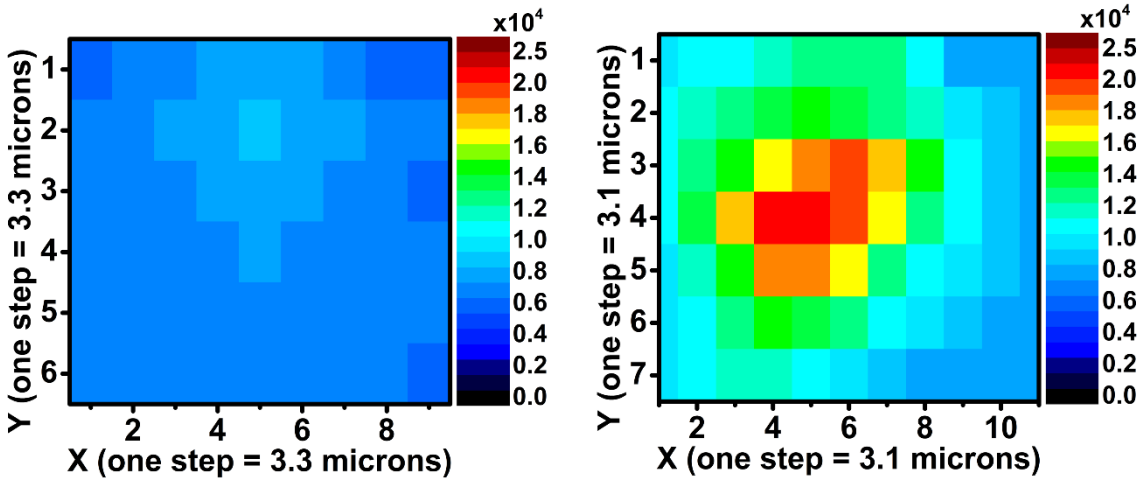

Figure 4.21. Spectral microscopy fluorescence intensity map of untreated NIH 3T3 cells (l*eft*) and NIH 3T3 cells after incubation with nano-Yb-PVDC-3 (*right*) (λ_{ex} = 340 nm, λ_{em} = 390-650 nm).

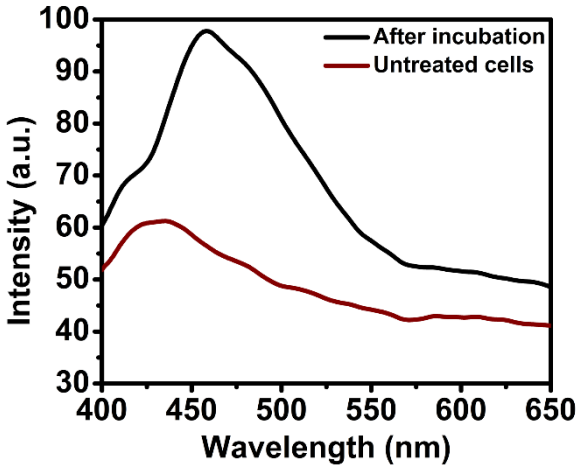

Figure 4.22. Spectra corresponding to the mean intensity of each fluorescence intensity map in Figure 4.21.

4.3.10 NIR epifluorescence microscopy

The ability to use nano-Yb-PVDC-3 as a NIR lanthanide-based imaging agent was tested in a NIR microscopy experimental setup. HeLa and NIH 3T3 cells were incubated with 30 μg/mL nano-Yb-PVDC-3 for 24 hours. Visible chromophore (PVDC) and NIR Yb^{3+} emission signals were both observed by epifluorescence microscopy in the same field (Figure 4.23). In the NIR microscopy mode, the specific Yb^{3+} emission signal was collected with good sensitivity (1 second exposure time can be considered short for NIR signals) as the result of a high signal-to-noise ratio. In parallel, switching to visible detection mode, the specific fluorescence arising from the PVDC was observed in addition to the cellular autofluorescence, and the resulting images were used as a comparison. The difference observed between the PVDC and Yb^{3+} emission signal results from the discrimination of the NIR signal from the visible

autofluorescence arising from the biological material. Control experiments were also conducted in which cells were untreated but underwent the same imaging (Figure 4.24). Autofluorescence was observed in the visible region, but there was virtually no emission in the NIR region. The images presented in Figure 4.23 report NIR microscopy experiments obtained with a lanthanide compound in living cells using a conventional excitation source.

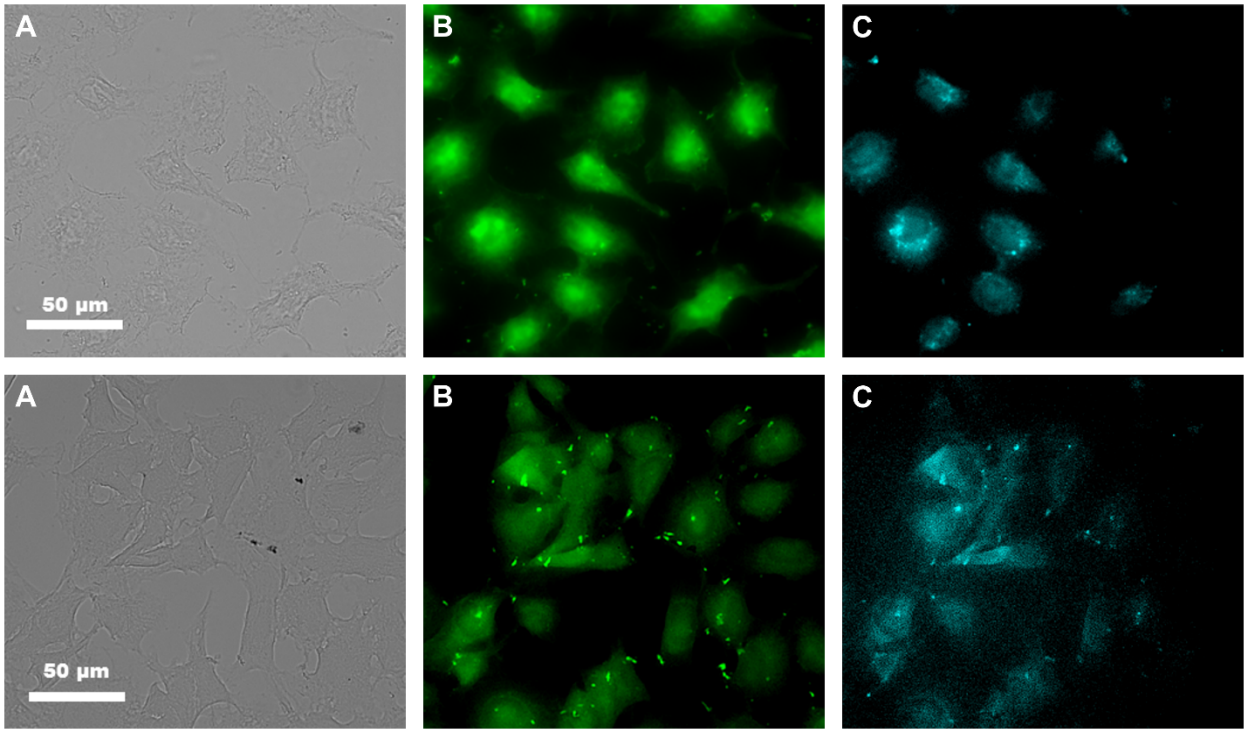

Figure 4.23. Visible and NIR microscopy images of nano-Yb-PVDC-3 in HeLa cells (*upper*) and NIH 3T3 cells (*lower*) (λ_{ex} = 340 nm). Brightfield (A), H_2-PVDC emission (λ_{ex} = 377/50 nm, λ_{em} = 445/50 nm) (B), and Yb^{3+} emission (λ_{ex} = 377/50 nm, λ_{em} = long pass 770 nm) (C) images are shown.

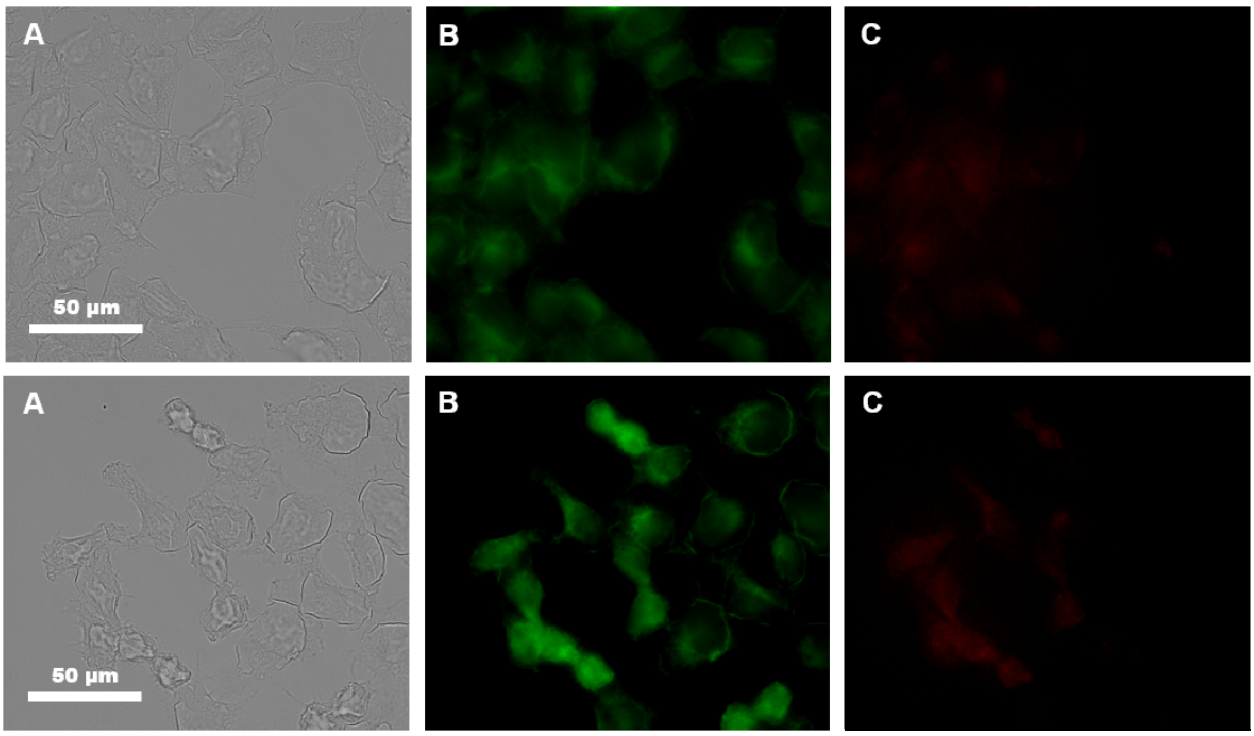

Figure 4.24. Visible and NIR microscopy images of untreated HeLa cells (*lower*) and NIH 3T3 cells (*upper*) (λ_{ex} = 340 nm). Brightfield (A), visible emission (λ_{ex} = 377/50 nm, λ_{em} = 445/50 nm) (B), and NIR emission (λ_{ex} = 377/50 nm, λ_{em} = long pass 770 nm) (C) images are shown.

4.4 CONCLUSION

We have designed and synthesized a series of barcoded nanoMOFs, nano-Nd_xYb_{1-x}-PVDC-3, which are isostructural and simultaneously emit in the NIR upon excitation. The amount of each Ln^{3+} utilized in the synthesis correlated well with the amount incorporated into the nanoMOF and the resulting emission intensity. Nano-Yb-PVDC-3 was tested for its ability to operate as a NIR imaging agent in cells. The overlap of the excitation spectra of nano-Yb-PVDC-3 with the

absorbance spectra of H_2-PVDC demonstrated that the Yb^{3+} is sensitized through the antenna effect, where the sensitizers embedded in the MOF structure are excited and transfer energy to the accepting level of the Yb^{3+} cations. Nano-Yb-PVDC-3 was shown to be luminescent in water and HEPES buffer. As expected, its quantum yield was low in water, due to the energy level of the −OH overtone vibration being so close to that of Yb^{3+}, and it further decreased when the nanoMOF was placed in HEPES, likely due to the increase in number of moieties with −OH vibrations in solution. This low quantum yield does not prevent imaging applications because of the polysensitizer and polymetallic design. The energy transfer was conserved after 24 hours of incubation in cellular media, indicating that crystalline nano-Yb-PVDC-3 remains in the cells. This stability, combined with cytotoxicity results, is promising for using nano-Yb-PVDC-3 as a biological probe for in vivo applications. We have been able to observe NIR microscopy images in living cells based on the signal arising from Yb^{3+}, sensitized via the antenna effect. This achievement has been realized by the use of a unique nanoMOF that is able to incorporate a large number of lanthanide sensitizers (PVDC) and a large number of NIR-emitting lanthanide cations, resulting in an increase in the number of emitted NIR photons per unit volume.

4.5 REFERENCES

(1) Mahmood, U.; Weissleder, R. *Mol. Cancer Ther.* **2003**, *2*, 489-496.
(2) Lim, Y. T.; Kim, S.; Nakayama, A.; Stott, N. E.; Bawendi, M. G.; Frangioni, J. V. *Mol. Imaging* **2003**, *2*, 50-64.
(3) Frangioni, J. V. *Curr. Opin. Chem. Biol.* **2003**, *7*, 626-634.
(4) Mujumdar, R. B.; Ernst, L. A.; Mujumdar, S. R.; Lewis, C. J.; Waggoner, A. S. *Bioconjugate Chem.* **1993**, *4*, 105-111.
(5) Roederer, M.; Kantor, A. B.; Parks, D. R.; Herzenberg, L. A. *Cytometry* **1996**, *24*, 191-197.
(6) Sargent, E. H. *Adv. Mater.* **2005**, *17*, 515-522.

(7) Alcala, M. A.; Shade, C. M.; Uh, H.; Kwan, S. Y.; Bischof, M.; Thompson, Z. P.; Gogick, K. A.; Meier, A. R.; Strein, T. G.; Bartlett, D. L.; Modzelewski, R. A.; Lee, Y. J.; Petoud, S.; Brown, C. K. *Biomaterials* **2011**, *32*, 9343-9352.
(8) Alcala, M. A.; Kwan, S. Y.; Shade, C. M.; Lang, M.; Uh, H.; Wang, M.; Weber, S. G.; Bartlett, D. L.; Petoud, S.; Lee, Y. J. *Nanomedicine* **2011**, *7*, 249-258.
(9) Nockemann, P.; Beurer, E.; Driesen, K.; Van Deun, R.; Van Hecke, K.; Van Meervelt, L.; Binnemans, K. *Chem. Commun.* **2005**, 4354-4356.
(10) Weissman, S. I. *J. Chem. Phys.* **1942**, *10*, 214-217.
(11) Eliseeva, S. V.; Bünzli, J.-C. G. *Chem. Soc. Rev.* **2010**, *39*, 189-227.
(12) Zhang, J.; Petoud, S. *Chem. Eur. J.* **2008**, *14*, 1264-1272.
(13) Zhang, J.; Badger, P. D.; Geib, S. J.; Petoud, S. *Angew. Chem., Int. Ed.* **2005**, *44*, 2508-2512.
(14) Comby, S.; Imbert, D.; Chauvin, A. S.; Bünzli, J.-C. G. *Inorg. Chem.* **2006**, *45*, 732-743.
(15) Korovin, Y. V.; Rusakova, N. V.; Popkov, Y. A.; Dotsenko, V. P. *J. Appl. Spectrosc.* **2002**, *69*, 841-844.
(16) Bünzli, J.-C. G.; Eliseeva, S. V. *Chem. Sci.* **2013**, *4*, 1939-1949.
(17) D'Aléo, A.; Bourdolle, A.; Brustlein, S.; Fauquier, T.; Grichine, A.; Duperray, A.; Baldeck, P. L.; Andraud, C.; Brasselet, S.; Maury, O. *Angew. Chem., Int. Ed.* **2012**, *51*, 6622-6625.
(18) White, K. A.; Chengelis, D. A.; Zeller, M.; Geib, S. J.; Szakos, J.; Petoud, S.; Rosi, N. L. *Chem. Commun.* **2009**, 4506-4508.
(19) White, K. A.; Chengelis, D. A.; Gogick, K. A.; Stehman, J.; Rosi, N. L.; Petoud, S. *J. Am. Chem. Soc.* **2009**, *131*, 18069-18071.
(20) Rieter, W. J.; Taylor, K. M. L.; An, H.; Lin, W.; Lin, W. *J. Am. Chem. Soc.* **2006**, *128*, 9024-9025.
(21) Rieter, W. J.; Taylor, K. M. L.; Lin, W. *J. Am. Chem. Soc.* **2007**, *129*, 9852-9853.
(22) Taylor, K. M. L.; Rieter, W. J.; Lin, W. *J. Am. Chem. Soc.* **2008**, *130*, 14358-14359.
(23) Taylor, K. M. L.; Jin, A.; Lin, W. *Angew. Chem., Int. Ed.* **2008**, *47*, 7722-7725.
(24) Taylor-Pashow, K. M. L.; Rocca, J. D.; Xie, Z.; Tran, S.; Lin, W. *J. Am. Chem. Soc.* **2009**, *131*, 14261-14263.
(25) Horcajada, P.; Chalati, T.; Serre, C.; Gillet, B.; Sebrie, C.; Baati, T.; Eubank, J. F.; Heurtaux, D.; Clayette, P.; Kreuz, C.; Chang, J.-S.; Hwang, Y. K.; Marsaud, V.; Bories, P.-N.; Cynober, L.; Gil, S.; Férey, G.; Couvreur, P.; Gref, R. *Nat. Mater.* **2010**, *9*, 172-178.
(26) deKrafft, K. E.; Xie, Z.; Cao, G.; Tran, S.; Ma, L.; Zhou, O. Z.; Lin, W. *Angew. Chem., Int. Ed.* **2009**, *48*, 9901-9904.
(27) Rieter, W. J.; Pott, K. M.; Taylor, K. M. L.; Lin, W. *J. Am. Chem. Soc.* **2008**, *130*, 11584-11585.
(28) Aebischer, A.; Gumy, F.; Bünzli, J.-C. G. *Phys. Chem. Chem. Phys.* **2009**, *11*, 1346-1353.
(29) Giuliani, A.; Jamme, F.; Rouam, V.; Wien, F.; Giorgetta, J.-L.; Lagarde, B.; Chubar, O.; Bac, S.; Yao, I.; Rey, S.; Herbeaux, C.; Marlats, J.-L.; Zerbib, D.; Polack, F.; Refregiers, M. *J. Synchrotron. Radiat.* **2009**, *16*, 835-841.
(30) Wagnieres, G. A.; Star, W. M.; Wilson, B. C. *Photochem. Photobiol.* **1998**, *68*, 603-632.

5.0 LUMINESCENT SIZE-CONTROLLABLE NANOSCALE METAL-ORGANIC FRAMEWORKS WITH BIOLOGICAL NEAR-INFRARED EXCITATION AND EMISSION WAVELENGTHS

This work was performed in collaboration with Sandrine Villette and Sunčica Vujica (Centre de Biophysique Moléculaire, Centre National de la Recherche Scientifique, Orléans, France), and Alexander B. Spore (Nathaniel L. Rosi Research Group, University of Pittsburgh).

5.1 INTRODUCTION

Imaging biological systems in real time is a powerful diagnostic tool, and a good deal of focus has been placed on utilizing the near-infrared (NIR) region of the electromagnetic spectrum to do so. There is a "NIR window" in which biological species absorb significantly less, allowing for deeper penetration into tissue and non-invasive investigations.[1,2] Lower biological autofluorescence signal in the NIR makes it easier to discriminate the desired signal from biological background therefore increasing the detection sensitivity and decreasing interpretation ambiguity. NIR light scatters less than visible light leading to enhanced image resolution.[3,4]

An ideal luminescent biological imaging reporter would be able to be excited in the NIR, emit in the NIR, be non-toxic, and resist biological-, thermal-, and photo-degradations. There are a variety of materials which meet some, but not all, of these requirements.[5-7] There are a multitude of organic dyes which have both excitation and emission it the biological NIR.[6] A cyanine dye, indocyanine green (ICG), is approved by the Food and Drug Administration (FDA) for direct administration in medical ophthalmologic diagnostics, although it suffers from poor photostability. One way to increase the photostability has been to encapsulate dyes in nanoparticles.[8,9] While some improvements were achieved over the years, organic fluorophores suffer from broad emission spectra which render them unsuitable for multiplexing or barcoding. Quantum dots (QDs) are typically brighter and more photostable than organic dyes[10], and their size-dependent emission allows for the ability to tune the emission wavelength[11]. The downfall of QDs is the blinking phenomenon they exhibit.[12]

Another complementary approach worth testing is to use lanthanide cations whose unique properties explain their emergence for bioanalytical and optical imaging applications.[13,14] Their emission bands are sharp compared with organic fluorophores and semiconductor nanocrystals, and their emission wavelengths are not affected by their chemical and biological environments allowing them to be used in a broad range of conditions, including varying pH.[14] Lanthanide complexes possess long emission lifetimes and a good resistance to photobleaching[15-17], which enables them to be used repeatedly over long periods of time.

Lanthanide cations have very low molar extinction coefficients due to the forbidden nature of the $f \rightarrow f$ transition.[14] In order to overcome this limitation, an organic chromophore needs to be placed in sufficiently close proximity to the lanthanide to act as an "antennae" and sensitize the lanthanide cations.[18] Additionally, luminescent lanthanide complexes are often limited by their low quantum yield. One way to overcome this is to utilize lanthanides as the metal in metal-organic frameworks (MOFs) to create a polymetallic species. MOFs have well-defined structures which allow the tridimensional control of the incorporation of a large number of chromophoric sensitizers and lanthanide cations in the structure. Consequently, this results in a large number of photons emitted per volume unit, an important advantage that enhances the detection sensitivity.[17] Another advantage of the MOF structure is that it can be tailored to tune and optimize the photoluminescence properties of the luminescent lanthanides.[19] Since MOFs are porous it is possible to incorporate a variety of molecules and nanomaterials into the pores, including therapeutic agents such as anticancer drugs, biogases (nitric oxide), and imaging agents (Gd^{3+}).[20-23]

We have recently reported the creation and biological use of nanoscale luminescent metal-organic frameworks for *in vivo* cellular imaging which were internalized by cells, were demonstrated to be non-cytotoxic, photostable, and emitted in the NIR with a sufficient intensity to allow for sensitive detection.[17] This nano-Yb-PVDC-3 MOF used PVDC as the ligand and

chromophore with the Yb^{3+} being both the metal and the NIR emitter. Here we have transitioned to a more biologically-friendly ligand[21,24], 1,3,5-benzenetricarboxylic acid (BTC), to synthesize a series of Yb^{3+} MOFs. Several MOFs have been synthesized with this linker and various lanthanides[25-29], including the miniaturization[29] of Dy(BTC)(H_2O), but to the best of our knowledge, we describe here the first example of the miniaturization of the Yb(BTC)(H_2O) MOF and study of its NIR Yb^{3+} emission.

In order to shift the excitation wavelength to the NIR we used a totally new approach: the incorporation of a NIR absorbing chromophore, 4-hydroxyl-1-(4-methyl-2-sulfoanilino)-anthraquinone (4hAQ) to act as an antennae within the nanoscale Yb(BTC)(H_2O) MOF. We achieved what we believe to be the first example of a nanoscale MOF for biological imaging which can both be excited and emit in the NIR. To further protect the Yb^{3+} and enhance the luminescence signal in water, the dye-incorporated nanoMOFs were coated with a silica shell which can be easily functionalized in the future.

5.2 EXPERIMENTAL

5.2.1 Reagents

All reagents were used as received without further purification. 1,3,5-benzentricarboxylic acid (BTC; 95%), ammonium hydroxide solution, tetraethyl orthosilicate (TEOS), indocyanine green (ICG), and deuterium chloride (DCl; 35 wt% in D_2O, 99 atom% D) were purchased from Aldrich. Ytterbium (III) nitrate pentahydrate ($Yb(NO_3)_3 \cdot 5H_2O$; 99.9%) was purchased from Strem. *N,N*-dimethylformamide (DMF; Certified ACS) and Alexa Fluor 647 (AF647) were

purchased from Fisher. Sodium acetate (NaOAc, anhydrous) was purchased from EM. Ethanol (EtOH; 200 proof) was purchased from Decon Laboratories, Inc. 4-hydroxyl-1-(4-methyl-2-sulfoanilino)-anthraquinone (4hAQ; >95.0%) was purchased from TCI. Dimethylsulfoxide (DMSO; ACS Reagent, >99.9%) was purchased from Sigma-Aldrich. Deuterated dimethylsulfoxide (DMSO-d_6; 99.9%) was purchased from Cambridge Isotope Laboratories. Hydrochloric acid (HCl; 36.5-38.0%, Baker Analyzed ACS Reagent) was purchased from J.T. Baker.

5.2.2 Synthetic Procedures

5.2.2.1 Synthesis of Yb(BTC)(H_2O)·DMF MOF

The following materials were placed in a 20 mL scintillation vial: 0.10 mmol BTC, 0.13 mmol $Yb(NO_3)_3 \cdot 5H_2O$, 8 mL DMF, and 2 mL distilled H_2O. The vial was capped, sonicated for ~10 seconds to completely dissolve the Yb^{3+} salt, and placed in an isotemp oven at 60 °C for 72 hours. The vial was cooled to room temperature, and the white solid was collected via vacuum filtration and washed with DMF. Elemental analysis (EA) calcd (%) for Yb(BTC)(H_2O)·DMF: C, 30.58; H, 2.57; N, 2.97. Found: C, 29.86; H, 2.30; N, 3.01.

5.2.2.2 Synthesis of Yb(BTC)(H_2O)·DMF nanoMOF

The following materials were placed in a 20 mL scintillation vial: 0.10 mmol BTC, 0.13 mmol $Yb(NO_3)_3 \cdot 5H_2O$, 8 mL DMF, and 2 mL distilled H_2O. The mixtures were stirred until the solutions were clear. Either 0.1 mmol (1 equivalent wrt BTC), 0.2 mmol (2 equivalents wrt BTC), 0.3 mmol (3 equivalents wrt BTC), or 0.35 mmol (3.5 equivalents wrt BTC) NaOAc was added, and the mixture was stirred for 10 minutes at room temperature during which time a white

precipitate was observed. The vial was capped and placed in an isotemp oven at 60 °C for 24 hours. The vial was cooled to room temperature, and the solid material was collected via centrifugation at 10,000 rpm for 5 minutes. The solid was washed three times with DMF and air dried. Elemental analysis (EA) calcd (%) for Yb(BTC)(H_2O)·DMF: C, 30.58; H, 2.57; N, 2.97. For 1 equivalent of NaOAc, found: C, 29.60; H, 2.28; N, 2.90. For 2 equivalents of NaOAc, found: C, 29.94; H, 2.33; N, 3.01. For 3 equivalents of NaOAc, found: C, 30.09; H, 2.39; N, 3.10. For 3.5 equivalents of NaOAc, found: C, 30.10; H, 2.34; N, 3.10.

5.2.2.3 Solvent exchange of Yb(BTC)(H_2O)·DMF nanoMOF

Yb(BTC)(H_2O)·DMF synthesized with 3 equivalents of NaOAc was solvent exchanged by removing the solvent (initially DMF, subsequently EtOH) and replacing with fresh EtOH after 10 min (×3), 12 hours, and 24 hours. Elemental analysis (EA) calcd (%) for Yb(BTC)(H_2O)·EtOH: C, 29.74; H, 2.50; N, 0.00. Found: C, 29.12; H, 2.23; N, 0.17.

5.2.2.4 Anthraquinone incorporation

A small amount (*X* mg, where typically *X*=1) of solid Yb(BTC)(H_2O) nanoMOF (3 eq. NaOAc) was diluted with EtOH (0.9 × *X* mL) to achieve a concentration of 1.1 mg/mL. This solution was sonicated for at least 10 hours but up to several days with intermittent periods of mixing in order to achieve a homogeneous suspension as determined by visual inspection. Separately, 4-hydroxyl-1-(4-methyl-2-sulfoanilino)-anthraquinone (4hAQ) was dissolved in EtOH to create a solution with a concentration of 1 mg/mL. A small volume of 4hAQ solution (*X*/10 mL) was added to the nanoMOF suspension to result in a final concentration of 100 μg/mL 4hAQ and 1 mg/mL nanoMOF. This suspension was stirred in the dark for at least 24 hours. The sample was washed twice by centrifugation at 2800×*g* for 10 minutes, removing the supernatant, and adding

EtOH (*X* mL) to redissolve the pellet. The final concentration of the suspension was 1 mg/mL Yb(BTC)(H_2O)+4hAQ. The sample was either used immediately or it was centrifuged at 2800×*g* for 10 minutes, the supernatant was removed, and the Yb(BTC)(H_2O)+4hAQ was dried under vacuum for a few minutes.

5.2.2.5 Silica coating

Yb(BTC)(H_2O)+4hAQ was coated with a silica shell using a sol-gel procedure adapted from the literature.[30] 1 mL of Yb(BTC)(H_2O)+4hAQ solution at 1 mg/mL in EtOH was further diluted with 8.6 mL of EtOH. Aqueous ammonia (400 μL) was added drop by drop under vigorous stirring. Then 20 μL of tetraethyl orthosilicate (TEOS) was added, and the mixture was left stirring for 2 hours in the dark. An additional aliquot of TEOS (20 μL) was added and the suspension was left to stir for an additional 3 hours before purification by two steps of centrifugation (2800×*g*) and re-suspension in EtOH. After the second step of centrifugation the supernatant was removed and either replaced by 1 mL of EtOH for immediate measurement or the pellet was dried under vacuum for a few minutes.

5.2.3 Instrumentation

5.2.3.1 Elemental analysis

The elemental microanalysis (CHN) was performed by the Microanalysis Laboratory at the University of Illinois Urbana-Champaign. Samples were dried under nitrogen flow to remove excess solvent prior to submission for analysis.

5.2.3.2 Fourier transform infrared spectroscopy

Fourier-transform infrared (FTIR) spectra were collected on a Perkin Elmer Spectrum 100 FTIR with a universal attenuated total reflectance (ATR) sampling accessory coupled to a computer using Perkin Elmer Spectrum Express software.

5.2.3.3 Powder X-ray diffraction

Powder X-ray diffraction (PXRD) patterns were collected using a Phillips PW 1830 diffractometer at 40 kV, 40 mA, for Cu Kα (λ = 1.54056 Å) with a scan speed of 0.20 seconds per step and a step size of 0.020°.

5.2.3.4 Scanning electron microscopy

Samples were coated with palladium for 60 seconds before analysis with a Phillips XL 30 scanning electron microscope (SEM). ImageJ 1.47v software (National Institutes of Health) was used to measure particle dimensions. OriginPro 9.1 software (OriginLab Corporation) was used to process the data.

5.2.3.5 Transmission electron spectroscopy

All images were collected with a Philips CM20 transmission electron microscope (TEM) operating at 200 kV and equipped with a filament Lab6.

5.2.3.6 Thermogravimetric analysis

Thermogravimetric analysis (TGA) was conducted on a TGA Q500 thermal analysis system. Prior to analysis, samples were dried under nitrogen flow to remove excess solvent.

Approximately 5 mg of sample were loaded into a platinum pan and heated under a constant N_2 (UHP) flow from room temperature to 600 °C at a rate of 5 °C/min.

5.2.3.7 Adsorption

Gas adsorption isotherms were collected on a Quantachrome Autosorb-1 instrument. The samples were first washed thoroughly with absolute ethanol. Approximately 100-140 mg of each sample was added into a pre-weighed sample analysis tube that had been evacuated and backfilled with He before massing. The samples were degassed at 100 °C under vacuum for ~24 hours until the pressure change rate was no more than 3 mTorr/min. A liquid N_2 bath was used for the N_2 adsorption experiments at 77 K. Ultra high purity (UHP) grade N_2 gas adsorbates (99.999 %) were used in this study.

5.2.3.8 Nuclear magnetic resonance spectroscopy

A solution of 23 μL DCl (35% in D_2O) and 1000 μL DMSO-*d*$_6$ was used to dissolve the solid samples for ^{1}H NMR analysis. A small amount of solid was dissolved in 150 μL of the DCl/DMSO solution and diluted with an additional 500 μL DMSO-*d*$_6$. Samples were analyzed with either a Bruker Avance III 300 MHz or 400 MHz NMR.

5.2.3.9 Absorption spectroscopy

Ultraviolet-visible (UV-vis) absorption spectra for the quantification of 4hAQ were collected on an Agilent 8453 spectrometer coupled to a personal computer with software supplied by Agilent. The solvent for quantification via absorption was analogous to that used for NMR except it was not deuterated; 690 μL of concentrated HCl was combined with 130 mL DMSO. Standard solutions of 4hAQ ranged in concentration from 5×10^{-7} to 1×10^{-5} M. 4.5 mg of

Yb(BTC)(H_2O)+4hAQ was dissolved in 2.0 mL of the solvent. All other absorption measurements were recorded on a Jasco V670.

5.2.3.10 Luminescence spectroscopy

Excitation and emission spectra were measured using a HORIBA Jobin Yvon Fluorolog 3-22 spectrofluorometer equipped with a R928 Hamamatsu detector for visible detection and with either a DSS-IGA020L detector (Electro-Optical Systems, Inc.) or a H10330-75 detector (Hamamatsu) for the NIR. The sample holder was an integrating sphere using quartz tubes developed by Frédéric Gumy and Jean-Claude G. Bünzli (Laboratory of Lanthanide Supramolecular Chemistry, École Polytechnique Féderale de Lausanne, Lausanne, Switzerland) as an accessory to the Fluorolog 3-22 spectrofluorometer (patent pending) and commercialized and manufactured by GMP.[31] Spectra were corrected for variations in lamp intensity over the spectra range, as well as for excitation monochromator, emission monochromator, and detector responses. The data were analyzed using OriginPro 9.1 software.

5.2.3.11 Quantum yield measurements

Quantum yield measurements were also collected on the Fluorolog-322 with the integrating sphere. Collecting NIR quantum yields requires the use of both a visible and a NIR detector; ytterbium tropolonate ($[Yb(trop)_4]^-$ in DMSO, $\Phi_{Yb} = 1.9(\pm 0.1)\times 10^{-3}$) was used as a reference[32]. The process for collecting a relative quantum yield using the integrating sphere is the following step by step process:

1) Emission spectra of the lamp were collected for the sample (R_{S+SB}), the solvent in which the sample is placed (R_{SB}), the reference (*see above*, R_{R+RB}), and the solvent in which the reference is dissolved (R_{RB}). Neutral density filters were placed at the excitation port of

the integrating sphere to control the high intensity of the lamp. The spectra were corrected, as described above, and the bands were integrated. The resulting integration values were used to determine the amount of light that was absorbed by the sample and the reference, given by:

$$R_S = R_{SB} - R_{S+SB}$$

Equation 5.1.

and

$$R_R = R_{RB} - R_{R+RB}$$

Equation 5.2.

2) Emission spectra of the sample (I_{S+SB}), of the sample solvent (I_{SB}), of the reference (I_{R+RB}), and of the reference solvent (I_{RB}) were collected in the NIR range. A 780 nm long-pass filter was placed at the NIR emission port of the integrating sphere to eliminate contributions from second order bands. Emission spectra were corrected for the lamp variation, the solvent spectra were subtracted from the appropriate sample and reference spectra:

$$I_S = I_{S+SB} - I_{SB}$$

Equation 5.3.

and

$$I_R = I_{R+RB} - I_{RB}$$

Equation 5.4.

and the resulting spectra were corrected for detector response. The spectra were not corrected for the filters because in the case of a relative quantum yield measurement the use of a scalar (*see below how such scalar is calculated*) corrects for the filters during the calculations.

3) The known quantum yield of the reference was used to create a scalar ($X_{NIR\text{-}VIS}$) which accounts for the use of two different detectors in the visible and in the NIR with a domain of overlapping response:

$$X_{NIR-VIS} = \frac{\Phi_R R_R}{I_R}$$

Equation 5.5.

4) The quantum yield of the sample was calculated using the following equation:

$$\Phi_S = \frac{X_{NIR-VIS} I_S}{R_S}$$

Equation 5.6.

5.2.3.12 Photobleaching studies

Photobleaching experiments were performed using the same instrumental set-up. A similar volume of 60 μL was used for each sample: 4hAQ, (Yb(BTC)(H_2O)+4hAQ)@SiO_2, Alexa Fluor 647 (AF647), and indocyanine green (ICG). All samples were in HEPES buffer (10 mM, pH 7.4) and were manually mixed using a micropipette prior to each measurement. A series of 10 spectra (λ_{ex} = 580 nm, 14 nm bandpass) were recorded with a 5 minute delay between spectra. The samples were maintained under continuous illumination for a total time of one hour. Luminescence signal was determined as the integral of the luminescence band of each spectrum divided by the integral of the luminescence band of the first recorded spectrum (time = 0 minutes). It must be noted that (Yb(BTC)(H_2O)+4hAQ)@SiO_2 was left in HEPES buffer for 4 hours prior to the photobleaching experiment in order to reduce the loss of luminescence signal due to the penetration of water inside the silica shell.

5.2.3.13 Luminescence lifetimes

Luminescence lifetimes were measured using a neodymium yttrium aluminum garnet (Nd:YAG) Continuum Powerlite 8010 laser (355 nm, third harmonic) as the excitation source. Emission was collected at a right angle to the excitation beam, and wavelengths were selected by a Spectral Products CM110 1/8m monochromator. The signal was monitored by a Hamamatsu R316-02 photomultiplier tube and collected on a 500-MHz bandpass digital oscilloscope (Tektronix TDS 754D). Signals from >1,000 flashes were collected and averaged. Three decay curves were collected for each sample, and the data were analyzed using OriginPro 9.1 software with exponential fitting modes.

5.3 RESULTS AND DISCUSSION

5.3.1 Bulk and nanoscale Yb(BTC)(H_2O) MOFs

A previously reported synthesis[29] for Dy(BTC)(H_2O) was modified to use the NIR-emitting Yb^{3+}. As was reported with the Dy^{3+} system[29], altering the number of equivalents of sodium acetate (NaOAc) with respect to the equivalents of 1,3,5-benzenetricarboxylic acid (BTC) ligand (Figure 5.1) in the synthesis allowed for excellent size control in the Yb^{3+} system. In the absence of NaOAc the bulk crystals were long and needle-like (Figure 5.2). The addition of one, two, three, or three and one-half equivalents of NaOAc resulted in increasingly smaller rod-like nanoparticles which, upon addition of three and one-half equivalents were spherical (Figure 5.3). A size comparison is summarized in Table 5.1, and the corresponding histograms are depicted in Figures 5.4-5.8.

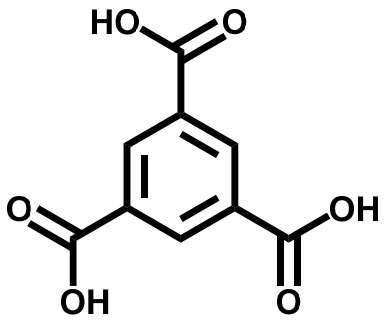

Figure 5.1. Structure of 1,3,5-benzenetricarboylic acid (BTC) ligand.

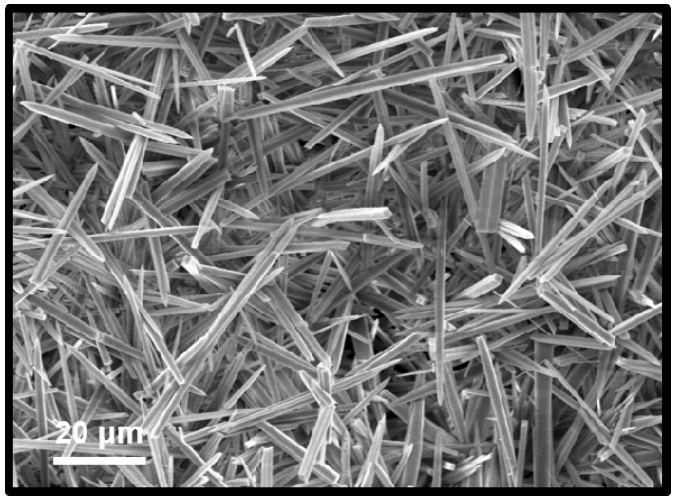

Figure 5.2. Representative scanning electron microscopy (SEM) image of Yb(BTC)(H_2O) MOF synthesized in absence of sodium acetate.

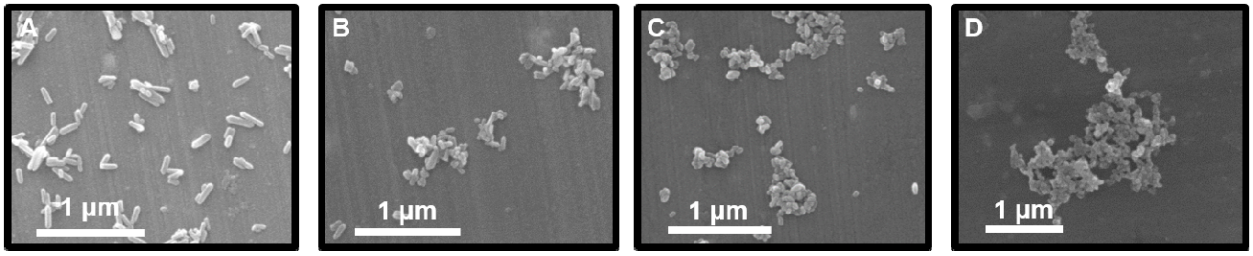

Figure 5.3. Representative scanning electron microscopy (SEM) images of Yb(BTC)(H_2O) nanoMOF synthesized with 1 equivalent (A), 2 equivalents (B), 3 equivalents (C), and 3.5 equivalents (D) of NaOAc.

Table 5.1. Length and width dimensions of Yb(BTC)(H_2O) MOFs synthesized with various amounts of sodium acetate. Errors reported are standard deviations based on at least 50 measurements.

	0 eq. NaOAc	1 eq. NaOAc	2 eq. NaOAc	3 eq. NaOAc	3.5 eq. NaOAc
Length (nm)	$28(\pm16)\times10^3$	166(±64)	129(±45)	79(±23)	-
Width (nm)	$1.9(\pm0.8)\times10^3$	54(±11)	51(±10)	46(±9)	64(±19)

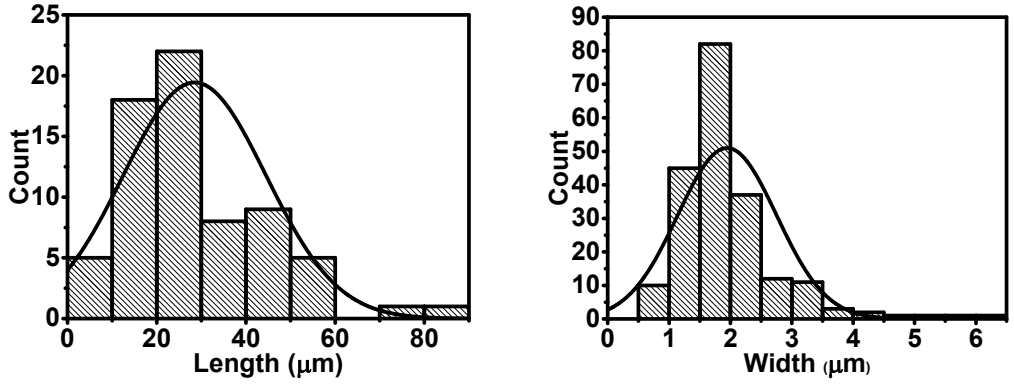

Figure 5.4. Histograms for length (*left*) and width (*right*) measurements for Yb(BTC)(H_2O) MOF synthesized with 0 equivalents of NaOAc.

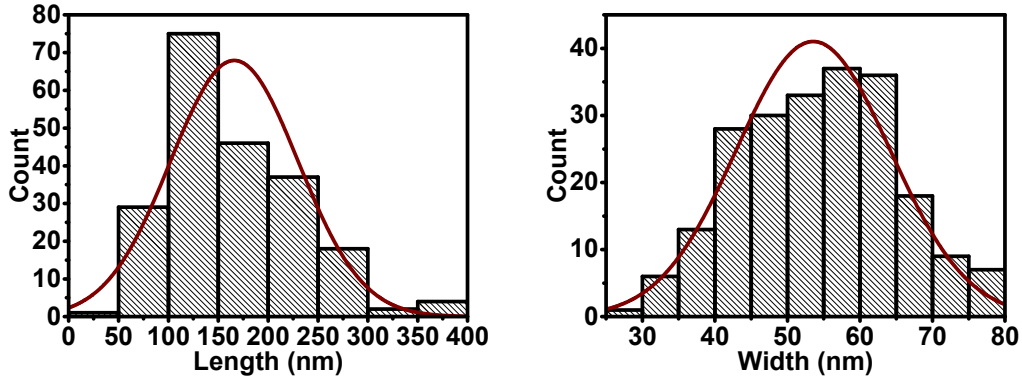

Figure 5.5. Histograms for length (*left*) and width (*right*) measurements for Yb(BTC)(H_2O) nanoMOF synthesized with 1 equivalent of NaOAc.

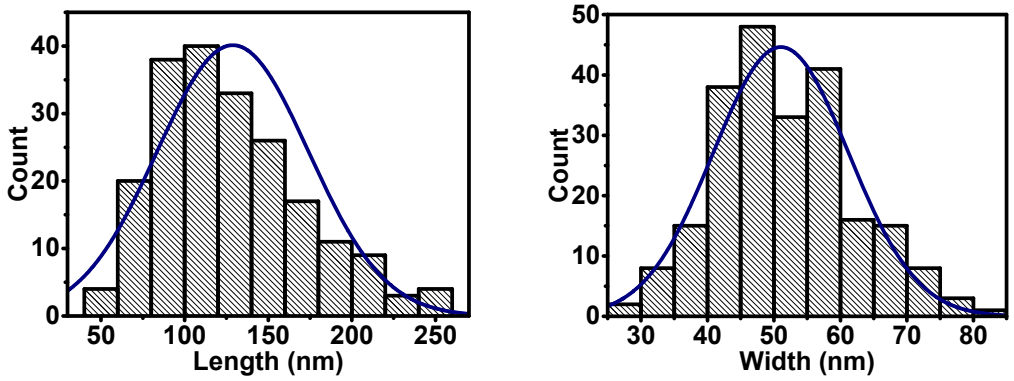

Figure 5.6. Histograms for length (*left*) and width (*right*) measurements for Yb(BTC)(H_2O) nanoMOF synthesized with 2 equivalents of NaOAc.

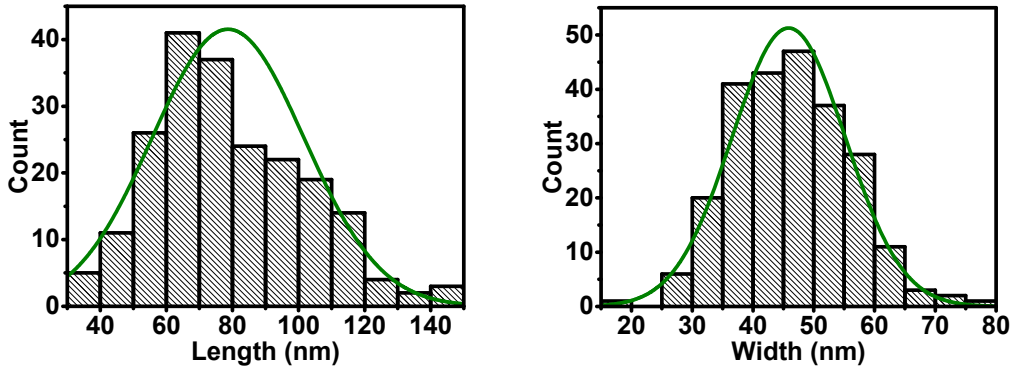

Figure 5.7. Histograms for length (*left*) and width (*right*) measurements for Yb(BTC)(H_2O) nanoMOF synthesized with 3 equivalents of NaOAc.

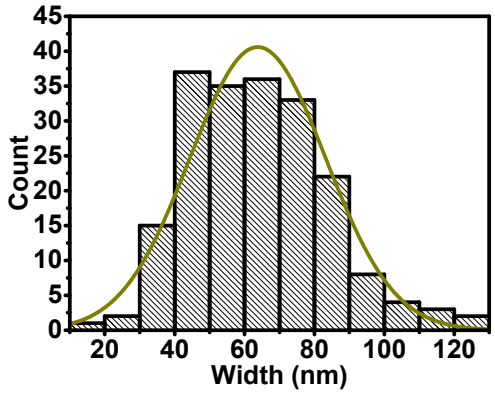

Figure 5.8. Histogram for width measurements for Yb(BTC)(H_2O) nanoMOF synthesized with 3.5 equivalents of NaOAc.

The powder X-ray diffraction (PXRD) patterns (Figure 5.9) collected for these materials were identical to each other and an exact match to the previously reported pattern[27] for Yb(BTC)(H_2O)·guest MOF (Figure 5.10). This chemical formula was corroborated by both elemental analysis *(see Sections 5.2.2.1 and 5.2.2.2*) and thermogravimetric analysis (Figure 5.11).

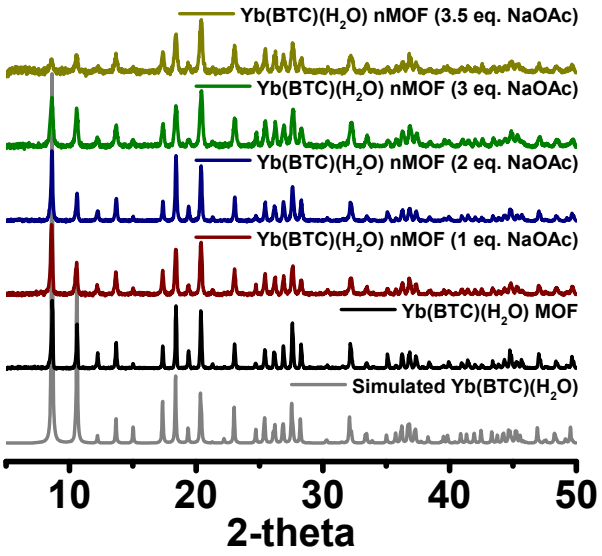

Figure 5.9. Powder X-ray diffraction (PXRD) patterns for Yb(BTC)(H_2O) MOFs synthesized with 0, 1, 2, 3, and 3.5 equivalents of NaOAc, and the simulated pattern[27] for Yb(BTC)(H_2O)·DMF.

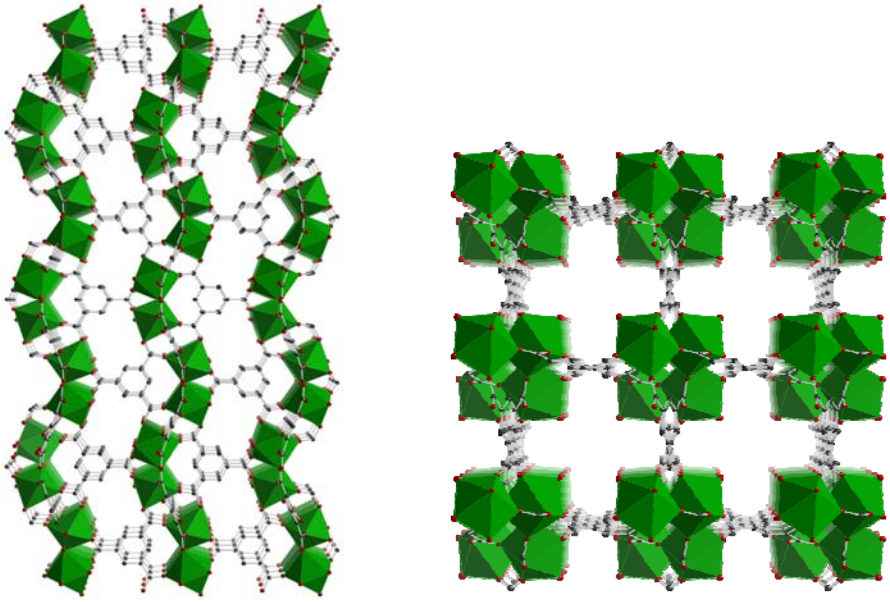

Figure 5.10. Infinite secondary building units (SBUs) of Yb(BTC)(H_2O) MOF (*left)* (Yb^{3+}, green; C, gray; O, red) and crystal structure of Yb(BTC)(H_2O) MOF viewed along the *c*-crystallographic direction (*right)*. Uncoordinated molecules of H_2O and DMF are not shown for clarity; fully evacuated pore dimensions are 7×7 Å.

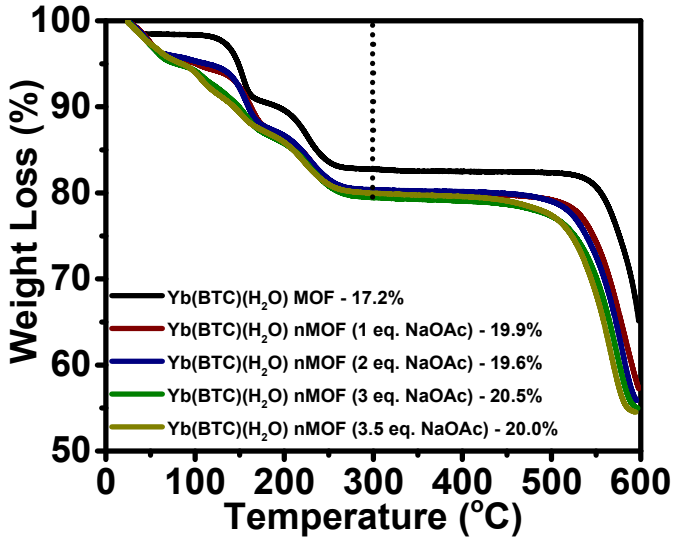

Figure 5.11. Thermogravimetric analysis (TGA) for each of the Yb(BTC)(H_2O)·DMF MOFs synthesized. The percent weight loss at 300 °C (represented by the dotted line) is shown in the legend and corresponds to the loss of one DMF molecule from the pore and one H_2O molecule from the framework.

5.3.2 Stability of Yb(BTC)(H_2O) MOF

In order to evaluate the water stability of these materials, the bulk MOF was soaked in water for 28 days. At various time points the solid was removed from the water and analyzed using PXRD (Figure 5.12) and SEM (Figure 5.13) techniques. These experiments qualitatively demonstrated that the material maintains its crystallinity in an aqueous environment.

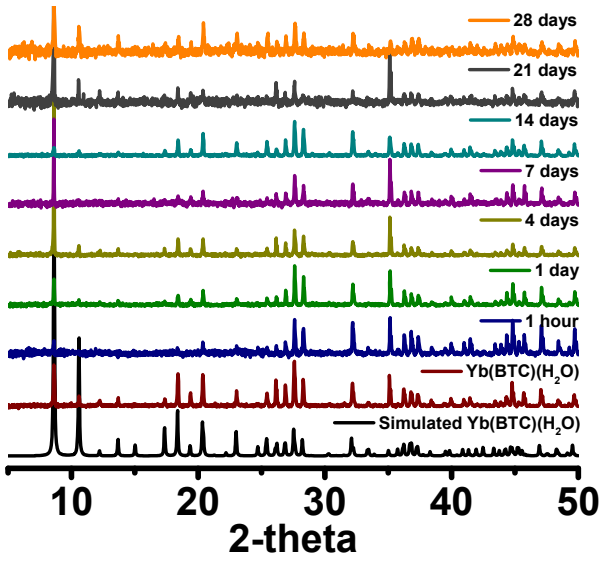

Figure 5.12. Powder X-ray diffraction (PXRD) patterns for Yb(BTC)(H_2O) MOF after soaking in water for various amounts of time and the simulated pattern[27] for Yb(BTC)(H_2O)·DMF.

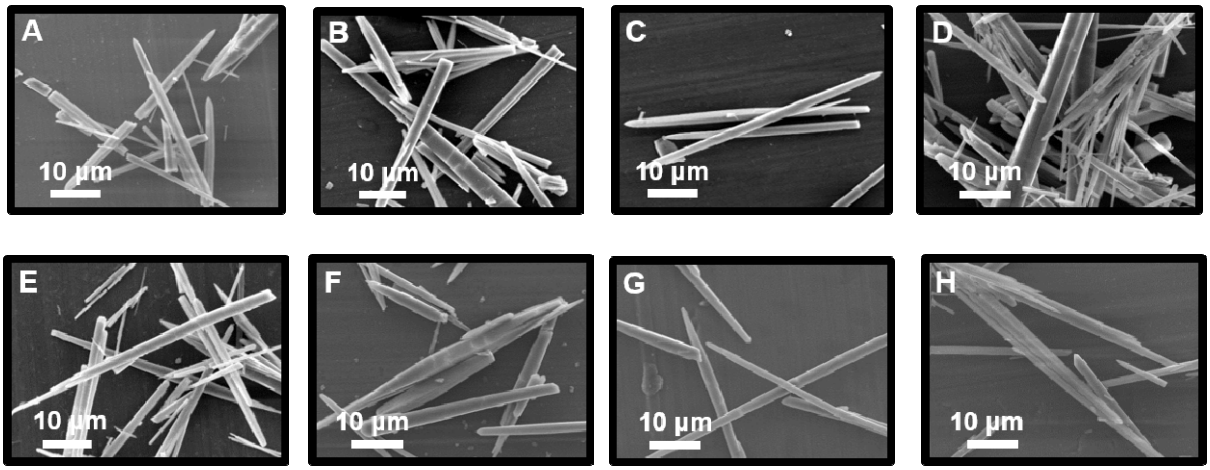

Figure 5.13. Representative scanning electron microscope (SEM) images of Yb(BTC)(H_2O) (A) after soaking in water for 1 hour (B), 1 day (C), 4 days (D), 7 days (E), 14 days (F), 21 days (G), and 28 days (H).

5.3.3 Spectroscopic properties of Yb(BTC)(H_2O) MOFs

The spectrophotometric properties of the MOF and nanoMOFs were initially investigated as solid crystalline materials under DMF (Figures 5.14-5.18). The excitation spectra collected while monitoring the Yb^{3+} emission at 980 nm exhibited one distinct band centered at 285 nm which overlays well with the absorption spectrum of BTC (Figure 5.14). This indicates that the BTC ligand is a suitable antenna. As Yb^{3+} does not possess accepting electronic levels in the ultraviolet-visible range, the only way to obtain the sharp emission band of Yb^{3+} in this experiment is to use the electronic levels present in the BTC. Excitation at 285 nm resulted in the strongest emission intensity, but excitation at 355 nm still produced a measurable signal (although ~91% less intense) despite being far on the red shoulder of the excitation band. Nevertheless, such excitation wavelength is not optimal for the excitation of imaging agents in biological conditions as biological systems absorb an appreciable amount of light in this 285–355 nm wavelength range.

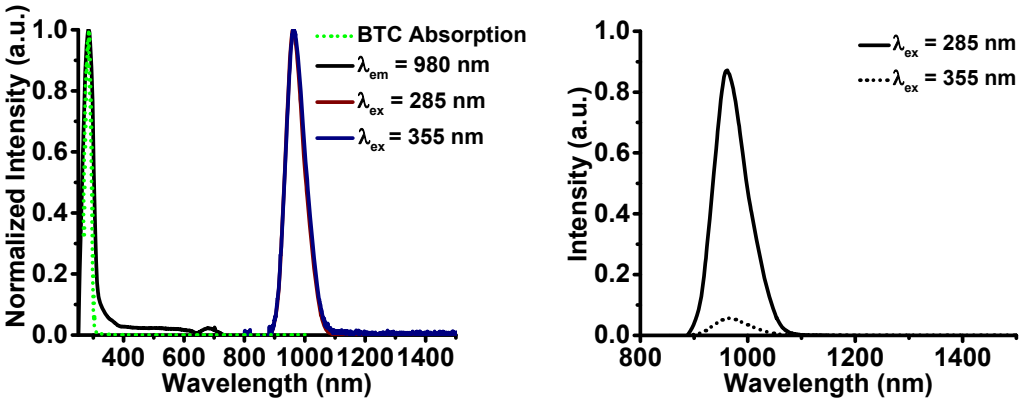

Figure 5.14. Excitation and emission spectra of Yb(BTC)(H_2O) MOF in DMF. *Left:* Normalized excitation and emission spectra overlaid with the normalized absorption spectrum of BTC. *Right:* Non-normalized emission spectra demonstrating the ~91% decrease in emission intensity when red-shifting the excitation wavelength.

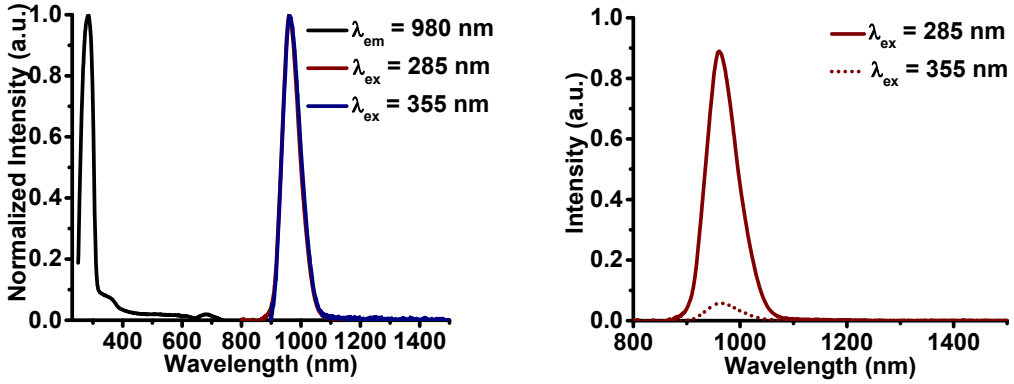

Figure 5.15. Excitation and emission spectra of Yb(BTC)(H_2O) nanoMOF (synthesized with 1 eq. NaOAc) in DMF. *Left:* Normalized excitation and emission spectra. *Right:* Non-normalized emission spectra demonstrating the ~91% decrease in emission intensity when red-shifting the excitation wavelength.

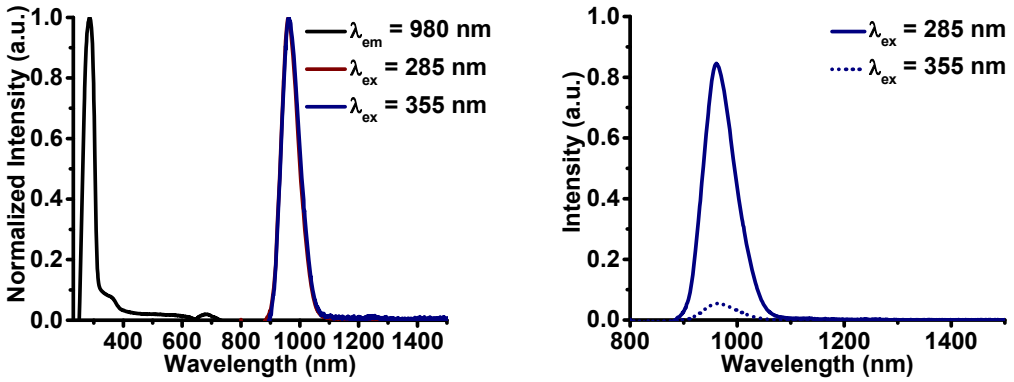

Figure 5.16. Excitation and emission spectra of Yb(BTC)(H_2O) nanoMOF (synthesized with 2 eq. NaOAc) in DMF. *Left:* Normalized excitation and emission spectra. *Right:* Non-normalized emission spectra demonstrating the ~91% decrease in emission intensity when red-shifting the excitation wavelength.

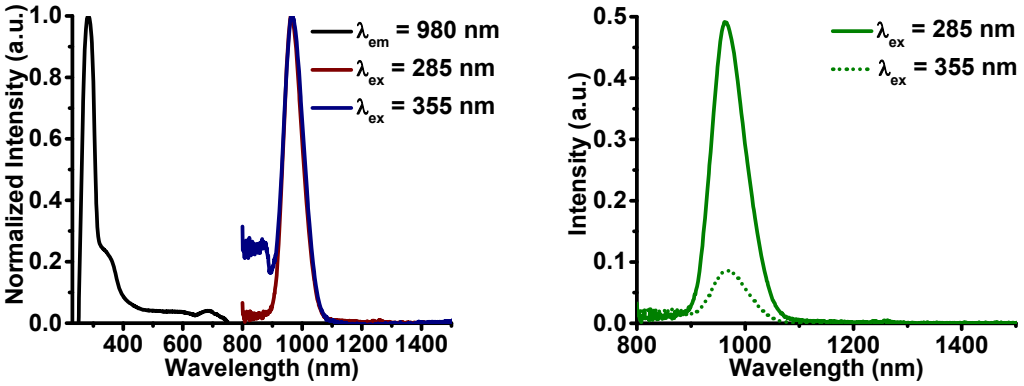

Figure 5.17. Excitation and emission spectra of Yb(BTC)(H_2O) nanoMOF (synthesized with 3 eq. NaOAc) in DMF. *Left:* Normalized excitation and emission spectra. *Right:* Non-normalized emission spectra demonstrating the ~91% decrease in emission intensity when red-shifting the excitation wavelength.

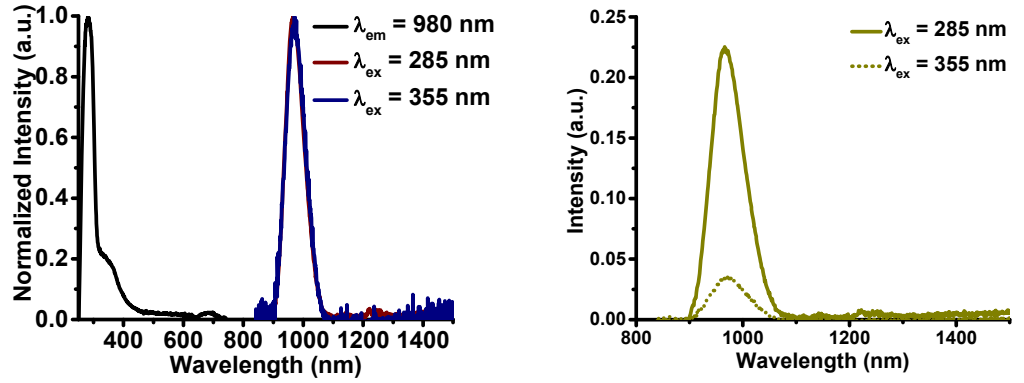

Figure 5.18. Excitation and emission spectra of Yb(BTC)(H_2O) nanoMOF (synthesized with 3.5 eq. NaOAc) in DMF. *Left:* Normalized excitation and emission spectra. *Right:* Non-normalized emission spectra demonstrating the ~91% decrease in emission intensity when red-shifting the excitation wavelength.

Quantum yields (Table 5.2) were collected upon excitation at wavelengths of 285 nm and 355 nm. The different amounts of NaOAc used for these different syntheses did not affect the values of quantum yields for each of the two excitation wavelengths, indicating that the size of the Yb(BTC)(H_2O) MOF does not significantly affect the sensitizer-to-lanthanide energy transfer or the protection of the luminescent lanthanide cations against non-radiative deactivations.

For each of the two wavelengths used for this experiment, a different quantum yield was recorded with a significant decrease when the 355 nm excitation wavelength was used. Such observations suggest that two energy paths that do not communicate with each other are present in these MOFs. From these quantitative values it can be concluded that the excitation at 355 nm does not generate a large number of photons as both the extinction coefficient and quantum yield are lower in comparison to the situation corresponding to an excitation at 285nm. The number of photons emitted by the Yb(BTC)(H_2O) MOFs are proportional to its brightness which is the result of the multiplication of its extinction coefficient by its quantum yield.

Table 5.2. Relative quantum yield values (Φ_{Yb}) measured for Yb(BTC)(H_2O) MOFs* synthesized with various amount of sodium acetate.

	0 eq. NaOAc	**1 eq. NaOAc**	**2 eq. NaOAc**	**3 eq. NaOAc**	**3.5 eq. NaOAc**
λ_{ex} = 285 nm	$2.0(\pm0.6)\times10^{-2}$	$2.0(\pm0.6)\times10^{-2}$	$1.8(\pm0.7)\times10^{-2}$	$1.6(\pm0.5)\times10^{-2}$	$1.4(\pm0.6)\times10^{-2}$
λ_{ex} = 355 nm	$9(\pm3)\times10^{-4}$	$1.2(\pm0.4)\times10^{-3}$	$1.3(\pm0.4)\times10^{-3}$	$1.0(\pm0.4)\times10^{-3}$	$1.6(\pm0.6)\times10^{-3}$

*MOFs as a crystalline solid under DMF

Experimental luminescence decay curves were collected for all of the Yb(BTC)(H_2O) MOFs, and the results are summarized in the Table 5.3. Each curve was best fit to a mono-

exponential decay which is indicative of a single environment for the Yb^{3+} cations in the Yb(BTC)(H_2O) MOFs. The calculated Yb^{3+} lifetime values were similar for the Yb(BTC)(H_2O) MOFs synthesized with different amounts of NaOAc. Such results demonstrate that the size of these Yb(BTC)(H_2O) MOFs does not affect the position or the protection of Yb^{3+} in the crystal. In our group we have previously observed[17,19] two luminescence lifetimes for each lanthanide coordination site in MOFs where lanthanide cations are the metal connecting the backbone ligands. We rationalized that the longer value was associated with the cations located in the interior of the MOF and the shorter value was associated with lanthanide cations located at the surface of the MOFs which were more exposed to sources of non-radiative deactivations. We were surprised not to observe a similar situation with this new system. One hypothesis is that the signal that corresponds to the shorter-lived lanthanide cations located on the surface of the MOF has a sufficiently low intensity that is below the detection capability of our equipment.

Table 5.3. Luminescence lifetimes (τ) recorded for Yb(BTC)(H_2O) MOFs* synthesized with various amount of sodium acetate.

	0 eq. NaOAc	**1 eq. NaOAc**	**2 eq. NaOAc**	**3 eq. NaOAc**	**3.5 eq. NaOAc**
τ_1† (ns)	9.09(±0.03)	9.15(±0.06)	9.15(±0.04)	9.09(±0.04)	8.9(±0.4)

*MOFs as a crystalline solid under DMF; †λ_{ex} = 354 nm

Excitation and emission spectra recorded for the nanoMOFs under water produced markedly lower intensities in comparison to the respective measurements performed in DMF. Such results can be explained by the exposure of the Yb^{3+} cations to the presence of an increased number of quenching –OH vibrations. As a consequence, while the Yb^{3+} emission band upon

excitation at 285 nm was easily observed, it was very difficult to discriminate the emission band from the background when exciting further red at 355 nm (Figures 5.19-5.22).

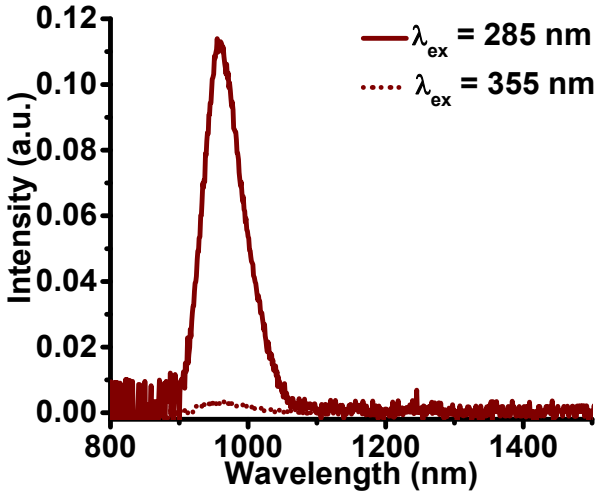

Figure 5.19. Emission spectra for Yb(BTC)(H_2O) nanoMOF (synthesized with 1 eq. NaOAc) in H_2O.

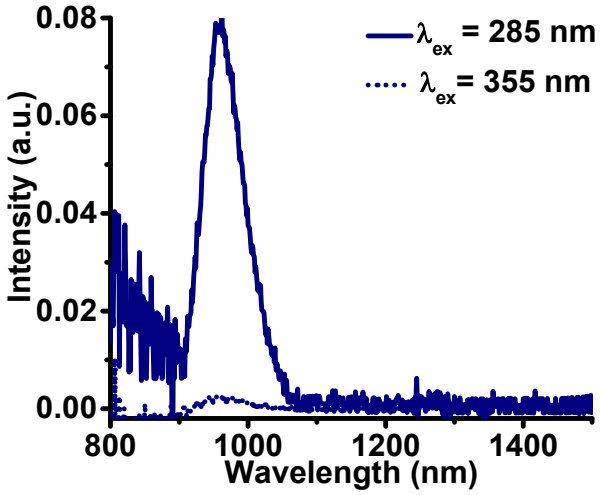

Figure 5.20. Emission spectra for Yb(BTC)(H_2O) nanoMOF (synthesized with 2 eq. NaOAc) in H_2O.

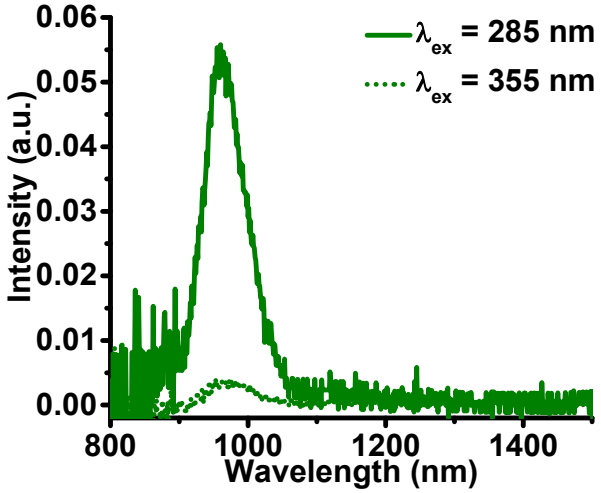

Figure 5.21. Emission spectra for Yb(BTC)(H_2O) nanoMOF (synthesized with 3 eq. NaOAc) in H_2O.

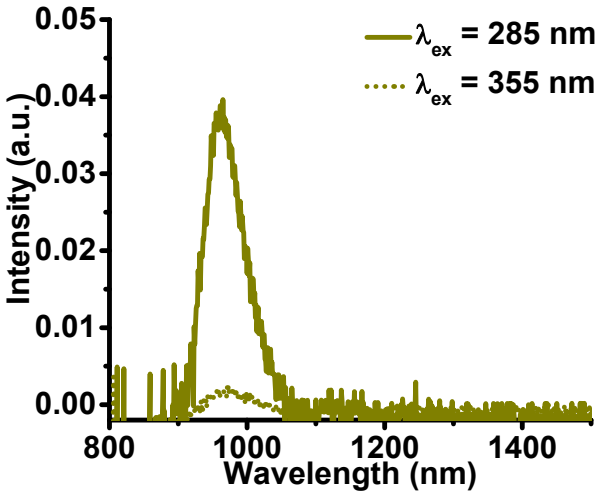

Figure 5.22. Emission spectra for Yb(BTC)(H_2O) nanoMOF (synthesized with 3.5 eq. NaOAc) in H_2O.

5.3.4 4-hydroxyl-1-(4-methyl-2-sulfoanilino)-anthraquinone

We have been able to synthesize a new family of nanoMOFs, the size of which makes them promising imaging agents for biological analysis as they should have minimal interactions in biological systems. Nevertheless, the high energy excitation wavelength of BTC poses a serious problem as such photons will strongly interact with and possibly damage biological systems to be analyzed. We therefore decided to evaluate an unpreceded sensitization strategy. It was hypothesized that by sequestering a dye with a more biologically friendly absorption wavelength within the pores of the nanoMOF, it would be possible to excite the dye and have it act as the antennae to sensitize the Yb^{3+}. The dye that was selected on the basis of its absorption and

relative solubility in water was 4-hydroxyl-1-(4-methyl-2-sulfoanilino)-anthraquinone (4hAQ, Figure 5.23).

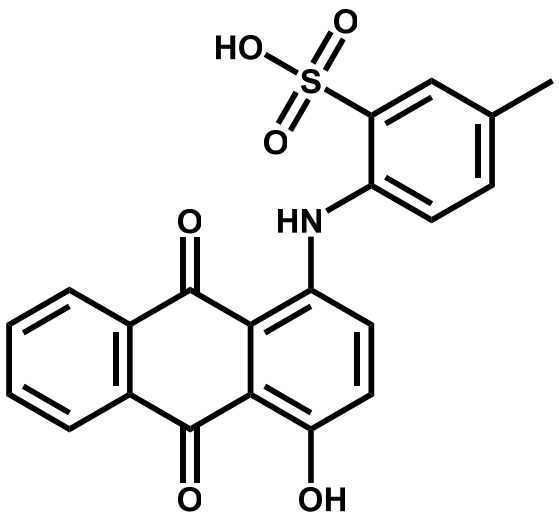

Figure 5.23. Structure of 4-hydroxyl-1-(4-methyl-2-sulfoanilino)-anthraquinone (4hAQ).

An absorption spectrum of 4hAQ was collected in EtOH (50 μg/mL), and a large band with an apparent maximum at 600 nm was observed. Upon the addition of small amounts of 7.5 mM NaOH the absorption increases and a shoulder of the main band appears around 635 nm (Figure 5.24), an indication that the electronic structure of this chromophore is significantly affected by the pH of the solution.

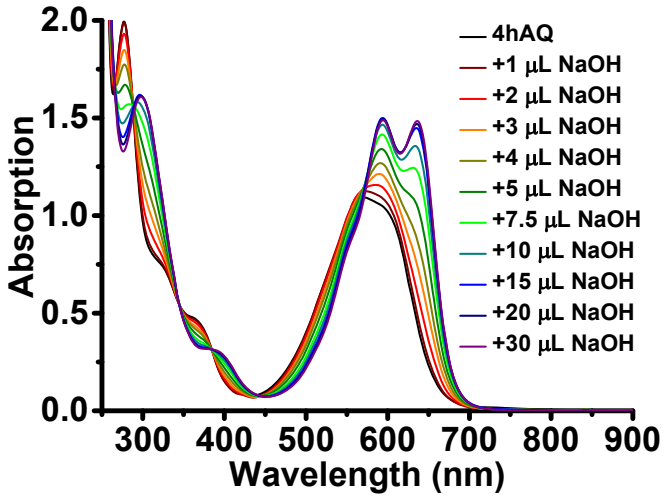

Figure 5.24. Absorption spectra of a solution of 4hAQ (50 µg/mL) in EtOH to which was added various amounts of a 7.5 mM NaOH solution.

Fluorescence spectra of 4hAQ were collected in EtOH (10 µg/mL) with the addition of 10 µL of 7.5 mM NaOH (Figure 5.25). The absorption band matches well with the excitation spectra collected monitoring the emission at 710 nm. Excitation in the visible region results in the generation of an emission band centered at 675 nm.

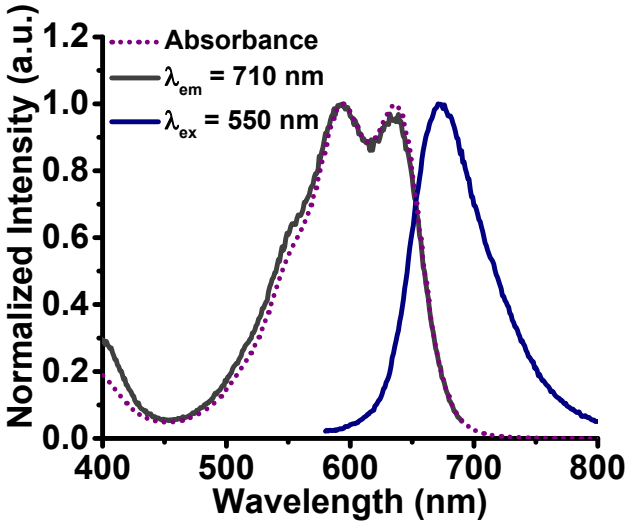

Figure 5.25. Excitation and emission spectra of 4hAQ in EtOH, overlaid with the absorption spectrum from Figure 5.24 (+30 μL NaOH).

5.3.5 Shifting the excitation wavelength

A 1 mg/mL suspension of Yb(BTC)(H_2O) nanoMOF (synthesized with 3 equivalents of NaOAc) in EtOH was incubated with a 100 μg/mL solution of 4hAQ in EtOH to create a new material, Yb(BTC)(H_2O)+4hAQ which is blue in appearance (Figure 5.26).

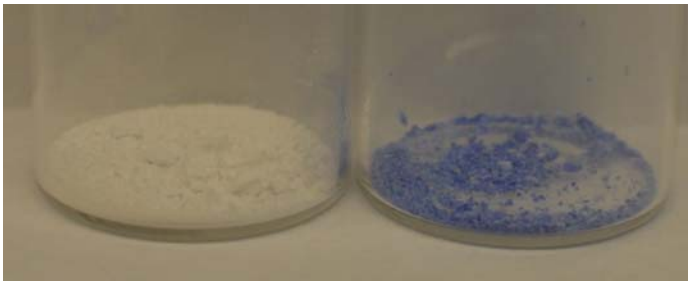

Figure 5.26. Picture comparing the colors of Yb(BTC)(H_2O) nanoMOF (*left,* white) and Yb(BTC)(H_2O)+4hAQ (*right*, blue).

EtOH was chosen as solvent due to the solubility of 4hAQ and the ability to maintain a suspension of the nanoMOF during the incubation period. Different concentrations of 4hAQ for incubation were tested. The use of higher concentrations of 4hAQ did not result in increased efficiency of sensitization, as determined by comparing the intensity of excitation spectra of the resulting Yb(BTC)(H_2O)+4hAQ (excitation band at 630 nm) while monitoring the emission signal at 980 nm (Figure 5.27) and alternately monitoring the Yb^{3+} emission at 980 nm upon excitation at 278 nm (Figure 5.28). Since the Yb^{3+} cation does not have absorbing levels in the ultraviolet-visible (UV-vis) region its emission can only be the result of sensitization through the antennae effect. Therefore the persistence of emission signal upon ligand excitation is a good indicator that the ligand is in close proximity to the Yb^{3+} and the nanoMOF remains intact.

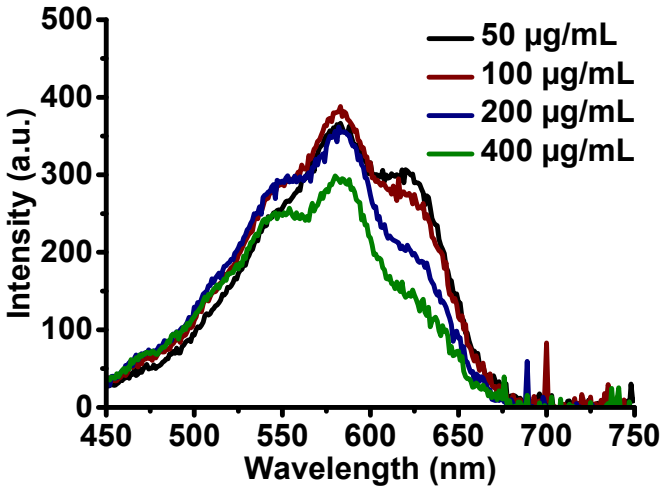

Figure 5.27. Excitation spectra recorded upon monitoring the emission signal of Yb^{3+} (λ_{em} = 980 nm) for Yb(BTC)(H_2O)+4hAQ obtained by incubation with various concentrations of 4hAQ.

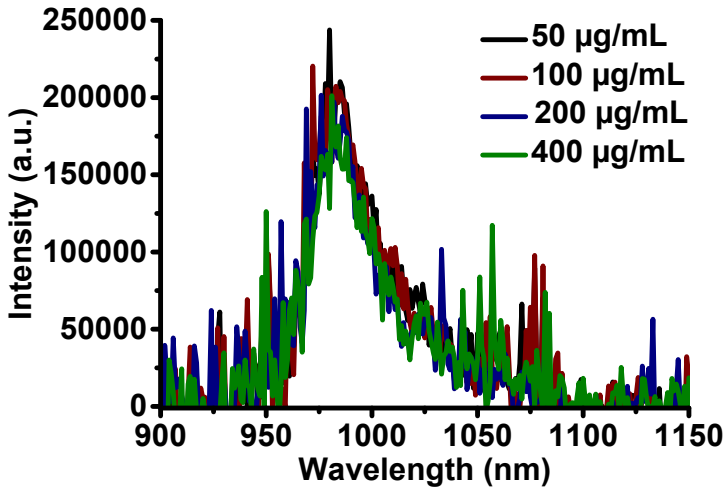

Figure 5.28. Emission spectra upon excitation of the BTC (λ_{ex} = 278 nm) for Yb(BTC)(H_2O)+4hAQ obtained by incubation with various concentrations of 4hAQ.

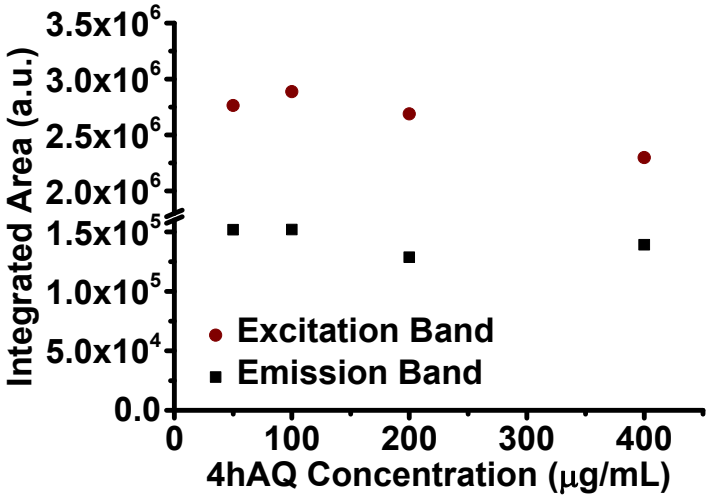

Figure 5.29. Plot representing both the integration of the excitation band centered at 600 nm monitoring the Yb^{3+} emission at 980 nm (*see Figure 5.27*) and the integration of the sharp Yb^{3+} emission band at 980 nm upon excitation at 278 nm (*see Figure 5.28*) versus different incubation concentrations of 4hAQ.

5.3.6 Physical characterization of Yb(BTC)(H_2O)+4hAQ

After dye incorporation, a powder X-ray diffraction (PXRD) pattern of Yb(BTC)(H_2O)+4hAQ was collected and compared to the as-synthesized material (Figure 5.30). The PXRD pattern indicates that the material has overall maintained its crystallinity and that the 4hAQ has not affected its long-range order.

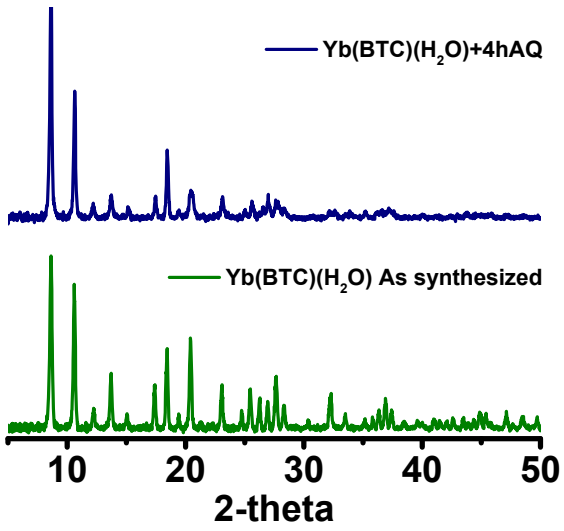

Figure 5.30. Powder X-ray diffraction (PXRD) patterns of the as-synthesized Yb(BTC)(H_2O) nanoMOF and the dye-incorporated Yb(BTC)(H_2O)+4hAQ.

Prior to the incorporation of the dye, the DMF in the pores of the as-synthesized nanoMOF was exchanged with EtOH. In order to be certain that all of the DMF molecules were removed, the nanoMOF was dissolved and analyzed using ^{1}H NMR (Figure 5.31). Three peaks are anticipated for DMF (2.73, 2.89, and 7.96 ppm).[33] The peak at 7.96 ppm was not observed, and the peak at 2.73 was artificially inflated by the presence of a solvent contaminant (Figure 5.32). Comparison of the integration of the peak assigned to the three protons of BTC at 8.63 ppm to the DMF -CH_3 peak at 2.90 ppm revealed that there were less than 0.01 DMF molecules per BTC which can be considered a negligible amount. This fact is important because the complete removal of DMF solvent means that no nitrogen is present. Therefore, after the incorporation of the dye, any nitrogen detected via elemental analysis can be attributed to the 4hAQ.

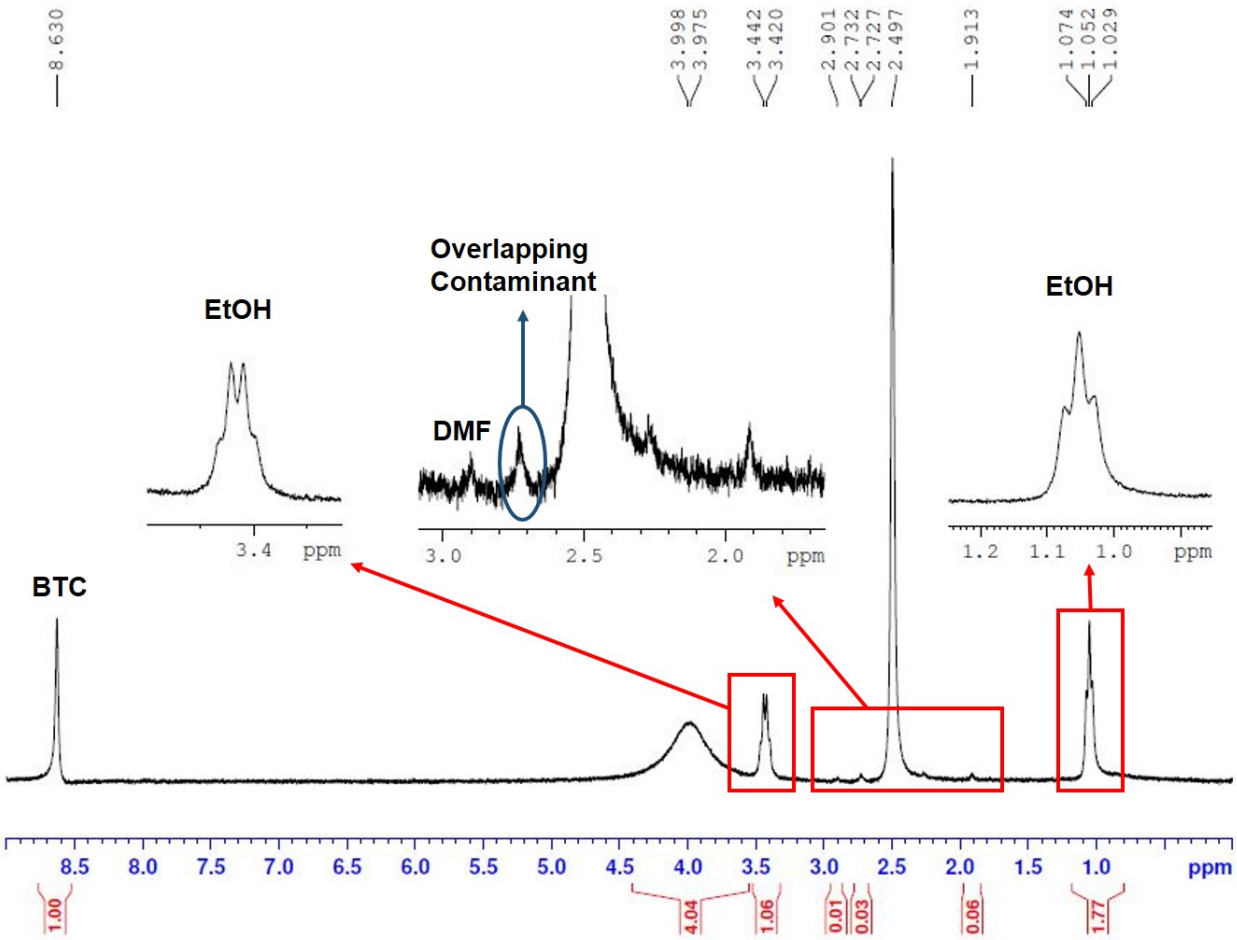

Figure 5.31. ^{1}H NMR spectrum and peak assignments for the ethanol exchanged Yb(BTC)(H_2O)·EtOH nanoMOF in DCl/DMSO-d_6.

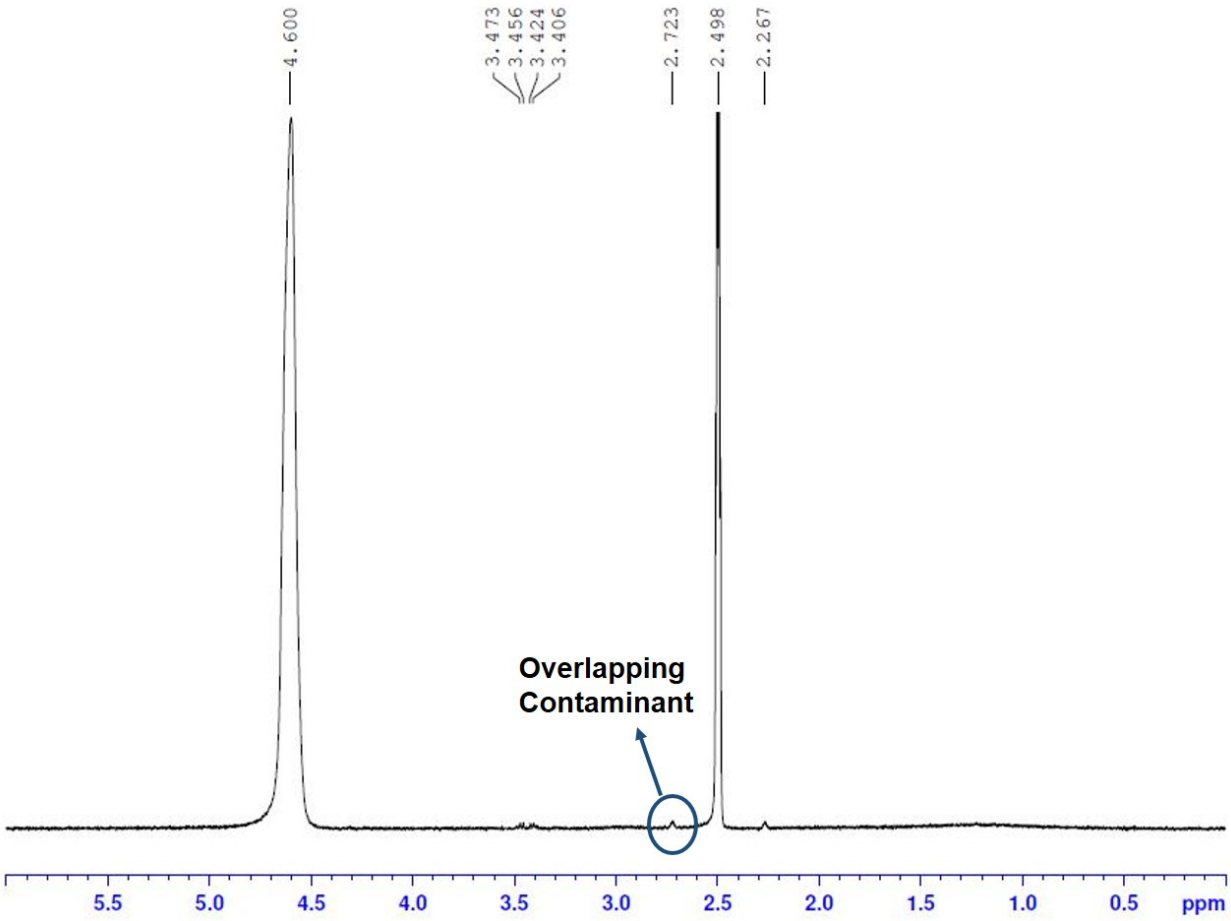

Figure 5.32. ^{1}H NMR spectrum of the solvent DCl/DMSO-d_6 identifying the contaminant which overlaps with the anticipated DMF peak at 2.7 ppm.

Likewise, ^{1}H NMR spectra were collected for the free 4hAQ and for the Yb(BTC)(H_2O)+4hAQ. The position and integration of peaks in the 4hAQ spectrum correspond to the structure (Figures 5.33, 5.34). The 4hAQ is not observable in the spectrum for the Yb(BTC)(H_2O)+4hAQ (Figure 5.35). Therefore, this technique cannot be used to quantify the amount of 4hAQ present in the Yb(BTC)(H_2O)+4hAQ.

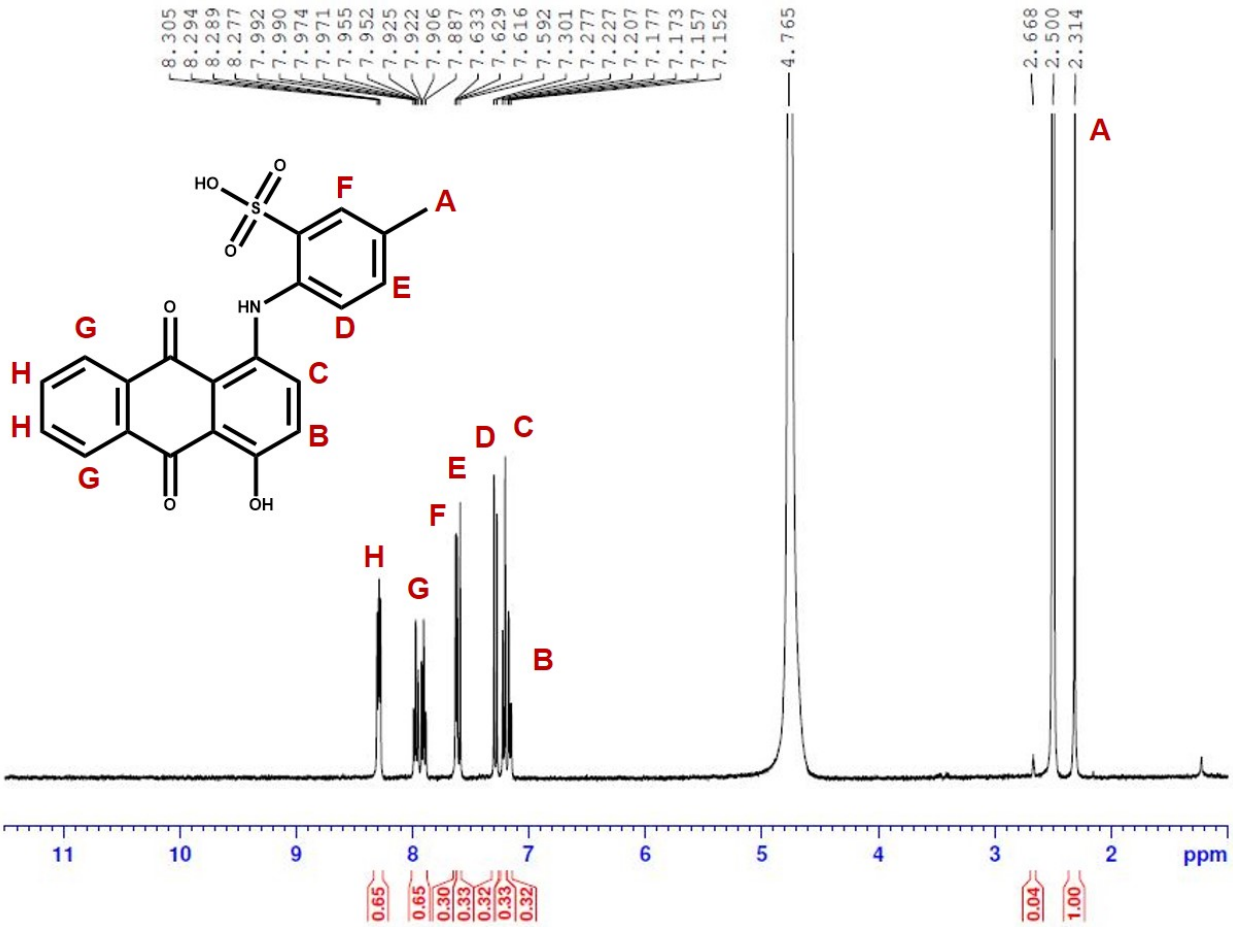

Figure 5.33. ^{1}H NMR spectrum and peak assignments for 4hAQ in DCl/DMSO-d_6.

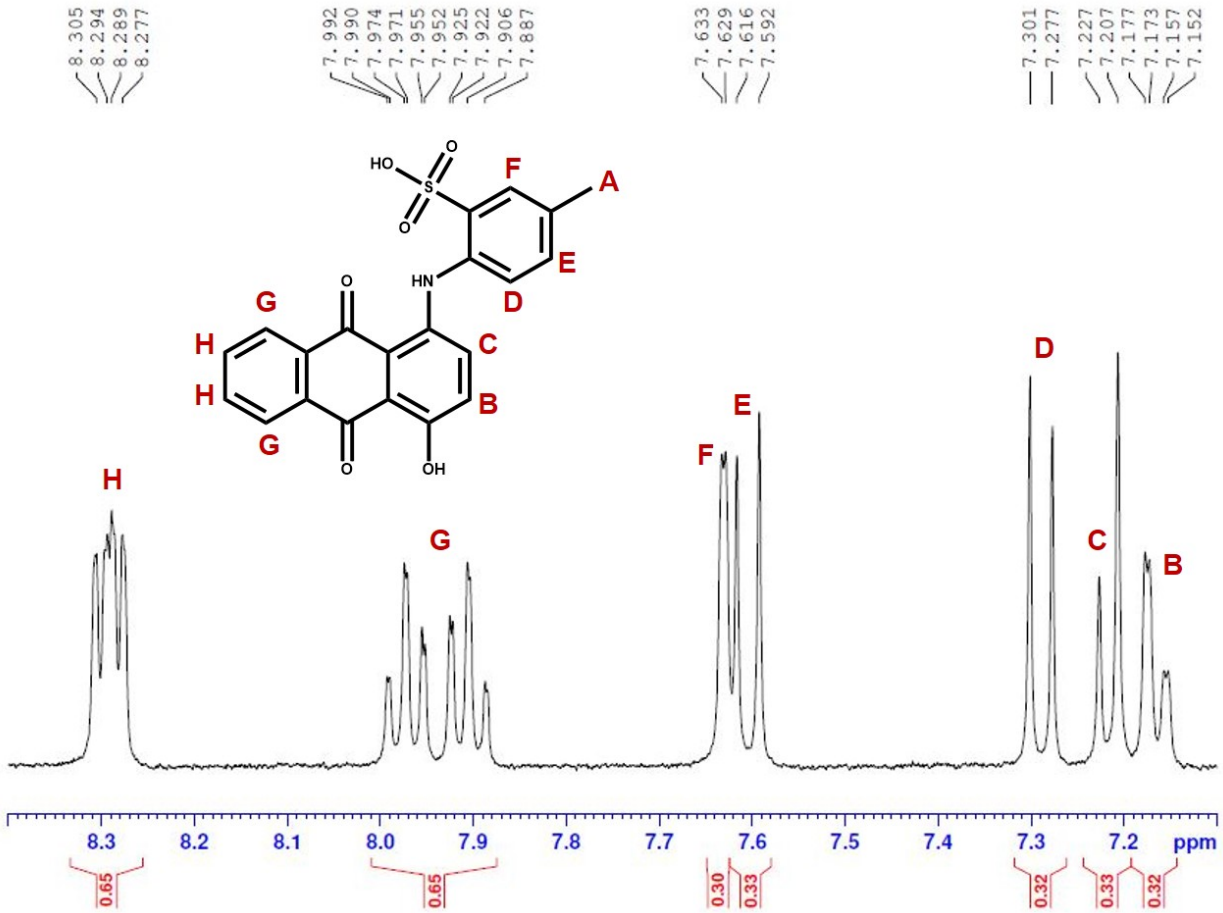

Figure 5.34. ^{1}H NMR spectrum and peak assignments for 4hAQ in DCl/DMSO-d_6, zoomed in on the 7.1-8.4 ppm region.

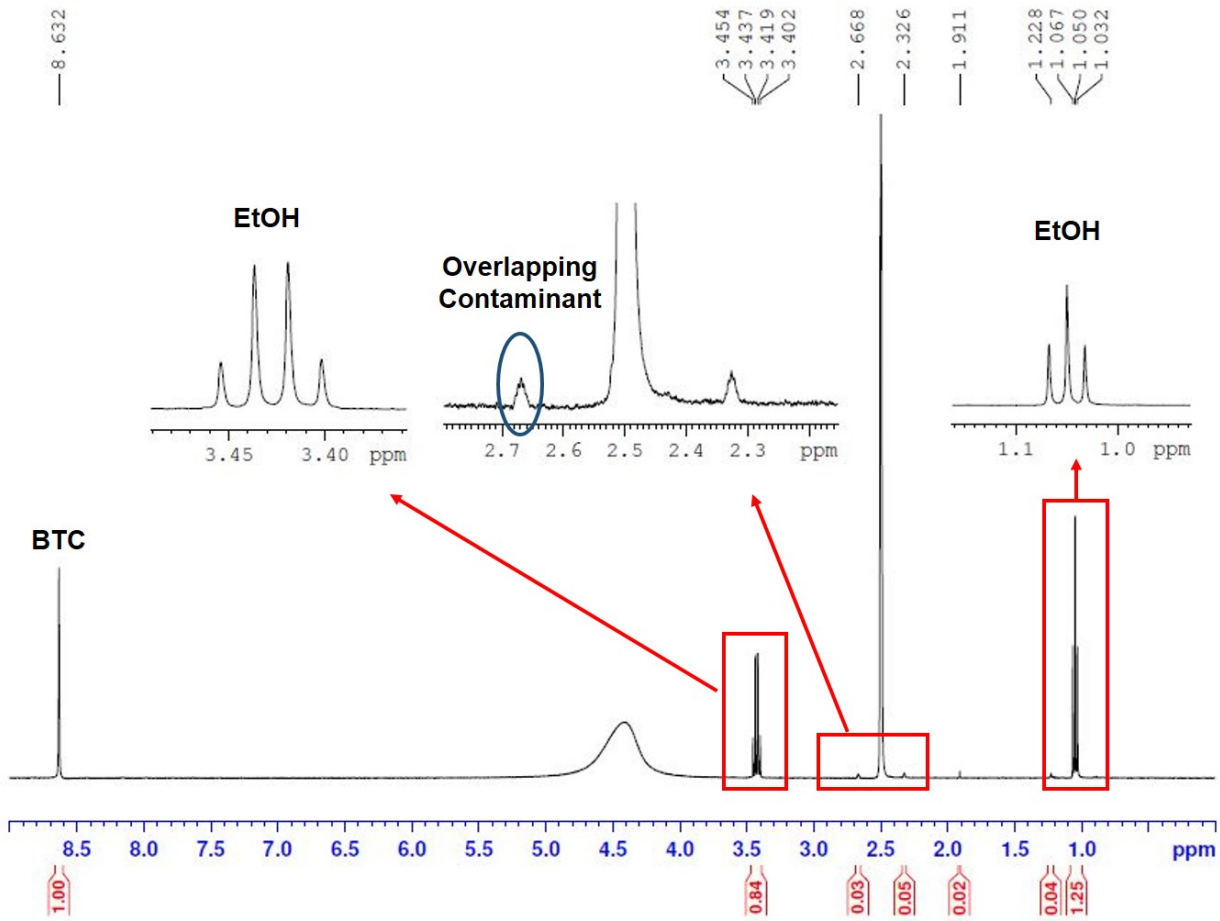

Figure 5.35. ^{1}H NMR spectrum and peak assignments for Yb(BTC)(H_2O)+4hAQ in DCl/DMSO-d_6 with no observable 4hAQ peaks.

Aanother approach to quantify the 4hAQ in the nanoMOF is thermogravimetric analysis (TGA) coupled with elemental analysis (EA). A TGA plot for the Yb(BTC)(H_2O)+4hAQ was compared to that of the ethanol exchanged (Yb(BTC)(H_2O)·EtOH) nanoMOF and the as-synthesized Yb(BTC)(H_2O)·DMF nanoMOF (Figure 5.36). The weight loss percentage of Yb(BTC)(H_2O)+4hAQ was smaller than that of Yb(BTC)(H_2O)·EtOH, which was expected, given that the dye-incorporated material should have a larger molar mass. The percent weight loss and elemental analysis of the EtOH exchanged material matched well with the calculated

values, with the exception of the nitrogen value (calculated, 0.00; found, 0.17). The experimental elemental analysis for Yb(BTC)(H_2O)+4hAQ was 28.26% C, 1.77% H, and 0.13% N. The fact that the experimental percent nitrogen was lower for this material than for the ethanol exchanged material (which contained no nitrogen) is a clear indication that elemental analysis is not a suitable method for the quantification of the small amount of 4hAQ present.

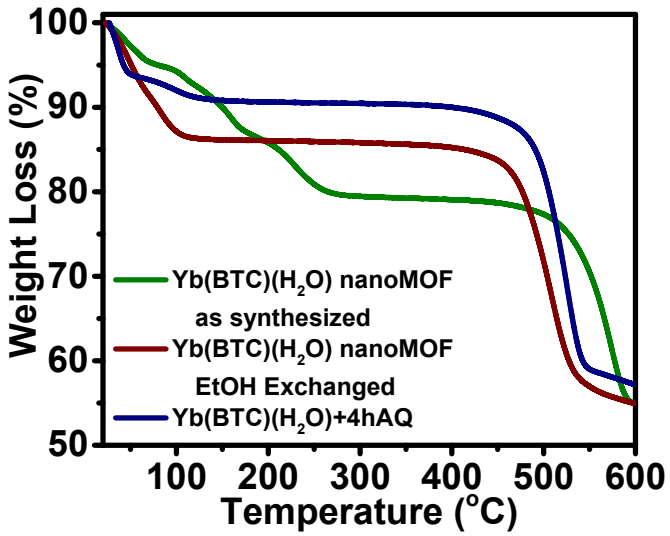

Figure 5.36. Thermogravimetric analysis (TGA) of the as-synthesized Yb(BTC)(H_2O)·DMF nanoMOF (green), ethanol exchanged Yb(BTC)(H_2O)·EtOH nanoMOF (red), and Yb(BTC)(H_2O)+4hAQ (blue).

Nitrogen isotherms were collected for Yb(BTC)(H_2O)·EtOH nanoMOF and Yb(BTC)(H_2O)+4hAQ at 77 K (Figure 5.37) to estimate the loading with 4hAQ. As expected, type I isotherms were observed with slightly lower nitrogen uptake for the dye-incorporated material at 1 bar. The calculated BET surface area of the Yb(BTC)(H_2O)·EtOH nanoMOF was 736 m^2/g; it was slightly lower, 544 m^2/g, for Yb(BTC)(H_2O)+4hAQ. This loss in surface area

can be attributed to the dye occupying part of the pore space in the nanoMOFs. However, porosity, albeit lower, is retained through the soaking with the dye, as evidenced by the type I isotherm.

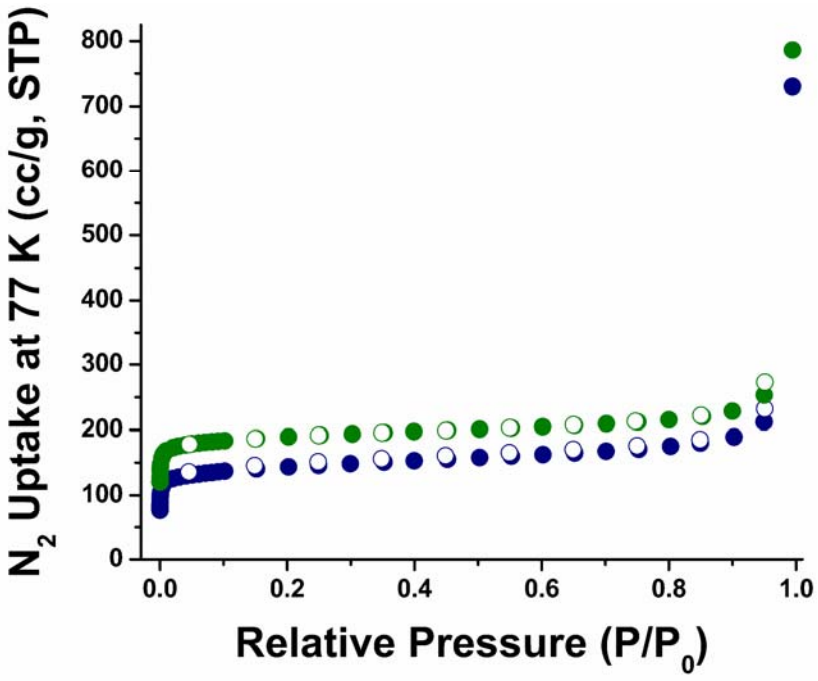

Figure 5.37. Nitrogen isotherm recorded at 77 K for Yb(BTC)(H_2O)·EtOH nanoMOF (green) and Yb(BTC)(H_2O)+4hAQ (blue). Adsorption (filled circles) and desorption (empty circles).

Thus far these experiments have all supported the assumption that the 4hAQ is indeed present in the Yb(BTC)(H_2O)+4hAQ material, but failed to quantify the amount of 4hAQ present.

UV-vis absorption spectroscopy was then used to quantify the amount of 4hAQ in the Yb(BTC)(H_2O)+4hAQ. In order to minimize the matrix effect, all of the 4hAQ standards were prepared using the same solvent system that would be required to dissolve the

Yb(BTC)(H_2O)+4hAQ. For NMR dissolution is accomplished by a mixture of DCl and DMSO-d_6; for UV-vis HCl and DMSO (in the same ratio) were used. Anthraquinone standards ranging in concentration from 5×10^{-7} to 1×10^{-5} M were prepared (Figure 5.38). Additionally, 4.5 mg of Yb(BTC)(H_2O)+4hAQ were dissolved in 2.0 mL of the HCl/DMSO solvent (Figure 5.38). Overlaid absorption spectra with apparent maxima at 590 nm (Figure 5.39) show clearly that as the concentration of 4hAQ increases the absorbance signal increases, and that the Yb(BTC)(H_2O)+4hAQ solution absorption falls within the range of the standard solutions. The absorbance at 590 nm was plotted against the concentration and fit with a linear trendline (Figure 5.39). The trendline (y = 88724x – 0.00131) was used to calculate the number of moles of 4hAQ present in the Yb(BTC)(H_2O)+4hAQ solution and subsequently to determine the molar ratio, 1:0.078, Yb(BTC)(H_2O):4hAQ.

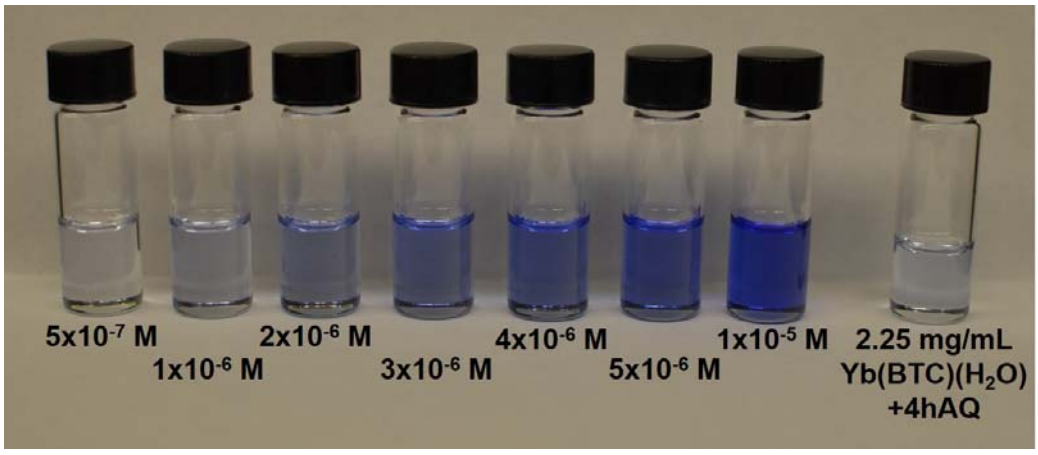

Figure 5.38. Picture of the 4hAQ standard solutions and the 2.25 mg/mL Yb(BTC)(H_2O)+4hAQ solution that were analyzed via UV-vis absorption spectroscopy.

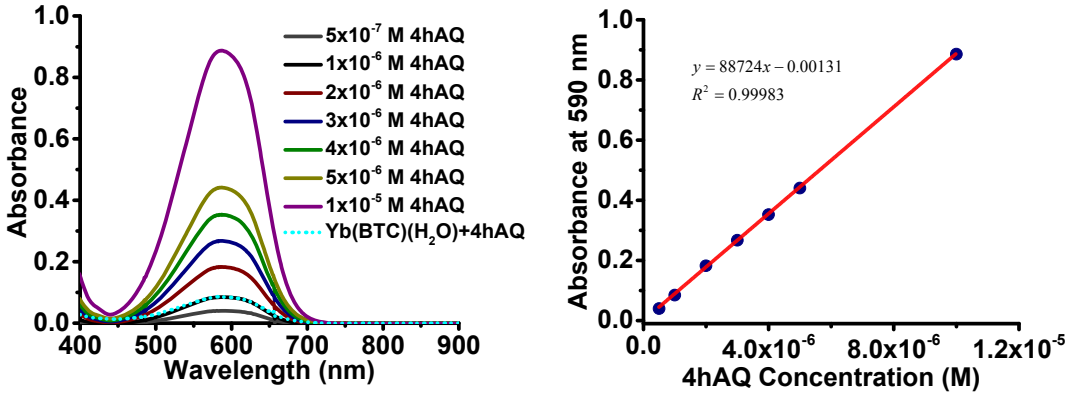

Figure 5.39. Absorption spectra of the 4hAQ standard solutions and the 2.25 mg/mL Yb(BTC)(H_2O)+4hAQ solution (*left*) and the resulting calibration curve based on the absorbance at 590 nm (*right*).

These experiments collectively reveal that there is very little 4hAQ present in Yb(BTC)(H_2O)+4hAQ. Despite this there is still a sufficient amount for the 4hAQ to sensitize the Yb^{3+} and generate NIR emission (*see Section 5.3.7)*. The exact location of the 4hAQ is also unclear. The dye is a fairly large molecule and it seems physically improbable that it could be entirely contained within the pores. It may, however, be partially inserted at the entrance of a pore or it may be "stuck" to the surface of the crystal.

5.3.7 Spectroscopic characterization of Yb(BTC)(H_2O)+4hAQ

The excitation spectrum recorded for Yb(BTC)(H_2O)+4hAQ in EtOH (Figure 5.40) shows that upon incorporation of the 4hAQ chromophore, a large excitation band with an apparent maximum at 600 nm is observed that was not present in the absence of 4hAQ (Figure 5.41) and

which matches well with the absorption band of pure 4hAQ (Figure 5.24). The emission spectra (Figure 5.40) indicated that Yb^{3+} emission signal can obtained by excitation through either the BTC ligand (λ_{ex} = 278 nm) or through the 4hAQ (λ_{ex} = 600 nm and 650 nm).

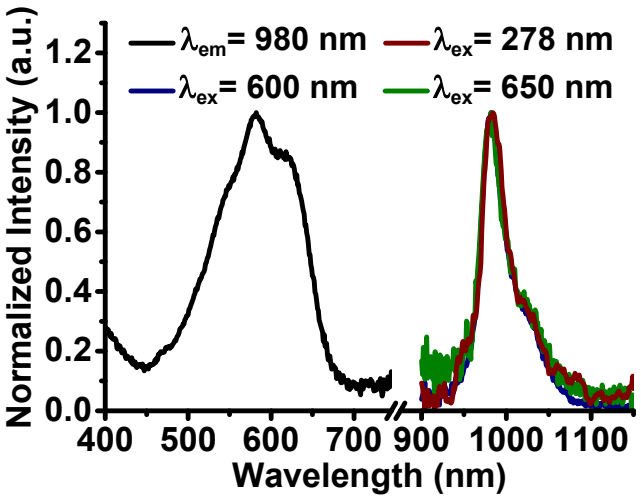

Figure 5.40. Excitation spectrum upon monitoring the Yb^{3+} signal (λ_{em} = 980 nm) and emission spectra of Yb(BTC)(H_2O)+4hAQ in EtOH upon excitation through both the BTC ligand (λ_{ex} = 278 nm) and the 4hAQ (λ_{ex} = 600 nm and 650 nm).

Control luminescence spectra were also recorded for the unmodified Yb(BTC)(H_2O) nanoMOF in EtOH. As observed in both DMF and H_2O, the band with the highest intensity present in the excitation spectrum (monitoring the Yb^{3+} signal, λ_{em} = 980) was located at 278 nm. In EtOH additional and significantly less intense bands were present at 400 nm and 600 nm (Figure 5.41). Excitation through the ligand (λ_{ex} = 278 nm) resulted in the expected Yb^{3+} emission centered at 980 nm. In the absence of 4hAQ, only a very small emission of Yb^{3+} can

be detected when exciting at 600 nm, only 3% of the intensity of the signal recorded in presence of 4hAQ (Figure 5.41).

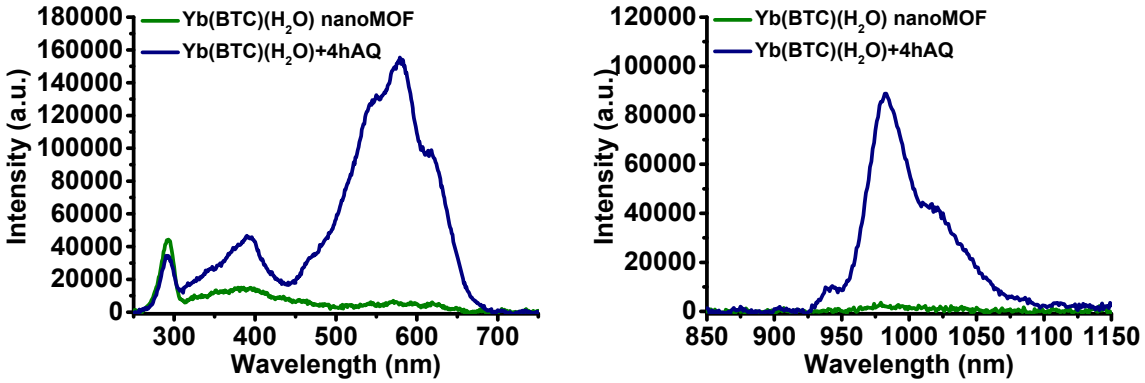

Figure 5.41. Excitation (λ_{em} = 980 nm, *left*) and emission spectra (λ_{ex} = 600 nm, *right*) of Yb(BTC)(H_2O) nanoMOF and Yb(BTC)(H_2O)+4hAQ in EtOH.

For biological applications, the system must be compatible with aqueous conditions. When Yb(BTC)(H_2O) was placed in water, its Yb^{3+} emission signal decreased by a factor 10 to 15. This observation can be explained by the high number of –OH quenchers from the water molecules and a good accessibility to the Yb^{3+} cations due to the limited ability of this MOF to protect the lanthanide cations.

5.3.8 Coating Yb(BTC)(H_2O)+4hAQ with silica

In order to both increase the Yb^{3+} emission intensity in water and be able to more easily functionalize and tune their biological behavior in the future, a silica shell was added. Yb(BTC)(H_2O)+4hAQ was coated with a silica shell using a sol-gel procedure adapted from the

literature[30] with tetraethyl orthosilicate (TEOS) in a mixture of EtOH and ammonium hydroxide solution (4%). Immediately after the coating, the luminescence of the resulting coated sample was measured in EtOH and compared to that of the uncoated sample (Figure 5.42). After coating with silica, an overall decrease in the intensity of the excitation spectrum was observed.

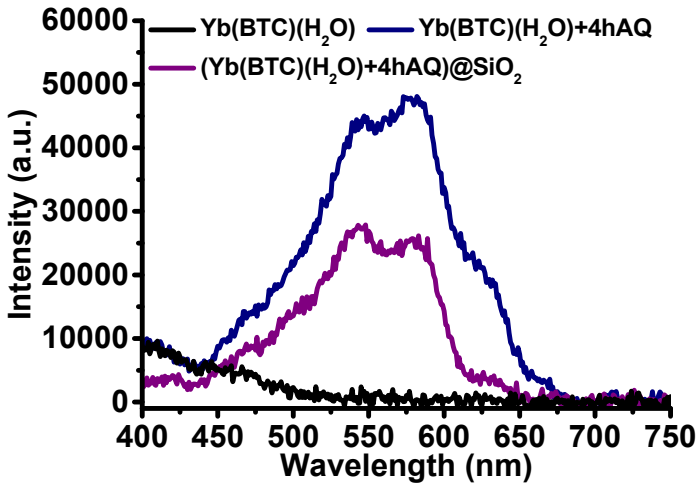

Figure 5.42. Excitation spectra (monitoring the Yb^{3+} signal, λ_{em} = 980 nm) of Yb(BTC)(H_2O) nanoMOFs in EtOH, before (Yb(BTC)(H_2O)) and after (Yb(BTC)(H_2O)+4hAQ) loading with 4hAQ, and after silica coating ((Yb(BTC)(H2O)+4hAQ)@SiO_2).

Then EtOH was removed from the samples and the (Yb(BTC)(H_2O)+4hAQ)@SiO_2 was re-suspended in pure water at a concentration of 1 mg/mL. The luminescence signal was monitored via recording the excitation spectrum (monitoring Yb^{3+}, λ_{em} = 980 nm) over a period of 5 hours (Figure 5.43). After a rapid (less than 4 minutes) initial decrease (loss of about 95% of luminescence) the signal intensity of Yb(BTC)(H_2O)+4hAQ remained stable indicating that quenching is indeed originating from water. A very rapid initial loss of luminescence is also

observed for (Yb(BTC)(H_2O)+4hAQ)@SiO_2, but is limited to a 70% loss of signal (Figure 5.43). After this first step, a slow decrease of luminescence occurs. After 5 hours, the signal is about 20% of the one in EtOH and remains constant. The silica coating is proven effective for protecting the nanoMOF from quenching due to water.

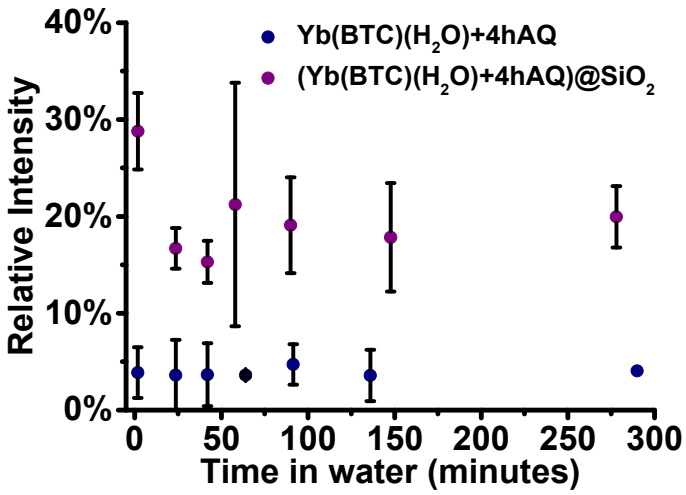

Figure 5.43. Comparison of the relative intensities of the excitation spectra (monitoring Yb^{3+}; λ_{em} = 980) of Yb(BTC)(H_2O)+4hAQ and (Yb(BTC)(H_2O)+4hAQ)@SiO_2 in water over a period of 5 hours. The error bars represent the standard deviation.

The characterization of the silica shell was done using transmission electron microscopy (TEM). The silica shell can be seen clearly around the Yb(BTC)(H_2O)+4hAQ (Figure 5.44). Typical thickness of the coating, 13.0(±4.8) nm, was evaluated by measuring more than 40 areas from 7 independent coating experiments.

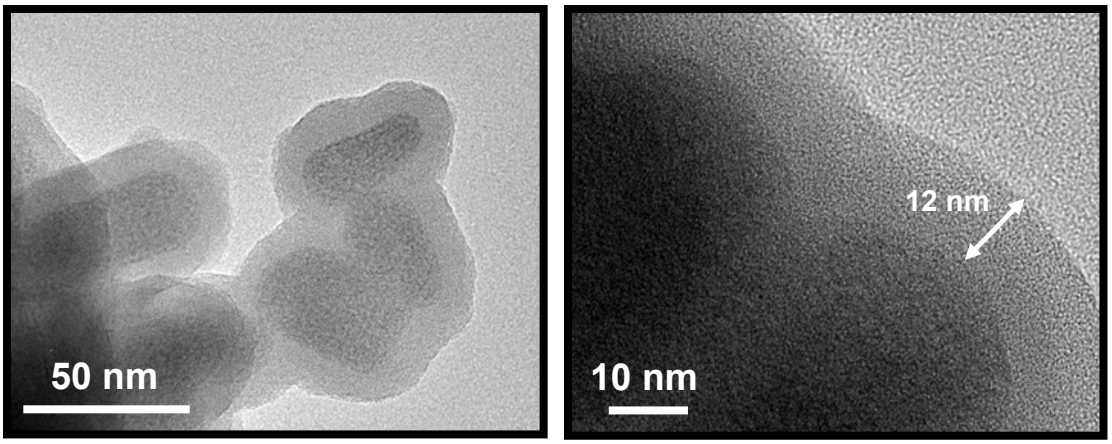

Figure 5.44. Representative transmission electron microscopy (TEM) images of (Yb(BTC)(H_2O)+4hAQ)@SiO_2.

5.3.9 Photobleaching studies

Photobleaching experiments (Figure 5.45) were performed to assess the photostability of (Yb(BTC)(H_2O)+4hAQ)@SiO_2 in 10 mM HEPES buffer (pH 7.4) to estimate its potential as an imaging agent and to compare its performance to commercial organic fluorophores absorbing and emitting in a comparable wavelength range, namely Alexa Fluor 647 (AF647) and indocyanine green (ICG). (Yb(BTC)(H_2O)+4hAQ)@SiO_2 was found to be more resistant to photobleaching than the highly photostable AF647, while ICG was poorly resistant. A similar measurement performed on 4hAQ in 10 mM HEPES buffer (pH 7.4) showed that the free 4hAQ is not resistant to photobleaching and benefits from the protection achieved by its incorporation into the lanthanide nanoMOF. It must be noted that (Yb(BTC)(H_2O)+4hAQ)@SiO_2 was left in HEPES buffer for 4 hours prior to the photobleaching experiment in order to take into account the reduction of luminescence signal due to the penetration of water molecules through the silica

shell. The observed decrease of emission signal is the combination of this effect with that of photobleaching.

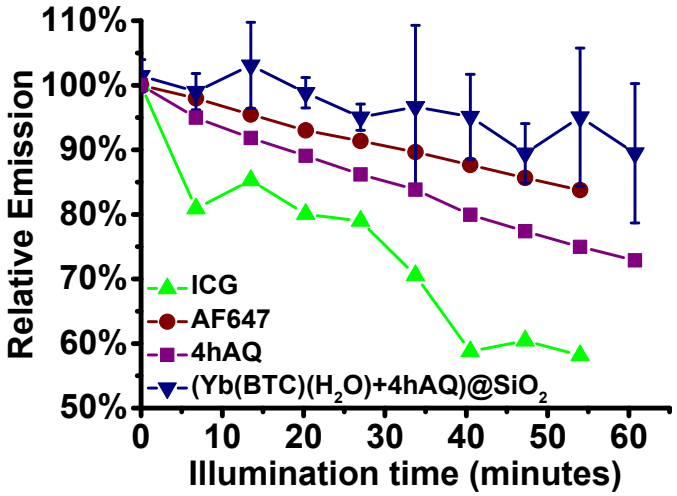

Figure 5.45. Plot comparing the decrease of signal of (Yb(BTC)(H_2O)+4hAQ)@SiO_2, indocyanine Green (ICG), Alexa Fluor 647 (AF647), and 4hAQ (10 mM HEPES buffer). Luminescence data are expressed as percentages derived from the integrated emission signal (λ_{ex} = 580 nm) divided by the integrated signal of the initial spectrum (time = 0 minutes).

5.4 CONCLUSION

We have designed, synthesized and characterized a series of size-controllable Yb(BTC)(H_2O) MOFs which range from long micron-scale needles to nanoscale spheres depending on the amount of NaOAc used during the synthesis. These materials all demonstrate their ability to

generate NIR emission arising from Yb^{3+} when excited at high energy wavelengths (typically 285 nm). The emission in water is significantly lower in intensity than in DMF or EtOH. In order to shift the excitation wavelength to a more biologically friendly lower energy wavelength, 4-hydroxyl-1-(4-methyl-2-sulfoanilino)-anthraquinone (4hAQ) was incorporated into the Yb(BTC)(H_2O) nanoMOF synthesized with 3 equivalents of NaOAc. The 4hAQ absorbs around 600 nm, and exciting the Yb(BTC)(H_2O)+4hAQ at this wavelength results in sensitized NIR Yb^{3+} emission. This material is limited as an imaging agents by its low emission intensity in water. A silica coating was successful in providing efficient protection against quenching. Indeed, the (Yb(BTC)(H_2O)+4hAQ)@SiO_2 exhibits a stronger emission intensity than Yb(BTC)(H_2O)+4hAQ in water over the course of five hours. Additionally, it retains its emission intensity in HEPES buffer better than commercially available organic fluorophores over a time span of one hour as the result of improved protection against photobleaching. This nanoscale material with low energy excitation and emission has great potential to be used as imaging agent for biological analysis and medical diagnostics.

5.5 REFERENCES

(1) Mahmood, U.; Weissleder, R. *Mol. Cancer Ther.* **2003**, *2*, 489-496.
(2) Weissleder, R.; Ntziachristos, V. *Nat. Med.* **2003**, *9*, 123-128.
(3) Taik Lim, Y.; Kim, S.; Nakayama, A.; Stott, N. E.; Bawendi, M. G.; Frangioni, J. V. *Mol. Imag.* **2003**, *2*, 50-64.
(4) Frangioni, J. V. *Curr. Opin. Chem. Biol.* **2003**, *7*, 626-634.
(5) Altinoğlu, E. İ.; Adair, J. H. *WIREs Nanomed. Nanobiotechnol.* **2010**, *2*, 461-477.
(6) Pansare, V. J.; Hejazi, S.; Faenza, W. J.; Prud'homme, R. K. *Chem. Mater.* **2012**, *24*, 812-827.
(7) Guo, Z.; Park, S.; Yoon, J.; Shin, I. *Chem. Soc. Rev.* **2014**, *43*, 16-29.
(8) Altinoğlu, E. I.; Russin, T. J.; Kaiser, J. M.; Barth, B. M.; Eklund, P. C.; Kester, M.; Adair, J. H. *ACS Nano* **2008**, *2*, 2075-2084.

(9) Muddana, H. S.; Morgan, T. T.; Adair, J. H.; Butler, P. J. *Nano Lett.* **2009**, *9*, 1559-1566.
(10) Chan, W. C. W.; Nie, S. *Science* **1998**, *281*, 2016-2018.
(11) Cai, W.; Hsu, A.; Li, Z.-B.; Chen, X. *Nanoscale Res. Lett.* **2007**, *2*, 265 - 281.
(12) Sargent, E. H. *Adv. Mater.* **2005**, *17*, 515-522.
(13) Faulkner, S.; Pope, S. J. A.; Burton-Pye, B. P. *Appl. Spectrosc. Rev.* **2005**, *40*, 1 - 31.
(14) Eliseeva, S. V.; Bünzli, J.-C. G. *Chem. Soc. Rev.* **2010**, *39*, 189-227.
(15) Alcala, M. A.; Shade, C. M.; Uh, H.; Kwan, S. Y.; Bischof, M.; Thompson, Z. P.; Gogick, K. A.; Meier, A. R.; Strein, T. G.; Bartlett, D. L.; Modzelewski, R. A.; Lee, Y. J.; Petoud, S.; Brown, C. K. *Biomaterials* **2011**, *32*, 9343-9352.
(16) Nockemann, P.; Beurer, E.; Driesen, K.; Van Deun, R.; Van Hecke, K.; Van Meervelt, L.; Binnemans, K. *Chem. Commun.* **2005**, 4354-4356.
(17) Foucault-Collet, A.; Gogick, K. A.; White, K. A.; Villette, S.; Pallier, A.; Collet, G.; Kieda, C.; Li, T.; Geib, S. J.; Rosi, N. L.; Petoud, S. *Proc. Natl. Acad. Sci.* **2013**, *110*, 17199-17204.
(18) Weissman, S. I. *J. Chem. Phys.* **1942**, *10*, 214-217.
(19) White, K. A.; Chengelis, D. A.; Zeller, M.; Geib, S. J.; Szakos, J.; Petoud, S.; Rosi, N. L. *Chem. Commun.* **2009**, 4506-4508.
(20) Chae, H. K.; Siberio-Perez, D. Y.; Kim, J.; Go, Y.; Eddaoudi, M.; Matzger, A. J.; O'Keeffe, M.; Yaghi, O. M. *Nature* **2004**, *427*, 523-527.
(21) McKinlay, A. C.; Morris, R. E.; Horcajada, P.; Férey, G.; Gref, R.; Couvreur, P.; Serre, C. *Angew. Chem., Int. Ed.* **2010**, *49*, 6260-6266.
(22) Huxford, R. C.; Della Rocca, J.; Lin, W. *Curr. Opin. Chem. Biol.* **2010**, *14*, 262-268.
(23) An, J.; Shade, C. M.; Chengelis-Czegan, D. A.; Petoud, S.; Rosi, N. L. *J. Am. Chem. Soc.* **2011**, *133*, 1220-1223.
(24) Horcajada, P.; Chalati, T.; Serre, C.; Gillet, B.; Sebrie, C.; Baati, T.; Eubank, J. F.; Heurtaux, D.; Clayette, P.; Kreuz, C.; Chang, J.-S.; Hwang, Y. K.; Marsaud, V.; Bories, P.-N.; Cynober, L.; Gil, S.; Férey, G.; Couvreur, P.; Gref, R. *Nat. Mater.* **2010**, *9*, 172-178.
(25) Rosi, N. L.; Kim, J.; Eddaoudi, M.; Chen, B.; O'Keeffe, M.; Yaghi, O. M. *J. Am. Chem. Soc.* **2005**, *127*, 1504-1518.
(26) Guo, X.; Zhu, G.; Li, Z.; Sun, F.; Yang, Z.; Qiu, S. *Chem. Commun.* **2006**, 3172-3174.
(27) Gustafsson, M.; Bartoszewicz, A.; Martín-Matute, B.; Sun, J.; Grins, J.; Zhao, T.; Li, Z.; Zhu, G.; Zou, X. *Chem. Mater.* **2010**, *22*, 3316-3322.
(28) Jiang, H.-L.; Tsumori, N.; Xu, Q. *Inorg. Chem.* **2010**, *49*, 10001-10006.
(29) Guo, H.; Zhu, Y.; Wang, S.; Su, S.; Zhou, L.; Zhang, H. *Chem. Mater.* **2012**, *24*, 444-450.
(30) Rieter, W. J.; Taylor, K. M. L.; Lin, W. *J. Am. Chem. Soc.* **2007**, *129*, 9852-9853.
(31) Aebischer, A.; Gumy, F.; Bünzli, J.-C. G. *Phys. Chem. Chem. Phys.* **2009**, *11*, 1346-1353.
(32) Zhang, J.; Badger, P. D.; Geib, S. J.; Petoud, S. *Angew. Chem., Int. Ed.* **2005**, *44*, 2508-2512.
(33) Gottlieb, H. E.; Kotlyar, V.; Nudelman, A. *J. Org. Chem.* **1997**, *62*, 7512-7515.

APPENDIX A

YB-PVDC-3 CRYSTALLOGRAPHIC DATA

A.1 SINGLE CRYSTAL X-RAY DIFFRACTION STUDY FOR YB-PVDC-3

An X-ray crystal structure was determined for $C_{42}H_{41}NO_{12}Yb$, Yb-PVDC-3, using a single crystal on a Bruker Smart Apex CCD diffractometer with graphite-monochromated MoK_α (λ= 0.71073 Å) radiation. The parameters used during the collection of diffraction data are summarized in Table A1. The crystal was mounted in a glass loop with Paratone® N oil and placed in a cold N_2 stream (203 K) for data collection.

Unit-cell parameters and lack of systematic absences indicated Yb-PVDC-3 crystallized in triclinic space groups *P* 1 or *P*-1; centrosymmetric *P*-1 was chosen based on E-values and the successful solution and refinement of the structure. Unit-cell dimensions were derived from the least-squares fit of the angular settings of 1373 reflections. Data were corrected for absorption using the Bruker program SADABS[1]. The structure was solved via direct methods, which located Yb and most of the remaining non-hydrogen atoms. Yb was found to be disordered over at least two sites. The two Yb sites are occupied at 56% and 44%. Remaining non-hydrogen atoms were gradually found from several subsequent different Fourier syntheses. All non-

hydrogen atoms were refined anisotropically excepting O6, O11, C24, C27, O12, N, C40, C41, C42, O10, C39A, C39B, and O13. A total of 47 restraints were applied to optimize the bond lengths, bond angles, and atomic displacement parameters. Idealized atom positions were calculated for all hydrogen atoms (*d*-(Cmethyl-H) = 0.97 Å, *d*-(Cphenyl-H) = 0.94 Å), *U* = 1.2 *Uiso* of attached carbon). The coordinated DMF seen in other Ln-PVDC isomorphs could not be resolved in this structure, probably because of overlap with the disordered Yb sites.

All computer programs used in the data collection and refinements are contained in the Bruker program packages SMART (vers. 5.625), SAINT (vers. 6.22)[1], and SHELXTL (vers. 6.10)[2].

Table A.1. Crystal data and structure refinement for Yb-PVDC-3.

Identification code	Yb-PVDC-3	
Empirical formula	C42 H41 N O12 Yb	
Formula weight	924.80	
Temperature	203(2) K	
Wavelength	0.71073 Å	
Crystal system	Triclinic	
Space group	P-1	
Unit cell dimensions	a = 8.811(2) Å	α= 77.152(5)°
	b = 10.951(3) Å	β= 87.703(5)°
	c = 21.944(5) Å	γ = 78.251(6)°
Volume	2021.1(9) $Å^3$	
Z	2	
Density (calculated)	1.520 Mg/m^3	
Absorption coefficient	2.377 mm^{-1}	
F(000)	932	
Crystal size	0.30 x 0.13 x 0.08 mm^3	
Theta range for data collection	1.90 to 23.33°	
Index ranges	-9<=h<=9, -12<=k<=12, -24<=l<=24	
Reflections collected	13440	
Independent reflections	5809 [R(int) = 0.0628]	
Completeness to theta = 23.33°	99.5 %	
Absorption correction	Multi-Scan (SADABS)	
Max. and min. transmission	0.8326 and 0.5358	
Refinement method	Full-matrix least-squares on F^2	
Data / restraints / parameters	5809 / 47 / 469	
Goodness-of-fit on F^2	1.043	
Final R indices [I>2sigma(I)]	R1 = 0.1240, wR2 = 0.2941	
R indices (all data)	R1 = 0.1946, wR2 = 0.3318	
Largest diff. peak and hole	2.609 and -1.103 e.$Å^{-3}$	

Table A.2. Atomic coordinates (x 10^4) and equivalent isotropic displacement parameters ($Å^2$x 10^3) for Yb-PVDC-3. U(eq) is defined as one third of the trace of the orthogonalized U^{ij} tensor.

	x	y	z	U(eq)
Yb	2868(2)	4658(4)	4952(1)	85(1)
Yb'	2770(3)	3647(6)	4893(1)	95(2)
O(1)	1350(19)	3760(20)	5765(6)	147(7)
C(1)	80(30)	4220(30)	5975(8)	96(8)
C(2)	-150(30)	3710(20)	6692(8)	79(6)
O(2)	-880(20)	5071(18)	5680(6)	114(6)
O(3)	-5318(12)	2141(10)	9236(4)	61(3)
C(3)	-1370(20)	4356(18)	6963(7)	73(5)
O(4)	-862(12)	1061(10)	11080(4)	61(3)
C(4)	-1650(20)	3916(14)	7592(6)	62(5)
C(5)	-762(18)	2814(13)	7925(6)	48(4)
O(5)	-6970(30)	-3110(30)	14275(7)	267(18)
C(6)	480(20)	2199(17)	7628(7)	73(5)
O(6)	-4643(15)	-2821(12)	14550(6)	92(4)
C(7)	790(20)	2640(20)	7018(8)	82(6)
O(7)	5710(30)	4594(18)	4345(9)	229(11)
C(8)	-1050(20)	2284(14)	8595(7)	61(4)
O(8)	3980(20)	3600(20)	4070(8)	199(10)
C(9)	-2431(18)	2474(13)	8855(6)	51(4)
C(10)	-2732(18)	2043(13)	9521(6)	46(4)
C(11)	-4247(18)	1875(13)	9702(6)	50(4)
O(11)	1960(30)	2110(20)	4938(12)	203(9)
C(12)	-4569(16)	1460(13)	10342(6)	46(3)
C(13)	-3446(18)	1186(12)	10788(6)	47(4)
C(14)	-1932(18)	1357(13)	10603(7)	54(4)
C(15)	-1640(18)	1761(12)	9970(6)	50(4)
C(16)	-3743(18)	692(14)	11455(7)	57(4)
C(17)	-4962(17)	157(13)	11678(7)	58(4)
C(18)	-5236(19)	-399(15)	12333(6)	57(4)
C(19)	-6380(20)	-1092(16)	12468(7)	74(5)
C(20)	-6590(20)	-1747(17)	13074(7)	74(5)
C(21)	-5680(20)	-1751(18)	13545(6)	73(5)
C(22)	-4530(20)	-1033(18)	13417(7)	77(5)
C(23)	-4350(20)	-368(16)	12819(7)	68(5)
C(24)	-5810(20)	-2590(20)	14204(9)	120(8)
C(25)	-6867(16)	2003(15)	9390(7)	62(4)
C(26)	685(18)	1206(16)	10907(7)	64(4)
C(27)	5030(30)	4160(30)	3970(12)	153(10)

C(28)	5770(20)	4130(20)	3316(9)	97(7)
C(29)	6700(20)	4880(20)	3109(8)	151(12)
C(30)	7390(20)	5000(20)	2535(9)	116(9)
C(31)	7062(19)	4330(18)	2145(7)	68(5)
C(32)	6140(20)	3484(18)	2356(8)	79(5)
C(33)	5470(20)	3400(20)	2932(9)	86(6)
C(34)	7770(20)	4369(18)	1507(8)	87(6)
C(35)	8800(30)	4747(15)	1254(8)	106(9)
C(36)	9370(20)	4828(14)	592(7)	62(5)
C(37)	10960(20)	4787(14)	515(7)	61(4)
C(38)	8419(18)	5052(14)	92(8)	59(4)
O(12)	-830(50)	670(40)	3050(20)	302(17)
N	870(30)	1960(30)	2892(15)	170(10)
C(40)	1290(70)	1690(60)	3560(30)	300(30)
C(41)	1750(40)	2580(30)	2295(16)	172(12)
C(42)	0(50)	1240(40)	2660(20)	198(15)
O(10)	1820(50)	6190(30)	5220(20)	410(30)
C(39A)	13630(40)	4620(30)	884(18)	70(13)
O(9)	12000(17)	4626(14)	995(6)	48(6)
C(39B)	13780(70)	4390(50)	740(30)	57(18)
O(13)	6900(40)	5070(30)	-76(15)	81(13)

Table A.3. Bond lengths [Å] and angles [°] for Yb-PVDC-3.

Yb-Yb'	1.163(3)
Yb-O(10)	1.95(3)
Yb-O(2)#1	2.209(16)
Yb-O(1)	2.345(13)
Yb-O(6)#2	2.360(13)
Yb-O(7)#3	2.40(3)
Yb-O(8)	2.54(2)
Yb-O(5)#4	2.59(3)
Yb-O(7)	2.78(2)
Yb-C(27)	2.89(2)
Yb-O(11)	3.06(2)
Yb-Yb#3	4.001(6)
Yb'-O(11)	1.94(2)
Yb'-O(6)#2	2.024(14)
Yb'-O(8)	2.064(16)
Yb'-O(2)#1	2.181(19)
Yb'-O(1)	2.257(13)
Yb'-C(27)	2.83(2)
Yb'-O(10)	2.98(3)
Yb'-O(7)	3.08(2)
O(1)-C(1)	1.24(3)
C(1)-O(2)	1.21(3)
C(1)-C(2)	1.57(2)
C(2)-C(3)	1.35(3)
C(2)-C(7)	1.36(3)
O(2)-Yb'#1	2.181(19)
O(2)-Yb#1	2.209(16)
O(3)-C(11)	1.361(17)
O(3)-C(25)	1.423(17)
C(3)-C(4)	1.389(19)
C(3)-H(3A)	0.9400
O(4)-C(14)	1.376(18)
O(4)-C(26)	1.431(17)
C(4)-C(5)	1.37(2)
C(4)-H(4A)	0.9400
C(5)-C(6)	1.38(2)
C(5)-C(8)	1.487(19)
O(5)-C(24)	1.254(16)
O(5)-Yb#5	2.59(3)

C(6)-C(7)	1.36(2)
C(6)-H(6A)	0.9400
O(6)-C(24)	1.254(15)
O(6)-Yb'#2	2.024(13)
O(6)-Yb#2	2.360(13)
C(7)-H(7A)	0.9400
O(7)-C(27)	1.264(18)
O(7)-Yb#3	2.40(3)
C(8)-C(9)	1.32(2)
C(8)-H(8A)	0.9400
O(8)-C(27)	1.195(18)
C(9)-C(10)	1.462(17)
C(9)-H(9A)	0.9400
C(10)-C(15)	1.346(19)
C(10)-C(11)	1.41(2)
C(11)-C(12)	1.413(18)
C(12)-C(13)	1.361(19)
C(12)-H(12A)	0.9400
C(13)-C(14)	1.42(2)
C(13)-C(16)	1.475(18)
C(14)-C(15)	1.392(18)
C(15)-H(15A)	0.9400
C(16)-C(17)	1.35(2)
C(16)-H(16A)	0.9400
C(17)-C(18)	1.462(19)
C(17)-H(17A)	0.9400
C(18)-C(23)	1.36(2)
C(18)-C(19)	1.36(2)
C(19)-C(20)	1.39(2)
C(19)-H(19A)	0.9400
C(20)-C(21)	1.34(2)
C(20)-H(20A)	0.9400
C(21)-C(22)	1.39(2)
C(21)-C(24)	1.544(17)
C(22)-C(23)	1.37(2)
C(22)-H(22A)	0.9400
C(23)-H(23A)	0.9400
C(25)-H(25A)	0.9700
C(25)-H(25B)	0.9700

C(25)-H(25C)	0.9700
C(26)-H(26A)	0.9700
C(26)-H(26B)	0.9700
C(26)-H(26C)	0.9700
C(27)-C(28)	1.556(19)
C(28)-C(29)	1.27(3)
C(28)-C(33)	1.35(3)
C(29)-C(30)	1.37(3)
C(29)-H(29A)	0.9400
C(30)-C(31)	1.32(2)
C(30)-H(30A)	0.9400
C(31)-C(32)	1.35(2)
C(31)-C(34)	1.50(2)
C(32)-C(33)	1.37(2)
C(32)-H(32A)	0.9400
C(33)-H(33A)	0.9400
C(34)-C(35)	1.15(3)
C(34)-H(34A)	0.9400
C(35)-C(36)	1.51(2)
C(35)-H(35A)	0.9400
C(36)-C(38)	1.36(2)
C(36)-C(37)	1.40(2)
C(37)-O(9)	1.38(2)
C(37)-C(38)#6	1.41(2)
C(38)-O(13)	1.39(4)
C(38)-C(37)#6	1.41(2)
O(12)-C(42)	1.25(5)
N-C(42)	1.39(4)
N-C(40)	1.48(6)
N-C(41)	1.58(4)
C(39A)-O(9)	1.45(4)
C(39B)-O(13)#6	1.53(6)
O(13)-C(39B)#6	1.53(6)

Yb'-Yb-O(2)#1	73.3(5)
O(10)-Yb-O(2)#1	87.8(16)
Yb'-Yb-O(1)	71.2(5)
O(10)-Yb-O(1)	79.7(16)
O(2)#1-Yb-O(1)	87.6(5)

Yb'-Yb-O(6)#2	59.0(4)
O(10)-Yb-O(6)#2	132.7(15)
O(2)#1-Yb-O(6)#2	132.3(6)
O(1)-Yb-O(6)#2	78.7(6)
Yb'-Yb-O(7)#3	133.6(5)
O(10)-Yb-O(7)#3	63.7(15)
O(2)#1-Yb-O(7)#3	151.1(8)
O(1)-Yb-O(7)#3	92.1(6)
O(6)#2-Yb-O(7)#3	75.6(6)
Yb'-Yb-O(8)	53.4(6)
O(10)-Yb-O(8)	148.9(16)
O(2)#1-Yb-O(8)	75.4(6)
O(1)-Yb-O(8)	124.5(8)
O(6)#2-Yb-O(8)	75.6(5)
O(7)#3-Yb-O(8)	126.6(7)
Yb'-Yb-O(5)#4	139.8(5)
O(10)-Yb-O(5)#4	60.2(16)
O(2)#1-Yb-O(5)#4	80.8(5)
O(1)-Yb-O(5)#4	138.5(8)
O(6)#2-Yb-O(5)#4	136.4(6)
O(7)#3-Yb-O(5)#4	80.4(5)
O(8)-Yb-O(5)#4	90.9(8)
Yb'-Yb-O(7)	93.6(5)
O(10)-Yb-O(7)	120.5(16)
O(2)#1-Yb-O(7)	113.9(7)
O(1)-Yb-O(7)	149.5(6)
O(6)#2-Yb-O(7)	70.8(5)
O(7)#3-Yb-O(7)	79.2(7)
O(8)-Yb-O(7)	49.0(6)
O(5)#4-Yb-O(7)	69.3(7)
Yb'-Yb-C(27)	75.4(6)
O(10)-Yb-C(27)	134.7(17)
O(2)#1-Yb-C(27)	91.1(7)
O(1)-Yb-C(27)	145.5(8)
O(6)#2-Yb-C(27)	76.9(7)
O(7)#3-Yb-C(27)	104.9(7)
O(8)-Yb-C(27)	24.4(5)
O(5)#4-Yb-C(27)	74.9(9)
O(7)-Yb-C(27)	25.7(4)

Yb'-Yb-O(11)	12.1(5)
O(10)-Yb-O(11)	133.6(16)
O(2)#1-Yb-O(11)	68.6(7)
O(1)-Yb-O(11)	60.7(7)
O(6)#2-Yb-O(11)	64.9(6)
O(7)#3-Yb-O(11)	135.0(6)
O(8)-Yb-O(11)	63.9(7)
O(5)#4-Yb-O(11)	144.0(6)
O(7)-Yb-O(11)	105.7(7)
C(27)-Yb-O(11)	86.8(7)
Yb'-Yb-Yb#3	117.3(2)
O(10)-Yb-Yb#3	95.0(15)
O(2)#1-Yb-Yb#3	143.8(3)
O(1)-Yb-Yb#3	128.4(4)
O(6)#2-Yb-Yb#3	67.8(3)
O(7)#3-Yb-Yb#3	43.1(5)
O(8)-Yb-Yb#3	84.3(5)
O(5)#4-Yb-Yb#3	69.7(5)
O(7)-Yb-Yb#3	36.1(6)
C(27)-Yb-Yb#3	61.8(5)
O(11)-Yb-Yb#3	127.8(5)
Yb-Yb'-O(11)	160.7(8)
Yb-Yb'-O(6)#2	91.4(4)
O(11)-Yb'-O(6)#2	96.9(8)
Yb-Yb'-O(8)	99.8(8)
O(11)-Yb'-O(8)	96.8(11)
O(6)#2-Yb'-O(8)	94.6(6)
Yb-Yb'-O(2)#1	76.0(5)
O(11)-Yb'-O(2)#1	95.4(8)
O(6)#2-Yb'-O(2)#1	167.4(6)
O(8)-Yb'-O(2)#1	86.6(6)
Yb-Yb'-O(1)	79.6(6)
O(11)-Yb'-O(1)	83.4(9)
O(6)#2-Yb'-O(1)	88.1(6)
O(8)-Yb'-O(1)	177.2(7)
O(2)#1-Yb'-O(1)	90.6(6)
Yb-Yb'-C(27)	81.1(6)
O(11)-Yb'-C(27)	116.9(10)
O(6)#2-Yb'-C(27)	83.6(7)

O(8)-Yb'-C(27)	21.9(7)
O(2)#1-Yb'-C(27)	93.3(7)
O(1)-Yb'-C(27)	158.8(8)
Yb-Yb'-O(10)	21.6(10)
O(11)-Yb'-O(10)	139.2(13)
O(6)#2-Yb'-O(10)	102.5(11)
O(8)-Yb'-O(10)	116.7(13)
O(2)#1-Yb'-O(10)	66.0(11)
O(1)-Yb'-O(10)	62.0(11)
C(27)-Yb'-O(10)	100.8(12)
Yb-Yb'-O(7)	64.2(4)
O(11)-Yb'-O(7)	135.0(9)
O(6)#2-Yb'-O(7)	68.4(6)
O(8)-Yb'-O(7)	45.9(7)
O(2)#1-Yb'-O(7)	104.4(6)
O(1)-Yb'-O(7)	135.2(7)
C(27)-Yb'-O(7)	24.2(4)
O(10)-Yb'-O(7)	85.7(11)
C(1)-O(1)-Yb'	145.3(15)
C(1)-O(1)-Yb	131.0(17)
Yb'-O(1)-Yb	29.20(18)
O(2)-C(1)-O(1)	124.6(17)
O(2)-C(1)-C(2)	120(2)
O(1)-C(1)-C(2)	115(2)
C(3)-C(2)-C(7)	121.9(16)
C(3)-C(2)-C(1)	117(2)
C(7)-C(2)-C(1)	121(2)
C(1)-O(2)-Yb'#1	170.3(16)
C(1)-O(2)-Yb#1	139.6(16)
Yb'#1-O(2)-Yb#1	30.7(2)
C(11)-O(3)-C(25)	119.2(11)
C(2)-C(3)-C(4)	118.9(18)
C(2)-C(3)-H(3A)	120.6
C(4)-C(3)-H(3A)	120.6
C(14)-O(4)-C(26)	116.7(11)
C(5)-C(4)-C(3)	120.4(15)
C(5)-C(4)-H(4A)	119.8
C(3)-C(4)-H(4A)	119.8
C(4)-C(5)-C(6)	118.3(13)

C(4)-C(5)-C(8)	122.5(13)
C(6)-C(5)-C(8)	119.2(14)
C(24)-O(5)-Yb#5	127.1(19)
C(7)-C(6)-C(5)	121.5(18)
C(7)-C(6)-H(6A)	119.2
C(5)-C(6)-H(6A)	119.2
C(24)-O(6)-Yb'#2	165.9(15)
C(24)-O(6)-Yb#2	136.3(14)
Yb'#2-O(6)-Yb#2	29.5(2)
C(6)-C(7)-C(2)	118.9(17)
C(6)-C(7)-H(7A)	120.6
C(2)-C(7)-H(7A)	120.6
C(27)-O(7)-Yb#3	177(2)
C(27)-O(7)-Yb	81.8(17)
Yb#3-O(7)-Yb	100.8(7)
C(27)-O(7)-Yb'	66.5(14)
Yb#3-O(7)-Yb'	115.4(6)
Yb-O(7)-Yb'	22.11(18)
C(9)-C(8)-C(5)	123.2(15)
C(9)-C(8)-H(8A)	118.4
C(5)-C(8)-H(8A)	118.4
C(27)-O(8)-Yb'	118(2)
C(27)-O(8)-Yb	95(2)
Yb'-O(8)-Yb	26.9(3)
C(8)-C(9)-C(10)	124.5(14)
C(8)-C(9)-H(9A)	117.8
C(10)-C(9)-H(9A)	117.8
C(15)-C(10)-C(11)	118.0(12)
C(15)-C(10)-C(9)	123.8(14)
C(11)-C(10)-C(9)	118.2(13)
O(3)-C(11)-C(12)	124.1(13)
O(3)-C(11)-C(10)	116.6(11)
C(12)-C(11)-C(10)	119.3(14)
Yb'-O(11)-Yb	7.2(3)
C(13)-C(12)-C(11)	121.7(13)
C(13)-C(12)-H(12A)	119.2
C(11)-C(12)-H(12A)	119.2
C(12)-C(13)-C(14)	118.7(12)
C(12)-C(13)-C(16)	122.4(14)

C(14)-C(13)-C(16)	118.9(14)
O(4)-C(14)-C(15)	126.0(14)
O(4)-C(14)-C(13)	115.3(12)
C(15)-C(14)-C(13)	118.6(15)
C(10)-C(15)-C(14)	123.7(14)
C(10)-C(15)-H(15A)	118.2
C(14)-C(15)-H(15A)	118.2
C(17)-C(16)-C(13)	125.2(15)
C(17)-C(16)-H(16A)	117.4
C(13)-C(16)-H(16A)	117.4
C(16)-C(17)-C(18)	126.1(16)
C(16)-C(17)-H(17A)	117
C(18)-C(17)-H(17A)	117
C(23)-C(18)-C(19)	116.8(14)
C(23)-C(18)-C(17)	124.6(15)
C(19)-C(18)-C(17)	118.4(14)
C(18)-C(19)-C(20)	121.1(16)
C(18)-C(19)-H(19A)	119.5
C(20)-C(19)-H(19A)	119.5
C(21)-C(20)-C(19)	121.7(16)
C(21)-C(20)-H(20A)	119.2
C(19)-C(20)-H(20A)	119.2
C(20)-C(21)-C(22)	117.8(13)
C(20)-C(21)-C(24)	121.6(15)
C(22)-C(21)-C(24)	120.5(15)
C(23)-C(22)-C(21)	119.8(16)
C(23)-C(22)-H(22A)	120.1
C(21)-C(22)-H(22A)	120.1
C(18)-C(23)-C(22)	122.8(16)
C(18)-C(23)-H(23A)	118.6
C(22)-C(23)-H(23A)	118.6
O(6)-C(24)-O(5)	128.7(19)
O(6)-C(24)-C(21)	115.7(16)
O(5)-C(24)-C(21)	114.4(16)
O(3)-C(25)-H(25A)	109.5
O(3)-C(25)-H(25B)	109.5
H(25A)-C(25)-H(25B)	109.5
O(3)-C(25)-H(25C)	109.5
H(25A)-C(25)-H(25C)	109.5

H(25B)-C(25)-H(25C)	109.5
O(4)-C(26)-H(26A)	109.5
O(4)-C(26)-H(26B)	109.5
H(26A)-C(26)-H(26B)	109.5
O(4)-C(26)-H(26C)	109.5
H(26A)-C(26)-H(26C)	109.5
H(26B)-C(26)-H(26C)	109.5
O(8)-C(27)-O(7)	129(3)
O(8)-C(27)-C(28)	113(2)
O(7)-C(27)-C(28)	118(2)
O(8)-C(27)-Yb'	40.2(15)
O(7)-C(27)-Yb'	89.3(15)
C(28)-C(27)-Yb'	153.1(18)
O(8)-C(27)-Yb	61.1(17)
O(7)-C(27)-Yb	72.5(15)
C(28)-C(27)-Yb	162.7(18)
Yb'-C(27)-Yb	23.5(2)
C(29)-C(28)-C(33)	116.3(17)
C(29)-C(28)-C(27)	119(2)
C(33)-C(28)-C(27)	125(2)
C(28)-C(29)-C(30)	125(2)
C(28)-C(29)-H(29A)	117.3
C(30)-C(29)-H(29A)	117.3
C(31)-C(30)-C(29)	119.2(19)
C(31)-C(30)-H(30A)	120.4
C(29)-C(30)-H(30A)	120.4
C(30)-C(31)-C(32)	117.4(16)
C(30)-C(31)-C(34)	123.9(18)
C(32)-C(31)-C(34)	118.6(18)
C(31)-C(32)-C(33)	121.3(18)
C(31)-C(32)-H(32A)	119.4
C(33)-C(32)-H(32A)	119.4
C(28)-C(33)-C(32)	120.3(18)
C(28)-C(33)-H(33A)	119.8
C(32)-C(33)-H(33A)	119.8
C(35)-C(34)-C(31)	135(2)
C(35)-C(34)-H(34A)	112.4
C(31)-C(34)-H(34A)	112.4
C(34)-C(35)-C(36)	132(3)

C(34)-C(35)-H(35A)	114.1
C(36)-C(35)-H(35A)	114.1
C(38)-C(36)-C(37)	121.1(14)
C(38)-C(36)-C(35)	123.4(18)
C(37)-C(36)-C(35)	115.2(18)
O(9)-C(37)-C(36)	124.8(15)
O(9)-C(37)-C(38)#6	116.1(17)
C(36)-C(37)-C(38)#6	119.1(15)
C(36)-C(38)-O(13)	143(2)
C(36)-C(38)-C(37)#6	119.8(15)
O(13)-C(38)-C(37)#6	97.0(19)
C(42)-N-C(40)	122(4)
C(42)-N-C(41)	103(3)
C(40)-N-C(41)	130(4)
O(12)-C(42)-N	115(4)
Yb-O(10)-Yb'	12.7(5)
C(37)-O(9)-C(39A)	122.2(19)
C(38)-O(13)-C(39B)#6	125(3)

Symmetry transformations used to generate equivalent atoms:

#1 -x,-y+1,-z+1	#2 -x,-y,-z+2	#3 -x+1,-y+1,-z+1
#4 x+1,y+1,z-1	#5 x-1,y-1,z+1	#6 -x+2,-y+1,-z

Table A.4. Anisotropic displacement parameters ($Å^2 x\ 10^3$) for Yb-PVDC-3. The anisotropic displacement factor exponent takes the form: $-2\pi^2[\ h^2\ a^{*2}U^{11} + ... + 2\ h\ k\ a^*\ b^*\ U^{12}\ ]$.

	U^{11}	U^{22}	U^{33}	U^{23}	U^{13}	U^{12}
Yb	88(1)	125(3)	43(1)	-15(1)	41(1)	-37(1)
Yb'	107(2)	146(4)	36(1)	-6(1)	38(1)	-59(2)
O(1)	110(11)	280(20)	51(8)	-15(10)	48(8)	-75(13)
C(1)	105(17)	190(20)	23(9)	-10(12)	23(11)	-114(18)
C(2)	93(14)	125(17)	44(10)	-30(11)	39(11)	-73(14)
O(2)	125(13)	198(17)	26(6)	13(8)	7(7)	-88(12)
O(3)	63(7)	84(8)	33(5)	-9(5)	-2(5)	-9(6)
C(3)	106(14)	94(13)	28(8)	-8(8)	3(9)	-50(12)
O(4)	61(7)	92(8)	30(5)	-8(5)	5(5)	-24(6)
C(4)	101(13)	35(9)	42(8)	-4(7)	30(9)	-5(9)
C(5)	74(10)	42(9)	35(7)	-18(7)	19(8)	-21(8)
O(5)	220(20)	570(50)	54(9)	47(16)	-2(11)	-300(30)
C(6)	82(12)	84(12)	53(10)	-12(9)	23(9)	-24(10)
C(7)	67(12)	141(19)	46(10)	-31(12)	27(9)	-29(13)
O(7)	370(20)	123(13)	146(15)	31(12)	167(17)	-40(16)
C(8)	80(12)	56(10)	39(8)	-6(7)	9(8)	-2(9)
O(8)	107(12)	300(20)	106(12)	59(13)	54(10)	28(14)
C(9)	64(10)	44(9)	30(7)	10(6)	8(7)	-1(8)
C(10)	65(10)	40(8)	26(7)	-1(6)	1(7)	2(8)
C(11)	75(11)	41(9)	30(8)	-8(6)	17(8)	-6(8)
C(12)	45(8)	50(9)	40(8)	-8(7)	2(7)	-5(7)
C(13)	68(10)	32(8)	36(8)	-5(6)	15(8)	-4(7)
C(14)	72(11)	36(8)	48(9)	-6(7)	21(8)	-6(8)
C(15)	61(9)	33(8)	42(8)	7(6)	19(8)	4(7)
C(16)	62(10)	57(10)	44(8)	-4(7)	9(8)	-5(8)
C(17)	53(9)	52(10)	49(9)	13(7)	15(7)	5(8)
C(18)	67(10)	77(11)	28(8)	-13(7)	6(8)	-17(9)
C(19)	90(13)	85(13)	54(10)	-5(9)	9(9)	-49(11)
C(20)	96(13)	90(13)	43(9)	0(9)	25(9)	-55(11)
C(21)	93(13)	121(15)	18(7)	-18(8)	17(8)	-50(12)
C(22)	90(13)	119(15)	34(8)	-13(9)	19(8)	-57(12)
C(23)	73(11)	95(13)	45(9)	-18(9)	25(9)	-40(10)
C(25)	43(9)	71(11)	62(10)	-13(8)	-4(8)	11(8)
C(26)	63(11)	71(11)	57(10)	-16(8)	-6(8)	-8(9)
C(28)	112(16)	96(16)	61(12)	14(12)	56(12)	-12(13)
C(29)	270(30)	190(30)	43(11)	-49(14)	66(17)	-140(30)
C(30)	170(20)	150(20)	62(13)	-26(13)	36(14)	-114(19)
C(31)	63(11)	96(14)	38(9)	0(9)	0(8)	-19(10)

C(32)	95(14)	81(13)	61(11)	-15(10)	10(11)	-20(12)
C(33)	87(14)	99(15)	60(12)	19(11)	19(11)	-37(12)
C(34)	93(14)	89(14)	51(10)	7(9)	44(10)	18(11)
C(35)	170(20)	42(10)	58(11)	29(8)	58(13)	43(12)
C(36)	80(12)	49(10)	44(9)	-4(7)	24(9)	4(9)
C(37)	98(14)	41(9)	45(9)	-18(7)	-6(10)	-7(9)
C(38)	56(10)	35(9)	80(12)	-11(8)	-4(9)	5(8)
O(9)	55(10)	65(11)	29(9)	-25(7)	8(7)	-11(8)

Table A.5. Hydrogen coordinates (x 10^4) and isotropic displacement parameters ($Å^2$ x 10^3) for Yb-PVDC-3.

	x	y	z	U(eq)
H(3A)	-2005	5092	6729	87
H(4A)	-2463	4379	7791	74
H(6A)	1124	1459	7855	87
H(7A)	1636	2213	6822	99
H(8A)	-204	1791	8845	74
H(9A)	-3279	2916	8595	61
H(12A)	-5583	1371	10463	55
H(15A)	-623	1842	9849	60
H(16A)	-3028	754	11747	68
H(17A)	-5704	141	11385	70
H(19A)	-7026	-1128	12145	89
H(20A)	-7406	-2199	13154	89
H(22A)	-3872	-1003	13738	92
H(23A)	-3584	131	12742	82
H(25A)	-7484	2216	9011	93
H(25B)	-7303	2573	9662	93
H(25C)	-6870	1127	9604	93
H(26A)	1332	975	11279	96
H(26B)	678	2088	10701	96
H(26C)	1093	654	10624	96
H(29A)	6939	5384	3373	181
H(30A)	8082	5562	2419	140
H(32A)	5958	2940	2102	95
H(33A)	4790	2833	3063	103
H(34A)	7242	3994	1257	105
H(35A)	9396	5065	1505	127

A.2 REFERENCES

(1) In *APEX II software suite*; Bruker AXS: 2006.
(2) Sheldrick, G. M. *Acta Crystallogr. Sect. A* **2008**, *64*, 112-122.